Study of Heat and Mass transfer in Superfluid Helium in Confined Geometries

Andrea Vitrano

université PARIS-SACLAY

Study of Heat and Mass transfer in Superfluid Helium in Confined Geometries

Etude des transferts de masse et de chaleur en hélium superfluide en milieux confinés

Thèse de doctorat de l'université Paris-Saclay

École doctorale n° 576 Particules, Hadrons, Energie, Noyau, Instrumentation, Imagerie, Cosmos, et Simulation (PHENIICS)
Spécialité de doctorat: Physique des accélérateurs
Unité de recherche : Université Paris-Saclay, CEA, Département des Accélérateurs, de la Cryogénie et du Magnétisme, 91191, Gif-sur-Yvette, France.
Référent : Faculté des sciences d'Orsay

Thèse présentée et soutenue à Paris-Saclay, le 23/07/2021, par

Andrea VITRANO

Composition du Jury

Slawomir PIETROWICZ Professeur, Wroclaw University	Président
Luca BOTTURA Docteur (HDR), CERN	Rapporteur & Examinateur
Marco BRESCHI Professeur, University of Bologna	Rapporteur & Examinateur
Rob VAN WEELDEREN Docteur, CERN	Examinateur
Philippe BREDY E7 (HDR), CEA Paris-Saclay	Examinateur

Direction de la thèse

Bertrand BAUDOUY Docteur (HDR), CEA Paris-Saclay	Directeur de thèse

Thèse de doctorat

NNT : 2021UPASP057

Study of Heat and Mass Transfer in Superfluid Helium in Confined Geometries

Andrea Vitrano

Study of Heat and Mass Transfer in Superfluid Helium in Confined Geometries
Andrea Vitrano
PhD Thesis, Université Paris-Saclay, France
http://www.theses.fr/en/s202250

Layout: https://github.com/Flythe/Precious-Thesis-Template

Palettes: [116], [166], [10], [104]

Text fonts: Gentium Book Basic, Open Sans, Inconsolata.

EASITrain – European Advanced Superconductivity Innovation and Training. This Marie Skłodowska-Curie Action (MSCA) Innovative Training Networks (ITN) receives funding from the European Union's H2020 Framework Programme under grant agreement no. 764879.

Ai miei genitori,

per avermi dato la possibilità di inseguire i miei sogni

Abstract

Particle accelerators play a central role in the advancement of fundamental physics research. In circular accelerators such as the Large Hadron Collider (LHC) at CERN, the trajectory of the particle beams must be bent with magnetic fields. For this purpose, the LHC utilizes superconducting dipole magnets, which allow the electric current to flow without resistance. A cooling system of superfluid helium (He II) ensures the superconducting state by maintaining the magnets at temperatures below 2 K. However, the confined structures surrounding the dipole coils hinder the cooling process. The metal collars, which restrict the dipoles to counter the electromagnetic forces, are spaced 200 microns apart from each other. If the magnets lose the superconductive properties (i.e., during a magnet quench), the energy dissipated is such that helium undergoes drastic thermodynamic changes, causing the failure of the machine and severe damages to its components.

The present work focuses on the thermal phenomena occurring at this level of geometrical confinement in He II when subject to high heat fluxes. Experiments were conducted in a cryostat with pressurized He II at various bath temperatures. The tests consisted of applying a clamped heat flux in rectangular cross-section channels with high aspect ratios, resembling the gap between the collars. Numerous tests were carried out with different channel orientations and thicknesses. A thermo-fluid dynamic numerical model was developed to simulate the heat and mass transfer in He II. Novel dimensionless numbers were derived to validate the assumption at the basis of the single-fluid governing equations implemented in the model. The numerical model, which is based on the finite volume method, is capable of simulating transient conjugate heat transfer events in multi-dimensional geometries. Moreover, a novel algorithm was conceptualized to deal with the second and first-order phase transitions that helium undergoes above the critical heat fluxes. At atmospheric pressure, the second-order one (i.e., lambda transition) is associated with the threshold of the superfluid state, whereas the first-order one relates liquid helium to helium vapour.

The experiments in He II resulted in reliable temperature measurements with a precision uncertainty of around 0.12 %. The superfluid helium model was successfully validated against experimental data from both the literature and this work with a relative error around 1 %. The experiments that involved multiple helium phases revealed a significant dependence of the proportion between the different phases on the channel thickness and

orientation, as well as the initial temperature of the fluid. The speed at which the liquid helium-He II interface travels appears to be highly affected by the presence of a helium vapour film. At high heat fluxes, the phase change fronts propagate at a similar rate, indicating a strong correlation between the two. The phase transitions algorithm was tested at moderate heat fluxes in both subcooled liquid helium and He II. The comparison with the channel experiments showed satisfactory agreement in the temperature profiles and propagation of the phase change fronts with a relative error around 10 %. The computational model may constitute the basis of further development of the code for the simulation of events at greater pressure and temperature variations.

Résumé

Les accélérateurs de particules jouent un rôle central dans l'avancement de la recherche en physique fondamentale. Dans les accélérateurs circulaires tels que le Large Hadron Collider (LHC) du CERN, la trajectoire des faisceaux de particules doit être courbée par des champs magnétiques. À cette fin, le LHC utilise des aimants dipolaires supraconducteurs, qui permettent au courant électrique de circuler sans résistance. Un système de refroidissement à l'hélium superfluide (He II) assure l'état supraconducteur en maintenant les aimants à des températures inférieures à 2 K. Toutefois, les structures confinées qui entourent les bobines dipôlaires entravent le processus de refroidissement. Les colliers métalliques, qui permettent de contrer les forces électromagnétiques, sont espacés de 200 microns les uns des autres. Si les aimants perdent leurs propriétés supraconductrices (par exemple, lors d'un quench de l'aimant), l'énergie dissipée est telle que l'hélium subit des changements thermodynamiques drastiques, pouvant entraîner la défaillance de la machine et de graves dommages à ses composants.

Le présent travail se concentre sur les phénomènes thermiques en He II se produisant à ce niveau de confinement géométrique lorsqu'il est soumis à des flux de chaleur élevés. Des expériences ont été menées dans un cryostat en He II pressurisé à différentes températures de bain. Les essais ont consisté à appliquer un flux de chaleur de confinement dans des canaux de section rectangulaire avec des rapports d'aspect élevés, ressemblant à l'espace entre les colliers métalliques. De nombreux essais ont été réalisés avec différentes orientations et épaisseurs de canaux. Un modèle numérique dynamique thermo-fluide a été développé pour simuler le transfert de chaleur et de masse dans l'He II. De nouveaux nombres sans dimension ont été dérivés pour valider l'hypothèse à la base des équations gouvernantes monofluide mises en œuvre dans le modèle. Le modèle numérique, qui est basé sur la méthode des volumes finis, est capable de simuler des événements transitoires de transfert de chaleur conjugués dans des géométries multidimensionnelles. De plus, un nouvel algorithme a été conceptualisé pour traiter les transitions de phase de second et premier ordre que l'hélium subit au-dessus des flux de chaleur critiques. À la pression atmosphérique, la transition de second ordre (c'est-à-dire la transition lambda) est associée au seuil de l'état superfluide, tandis que la transition de premier ordre relie l'hélium liquide à la vapeur d'hélium.

Les expériences en He II ont permis d'obtenir des mesures de température fiables avec une incertitude de précision d'environ 0.12 %. Le modèle de l'hélium superfluide a été

validé avec succès par rapport aux données expérimentales de la littérature et de ce travail avec une erreur relative d'environ 1 %. Les expériences impliquant plusieurs phases de l'hélium ont révélé une dépendance significative de la proportion entre les différentes phases sur l'épaisseur et l'orientation du canal, ainsi que sur la température initiale du fluide. La vitesse à laquelle l'interface hélium liquide-He II se déplace semble être fortement affectée par la présence d'un film de vapeur d'hélium. À des flux de chaleur élevés, les fronts de changement de phase se propagent à une vitesse similaire, indiquant une forte corrélation entre les deux. L'algorithme des transitions de phase a été testé à des flux de chaleur modérés dans de l'hélium liquide sous-refroidi et de l'He II. La comparaison avec les expériences en canal a montré un accord satisfaisant dans les profils de température et la propagation des fronts de changement de phase avec une erreur relative d'environ 10 %. Le modèle de calcul peut constituer la base d'un développement ultérieur du code pour la simulation d'événements à des variations de pression et de température plus importantes.

Acknowledgements

This manuscript is the result of more than three years of scientific work carried out at the Cryogenics and Test Stations Laboratory (LCSE) of the Department of Accelerators, Cryogenics and Magnetism (DACM) within the Institute for Research on the Fundamental Laws of the Universe (IRFU) at the French Alternative Energies and Atomic Energy Commission (CEA) in Saclay (Paris). I would like to acknowledge in this brief paragraph the contributions of all the institutions and people who accompanied me on this challenging and fulfilling journey.

Firstly, I am grateful to the European Union's H2020 Framework Programme, which largely funded this work through the European Advanced Superconductivity Innovation and Training (EASITrain) network. I am also grateful to the CERN CryoLab and Rob Van Weelderen for proposing and supporting forward-looking experiments through a CERN-CEA collaboration. Additionally, I am grateful to the directorate of the IRFU and DACM for supporting my work during tough moments and a worldwide epidemic. In particular, I would like to thank Pierre Védrine, Philippe Brédy, Christophe Mayri, and Roser Vallcorba, who welcomed me to the world-class scientific research facilities of the DACM.

The international European network this project belongs to gave me the unique chance to grow as a researcher by collaborating with outstanding research centers and companies. In particular, I am grateful to the CERN CryoLab and Rob Van Weelderen for introducing me to the CERN scientific environment, where I could deepen my understanding of particle accelerator engineering. I am also grateful to CFD Direct Ltd and Will Bainbridge, whose exceptional knowledge of numerical methods enriched me with precious notions.

I am grateful to the internationally recognized scientists who accepted to be the jury members of my PhD defense: Slawomir Pietrowicz, Luca Bottura, Marco Breschi, Rob Van Weelderen, Philippe Brédy. I would like to thank them for their availability and willingness to review this manuscript, for their high-quality and fruitful feedback, and suggestions on both the present work and its further developments.

I am deeply grateful to the people who worked closely with me. In particular, I would like to thank Gilles Authelet for his technical support in the design process of the experimental setup. I would like to thank Vadim Stepanov for his kindness, invaluable technical competence and support throughout all the experimental work. I would like to thank most of all my mentor and supervisor Bertrand Baudouy, who welcomed me to the world of cryogenics, introduced me to the marvels of superfluidity, and supported

me inside and outside the laboratory with scientific and human advice throughout this journey.

I would like to thank the members of the LCSE and LEAS for the cheerful moments of leisure spent together. In particular, I would like to thank Gilles Authelet, Bertrand Baudouy, Romain Bruce, Tisha Dixit, Aurélien Four, Jean-Marc Gheller, Clément Hilaire, François-Paul Juster, Charles Mailleret, Vadim Stepanov. Special thanks go to Asun Barba Higueras and Valerio Calvelli, who helped me greatly in getting acquainted with the new environment and smoothed out the transition to this experience. I would also like to thank the administrative staff, Séverine Candau and Armelle Le Noa, and the IT team with Denis De Ménèzes, for their help and patience.

Last but not least, I would like to thank my family and friends for their constant and genuine support despite the distance, for believing in me in any circumstances and celebrating the successes throughout all these arduous years. I want to thank most of all Linn, a fundamental pillar of my happiness, for sharing every moment with me, putting up with me daily, cheering me up in difficult moments, and never giving up on me.

Andrea Vitrano
Gif-sur-Yvette
July 2021

Contents

List of Figures

List of Tables

Nomenclature

Acronyms

BEC	Bose-Einstein Condensate
CAE	Computer-Aided Engineering
CDS	Central-Difference Scheme
CFD	Computational Fluid Dynamics
CNS	Crank-Nicolson Scheme
FVM	Finite Volume Method
LHC	Large Hadron Collider
LHS	Left-Hand Side
PDE	Partial Differential Equation
PISO	Pressure-Implicit with Splitting of Operators
RHS	Right-Hand Side
SIMPLE	Semi Implicit Method for Pressure Linked Equations
US	Upwind Scheme

Dimensionless Numbers

$\mathcal{A}$	Thermo-mechanical effect number	$\Delta T_0 \rho^2 \rho_s^2 s^3 T_b^2 \left(\rho \rho_s s T_b v_0 - \rho_n q_0\right)^{-2}$
$\mathcal{B}$	Energy diffusion number	$0.5 \rho \rho_n q_0^2 \left(\rho \rho_s s T_b v_0 - \rho_n q_0\right)^{-2}$
$\mathcal{C}$	Mutual friction force number	$A_{GM} \rho_n \rho^2 q_0^3 D \rho_s^{-1} s^{-1} T_b^{-1} \left(\rho \rho_s s T_b v_0 - \rho_n q_0\right)^{-2}$
$\mathcal{E}$	Superfluid equivalent of the Euler number	$\Delta p_0 \rho \rho_s^2 s^2 T_b^2 \left(\rho \rho_s s T_b v_0 - \rho_n q_0\right)^{-2}$
$\mathcal{F}$	Superfluid equivalent of the Froude number	$\left(\rho \rho_s s T_b v_0 - \rho_n q_0\right) \left(\rho \rho_s s T_b \sqrt{g_0 D}\right)^{-1}$
Bo	Bond number	$D^2 g \left(\rho_l - \rho_v\right) \sigma^{-1}$

Co	Confinement number, Courant number	$Bo^{-\frac{1}{2}}$, $\mathbf{v}_f \cdot \mathbf{d}/\Delta t$
Di	Dimotakis number	$\rho_s A_{GM} v_{ns,0} D$
Eu	Euler number	$\Delta p_0 \rho^{-1} {v_0}^{-2}$
Fr	Froude number	$v_0 \left(g_0 D\right)^{-\frac{1}{2}}$

Greek Letters

$[\phi]$	unknowns array	-
α	thermal diffusivity, density ratio, volume fraction, expansivity	$m^2\ s^{-1}$, -, -, K^{-1}
β	constant depending on the momentum exchange cross-section	m
ϵ	quantum excitation energy	J
Γ	diffusivity	$m^2\ s^{-1}$
γ	weighing coefficient	-
κ	compressibility, interface curvature	Pa^{-1}, m^{-1}
λ	geometric factor	-
μ	roton effective mass, chemical potential, dynamic viscosity	kg, J kg^{-1}, Pa s
ϕ	Lennard-Jones potential, scalar quantity	J, -
ψ	numerical compressibility	$s^2\ m^{-2}$
ρ	density	$kg\ m^{-3}$
σ	thermal characteristic parameter of a solid, standard deviation, surface tension coefficient	W m^{-2} K^{-4}, -, N m^{-1}
τ	time to fully-developed quantum turbulence	s
θ	angle	rad
Δ	minimum roton energy	J

Latin Letters

$[A]$	coefficients matrix	-
$[b]$	constants array	-
$[x]$	unknowns array	-
$\dot{m}$	mass flux	$kg\ s^{-1}\ m^{-2}$

$\mathbf{C}$	distance vector between cell centroid and face	m
$\mathbf{D}$	pressure gradient coefficients vector	$\mathrm{m\,s^{-1}}$
$\mathbf{d}$	distance vector	m
$\mathbf{F}$	total force density vector	$\mathrm{N\,m^{-3}}$
$\mathbf{f}$	force vector	N
$\mathbf{g}$	gravitational acceleration vector	$\mathrm{m\,s^{-2}}$
$\mathbf{H}$	momentum equation coefficients vector	$\mathrm{m\,s^{-1}}$
$\mathbf{l}$	path vector	m
$\mathbf{n}$	normal vector	m
$\mathbf{q}$	heat flux vector	$\mathrm{W\,m^{-2}}$
$\mathbf{S}$	surface normal vector	$\mathrm{m^2}$
$\mathbf{v}$	velocity vector	$\mathrm{m\,s^{-1}}$
A	area, proportionality constant	$\mathrm{m^2}$, $\mathrm{W^4\,s\,m^{-8}}$
a	empirical coefficient, algebraic equation coefficients	-
A_{GM}	Gorter-Mellink coefficient	$\mathrm{m\,s\,kg^{-1}}$
b	source/sink coefficient	-
C	heat capacity	$\mathrm{J\,K^{-1}}$
c	sound speed, specific heat capacity, empirical constant	$\mathrm{m\,s^{-1}}$, $\mathrm{J\,kg^{-1}\,K^{-1}}$, -
D	hydraulic diameter	m
d	characteristic dimension, distance	m
E	energy	J
F	function of the elastic properties of a solid	-
f	heat conductivity function	$\mathrm{m^5\,K\,W^{-3}}$
g	specific Gibbs free energy	$\mathrm{J\,kg^{-1}}$
g_{peak}	empirical function	-
h	conductance, empirical function, specific enthalpy	$\mathrm{W\,m^{-2}\,K^{-1}}$, -, $\mathrm{J\,kg^{-1}}$
I	electrical current	A

K	kinetic energy, proportionality factor	J kg^{-1}, -
k	thermal conductivity	W m^{-1} K^{-1}
L	vortex line length	m
M	momentum diffusive-like parameter of superfluid helium	m^2 s^{-1} K^{-1}
m	mass, empirical power coefficient	kg, -
N	number of particles, number of measurements	-
n	conductive heat power law coefficient	-
P	momentum	kg m s^{-1}
p	pressure	Pa
Q	source/sink function	-
q	heat flux	W m^{-2}
R	electrical resistance, specific gas constant	Ω, J K^{-1} mol^{-1}
S	surface	m^2
s	specific entropy	J kg^{-1} K^{-1}
T	temperature	K
t	time, reduced temperature	s, -
U	total energy density	J m^{-3}
V	volume, voltage	m^3, V
v	velocity, specific volume	m s^{-1}, m^3 kg^{-1}
x	position coordinate, measured quantity	m, -
Y	mass fraction	-
y	variable computed from measurements	-
Z	compressibility factor	-

Physical Constants

$\hbar$	reduced Planck constant	$0.5h\pi^{-1} \approx 1.054571817 \times 10^{-34}$ J s
κ	quantum of circulation	$\approx 9.97 \times 10^{-4}$ cm^2 s^{-1}
π	Archimedes constant	≈ 3.14159

a_0	vortex core radius	$\approx 10^{-8}$ cm
g_0	gravitational acceleration	≈ 9.80665 m s^{-2}
h	Planck constant	$6.62607015 \times 10^{-34}$ J s
k_B	Boltzmann constant	$1.38064852 \times 10^{-23}$ J K^{-1}

Subscripts

0	ground state, standard condition, equilibrium, characteristic value
1	first sound
2	second sound
λ	lambda point, lambda transition related
ρ	constant density
σ	surface tension related
b	bath
c	critical
d	decay
eff	effective
f	cell face
$fict$	fictitious
g	generation
He	helium
I	reference to He I
i	incident
II	reference to He II
K	Kapitza
L	vortex line
l	liquid, linearly interpolated
min	minimum
N	neighbour cell centroid

n normal fluid component

nb neighbour cells

ns relative or mutual action between the two fluid components

P owner cell centroid

p constant pressure

ph phonon

s superfluid component, constant entropy, solid surface

sat saturation conditions

T constant temperature

t transmission

V constant volume

v vapour

Superscripts

$'$ correction

$*$ dimensionless, new iteration, peak, corrected

CHAPTER 1

Introduction

1.1 Background

Fundamental research in particle physics has yet many open problems to solve. Supersymmetry is only one of many conjectures that await experimental evidence to be proved or disproved [103]. In the search for answers to such unsolved problems, over the years various types of particle accelerators have been designed to investigate the basic structure of matter. Such devices boost charged particles via electromagnetic fields to reach high energies of several GeV. The particle beam eventually collides with either a target or another beam to produce radiations and fast decaying particles. The product of the collision is subject to a magnetic field in order for specific detectors to measure the characteristics of the newly generated particles. In facilities such as the Large Hadron Collider (LHC) at CERN, the accelerator is circular in order for the beam to cover more distance and hence gain more energy at each turn of the circumference. In this way, the LHC is able to accelerate particles at an energy of 6.5 TeV in its 26.7 km ring, where two beams are sped up in opposite directions in pipes situated 19 cm far from each other (see Fig. 1.1). A magnetic field must be then exerted to keep the beams in a circular

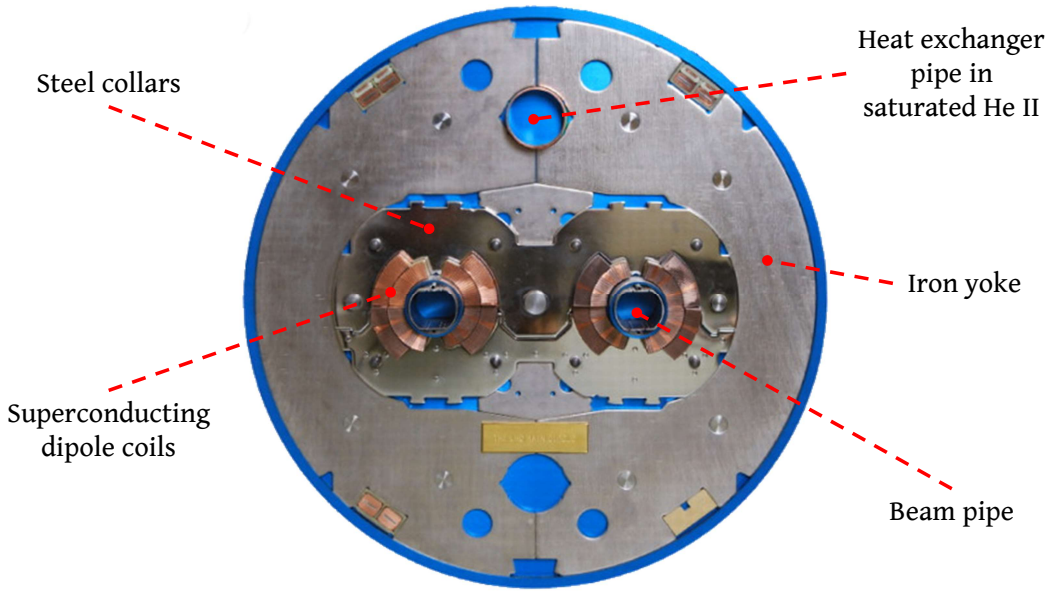

Figure 1.1: Cross section of the Large Hadron Collider at a location of bending magnets [49].

orbit. The bending magnets of the LHC operate at a magnetic field of 8.3 T with a nominal electric current of 12 kA. Because of the electrical resistance, the usage of an ordinary conductor such as copper would cause unaffordable power losses and require an enormous amount of wiring and energy to fulfill these requirements. For these reasons, the main magnet coils at the LHC are made out of niobium-titanium (NbTi), which acquires superconductive properties below certain critical values of current density, magnetic field,

and temperature. The superconductive state allows the electric current to flow without resistance, preventing the dissipation of energy. More specifically, the NbTi alloy becomes a superconductor below 9.3 K, which imposes cryogenic requirements on the accelerator technology. In order to maintain the desired operating conditions of the machine, the generated heat loads must be extracted by means of a working fluid below 2 K [96]. At this temperature, the obvious choice for the fluid was ^{4}He, a stable isotope of helium that has superfluid properties below 2.17 K at atmospheric pressure. Superfluid helium (He II) represents a great option as it does not solidify under its own vapour pressure, it is nearly inviscid, and it possesses an apparent thermal conductivity about two orders of magnitude higher than copper in the presence of a 10 kW/m^2 heat current. The LHC cooling system is schematized in Fig. 1.2. He II is utilized at 1.9 K both at saturation

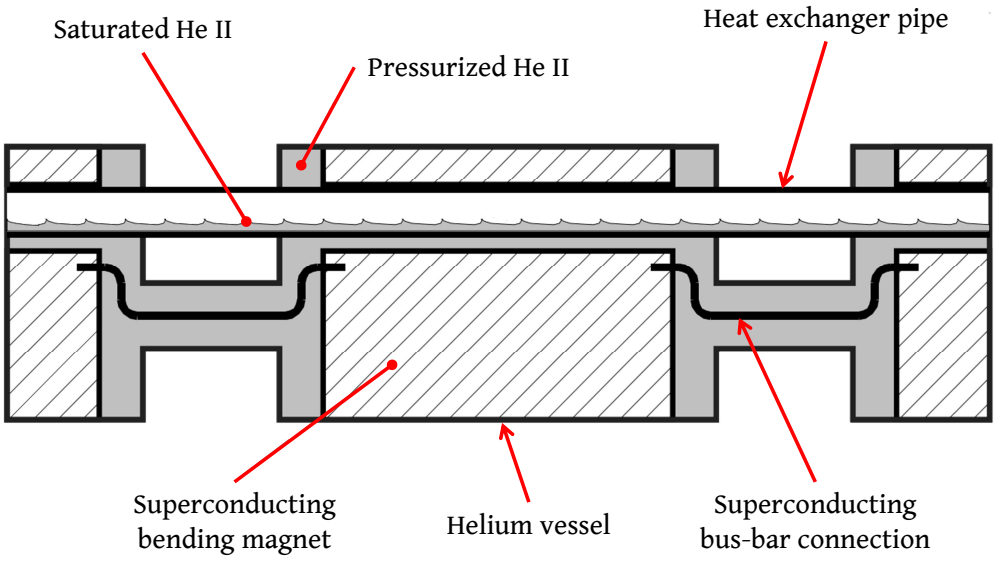

Figure 1.2: Scheme of the LHC helium cooling system [95].

and atmospheric pressure. The heat load is absorbed by the saturated two-phase mixture, which flows in forced-flow regime in the copper heat exchanger pipe also shown in Fig. 1.1. The phase stratification occurring in the pipe allows the liquid phase to be always directed towards the source of the load, which is effectively extracted by evaporation. The actual thermal link between the copper pipe and the superconducting magnets is a stagnant bath of pressurized He II, which quickly transports the load via conduction owing to its high thermal conductivity. The stagnant bath permeates the superconducting coils and the components surrounding the magnets. In particular, He II, because of its very low viscosity, is able to creep in between the polyimide tapes that are wrapped around the cables to insulate them electrically. He II is also present between the metal collars situated around the dipoles (see Fig. 1.1). The huge electric current that flows through the coils generates an outward horizontal Lorentz force of about 350 tonnes per meter for two poles. The

purpose of the collars consists of restricting the magnet dipoles to counter this force. They are made out of austenitic steel, which makes them essentially non-magnetic [15]. The helium vessel indicated in Fig. 1.2 is constituted by two outer stainless steel shells that are welded around the iron yoke (see Fig. 1.1), which, in turn, compresses the collars to secure the coils.

1.2 Motivation and Objectives

Despite the outstanding properties of He II, the confined structures surrounding the magnet coils hinder significantly the cooling process. The cable electrical insulation tapes create a network of micro-channels in the range of 10 µm, which constitutes a thermal barrier between the He II stagnant bath and the coils. The necessity to improve the magnet cooling incentivized extensive studies to investigate the heat transfer taking place in such conditions [108], [12], [131], [3], [61] and come up with novel tape configurations that enhance the heat removal [59].

Another example of thermal barrier is represented by the steel collars, which are stack in series along the two magnet dipoles and separated by spacings of about 200 µm (see Fig. 1.3). An inefficient heat extraction at this level of confinement may cause a

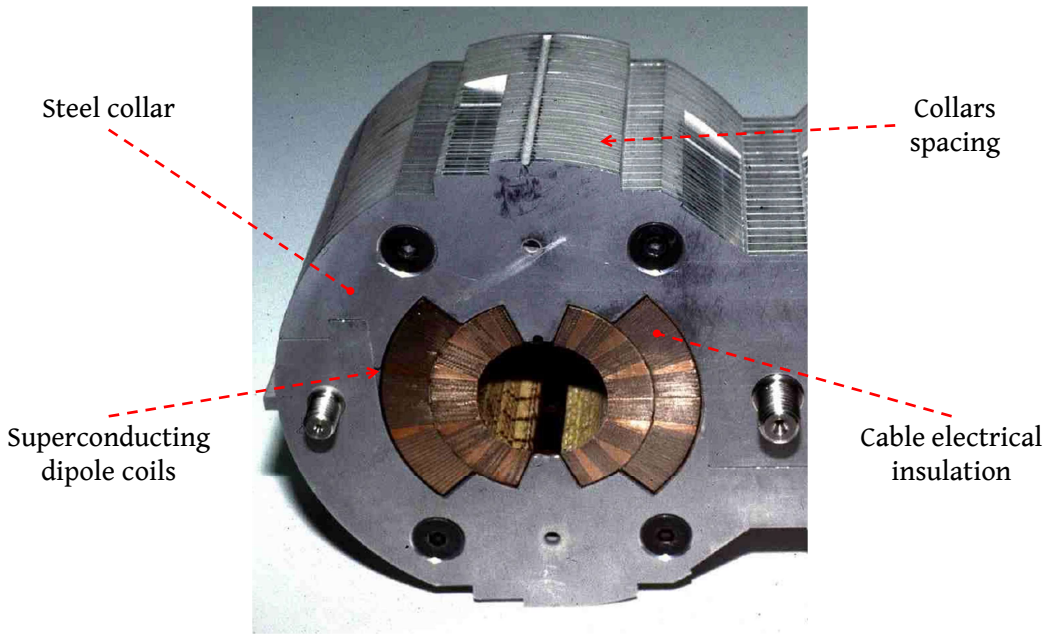

Figure 1.3: Detail of the steel collars stack around one superconducting magnet dipole [168].

temperature increase in the coil, upon which the coil may become resistive. This event, commonly known as “magnet quench”, can be caused by beam losses, which induce heat depositions that make the magnet’s temperature exceed locally the critical value. The enormous electric current flowing through the resistive part of the coils generates via the

Joule effect a heat burst that propagates quickly the quench throughout the whole magnet. The resulting energy dissipated is such that the pressurized He II instantly evaporates, causing an abrupt expansion that displaces and deforms the adjacent components. The risk of such sudden events motivated a series of studies to understand the quench phenomena and prevent them [20], [32], [60], [16].

Nevertheless, the phenomena arising in He II following high energy dissipations are yet to be clarified for geometrical confinements of few hundreds of microns. Unlike other fluids, ^{4}He has three different fluid states. Besides the already mentioned superfluid state, ^{4}He can take the form of either an ordinary viscous liquid or a gas depending on its thermodynamic conditions. It follows that there exist two phase transitions associated with ^{4}He as a fluid. Depending on the amount of energy released in He II contained in narrow spacings, one or both transitions can be triggered with consequent drastic changes in the thermophysical properties of the fluid. One goal of this work consists of unraveling the fundamental thermal phenomena occurring in He II when subject to high heat fluxes in thin geometries with high aspect ratios, resembling the space between the collars. The study focuses on the heat and mass transfer of superfluid helium as well as the other phases of ^{4}He. In particular, a wide range of heat fluxes will be tested to investigate the evolution and propagation of the helium phase transitions. In addition, the present work aims at developing a multi-dimensional numerical model capable of simulating the thermo-fluid dynamics of He II along with the conjugate heat transfer with solids. The rarely approached topic of simulation techniques applied to the helium phase changes will also be addressed in the effort to provide a computational tool to be coupled with magnet quench simulators.

This dissertation is divided into six chapters including this one. The second chapter (Ch. 2) is dedicated to the theory of superfluid helium. A summary of the historical background is reported before introducing the main features of helium superfluidity. The physical principles that determine He II thermo-fluid dynamics are presented and discussed together with the nature of its phase transitions. The third chapter (Ch. 3) describes the experimental and numerical tools utilized for this study. The characteristics of the test rig are detailed and illustrated along with the experimental setup. The main numerical methods that the chosen open-source toolbox is based on are explained. A brief overview of multiphase flow solvers is also discussed from the perspective of the problem under examination. The fourth chapter (Ch. 4) presents the methodology and results of the experiments and simulations conducted with helium in the superfluid state. The governing equations implemented in the code are derived and explained. The fifth chapter (Ch. 5) pertains to the study of the phase transitions in helium from both the experimental and numerical points of view. The multiphase model is described along with the algorithm utilized. The sixth and last chapter (Ch. 6) summarizes the results and draws the conclusions of this study.

CHAPTER 2

Thermo-Fluid Dynamics of Superfluid Helium

2.1 Quantum Fluid

Helium is the first element of the noble gas group in the periodic table and presents two stable isotopes, ^{3}He and ^{4}He. The latter is the most abundant in nature and the subject of this dissertation. Fig. 2.1 shows the different phases of ^{4}He in a pressure-temperature diagram. Below a certain temperature, called lambda temperature T_λ (2.17 K at saturated

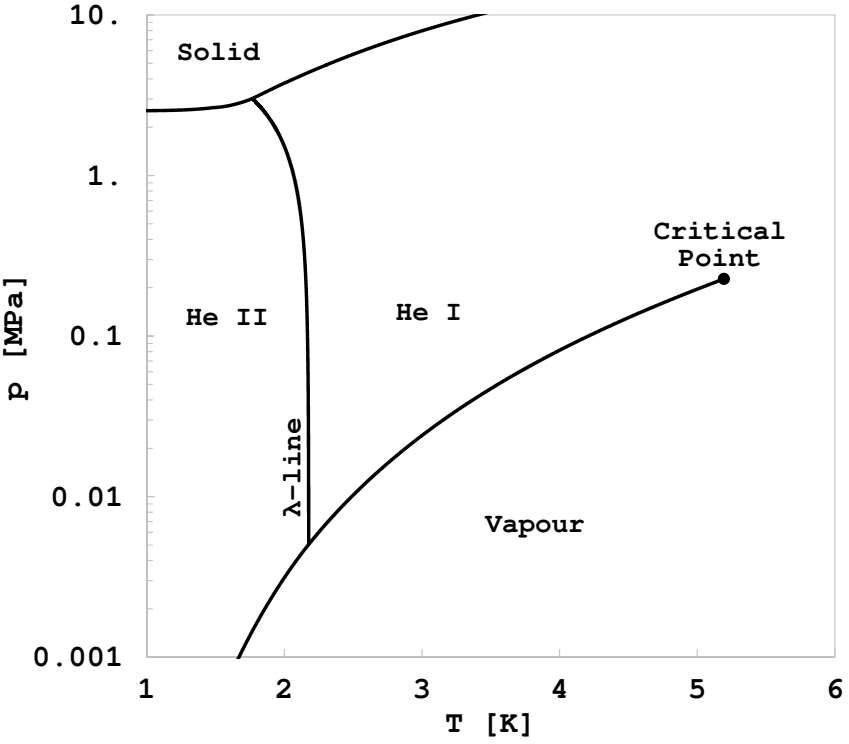

Figure 2.1: Phase diagram of ^{4}He.

vapour pressure), ^{4}He becomes a superfluid and acquires unique properties such as the ability to flow without resistance. The discovery of superfluidity is traditionally attributed to the experimental physicist Pyotr Kapitza, who found out in 1937 that the viscosity of ^{4}He below T_λ is "at least 1500 times smaller" than the one of normal liquid helium (He I) [80]. However, it must be said that several efforts were already made by other scientists who surely contributed in inspiring Kapitza's work [11]. During the same year, similar results were independently achieved by Allen and Misener [5], who would then have been officially mentioned 40 years later during the Nobel prize ceremony of Kapitza for his discoveries in low-temperature physics. In his paper, Kapitza suggests for the first time the name "superfluid", but he also mentions the terms "lambda point" and "helium II", both previously introduced by Keesom, Wolfke and Clusius [169], [82]. Keesom was able to find that, below the lambda point, ^{4}He shows anomalies such as a much larger thermal conductivity with respect to He I [83], which brought him to come up with the idea of a second state of ^{4}He, the so-called He II [84]. He also observed in 1930 the ability of He II

to flow through small capillaries that would be inaccessible by viscous fluids [85]. Another peculiar phenomenon was already observed in 1932 by McLennan, Smith, and Wilhelm, who noticed the disappearance of boiling in He II due to its high thermal conductivity [105].

This evidence pushed theoretical physicists to deepen the reasons for the strange behaviour of He II. In particular, an experiment conducted by Allen and Jones [4], in which the well-known "fountain effect" was observed for the first time, inspired Fritz London in creating the base of the theory of superfluid helium. The fountain effect manifests, for example, in a capillary filled with He II where the pressure increases following an applied heat flux, causing a rise of the helium level till the aperture of the capillary where a fountain-like flow develops. London associated this effect with the quantum statistics model developed by Einstein and based on the ideal gas statistics theory of Bose [18]. Einstein predicted in 1924 that for a Bose ideal gas, below a certain critical temperature T_c, a large fraction of the particles accumulates in the ground state giving rise to the so-called Bose-Einstein condensate (BEC) [47]. In 1938 London advanced the idea that He II obeys the Bose-Einstein statistics because of its high zero point motion of the atoms and, therefore, can be considered as a quantum fluid [99]. The zero point energy $\Delta E/k_B$ is the lowest possible energy of a quantum system and can be evaluated using the Heisenberg uncertainty principle through the kinetic energy uncertainty ΔE [158]:

$$\Delta P \Delta x \simeq \hbar, \tag{2.1a}$$

$$\Delta E \simeq \frac{(\Delta P)^2}{2m}, \tag{2.1b}$$

$$\frac{\Delta E}{k_B} \simeq \frac{\hbar^2}{2mk_B\,(\Delta x)^2} \approx 24\,\mathrm{K}, \tag{2.1c}$$

where $\hbar$ is the reduced Planck constant, P is the momentum associated with the atom mass m, k_B is the Boltzmann constant and Δx is the position uncertainty of an atom in the solid helium lattice structure. For ^{4}He, the zero point energy is much larger than the intermolecular forces, which can be estimated through the Lennard-Jones attractive potential energy ($\phi_{He}/k_B \approx 10$ K) [88]. This fact has the impressive consequence that ^{4}He does not solidify under its own vapour pressure as the temperature is lowered towards absolute zero. In order to achieve the solid state, an external pressure of at least 2.5 MPa must be exerted.

According to the Bose-Einstein statistics, the ground state fraction of the population N_0/N depends on the temperature:

$$\frac{N_0}{N} = \begin{cases} 1 - \left(\dfrac{T}{T_c}\right)^{\frac{3}{2}}, & \text{for } T \leq T_c, \quad (2.2a) \\ 0, & \text{for } T > T_c. \quad (2.2b) \end{cases}$$

It can be shown that, for the case of a Bose ideal gas as dense as ^{4}He, T_c is about 3.14 K [158]. Although its proximity to T_λ, the discrepancy suggests that He II cannot be entirely assumed as an ideal BEC because of its strong interactions between atoms. This

is supported, for instance, by the fact that, unlike a BEC, the transition between He I and He II is a second-order phase change. As explained in detail in Section 2.4, a second-order phase transition involves no latent heat and hence the two phases cannot coexist.

In 1937 the physicist László Tisza, trying to escape the Hungarian fascist persecution, moved to Paris, where he met London who was working at the "Institut Henri Poincaré". This encounter has great importance for the theory of superfluid helium because Tisza, inspired by the ideas of London about the quantum nature of He II, laid the foundation of what nowadays is widely used to describe the hydrodynamics of superfluid helium — the two-fluid model. He proposed for the first time that He II can be thought of as a mixture of two components: a normal fluid that behaves like a classical viscous fluid and a superfluid constituted by the quantum ground state population [154]. The normal component carries all the thermal energy and the superfluid component has no entropy (no internal energy) and no viscosity, which also means that the superfluid has to be irrotational. Moreover, each of the components is associated with a velocity that is independent of the other. Tisza also predicted the existence of "temperature waves" in He II that propagate as a result of entropy fluctuations in the fluid [153]. These temperature waves would have been referred to as "second sound" a few years later by Lev Landau, the physicist who developed a complete hydrodynamic model for He II starting from Tisza's two-fluid concept. In 1941 Landau published a theory based on the breakthrough idea that the motion of He II particles is quantized in elementary excitations [93], the set of which characterizes the energy spectrum of helium, shown in Fig. 2.2. The energy of these excitations depends on the momentum of energy carriers defined as quanta. Landau's model comprises two types of them: long-wavelength quanta (phonons), which are the typical longitudinal sound waves present in any liquid, and short-wavelength quanta of higher momentum and energy called rotons. Their energy ϵ is given by

$$\epsilon = \begin{cases} cP, & \text{for phonons,} \quad (2.3a) \\ \Delta + \dfrac{(P - P_0)^2}{2\mu}, & \text{for rotons,} \quad (2.3b) \end{cases}$$

where c is the speed of sound and Δ, P_0, and μ are spectrum parameters determined via neutron scattering experiments. In particular, Δ and μ are respectively the minimum energy and the effective mass of a roton [87]. Energy dissipation in superfluid helium can result just from the emissions of these excitations. Since in a quantum fluid these excitations are emitted in a discrete way, in order for the fluid to be excited there must be a minimum amount of energy below which ^{4}He is a frictionless superfluid. If one considers He II flowing in a capillary at zero temperature, the minimum value of energy corresponds to a critical velocity v_c, above which superfluidity disappears, defined as

$$v_c = \left.\frac{\epsilon}{P}\right|_{min}. \quad (2.4)$$

Therefore, a superfluid is characterized by the condition $v_c \neq 0$. The value of v_c at zero temperature (≈ 60 m/s) was calculated by Landau and can be derived in Fig. 2.2 from a

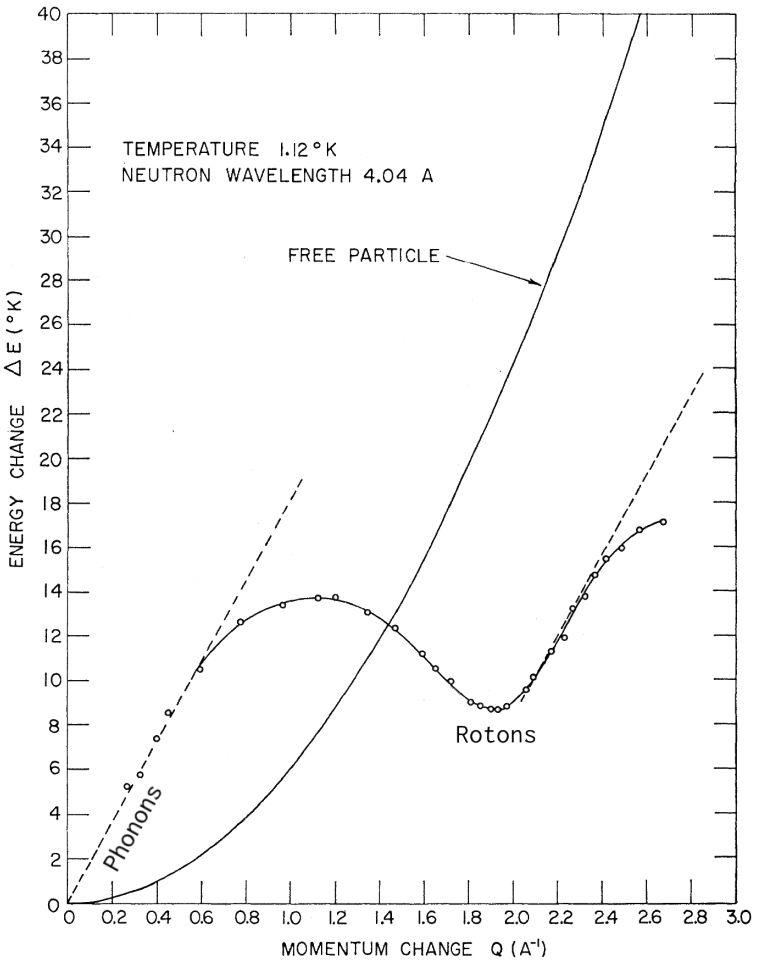

Figure 2.2: Experimental results of the energy spectrum of the elementary excitations in liquid helium obtained from neutron scattering [67]. The free particle curve represents the theoretical dispersion for free helium atoms at absolute zero.

straight line passing through the origin and the roton minimum of the curve. Above this velocity, He II has non-null vorticity, which means that the fluid is no more irrotational.

2.1.1 Two-Fluid Model

The quantum excitations present in He II give rise to two independent motions. The aforementioned two-fluid model captures the fluid mechanics of these motions. Each of them is associated with one of the two components of He II: the normal fluid and the superfluid. The normal fluid is characterized by the density ρ_n and the superfluid by ρ_s, which are related to the total density ρ of the liquid by

$$\rho = \rho_n + \rho_s. \tag{2.5}$$

The mass flux density of He II can be thus expressed as

$$\rho \mathbf{v} = \rho_n \mathbf{v}_n + \rho_s \mathbf{v}_s. \tag{2.6}$$

Eq. (2.6) suggests another peculiar feature of He II. Because of the two-motion nature of He II, a zero net mass flow (i.e., the LHS of Eq. (2.6) is equal to zero) does not imply that the fluid is static. Instead, from Eq. (2.6) follows that the two components can still flow in opposite directions giving rise to an internal convection known as "counterflow". The continuity equation for He II can be obtained from the principle of mass conservation:

$$\frac{\partial \rho}{\partial t} + \boldsymbol{\nabla} \cdot (\rho_n \mathbf{v}_n + \rho_s \mathbf{v}_s) = 0, \tag{2.7}$$

where t is time. A complete set of equations for He II can be achieved by deriving the Navier-Stokes equations for the two components.

In absence of dissipation, it is convenient to consider that the superfluid is accelerated by a thermodynamic driving force represented by the gradient of the chemical potential μ:

$$\frac{\partial \mathbf{v}_s}{\partial t} + (\mathbf{v}_s \cdot \boldsymbol{\nabla})\, \mathbf{v}_s = -\boldsymbol{\nabla} \mu. \tag{2.8}$$

The RHS of Eq. (2.8) can be derived from the expression of the total energy density U [126]:

$$U = U_0 + \mathbf{v}_s \cdot (\rho_n \mathbf{v}_{ns}) + \frac{1}{2} \rho \mathbf{v}_s^2, \tag{2.9}$$

where $\mathbf{v}_{ns}$ is the relative velocity between the normal and the superfluid component ($\mathbf{v}_{ns} \equiv \mathbf{v}_n - \mathbf{v}_s$) and U_0 is defined by the thermodynamic identity

$$\mathrm{d}U_0 = \mu \, \mathrm{d}\rho + T \, \mathrm{d}\left(\rho s\right) + \mathbf{v}_{ns} \cdot \mathrm{d}\left(\rho_n \mathbf{v}_{ns}\right), \tag{2.10}$$

where s is the specific entropy. The last term on the RHS of Eq. (2.10) shows that the velocity can be expressed by the derivative of the energy with respect to the momentum [94]. Let us consider the definition of the pressure p:

$$p = -\frac{\partial \left(UV\right)}{\partial V}, \tag{2.11}$$

where V is the volume. From Eqs. (2.9), (2.10) and (2.11) it is possible to obtain

$$\mathrm{d}p = \rho \, \mathrm{d}\mu + \rho s \, \mathrm{d}T + \left(\rho_n \mathbf{v}_{ns}\right) \cdot \mathrm{d}\mathbf{v}_{ns} \, . \tag{2.12}$$

Therefore, isolating the gradient of the chemical potential and using vector calculus identities, Eq. (2.8) becomes

$$\frac{\partial \mathbf{v}_s}{\partial t} + (\mathbf{v}_s \cdot \boldsymbol{\nabla})\, \mathbf{v}_s = s \boldsymbol{\nabla} T - \frac{1}{\rho} \boldsymbol{\nabla} p + \frac{\rho_n}{2\rho} \boldsymbol{\nabla} v_{ns}^2. \tag{2.13}$$

The total fluid momentum equation can be written as the incompressible form of the Navier-Stokes equation with the viscous term being associated with the normal component only:

$$\frac{\partial \mathbf{v}}{\partial t} + (\mathbf{v} \cdot \boldsymbol{\nabla})\, \mathbf{v} = \frac{\mu}{\rho} \nabla^2 \mathbf{v}_n - \frac{1}{\rho} \boldsymbol{\nabla} p, \tag{2.14}$$

where μ is the dynamic viscosity. Substituting Eq. (2.6) into Eq. (2.14) yields:

$$\rho_n \frac{\partial \mathbf{v}_n}{\partial t} + \rho_s \frac{\partial \mathbf{v}_s}{\partial t} + \rho_n \left(\mathbf{v}_n \cdot \boldsymbol{\nabla}\right) \mathbf{v}_n + \rho_s \left(\mathbf{v}_s \cdot \boldsymbol{\nabla}\right) \mathbf{v}_s = \mu \nabla^2 \mathbf{v}_n - \boldsymbol{\nabla} p. \tag{2.15}$$

The momentum equation for the normal component can be derived using Eqs. (2.13) and (2.15):

$$\frac{\partial \mathbf{v}_n}{\partial t} + \left(\mathbf{v}_n \cdot \boldsymbol{\nabla}\right) \mathbf{v}_n = \frac{\mu}{\rho_n} \nabla^2 \mathbf{v}_n - \frac{\rho_s}{\rho_n} s \boldsymbol{\nabla} T - \frac{1}{\rho} \boldsymbol{\nabla} p - \frac{\rho_s}{2\rho} \boldsymbol{\nabla} v_{ns}^2. \tag{2.16}$$

Eqs. (2.13) and (2.16) form the Navier-Stokes equations for incompressible He II valid within the so-called Landau regime, that is, when the superfluid velocity is below the critical value (Eq. (2.29)).

It is easy to picture the driving force of the counterflow by considering the linearized Euler's equation (i.e., the inviscid form of Eq. (2.14)), in which we neglect the quadratic term in the velocity ($\rho \partial \mathbf{v}/\partial t = -\boldsymbol{\nabla} p$). Substituting for the pressure gradient in Eq. (2.13) and neglecting again the quadratic terms, we obtain

$$\rho_n \frac{\partial \mathbf{v}_{ns}}{\partial t} = -\rho s \boldsymbol{\nabla} T. \tag{2.17}$$

It is clear from Eq. (2.17) that a temperature gradient generates counterflow. Moreover, in absence of dissipation, the relative motion of the two components is reversible and the resulting entropy conservation can be expressed by

$$\frac{\partial \left(\rho s\right)}{\partial t} = -\boldsymbol{\nabla} \cdot \left(\rho s \mathbf{v}_n\right), \tag{2.18}$$

where only the velocity of the component carrying energy appears. Eq. (2.18) implies that at zero net mass flow the heat flux $\mathbf{q}$ is given by

$$\mathbf{q} = \rho s T \mathbf{v}_n = \rho_s s T \mathbf{v}_{ns}. \tag{2.19}$$

The two-fluid model is particularly good at explaining some of the impressive macroscopic phenomena arising in He II as a manifestation of its quantum nature. The main ones are described in the following sub-sections.

2.1.1.1 Thermo-Mechanical Effect

Let us consider the experimental apparatus of Fig. 2.3. A vessel with a capillary tube is submerged in a He II bath. The bottom part of the tube is filled with semi-permeable materials that connect the bath to the internal part of the vessel. If the tube is heated up, for example, with light beams, a flow builds up through the capillary and generates a fountain at the upper exit of the tube. It is possible to explain this behaviour through Eq. (2.13). At equilibrium, the velocity does not change with time (i.e., $\partial \mathbf{v}_s/\partial t = 0$). Moreover, in Landau regime, the velocities are quite small and hence the terms that are quadratic in the velocity can be neglected. Eq. (2.13) becomes thus

$$\mathrm{d}p = \rho s \, \mathrm{d}T \,. \tag{2.20}$$

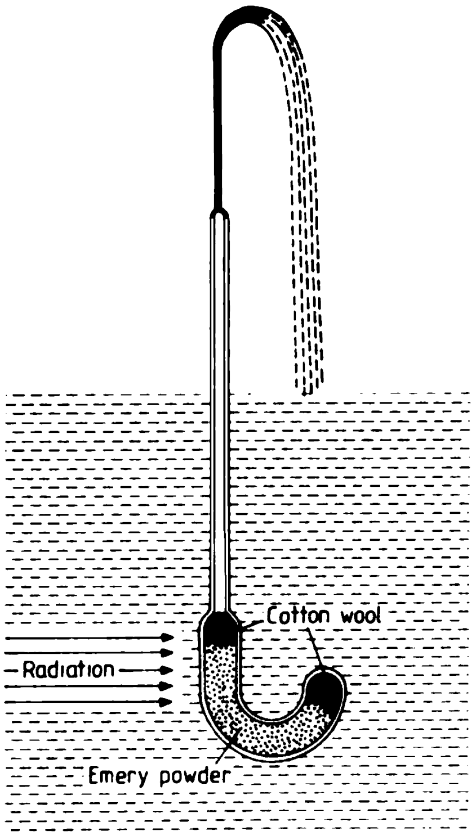

Figure 2.3: Schematic representation of the experimental apparatus used by Allen and Jones [4] to show the fountain effect [167].

Eq. (2.20) is named London's equation and shows that a temperature gradient causes a pressure difference in the superfluid. The normal component of He II, being the only one with an associated entropy, flows towards the zone at a lower temperature. The superfluid component, because of the counterflow, goes in the opposite direction driven by the pressure gradient. This phenomenon was called thermo-mechanical effect by London [98] and represents the base of the fountain effect discovered by Allen and Jones [4]. When the vessel in Fig. 2.3 is heated up, a temperature gradient is established throughout the tube. The temperature difference between the He II inside and outside the vessel causes a pressure difference that drives the superfluid component into the vessel. Since the porous membrane obstacles the flow of the viscous component towards the bath, the superfluid is pushed into the capillary and, if the driving pressure is higher than the hydrostatic head, rushes out with a fountain-like flow.

It is straightforward that, viceversa, if a pressure drop is established between two He II regions connected by a microcapillary tube (thus accessible by the superfluid component only), a temperature difference between the regions develops. This is another aspect of the same phenomenon and is named mechano-caloric effect. It is possible to interpret this effect also by considering that, when the superfluid is forced to flow by an applied external pressure towards a different region, the concentration of the superfluid component in that

region increases. Since the superfluid carries no energy, the total entropy in that region decreases, making the temperature drop. The mechano-caloric effect thus means that in He II it is possible to induce a heat transfer by forcing the superfluid to flow.

Another phenomenon related to the thermo-mechanical effect is the so-called Rollin film, named after the scientist who first explained its origin [132]. Let us consider the scheme in Fig. 2.4 representing one of the first experiments that showed the Rollin film. An empty beaker is submerged in a saturated He II bath. The beaker starts to be filled

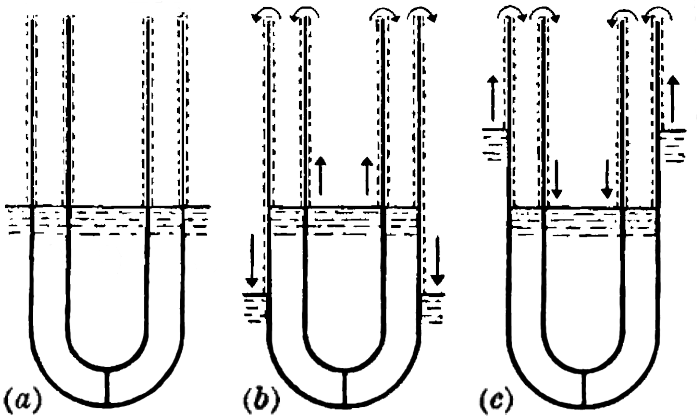

Figure 2.4: Scheme of the beaker experiment conducted by Daunt and Mendelssohn [41]: (a) equilibrium state, (b) beaker emptying, (c) beaker filling.

with helium (Fig. 2.4c) till the level equilibrium with the bath is reached (Fig. 2.4a). When the beaker is lifted from the bath, the helium starts to drop outside of the beaker into the bath trying to equalise the level (Fig. 2.4b). This mechanism can be explained through the properties of He II films. The surfaces of a container filled with a liquid at saturation are normally covered with a thin layer of the liquid being in equilibrium with its saturated vapour. In the case of He II, this film is able to move because of the frictionless superfluid component. If the helium levels inside and outside the beaker are not equal, the resulting hydrostatic head forces the helium to flow towards the lower level via the film that connects the beaker and the bath. The thermo-mechanical effect implies that, because of the pressure difference established between the two environments, the Rollin film is able to transmit heat flow.

2.1.1.2 Second Sound

The existence of two independent motions brings to unique properties of the sound propagation in He II. The two-fluid model is able to describe the sound mechanism in He II through the two equations presented below. One of these equations can be obtained by combining Eq. (2.7) with the linearized Euler's equation to give

$$\frac{\partial^2 \rho}{\partial t^2} = \nabla^2 p. \tag{2.21}$$

Let us take the divergence of Eq. (2.17) and substitute for $\boldsymbol{\nabla} \cdot \mathbf{v}_s$ from the steady-state version of the continuity equation (i.e., ρ does not vary with time) (Eq. (2.7)):

$$\frac{\rho_n}{\rho_s} \frac{\partial}{\partial t} (\rho \boldsymbol{\nabla} \cdot \mathbf{v}_n) = -\rho s \nabla^2 T. \tag{2.22}$$

Using the entropy conservation equation (Eq. (2.18)) and assuming small variations of s yields

$$\frac{\partial^2 s}{\partial t^2} = \frac{\rho_s}{\rho_n} s^2 \nabla^2 T. \tag{2.23}$$

Eqs. (2.21) and (2.23) form the system of equations that describes the sound propagation in He II. If we consider the variation of pressure and temperature in terms of entropy and density,

$$\mathrm{d}p = \left(\frac{\partial p}{\partial \rho}\right)_s \mathrm{d}\rho + \left(\frac{\partial p}{\partial s}\right)_\rho \mathrm{d}s\,, \tag{2.24a}$$

$$\mathrm{d}T = \left(\frac{\partial T}{\partial \rho}\right)_s \mathrm{d}\rho + \left(\frac{\partial T}{\partial s}\right)_\rho \mathrm{d}s\,, \tag{2.24b}$$

it is possible to express the solution of the system in the form of plane waves [167]:

$$\left(\frac{c^2}{c_1^2} - 1\right)\left(\frac{c^2}{c_2^2} - 1\right) = \frac{C_p - C_V}{C_p}. \tag{2.25}$$

In Eq. (2.25), c_1 is the ordinary sound speed (also called first sound) and c_2 is the so-called second sound. The speeds c_1 and c_2 are the solutions of the wave equations (2.21) and (2.23) respectively. Since the heat capacities of He II C_p and C_V, respectively at constant pressure and volume, are almost equal, the RHS of Eq. (2.25) can be set to zero and the sound speed c can assume two possible values, either c_1 or c_2:

$$c_1 = \sqrt{\left(\frac{\partial p}{\partial \rho}\right)_s}, \qquad \text{first sound,} \tag{2.26a}$$

$$c_2 = s\sqrt{\frac{\rho_s}{\rho_n}\left(\frac{\partial T}{\partial s}\right)_\rho}, \quad \text{second sound.} \tag{2.26b}$$

Eqs. (2.26) manifest the intrinsic difference between the two sound modes: the first sound propagates in the form of density waves driven by pressure variations, while the second sound propagates as thermal waves driven by temperature variations. Eq. (2.26a) shows that the first sound occurs in absence of entropy fluctuations, that is, when the temperature gradient is zero. It follows from Eq. (2.17) that the velocities of the two components equal each other and the fluid moves as a whole (i.e., the fluid components are in phase). On the other hand, second sound occurs at constant density, which means from the continuity equation that the total velocity is zero and the two components move in counterflow and out of phase. The two modes of sound propagation are related to each other by terms associated with the expansion coefficient, which are small enough to be neglected though. It is interesting to think about the second sound from the point of view of

the elementary excitations. Considering again Eq. (2.3a) in terms of second sound implies that temperature fluctuations cause oscillations in the excitation density. Therefore, the second sound can be viewed as the ordinary sound of the quantized excitations [87].

The implications of the two-fluid model about the sound propagation in He II were experimentally confirmed in various observations, the first of which was conducted by Peshkov [123]. The speed of first and second sound was measured to be roughly 240 m/s and 20 m/s (between 1 K and 2 K) respectively.

2.1.2 Thermophysical Properties

The quantum excitation theory and the two-fluid model allow to derive the temperature and pressure dependence of the thermophysical properties of liquid helium. The values of the thermophysical properties represented as a function of temperature in the figures below are taken from the commercial database HEPAK© [68]. From the contributions of phonons and rotons in the excitation spectrum it is possible to obtain expressions for the state properties of He II. Fig. 2.5 shows the density of the total fluid along with the density fraction of each component that constitutes it. The normal fluid density fraction can be

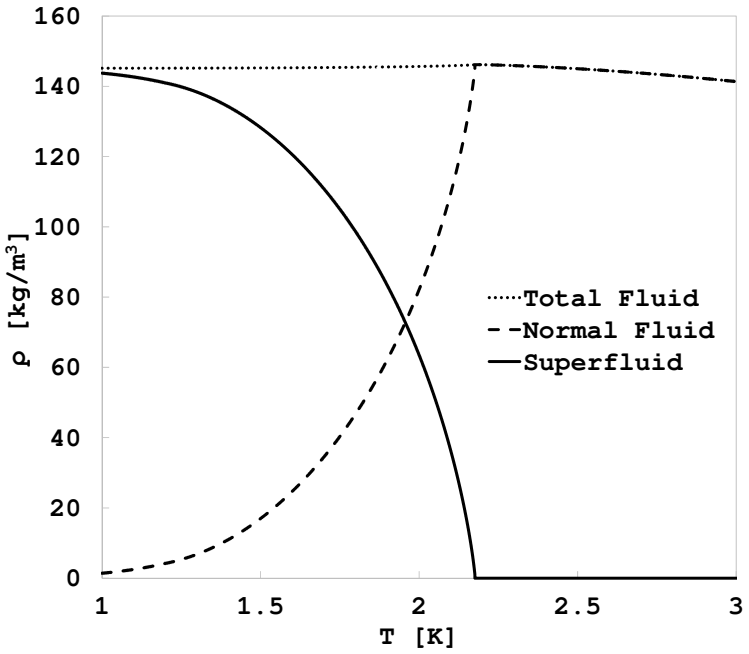

Figure 2.5: He II density as a function of temperature at the saturated vapour pressure.

extrapolated from the entropy temperature dependence by considering that the entropy associated with the total fluid corresponds to the one of the normal component (see Eq. (2.18)). The superfluid density follows directly from Eq. (2.5) and vanishes at T_λ, where helium turns into an ordinary liquid. Since entropy is a strong function of temperature, at 1 K He II is constituted by the superfluid already for the 99%. He II has a maximum density just above the lambda temperature T_λ. Below T_λ, He II exhibits a negative expansivity that

goes to zero towards absolute zero. At higher pressures, the energy gap Δ in the Eq. (2.3b) for the roton energy decreases [157]. Since the portion of the normal fluid density due to the rotons is proportional to the inverse of the exponential of Δ [167], ρ_n significantly increases with pressure. It follows that, at higher pressures, ρ_n matches the total density of the fluid at lower temperatures, which explains the shape of the lambda line in Fig. 2.1.

Other two state properties are shown in Fig. 2.6. Since the lambda point marks a second-

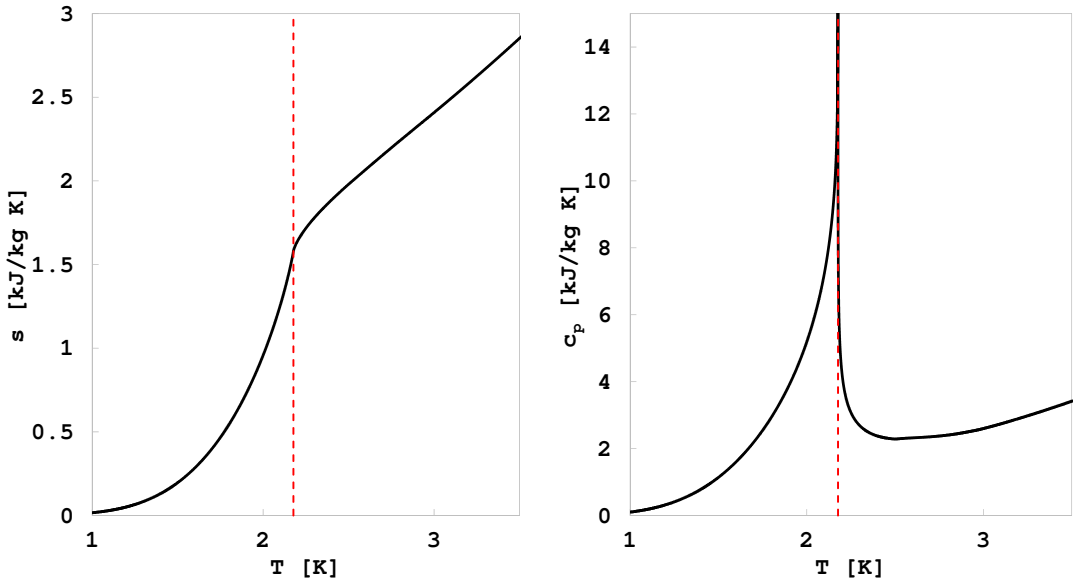

(a) Entropy (b) Specific Heat Capacity

Figure 2.6: He II state properties as a function of temperature at the saturated vapour pressure. The red dashed line marks the lambda temperature location.

order phase transition, at T_λ the entropy is continuous and the specific heat capacity is discontinuous. The reason behind this behaviour at the transition will be clear in Section 2.4. Above 1.1 K, the state properties are mainly determined by the rotons, which prevail as energy carrier in that range of temperature. The consequence in terms of temperature dependence is that entropy and specific heat are proportional to $T^{5.6}$ from 1.1 K to T_λ [158]. The discontinuity of the specific heat at T_λ manifests in a steep rise of its value resulting in a shape that reminds of the greek character "λ", which gives the name to this type of transition. In the vicinity of the lambda point, the specific heat seems to be proportional to $-\ln|T - T_\lambda|$ and hence it tends to infinite while approaching T_λ [25].

The transport properties of He II are defined by the equations of the two-fluid model. The dynamic viscosity, shown in Fig. 2.7a, above T_λ decreases along with the temperature. This is an uncommon behaviour for liquids and, instead, proper of gases. In fact, it was observed that liquid helium viscosity can be calculated through the Bose gas model [167]. A similar observation can be made for the thermal conductivity, shown in Fig. 2.7b, far from T_λ. Despite the similarity between He I and gas properties, there is an appreciable difference with respect to helium gas values. This is mainly due to the higher mean velocity

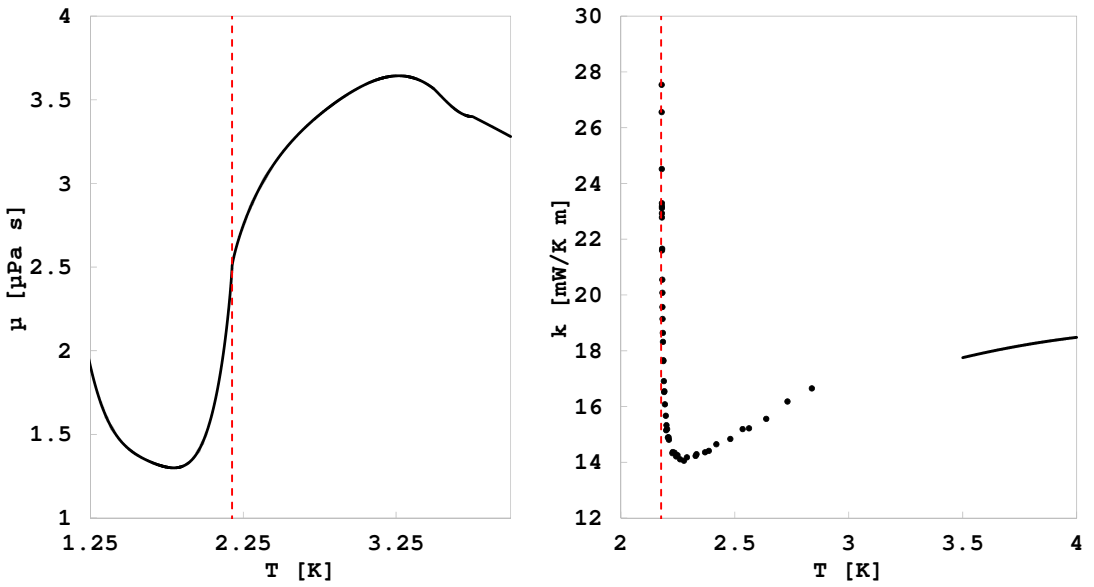

(a) Viscosity (b) Thermal Conductivity

Figure 2.7: He II transport properties as a function of temperature at the saturated vapour pressure. The red dashed line marks the lambda temperature location.

of the atoms in He I, which is attributed to its higher zero point energy. Accounting for this higher value in the gas model brings to a satisfactory agreement [150]. Below T_λ, the viscosity continues to drop till around 1.8 K and then acquires the typical behaviour of liquids, increasing with decreasing temperature. This is clearly due to the viscous forces of the normal component of He II, as shown by Andronikashvili in his experiment utilizing a rotating viscometer [7]. The measured values of the viscosity can change according to the settings of the experiment: in thin capillaries, where the normal component cannot access, no viscosity is detected [48]. Above T_λ, the thermal conductivity below a certain temperature is not available in the database HEPAK© because of the great uncertainty due to the vicinity with the He II phase state. The dots depicted in Fig. 2.7b are taken from a complete review paper about the observed properties of liquid helium [43]. The thermal conductivity of He II is a complicated function of temperature and pressure that strongly depends on the magnitude of heat currents potentially present. For this reason, it will be discussed in detail in Section 2.2.2.

2.2 Quantum Turbulence

In Section 2.1 we have seen that, at an ideal state at zero temperature, He II is a frictionless superfluid as long as its velocity is below a certain critical value. However, experimental evidence was in great disagreement with Landau's critical velocity. This was due to the fact that, at a finite temperature below the lambda point, there exist other excitations known as quantum vortices, which are a result of the turbulent motion of the superfluid

component of He II. This quantum turbulence is caused by the friction between the superfluid component and the normal component, which is present at finite temperatures and carries the excitations. The quantum vortex lines were theoretically predicted in 1949 by Onsager [118] and independently a few years later by Feynman [52]. Feynman's theory was based on quantum mechanics and allowed him to figure out that the circulation of the superfluid along a vortex line is quantized as

$$\kappa = \oint \mathbf{v}_s \cdot \mathrm{d}\mathbf{l} = \frac{h}{m}, \tag{2.27}$$

where the ratio h/m between the Planck constant and the helium atom mass represents the quantum of circulation ($\kappa \approx 9.97 \times 10^{-4}$ cm^2/s). The formation of these quantum vortices causes a considerable drop in the value of the critical velocity with respect to Landau's prediction. In fact, Feynman was able to derive a value of the critical velocity that is close to experimental evidence by linking the velocity to the phase of the wave function of the He II condensed population [8]:

$$v_{s,c} \simeq \frac{\hbar}{md} \ln\left(\frac{d}{2a_0}\right), \tag{2.28}$$

where a_0 is the vortex core radius ($a_0 \approx 10^{-8}$ cm). Shortly after, Hall and Vinen confirmed experimentally Feynman's results [63], which definitively established the connection between He II and a BEC. The critical velocity can be roughly estimated through the empirical formula [158]

$$v_{s,c} \simeq d^{-\frac{1}{4}} \left[\frac{\mathrm{cm}}{\mathrm{s}}\right], \tag{2.29}$$

where d (in cm) is the diameter of the channel. The critical velocity dependence on the inverse of the channel diameter suggests that it is hard to observe superfluidity in large pipes. By associating Eq. (2.29) with Eq. (2.19) it follows that there must be a critical heat flux q_c such that

$$q_c = \frac{\rho_s}{\rho_n} \rho s T v_{s,c}, \tag{2.30}$$

which marks the passage from laminar to turbulent regime. It was observed that, for heat fluxes above q_c, turbulence hinders the wave propagation of second sound and attenuates its speed [161]. By studying the onset of this attenuation as a function of the heat flux, Vinen was able to derive an empirical formula for the time needed to achieve a fully-developed turbulent regime:

$$\tau = a q^{-\frac{3}{2}}, \tag{2.31}$$

where a is a parameter that depends on the temperature and characteristic dimension of the channel. In the heat flux scale of engineering application, τ turns out to be very small [158].

The friction between the normal component and the superfluid moving along the quantum vortex lines produces a force called mutual friction. The idea of a mutual friction

force between the two components was first advanced by Gorter and Mellink in an attempt to explain the heat transfer in He II in the presence of a non-negligible heat current [58]. The theory behind it was later developed by Vinen, who approached the topic from the point of view of the vortex line length L per unit fluid volume [160]. Let us consider the velocity of the vortex line $\mathbf{v}_L$ with respect to $\mathbf{v}_s$ and $\mathbf{v}_n$. Making the assumption that the three velocities are equally directed allowed Vinen to distinguish between two cases in relation to the relative velocity v_{ns} and the drift velocity of the vortex $(v_L - v_s)$. When v_{ns} is lower than the drift velocity, the friction force tends to contract the vortex. Viceversa, if the relative velocity is higher than the drift one, the vortex is expanded. Since, as seen in Eq. (2.17), a temperature gradient generates relative velocity between the two components of the fluid, a heat flux tends to enhance the quantum turbulence. Therefore, the vortex line length changes in time according to the net value between the rates of generation and decay of the vortex lines:

$$\frac{\mathrm{d}L}{\mathrm{d}t} = \left.\frac{\mathrm{d}L}{\mathrm{d}t}\right|_g + \left.\frac{\mathrm{d}L}{\mathrm{d}t}\right|_d . \tag{2.32}$$

The steady-state form of Eq. (2.32) (i.e., in the presence of a steady heat current) allows to derive an expression for the vortex line length at equilibrium L_0 [158]:

$$L_0 = a(T) \left(\frac{\rho_n}{\rho} v_{ns}\right)^2 , \tag{2.33}$$

where $a(T)$ is some function of the temperature. Using dimensional considerations, Vinen derived the net force acting on a vortex line in an isotropic vortex tangle at steady state (see Fig. 2.8), which can be simplified into the form [167]

$$\mathbf{f} = \beta\kappa \frac{\rho_s \rho_n}{\rho} \left(\mathbf{v}_n - \mathbf{v}_L\right) , \tag{2.34}$$

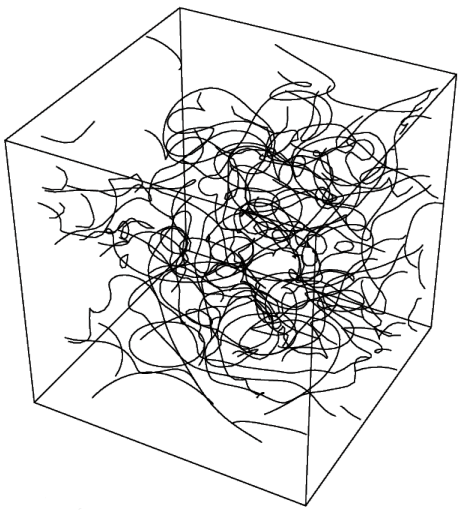

Figure 2.8: Simulation of a vortex tangle in presence of mutual friction at 1.6 K [156].

where β is a constant. Since in the tangle the vortex lines form an irregular mass, the average of the velocity $\mathbf{v}_L$ in the whole tangle can be assumed to be equal to the superfluid one [167]. The total mutual friction force per unit volume $\mathbf{F}_{ns}$ can be calculated as the product

$$\mathbf{F}_{ns} = L_0\mathbf{f} = A_{GM}\rho_s\rho_n \left|v_n - v_s\right|^2 (\mathbf{v}_n - \mathbf{v}_s)\,, \tag{2.35}$$

where the Gorter-Mellink coefficient A_{GM} is proportional to ρ_n^2/ρ^3 and hence is temperature dependent such that $A_{GM} \propto T^3$. Eq. (2.35) turns out to be the confirmation of the expression for $\mathbf{F}_{ns}$ supposed by Gorter and Mellink by observing heat current measurements in superfluid helium. Vinen also performed some heat pulse experiments to show the effect of the mutual friction force on the second sound propagation [161]. The second sound wave has a limit in the amount of energy that it can carry. When the heat current is high enough to produce quantum turbulence, the wave gets saturated and it is possible to observe the velocity at which the turbulent front propagates. Combining the mutual friction force with the equations of second sound brings to an additional term that diminishes the second sound velocity by an attenuation that is proportional to the square of the heat flux applied.

It is possible to produce quantum vortices also in the absence of mutual friction. A typical situation concerns a famous paradox that arises when He II is put in rotation. Let us consider a vessel in rotation containing He II. Let us assume that the temperature is much lower than the lambda temperature, which means that the total density is pretty much equal to the superfluid one, and that the fluid is incompressible ($\partial\rho/\partial t = 0$). It follows from the continuity equation (Eq. (2.7)) that $\boldsymbol{\nabla} \cdot \mathbf{v}_s = 0$. Also, since the superfluid component has no viscosity, the fluid is irrotational ($\boldsymbol{\nabla} \times \mathbf{v}_s = 0$). The solution to the Laplace's equation ($\nabla^2\mathbf{v}_s = 0$) thus implies that the fluid must be static. However, experiments by Osborne showed that He II actually rotates along with the bucket [120]. The contradiction can be solved by considering the existence of vortex lines generated by the rotation of the fluid (see Fig. 2.9). Each vortex core is associated with a circulation quantum given by Eq. (2.27). Each circulation cancels out with the neighbouring one keeping the fluid outside the vortices at rest. The fluid in contact with the rotating bucket though is put in motion because of the non-null circulation of the vortices next to the boundary.

2.2.1 HVBK Equations

The mutual friction force can strongly affect the thermo-dynamic behaviour of superfluid helium. In presence of dissipation, it is necessary to add this term into the two-fluid model to come up with a general system of equations that macroscopically characterizes He II. This system is constituted by the so-called Hall-Vinen–Bekharevich–Khalatnikov (HVBK) equations, named after the scientists who contributed the most in their development [64], [14]. The HVBK equations can be considered like a generalization of the Landau's two-fluid

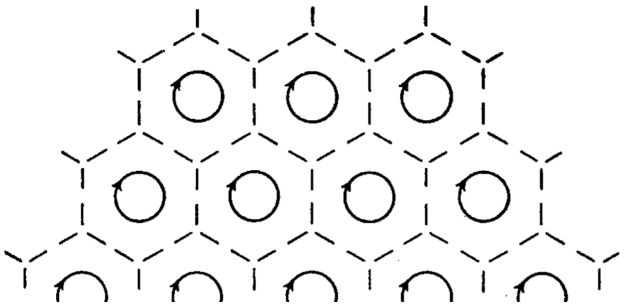

Figure 2.9: Representation of the quantum vortices in rotating He II [62]. On the dashed lines the velocity is zero.

model involving also quantum turbulence and read as follows:

$$\frac{\partial \rho}{\partial t} + \boldsymbol{\nabla} \cdot (\rho_n \mathbf{v}_n + \rho_s \mathbf{v}_s) = 0, \tag{2.36}$$

$$\frac{\partial \mathbf{v}_n}{\partial t} + (\mathbf{v}_n \cdot \boldsymbol{\nabla})\, \mathbf{v}_n = \frac{\mu}{\rho_n} \nabla^2 \mathbf{v}_n - \frac{\rho_s}{\rho_n} s \boldsymbol{\nabla} T - \frac{1}{\rho} \boldsymbol{\nabla} p - \frac{\rho_s}{2\rho} \boldsymbol{\nabla} v_{ns}^2 - A_{GM} \rho_s v_{ns}^2 \mathbf{v}_{ns}, \tag{2.37}$$

$$\frac{\partial \mathbf{v}_s}{\partial t} + (\mathbf{v}_s \cdot \boldsymbol{\nabla})\, \mathbf{v}_s = s \boldsymbol{\nabla} T - \frac{1}{\rho} \boldsymbol{\nabla} p + \frac{\rho_n}{2\rho} \boldsymbol{\nabla} v_{ns}^2 + A_{GM} \rho_n v_{ns}^2 \mathbf{v}_{ns}, \tag{2.38}$$

$$\frac{\partial (\rho s)}{\partial t} = -\boldsymbol{\nabla} \cdot (\rho s \mathbf{v}_n) + \frac{A_{GM} \rho_n \rho_s v_{ns}^4}{T}. \tag{2.39}$$

Eq. (2.36) matches the continuity equation previously introduced in Section 2.1.1 (Eq. (2.7)). Eqs. (2.37) and (2.38) are the incompressible momentum equations for the normal fluid and the superfluid respectively. In the superfluid momentum equation there should also be a term related to the vortex tension that, however, is proportional to the circulation quantum and hence negligible. Eq. (2.39) is the entropy equation that stands for the energy equation of the system.

2.2.2 Heat Transfer in He II

In order to describe the heat transport in superfluid helium, it is useful to take as starting point the HVBK equations. Let us take into account the steady-state version of Eqs. (2.37), (2.38) and multiply them by their respective densities. If we neglect the quadratic terms in the velocity, it is possible to derive the Poiseuille equation by adding together the two momentum equations:

$$\boldsymbol{\nabla} p = \mu \nabla^2 \mathbf{v}_n. \tag{2.40}$$

Let us consider again the superfluid momentum equation. If we neglect the same terms as previously, isolating for the pressure gradient yields

$$\boldsymbol{\nabla} p = s \rho \boldsymbol{\nabla} T + A_{GM} \rho \rho_n v_{ns}^2 \mathbf{v}_{ns}. \tag{2.41}$$

Combining Eqs. (2.40) and (2.41) by eliminating the pressure term allows to write an expression for the temperature gradient. Let us consider a one dimensional channel of diameter d to simplify the equation:

$$\frac{\mathrm{d}T}{\mathrm{d}x} = -\frac{b\mu}{s\rho d^2} v_n - \frac{A_{GM}\rho_n}{s} v_{ns}^3, \tag{2.42}$$

where $-bv_n/d^2 \simeq \nabla^2 \mathbf{v}_n$ and b is a constant that depends on the geometrical configuration of the channel ($b = 12$ for parallel plates, $b = 32$ for circular tubes). Let us use Eq. (2.19) to substitute the velocities and express Eq. (2.42) in function of the heat flux:

$$\frac{\mathrm{d}T}{\mathrm{d}x} = -\frac{b\mu}{s^2\rho^2 T d^2} q - \frac{A_{GM}\rho_n}{s^4\rho_s^3 T^3} q^3. \tag{2.43}$$

The terms on the RHS represent respectively the viscous and the turbulent contributions to the temperature gradient along the channel. Because of the third power of the heat flux associated with the second term, for relatively high heat currents the turbulent contribution largely dominates. On the other hand, the first term is proportional to the inverse of the square of the channel diameter and hence the viscous contribution prevails for small geometries and negligible heat fluxes. The latter case can be associated with the Landau regime, whereas the first one describes the thermal behaviour of He II above the critical heat flux (Eq. (2.30)) and is known as Gorter-Mellink regime. To have a better idea about the order of magnitude of these quantities, Fig. 2.10 shows how the temperature gradient varies with the heat flux in a 0.2 mm thick channel enclosed between two parallel plates. At low heat fluxes, the function is a straightline because the linear behaviour of the viscous term prevails. The function begins to rise with the cubic power when the heat current increases. Although the transition from laminar to turbulent regime seems to be

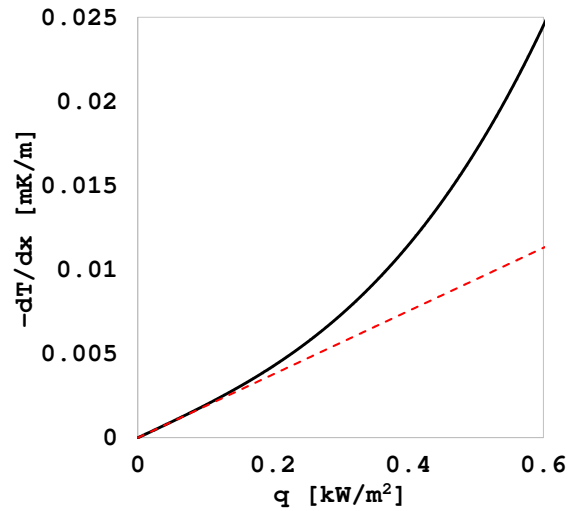

Figure 2.10: Temperature gradient as a function of the heat flux applied in a 0.2 mm thick channel constrained by two flat plates. The red dashed line represents the viscous contribution only.

continuous according to (2.43) (shown in Fig. 2.10), in reality there exists hysteresis: when the turbulent regime is established, decreasing the heat flux down below the critical value does not cause transition to laminar regime because of the presence of the vortices.

In superconducting magnets cooling applications of He II, usually the heat fluxes involved are much higher than the ones showed in Fig. 2.10. Therefore, the viscous term in Eq. (2.43) can be neglected and the following steady-state heat transport equation is obtained:

$$\frac{\mathrm{d}T}{\mathrm{d}x} = -f(T,p)q^n, \tag{2.44}$$

where $f(T,p)$ is the heat conductivity function and is defined as

$$f(T,p) = \frac{A_{GM}\rho_n}{s^4\rho_s^3 T^3}. \tag{2.45}$$

Fig. 2.11 shows values for $f(T,p)$ at different pressures from the database HEPAK© [68]. At the saturated vapour pressure, the inverse of $f(T,p)$ has a maximum at around 1.95 K, which decreases with increasing pressure. In engineering applications of He II, a pressurized helium bath is usually kept at around the temperature at which a curve in Fig. 2.11 has the peak, in order to maximise the conductive properties of He II. From Eq.

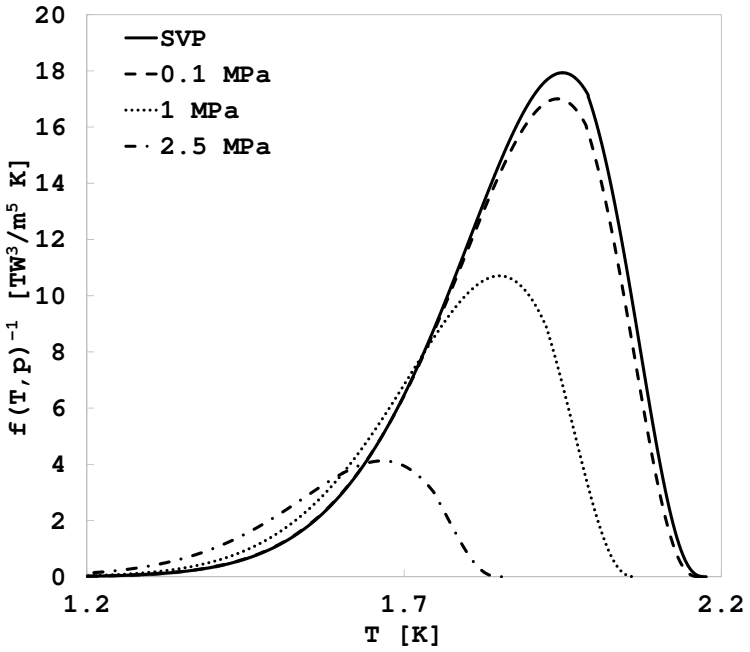

Figure 2.11: Temperature dependence of the He II heat conductivity function at different pressures.

(2.43) we see that the coefficient n should be equal to 3. In reality, several experiments showed that n depends on the temperature and ranges from 3 to about 4 around T_λ [2], [24], [31], [86], [97]. Some authors used 3.4, which seems to be a good approximation in the range of temperatures between 1.7 K and T_λ [17]. In particular, Sato performed a series

of experiments at steady state to derive an accurate correlation for the heat conductivity function for $n = 3.4$ [134]:

$$f_S(T,p)^{-1} = h(t)g_{peak}(p), \tag{2.46}$$

where $h(t)$ and $g_{peak}(p)$ are empirical functions and equal to

$$h(t) = 1 + (t - t_{peak})^2 \sum_{n=0}^{9} \left[a_n (t-1)^n\right], \tag{2.47a}$$

$$g_{peak}(p) = \exp\left(a + bp + cp^2\right). \tag{2.47b}$$

The reduced temperature t is equal to the ratio between the temperature and T_λ at the pressure of interest, while a_n, a, b, c are empirically determined coefficients.

Eq. (2.44) can be generalized through the Fourier's law into a heat diffusion equation to describe the thermal behaviour of He II in transient conditions:

$$\rho c_p \frac{\partial T}{\partial t} = \frac{\partial}{\partial x}\left(\frac{1}{f(T,p)}\frac{\partial T}{\partial x}\right)^{\frac{1}{n}}, \tag{2.48}$$

where c_p is the specific heat capacity. The unusual conductive heat exponential coefficient makes Eq. (2.48) strongly non-linear and difficult to solve analytically. Dresner proposed an analytic method to solve the equation for $n = 3$ based on the so-called similarity solutions [44], [45]. Basically, temperature profiles at different time instants are connected to each other and belong to groups of solutions with similar characteristics. Exploiting this fact, Dresner was able to turn the diffusion partial differential equation into an ordinary differential one that can be solved analytically. However, this method requires strong simplifications (e.g., constant properties, one-dimensionality) that restrict its applicability to relatively simple problems.

2.3 Kapitza Resistance

When a heat flux is established through two different materials that are in contact, a thermal boundary resistance takes place between them. This resistance strongly depends on the inverse of the temperature and hence it is usually negligible in the majority of the cases. In He II though, below the lambda point the temperatures are low enough to make this resistance considerably important in the heat transfer mechanism between helium and a solid. This phenomenon results in a significant temperature jump across the solid-helium interface, which was first observed by Kapitza in 1941 [79]. The heat flux through the two materials can be written in the form of radiation heat transfer:

$$q = \sigma\left(T_s^4 - T_{He}^4\right), \tag{2.49}$$

where T_s and T_{He} are the temperatures of the solid and the helium at the interface and σ is a quantity that depends on the thermal characteristics of the solid. For small enough

temperature differences between the two media ($\Delta T \ll T$), $T_s^4 - T_{He}^4 \simeq 4T_{He}^3 \Delta T$ and Eq. (2.49) can be formulated as [124]

$$q = h_K \left(T_s - T_{He}\right), \tag{2.50}$$

where the conductance h_K is the inverse of the Kapitza resistance. Various theories have been proposed over the years in order to explain the temperature dependence of the Kapitza conductance. The first one was the acoustic mismatch model of Khalatnikov [87], who tried to provide an explanation from the acoustic theory by considering the significant difference of the sound speed in liquid helium and solids. This discrepancy hinders the phonon transmission between the two media in a way that can be described by the Snell law:

$$\sin\theta_t = \frac{c_s}{c_{He}} \sin\theta_i, \tag{2.51}$$

where θ_t is the transmission angle of a helium phonon incident on the interface with an angle θ_i. Since the angle of transmission must be less than $90°$, the arcsine of the ratio c_{He}/c_s between the sound speeds in liquid helium and a solid determines the critical angle above which an incident phonon cannot be transmitted to the solid. The critical angle thus circumscribes a cone of incidence within which the phonons are able to be transmitted. The energy transferred to the solid by the phonons incident on the interface within the cone can be evaluated by integrating the heat flux per unit area over the cone [158]:

$$q = \frac{c_s}{4} E_{ph} \left(\frac{c_{He}}{c_s}\right)^3, \tag{2.52}$$

where E_{ph} is the phonon energy density and can be estimated through the Debye theory by assuming that the temperatures involved are much lower than the Debye temperature of the solid. Eq. (2.52) must be corrected to take into account a coefficient of transmission between the two media [145]. The transmission coefficient t indicates the probability of phonon transmission and can be determined after associating an acoustic impedance with each material. In cases involving liquid helium and a solid, the impedance of He II is much smaller than the one of the solid and hence the transmission coefficient can be approximated as $t = 4\rho_{He}c_{He}/(\rho_s c_s)$ with ρ_s being the density of the solid. The final form of the net heat flux provides an expression for the Kapitza conductance:

$$h_K = \frac{\pi^2 k_B^4 \rho_{He} c_{He}}{30\hbar^3 \rho_s c_s^3} F T_{He}^3, \tag{2.53}$$

where the parameter F accounts for the fact that in solids also transverse waves are present as well as the longitudinal ones [124].

Although the Kapitza conductance predicted by the acoustic mismatch theory shows a temperature dependence in line with experiments, its value is always much lower than the actual one for any material. This evidence pushed Snyder to wonder about what could be the maximum Kapitza conductance for a phonon regulated heat current between two

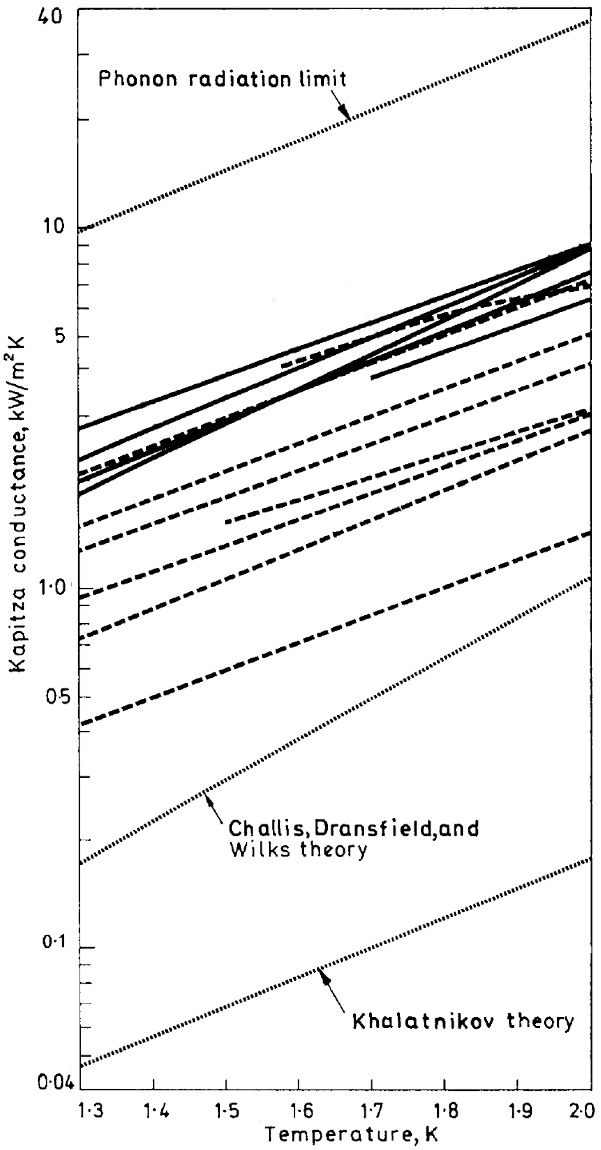

Figure 2.12: Kapitza conductance as a function of the helium bath temperature for copper-helium interfaces. The theoretical curves are labeled, whereas the solid and dashed lines refer to experimental values from various authors for clean and dirty surfaces respectively [139].

media [139]. This upper limit is known as phonon radiation limit and yields overestimated values for the Kapitza conductance via simplification of the Khalatnikov's model: in the calculation of the helium phonon energy density both longitudinal and transverse waves are considered, even though the latter is absent in liquids; the conductance depends on the characteristics of the solid but not of helium; the probability of phonon transmission is 100%. As shown in Fig. 2.12, the experimental values of the Kapitza conductance lie always in between the acoustic mismatch theory and the phonon radiation limit.

In Fig. 2.12 it is also depicted a curve from the theory of Challis, who modified the

acoustic mismatch model by taking into account the presence of a dense layer of helium formed at the interface because of Van der Waals forces [30]. After Challis's work, other theories were proposed based on quantum considerations [112], [106], [1]. Despite the theoretical interest in the thermal boundary resistance mechanism, the Kapitza conductance is strongly dependent on the materials involved and their surface characteristics (see Fig. 2.12) and hence quite difficult to estimate through mere theory. For this reason, for practical use the temperature dependence of h_K is usually obtained experimentally for each material and the resulting heat flux takes the form

$$q = \begin{cases} a_{II} T_b^{m_{II}} \left(T_s - T_b\right), & \text{for } \Delta T \ll T, \quad (2.54a) \\ a_I \left(T_s^{m_I} - T_b^{m_I}\right), & \text{for } \Delta T \approx T, \quad (2.54b) \end{cases}$$

where a and m are empirical coefficients that depend on the solid material and T_b is the bath temperature of the liquid helium.

2.4 Phase Transitions

As briefly mentioned at the beginning of this chapter, the so-called λ-transition between He I and He II is characterized by the absence of latent heat and a discontinuity of certain thermophysical properties such as the specific heat capacity c_p. In order to rigorously discern between this type of transition and boiling phenomena, it is useful to introduce the Ehrenfest classification [46], which was created after the first experimental evidence of the critical phenomena of liquid helium. This classification bases the differentiation of the phase changes on the Gibbs free energy g:

$$\mathrm{d}g = v\,\mathrm{d}p - s\,\mathrm{d}T\,. \quad (2.55)$$

Ehrenfest associated each transition type with a specific order n, which is determined by the lowest derivative of g that shows a discontinuity at the transition point. In other words, a nth-order phase transition presents continuous derivatives of g up to the order $n-1$. The first-order derivatives of the Gibbs free energy are the specific entropy s and volume v:

$$\left(\frac{\partial g}{\partial T}\right)_p = -s, \quad (2.56a)$$

$$\left(\frac{\partial g}{\partial p}\right)_T = v. \quad (2.56b)$$

First-order transitions show then an entropy discontinuity, which implies the presence of latent heat. It follows that phase changes such as vaporization/condensation belong to this category. It can be demonstrated that the Gibbs functions of the liquid and vapour phases of a substance at saturation equal each other [125]. In fact, this constitutes the necessary condition for two phases to be in equilibrium during a phase change, which is proper of first-order transitions only. In the present study, the first-order transition of

interest is represented by the helium vapour-He I phase change. On the other hand, second-order transitions are not isothermal processes and the temperature dependence of entropy is continuous, like in the case of the He I-He II phase change (see Fig. 2.6a). This type of transitions are discontinuous in the specific heat, isothermal compressibility κ_T, and isobaric expansivity α_p, which are the second derivatives of the Gibbs free energy:

$$\left(\frac{\partial^2 g}{\partial T^2}\right)_p = -\frac{c_p}{T}, \tag{2.57a}$$

$$\left(\frac{\partial^2 g}{\partial p^2}\right)_T = -v\kappa_T, \tag{2.57b}$$

$$\left(\frac{\partial}{\partial T}\right)_p \left(\frac{\partial g}{\partial p}\right)_T = v\alpha_p. \tag{2.57c}$$

The discontinuous specific heat of helium at the λ-point has already been shown (see Fig. 2.6b), while the compressibility and expansivity can be seen in Fig. 2.13. The phase change occurring at the λ-point is clearly a second-order transition.

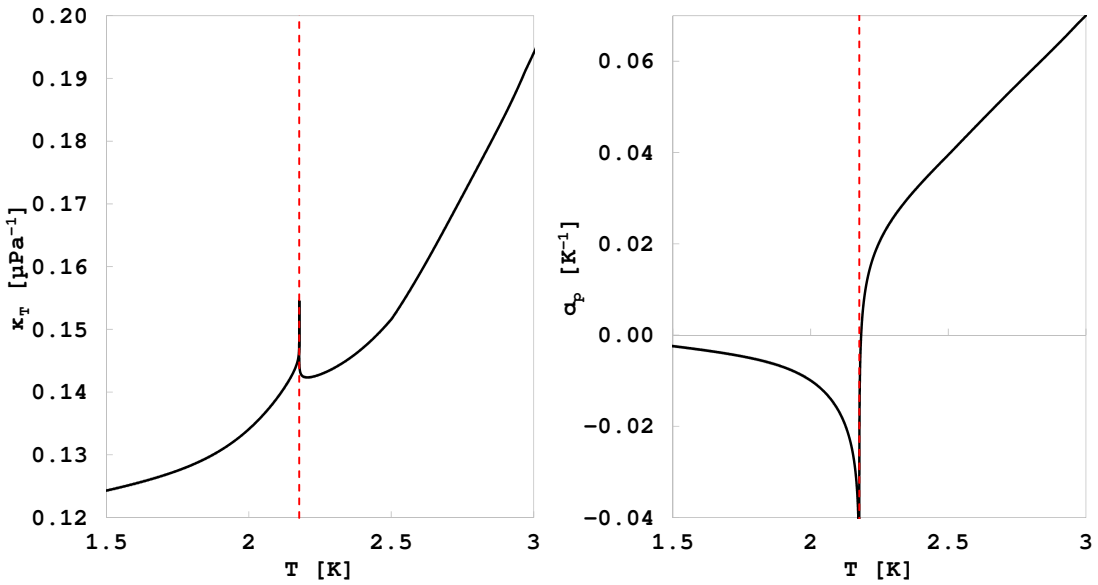

(a) Isothermal Compressibility

(b) Isobaric Expansivity

Figure 2.13: Compressibility and expansivity of helium across the λ-point as a function of the temperature at the saturated vapour pressure. The red dashed line marks the lambda temperature location.

Despite the impact that Ehrenfest's work had in the field of critical phenomena, his classification turned out to be simplistic in the attempt to categorize the various transitions witnessed in science [77]. More elaborated classifications were created either on the basis of the Ehrenfest's one [111], [142] or from a complete new theory [155]. Probably the most representative extension of the Ehrenfest classification was conceptualized by Pippard [125], who characterized a wider variety of transitions while still using Ehrenfest's

terminology. In particular, Pippard distinguished higher-order transitions according to the nature of the Gibbs free energy discontinuities. Fig. 2.14 shows a qualitative representation of some phase transitions in Pippard's classification. In the figure, 1

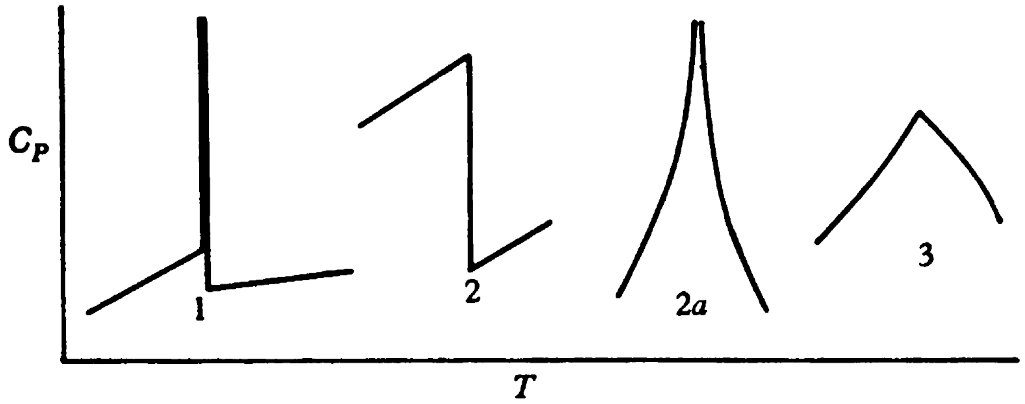

Figure 2.14: Phase transitions representation in a heat capacity-temperature graph: 1 first-order transition; 2 second-order transition; 2a λ-transition; 3 third-order transition. Adapted from [125].

corresponds to Ehrenfest's first-order phase transitions (e.g., liquid-vapour). Pippard considered true second-order phase transitions only those with a finite discontinuity in the second derivatives (2 in the figure). An example within this category is the transition to the superconductive state of a conductor. In the case of superfluid helium though, the specific heat tends logarithmically to infinite at T_λ as seen in Sec. 2.1.2. In Pippard's classification, such phase transitions associated with an infinite discontinuity belong to a separate category named λ-transitions (2a in the figure). Besides the He I-He II phase change, another example of λ-transition is the antiferromagnetic-paramagnetic shift at the Néel temperature of a material like magnesium bromide. The c_p evolution 3 in Fig. 2.14 is a third-order transition, which is continuous in the second derivatives of the Gibbs free energy. An example of this category is the ferromagnetic-paramagnetic shift at the Curie temperature of a material. Nevertheless, such distinctions are beyond the scope of the present study. For this reason, the λ-transition of He I-He II will be referred to as well as second-order transition to distinguish it from the first-order one.

2.4.1 Lambda Transition

It is of interest investigating the heat transfer conditions that govern the onset of the λ-transition. Let us consider a one-dimensional channel of length L filled with static subcooled He II at an initial temperature T_b. The temperature at one side of the channel is kept constant at the initial value T_b, whereas a heat flux is applied on the other side. It is then possible to compute the minimum heat flux necessary to reach the λ-point by integrating the heat conductivity function f of He II over the range of temperatures

between T_b and T_λ:

$$q_{min} = \left(\frac{1}{L} \int_{T_b}^{T_\lambda} f^{-1}(T)\, \mathrm{d}T \right)^{\frac{1}{n}}. \tag{2.58}$$

Above q_{min}, the fluid in contact with the heating surface will eventually undergo λ-transition. It is straightforward that the λ-time t_λ needed to achieve the λ-transition varies with the heat flux. Dresner derived a formula for t_λ as a function of the heat flux and temperature difference utilizing his own analytical method [44]:

$$t_\lambda = \frac{\overline{\rho c_p}\,(T_\lambda - T_b)^2}{(aq)^4\,\overline{f(T)}}, \tag{2.59}$$

where the thermophysical properties of He II are averaged in the range of temperatures between T_b and T_λ, while the proportionality constant a is equal to 1.16 [137]. The λ-time appears to depend strongly on the heat flux, decreasing with the fourth power of its reciprocal. Eq. (2.59) was validated experimentally with an agreement of 20 % [158]. An equivalent equation for the λ-time was derived by Baudouy, who proposed a solution independent of experimentally fitted parameters [13]. Another confirmation came from the heat pulse experiments by Seyfert et al. [136], who obtained an equivalent relation in terms of the energy ΔE dissipated during the pulse:

$$\Delta E q^3 = t_\lambda q^4 = A, \tag{2.60}$$

where A can be derived from Eq. (2.59) and agrees satisfactorily with Seyfert's calculations.

Once t_λ is reached, a λ-front is formed close to the heating surface. The rate of transformation of He II into He I determines the way this front propagates throughout the channel. In the context of the superfluid recovery in helium-cooled copper conductors, Dresner was able to approximate the speed of the front v_λ as [45]

$$v_\lambda = \frac{\left[x_\lambda^{-1} f^{-1}(T)\,(T_\lambda - T_b)\right]^{\frac{1}{3}}}{\overline{\rho c_p}\,(T_s - T_\lambda)}, \tag{2.61}$$

where x_λ is the front position, T_s is the fluid temperature at the heating surface, and the properties of helium are averaged between T_s and T_λ. Despite the absence of copper parameters, Eq. (2.61) was derived with the assumption that the longitudinal conduction is mainly due to the copper conductor.

2.4.2 Triple-Phase Phenomena

For heat fluxes higher than q_{min}, different fluid configurations can be established in the previous static He II channel according to the thermodynamic conditions at the location of the heating surface. If the pressure is lower than the value at the λ-point ($p_\lambda \approx 5.04$ kPa) (see Fig. 2.1), He II turns into helium vapour without the presence of He I (see Fig. 2.15a). If the pressure is higher than p_λ (e.g., atmospheric pressure), a He II-He I transformation occurs instead. In the latter case, the potential formation of the vapour

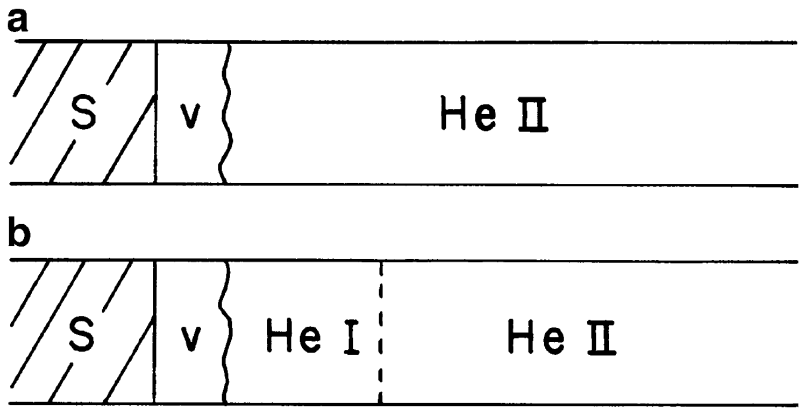

Figure 2.15: Boiling regimes in horizontal He II channels below p_λ (a) and above (b) [158].

phase via evaporation of He I depends on various parameters such as the channel geometry and initial temperature of the fluid. In pool boiling experiments [100], where the amount of He I is large compared to the size of the heater, it is possible to distinguish three main regimes depending on the heat flux applied: natural convection [69]; nucleate boiling [135]; film boiling [73]. In the convection regime, no phase change occurs. The heat transfer is driven by the density difference between the liquid next to the heater and the bulk He I. At higher heat fluxes, vapour bubbles start to appear at preferential locations named nucleation sites, which strongly depend on the heating surface characteristics. As the

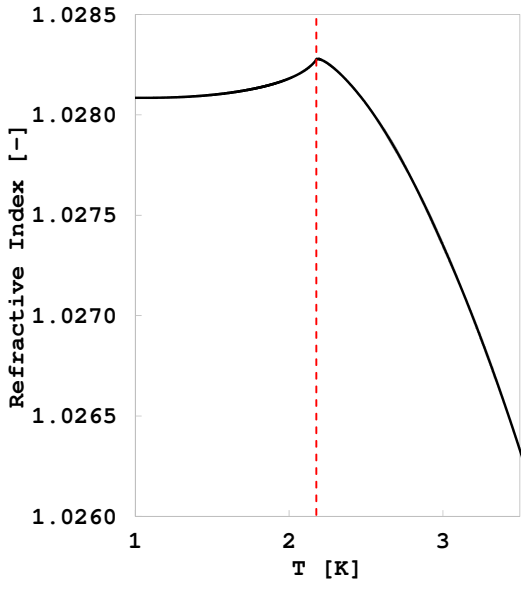

(a) Refractive Index

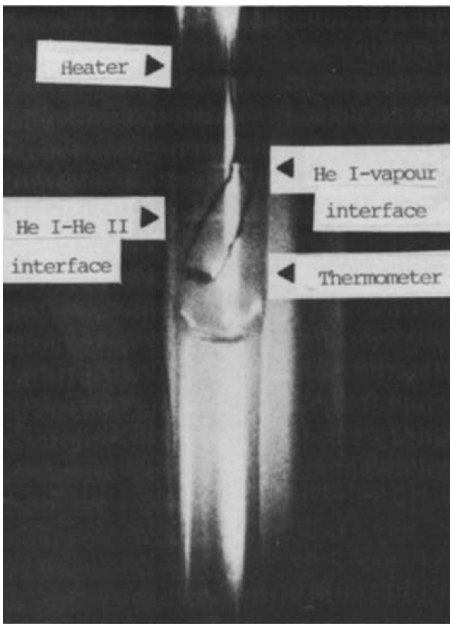

(b) Triple-Phase Visualization [23]

Figure 2.16: The He II-He I front is visible despite the absence of a discontinuity in the refractive index of liquid helium across the lambda point. Picture taken during a vertical channel experiment by Breon and Van Sciver [23].

heat flux is further increased, the number of bubbles generated is such that they coalesce into a vapour film that blankets the heating surface. More specifically, the vapour film arises when a certain peak nucleate boiling heat flux q^* is reached. However, in confined geometries like horizontal narrow channels, the coolant volume is small and thus the heat removal due to convection and nucleate boiling is limited. As a consequence, q^* is much lower and the vapour film is easily established. In engineering applications, this phenomenon is undesirable as the heat transfer coefficient in the film boiling regime is up to 100 times smaller than the Kapitza conductance [158]. Furthermore, even in pool boiling configurations, q^* is usually significantly lower than q_{min} (Eq. (2.58)). It follows that, except when the initial temperature is very close to T_λ, if He II undergoes λ-transition the heat flux is likely to be large enough to trigger the first-order transition too, resulting in a stable triple-phase phenomenon (see Fig. 2.15b) [28], [23]. A photographic evidence of the phenomenon is shown in Fig. 2.16b. The picture was taken during a vertical channel experiment by Breon et al. [23]. It is important to underline that the clear observation of the He II-He I interface is not an obvious outcome of the experiment. The density of liquid helium is indeed continuous across the λ-point and, most importantly, so is its refractive index (Fig. 2.16a).

CHAPTER 3

Experimental and Numerical Tools

3.1 Experimental Rig

As introduced in Ch. 1, part of this dissertation is dedicated to the results of experiments realized in superfluid helium. The experimental rig needed to conduct the tests is presented in this section along with the main components and sensors utilized. The extremely low temperature necessary to achieve the superfluid state of helium sets various limits and requirements on the experimental tools. Firstly, an isolated environment capable of keeping the temperature at values below 2 K must be created. This is usually obtained by means of a cryostat, a device that allows maintaining cryogenic conditions. The tests are carried out within the cryostat, where the experimental setup is located. The setup is constituted by solid components arranged together to form a thin channel, which is submerged in He II during the tests. Another requirement concerns the sensors used for monitoring the cryostat parameters and for experimental measurements. Temperature, pressure, and level sensors must withstand cryogenic conditions without repercussions on their accuracy and stability.

3.1.1 Cryostat

The cryostat used for the experiments is a typical Claudet cryostat, named after the scientist who conceptualized it [33]. As such, it allows conducting the tests in a pressurized He II bath rather than at saturated conditions. This is particularly useful for the goal of the present study as the stagnant bath that surrounds the dipoles of the LHC is pressurized. The cryostat, the scheme of which is shown in Fig. 3.1, is constituted by an outlying stainless steel shell (see Fig. 3.2) and two copper vessels. The outer vessel is separated from the shell by two radiation shields that minimize the radiative heat fluxes from the ambient condition of the laboratory. A vacuum environment is created between the outer vessel and the shell in order to enhance the thermal insulation of the cryostat. The external radiation shield is surrounded by a helical pipe in which liquid nitrogen is forced to flow in order to pre-cool the cryostat before the transfer of liquid helium. During the pre-cooling process, a thermal switch connects the two radiation shields and ensures the thermal link with the vessels. Once the pre-cooling is over, the switch is deactivated by means of a pressure input in order to isolate the inner vessel before the helium transfer. The inner vessel is the actual test environment that accommodates the setup, which is fixed to insert shown in Fig. 3.3. This insert is a support frame that is composed of a few G10 bars, an insulating G10 plate, four radiation shields, and an upper metal plate that serves to seal the cryostat when the frame is placed inside it. The channel setup is anchored to the bars along with the wirings that transmit the sensor signals to conjunction points on the metal plate, where proper cables are connected and transfer the information to the data acquisition system. The thick G10 plate is a thermal insulation that separates two environments of the inner vessel. The outer vessel is connected to a pumping system that allows regulating the pressure inside the vessel. The baths environment is shared with a recovery system that allows to minimize helium losses and ensures safe operations. The two vessels are linked to each other by a

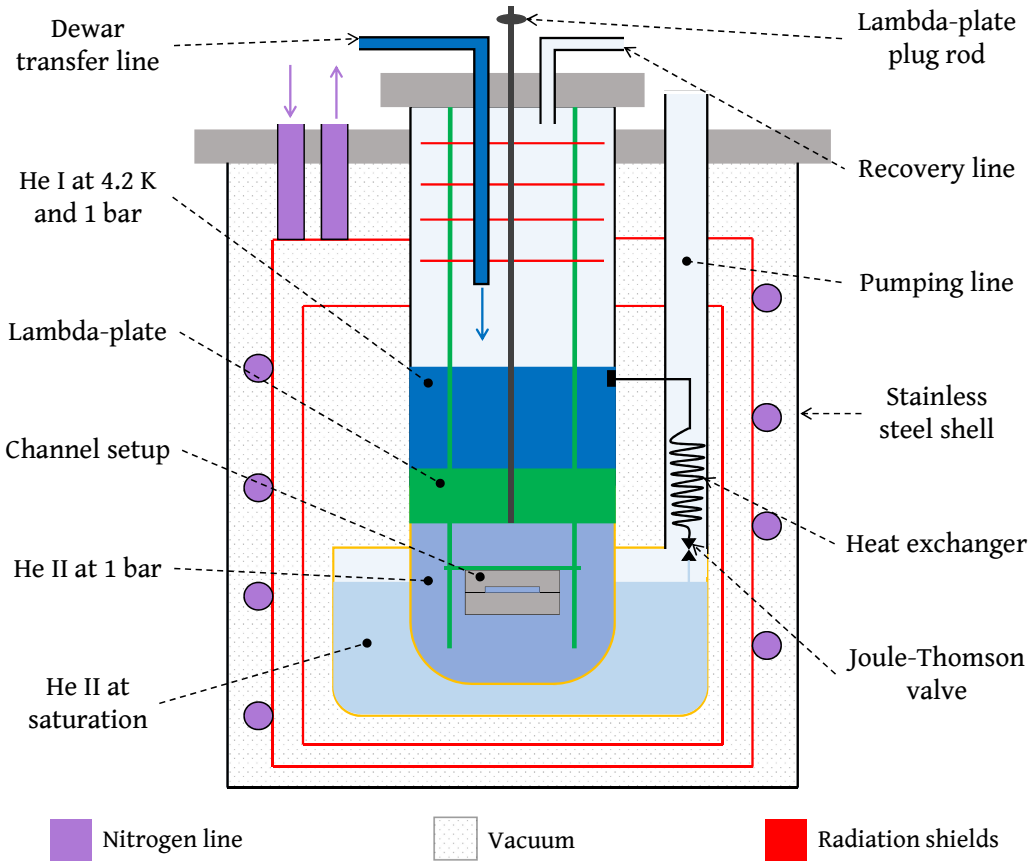

Figure 3.1: Cryostat system scheme.

heat exchanger equipped with a throttling valve that exploits the Joule-Thomson effect.

When the support frame is placed inside the inner vessel and the cryostat is sealed, the two vessels undergo multiple purge cycles to make sure that helium is the only gas present in the experimental environments. After pre-cooling with nitrogen, liquid helium is finally transferred into the inner vessel from a pressurized dewar through an insulated line. A hole in the G10 plate allows the helium to flow beneath it and fill up the lower environment of the inner vessel. In order to ensure thermal insulation between the two environments, the hole is plugged with a metal rod when the filling process is over. The experiment takes place in the lower bath ($\approx$ 12.3 L), which hence must be cooled down below the lambda point. Whereas the bath above the G10 plate is kept at the atmospheric boiling point. For this reason, this thick insulating plate is called λ-plate. A level sensor above the λ-plate measures the height of the bath free surface. The injection of liquid helium into the cryostat is repeated whenever the bath level is below a certain predefined value. As mentioned above, the inner vessel is connected to the outer one through a heat exchanger and a Joule-Thomson valve. When the bath above the λ-plate is full, helium starts expanding isenthalpically as it flows through the valve to the outer vessel. Since the liquid temperature is much lower than the inversion temperature of helium ($\approx$ 45 K at

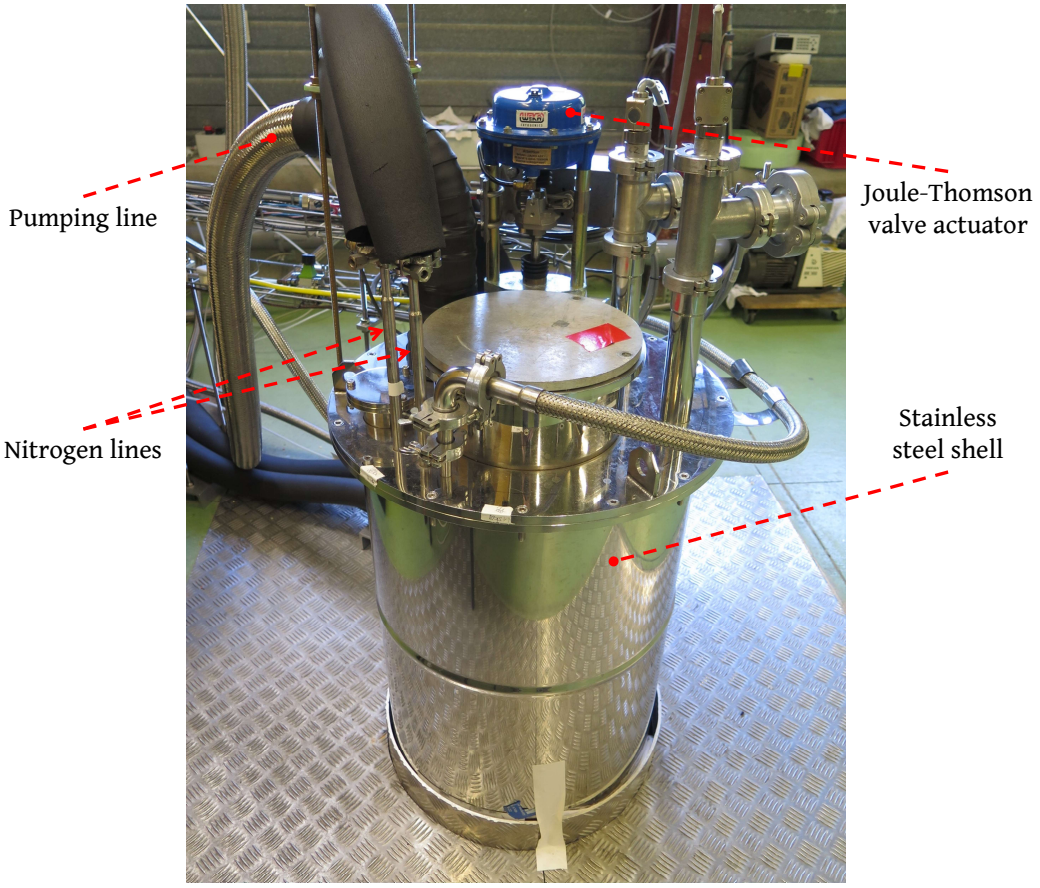

Figure 3.2: External view on the cryostat.

ambient pressure), the reduction in pressure causes a first temperature drop. This process continues until another level sensor in the outer vessel indicates that the free surface reached the desired height.

At this point, both vessels are full of liquid helium and the cooling process to achieve the superfluid state can be initiated. Since the outer vessel encloses the inner one, the helium contained in the outer vessel wets the external surface of the inner vessel, establishing a thermal link between the two baths. The pumping system connected to the outer vessel is switched on to decrease the pressure of the bath. The pumped mass flow is controlled by means of a butterfly valve that automatically adjusts according to the pressure requirement. The pressure is then reduced by pumping on the liquid, whose temperature decreases following the saturation line (see Fig. 3.4). In this way, the temperature of the outer bath can be easily regulated in saturated conditions. The outer bath is brought to the desired temperature below the lambda point. Because of the great thermal conductivity of He II, the temperature of the helium below the λ-plate quickly decreases as the saturated bath is cooled down. When the bath temperature below the λ-plate crosses the λ-line, the thermal link between the inner and outer baths is enhanced and results in a responsive behaviour of one bath with respect to the other. This link is hindered just by the thickness of the inner vessel, which is in copper though and

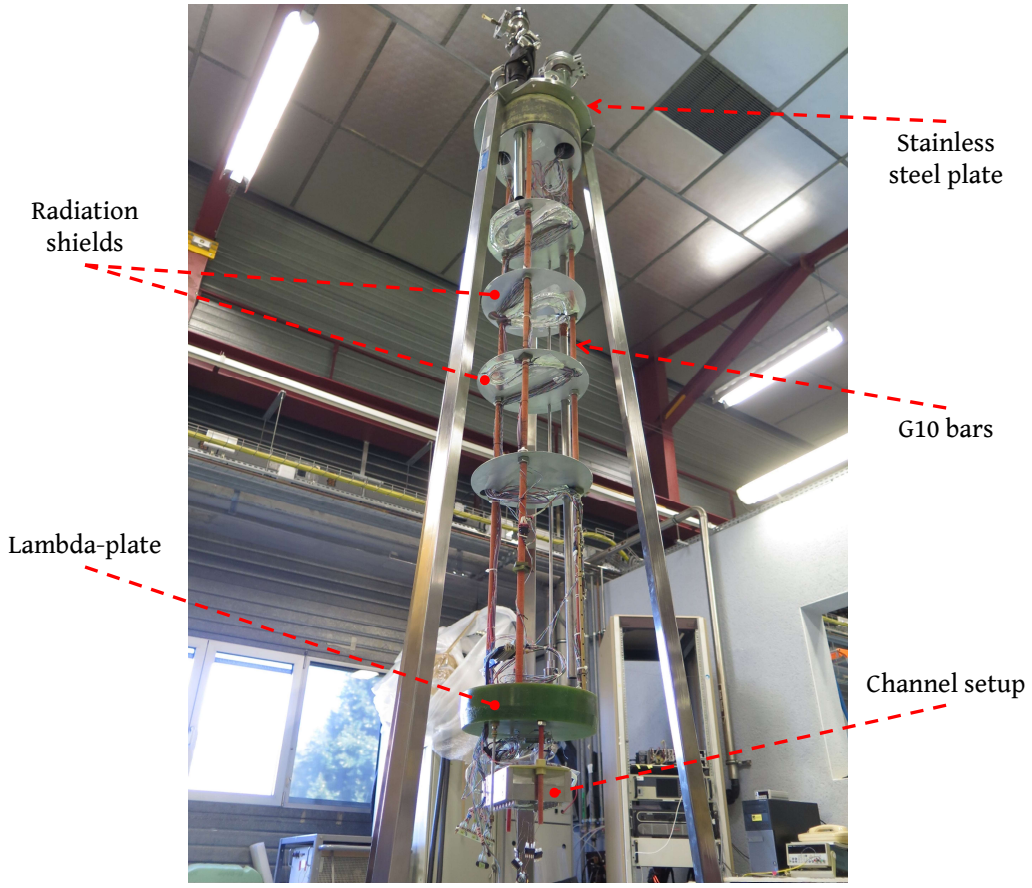

Figure 3.3: Insert and its components together with the channel setup installed.

hence highly conductive. Therefore, any change in pressure in the saturated bath causes a temperature variation of the inner bath, which is still at ambient pressure, and thus subcooled superfluid helium can be achieved. The phase state of each helium environment of the cryostat is represented in Fig. 3.4, which refers to the phase diagram of helium (see Fig. 2.1).

The cryostat is equipped with four calibrated Cernox® CX-1050-SD-HT-1.4L [29] temperature sensors located respectively in the subcooled bath, above the λ-plate, in the saturated bath, and in the pumping line. These sensors are specifically designed for cryogenic conditions due to their consistency and accuracy over a wide temperature range (calibrated from 1.4 K to 325 K). The subcooled bath is also equipped with a heater that regulates its temperature during experiments, as will be clear in the following section. The heater is controlled by a LakeShore® 336 [92] temperature controller, which utilizes a proportional–integral–derivative (PID) control system to automatically correct the amount of heat dissipated to the bath based on the bath sensor reading. The pressure of the saturated bath, which needs to be regulated by the pumping system, is monitored with an MKS© [109] Baratron® 627B absolute pressure sensor. The level of helium above the λ-plate and in the outer vessel is monitored with two AMI© [6] level controllers.

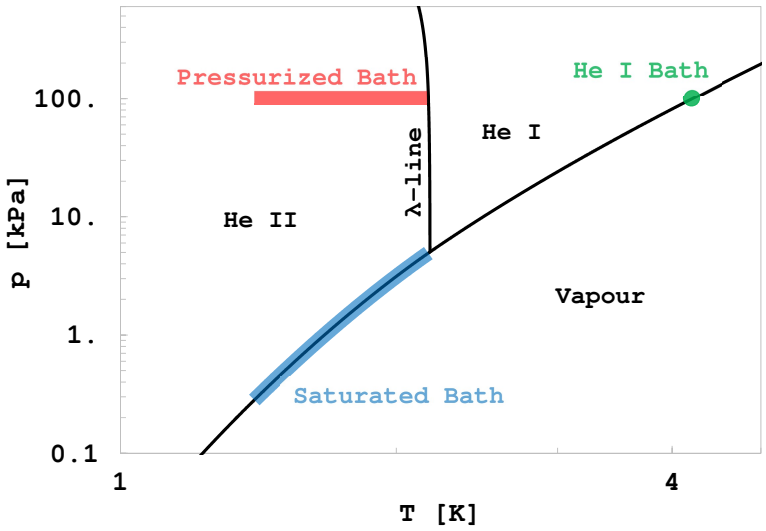

Figure 3.4: Pressure-temperature state of the liquid helium baths in the cryostat.

3.1.2 Channel Setup

One of the research questions of this dissertation focuses on the thermo-hydraulic response of superfluid helium following a significant release of heat load in confined geometries of the size of few hundreds of microns. The experimental setup used for this purpose is designed to form the desired geometry, which is meant to resemble the space in between the collars surrounding the superconducting coils. The concept of the experiment is represented in Fig. 3.5. He II fills a thin channel that is open to the bath of the experimental

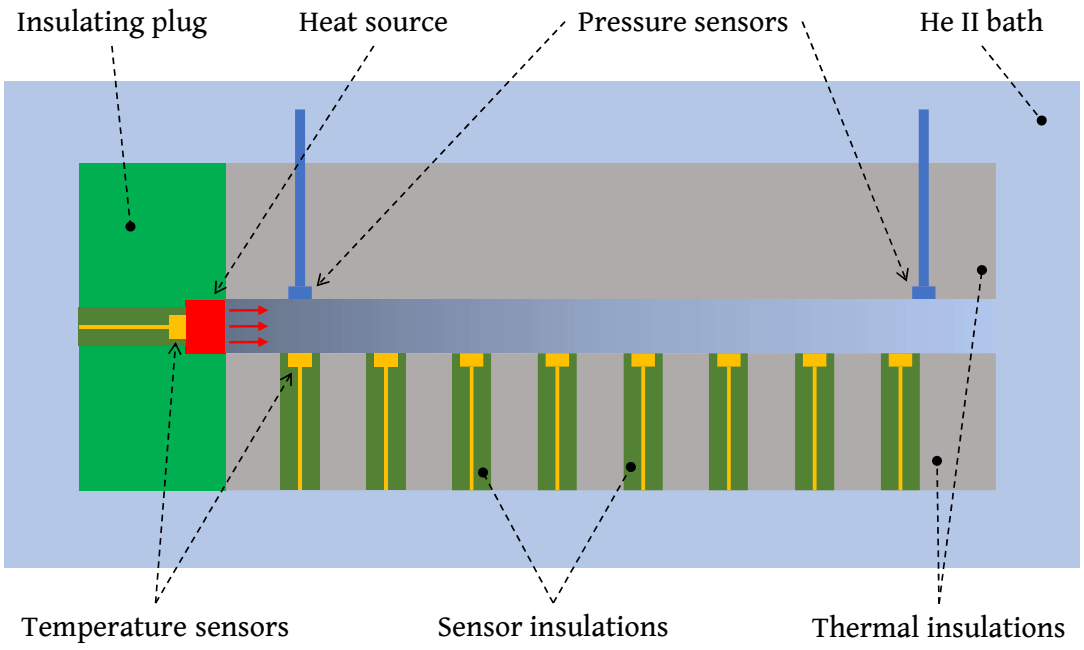

Figure 3.5: Channel experiment concept representation.

environment on one extremity and closed on the other by a heating source. The channel is enclosed by thick solid pieces that insulate thermally the He II contained in the channel from the bath. The heat source is supposed to dissipate energy only inside the channel. This preferential direction of the heat flux is obtained by means of an insulating plug posed behind the source and attached to the other solid parts. Several sensors mounted on the solid pieces will provide information about the temperature and the pressure of the He II in the channel.

The actual setup, the drawings of which are presented in Figs. 3.6 and 3.7, is constituted by five main components: two stainless steel plates, two side stainless steel flanges, and one G10 support. These five pieces are assembled together in order to shape a rectangular

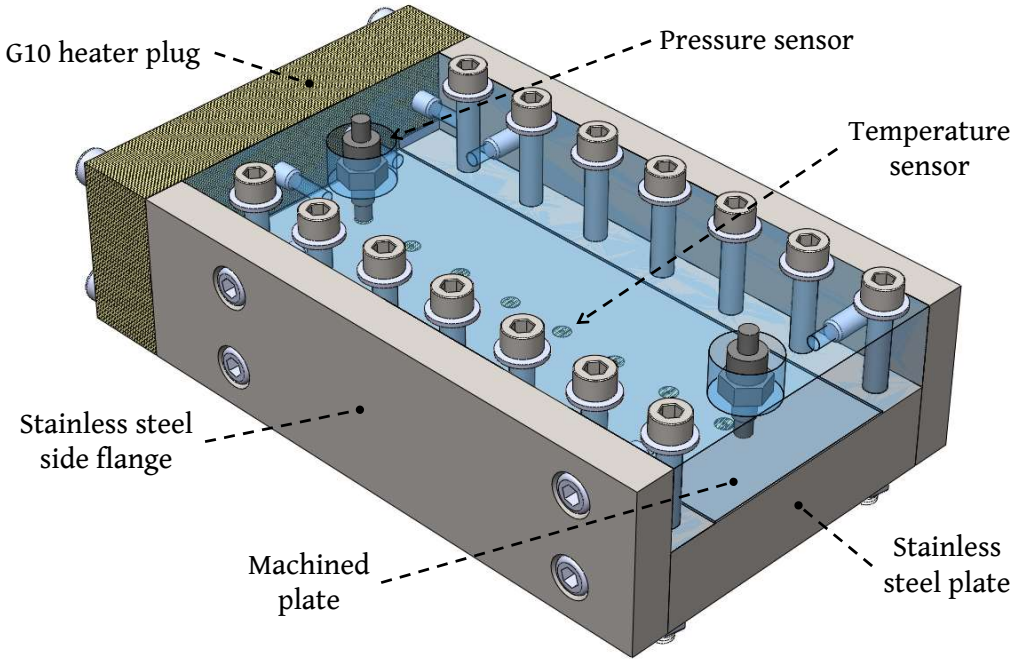

Figure 3.6: Channel components description with transparent upper plate [9].

cross-section channel. The relative position of all the pieces is fixed and ensured by several stainless steel screws covered with vacuum grease, which does not crack at cryogenic conditions. One of the metal plates is machined on the central part of one surface to house the channel, which emerges when the other plate is put in contact with the machined one. These two plates are placed between the two side flanges, which minimize lateral leaks. The vacuum grease is also inserted in the space between the main pieces, with particular attention to the contact surface of the two plates in order to not obstruct the channel zone with impurities. The channel is 14 cm long and 5 cm wide, whereas its thickness is determined by the machined surface. Since the thickness is one of the study parameters, two machined plates were prepared in order to produce two channels of

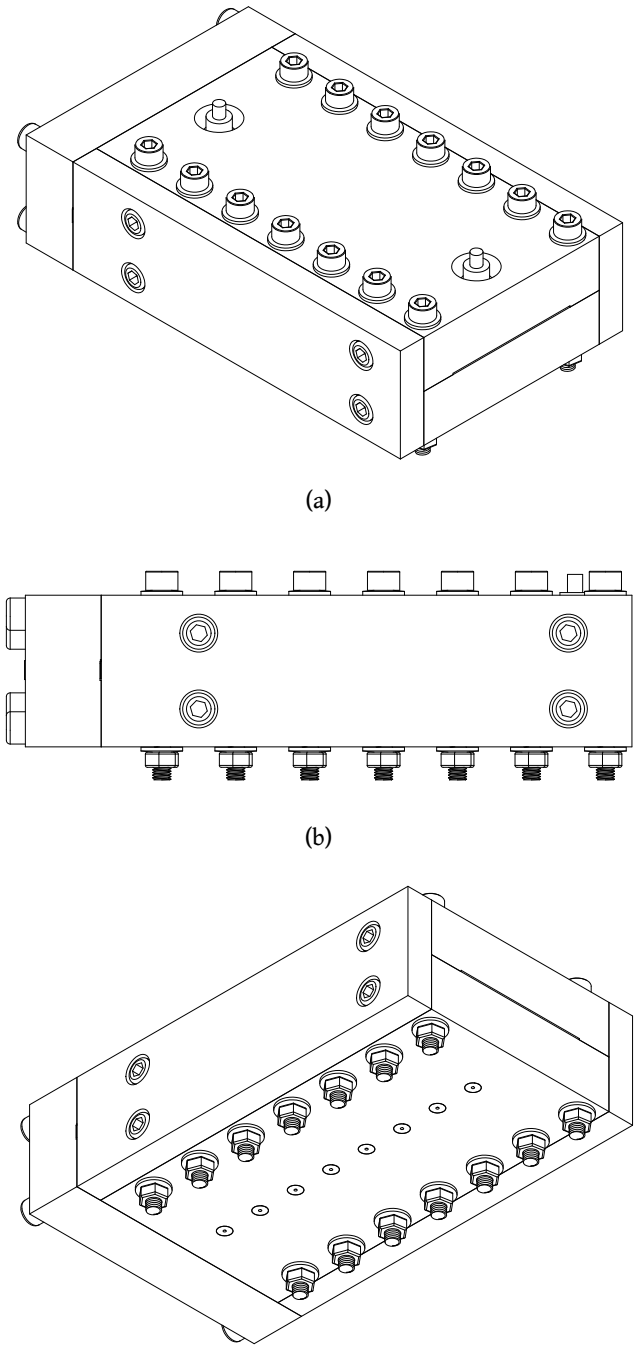

(a)

(b)

(c)

Figure 3.7: Channel structure drawing [9]: (a) view on the pressure sensors plate; (b) side view; (c) view on the temperature sensors plate.

different thicknesses: 0.5 mm and 0.2 mm. Both plates are 2 cm thick and the overall side metal thickness (side flange plus unmachined plate portion) is 2.25 cm per side. Because of the small confined space inside the channel, a rough surface could affect the fluid motion. Stainless steel was therefore chosen as the material in contact with helium to ensure the smoothness of the contact surfaces. The G10 support stands for the heater plug previously

mentioned and is 2 cm thick. The G10, which is fiberglass, was selected as a plug material to ensure high thermal and electrical insulation for the heater. The surface of the plug that faces the helium channel is grooved to house the heating source, which was chosen to be a highly resistive wire made out of Manganin® [101] that allows producing Joule heating through electric currents. The wire is as thick as the channel and as long as the width of the channel, which means that the heater matches entirely one side of the channel. The extremities of the wire are soft-soldered to high-temperature superconductive (HTS) current leads on each side of the channel. The HTS leads, made out of a YBCO compound, prevents heat dissipation outside of the channel. These tapes together with the heater are glued to the grooved surface of the plug with a polymerized epoxy resin (3M™ Scotch-Weld™ DP190) (see Fig. 3.8). The HTS leads, which are located between the side flanges and

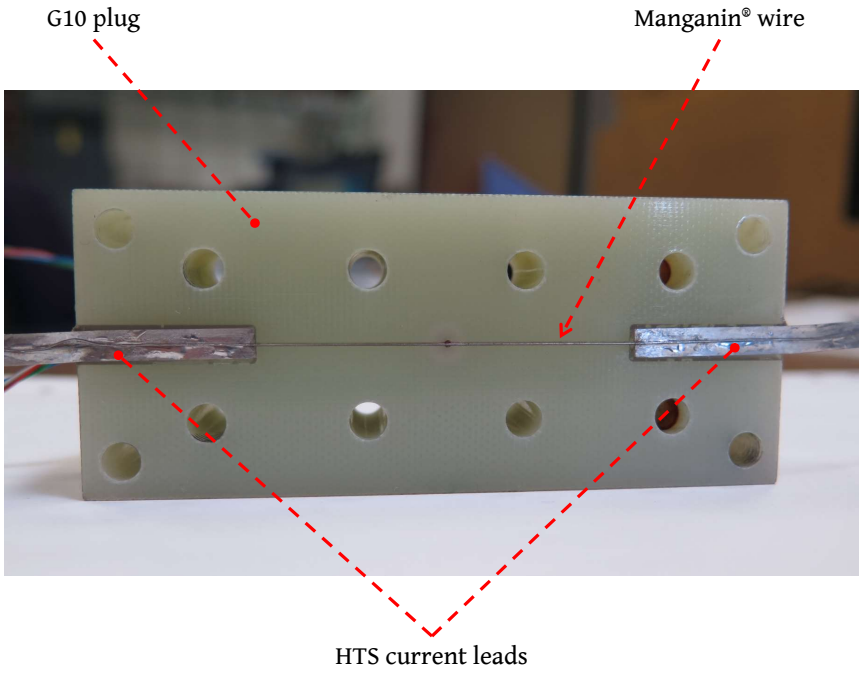

Figure 3.8: Manganin® wire soft-soldered to the HTS current leads and glued on the G10 heater plug.

the plug, are in turn soft-soldered to NbTi superconducting wires with gold connectors to reduce the heat deposition in the pressurized helium bath. The current led by the NbTi wires to the heater is provided externally by a Tektronix® PWS4305 DC [151] power supply. A picture of the channel setup installed in the insert is shown in Fig. 3.9.

As mentioned in the previous section, the pressurized bath is equipped with a heater that acts to regulate and maintain the temperature of the bath at the desired value. When a heat flux is applied through the Manganin® wire during a test, the heat released into the channel alters the bath temperature. Since some experiments require a fixed boundary condition at the aperture of the channel, in order to avoid temperature changes at that

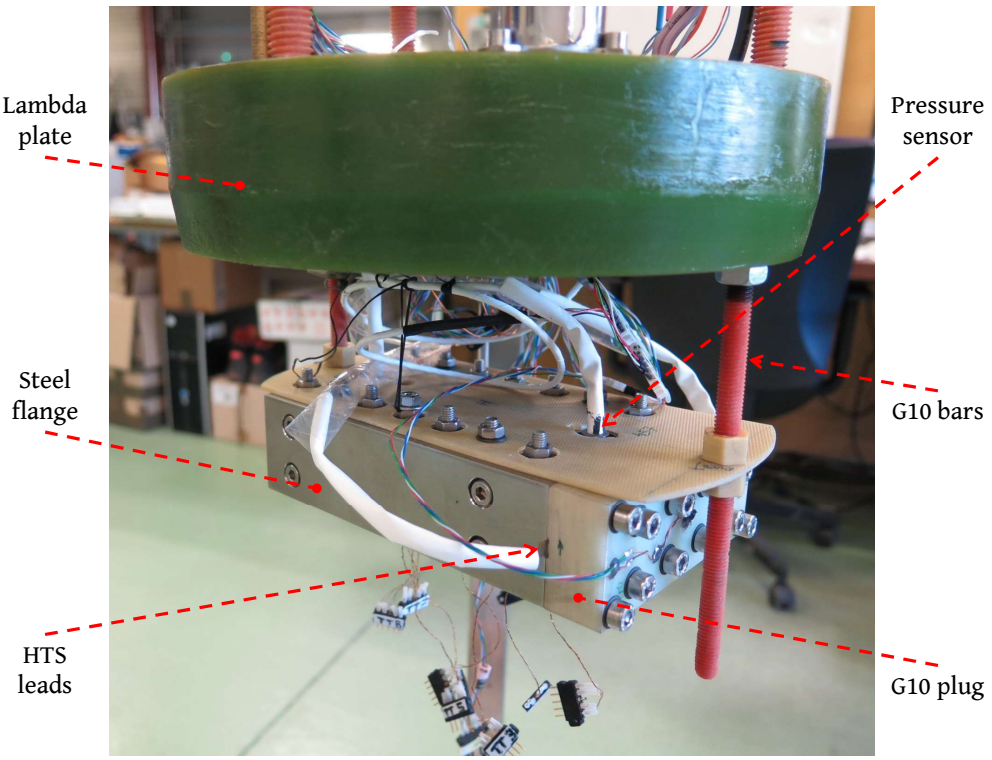

Figure 3.9: Channel setup anchored to the frame bars in horizontal position.

location the pressure of the saturated bath is kept at a value that corresponds to a lower temperature than the desired one, which is then reached via a heat load provided by the bath heater. When the channel heater causes an increment in the temperature of the bath, the bath heater decreases the heat load to match again the desired temperature. This system is automatically controlled by the LakeShore® PID controller previously introduced.

The channel setup is equipped with nine temperature sensors and two pressure sensors. Due to the size of the channel and the consequent small amount of helium contained in it, the temperature sensors are required to have a small size and thermal mass. For this reason, bare chip Cernox® CX-1050-BC temperature sensors with a sapphire base are adopted to ensure fast thermal response (1.5 ms at 4.2 K). Eight of them are inserted in appropriate holes machined in one of the steel plates. Their position in the holes is fixed by gluing them with epoxy resin to G10 supports, which also serve the purpose of electrically and thermally insulating the sensors from the metal plate. The supports are placed inside the holes so that the sensors are situated on the internal edge of the plate, without altering the thickness of the channel at the hole location. The eight sensors are distanced 1.5 cm from each other along the centerline of the unmachined plate and the closest sensor to the heater is 1.5 cm far from it. This means that the farthest sensor from the heater is 2 cm far from the aperture of the channel. The final assembly of the setup is shown in

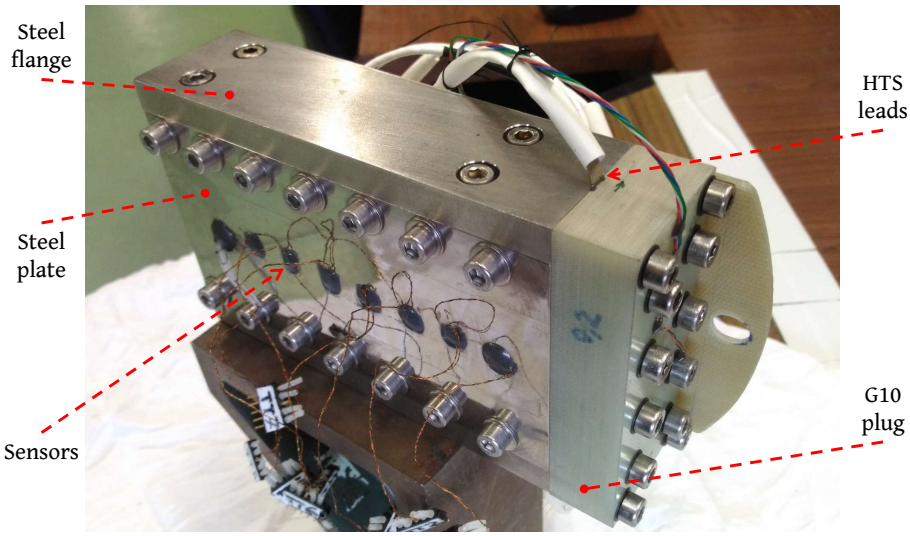

(a) View on the heater plug and temperature sensors plate

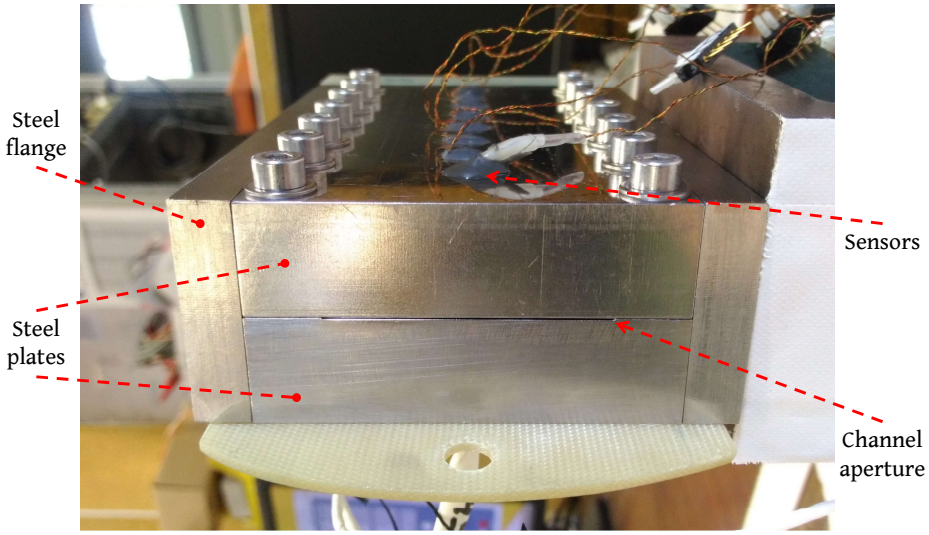

(b) View on the channel aperture

Figure 3.10: Channel assebly.

Fig. 3.10. The ninth temperature sensor is meant to measure indirectly the temperature of the heater. Because of the small thickness of the wire, it was not possible to make a measurement with a sensor in direct contact with it. Therefore, a workaround, shown in Fig. 3.11, was conceptualized and implemented. Inside a hole in the G10 support, a small copper rod is put in direct contact with the heater. This rod is soldered to a bigger hollow copper piece that expands the measurable surface. Finally, the sensor is glued inside the

hollow piece at a total distance of 2.8 mm from the heater.

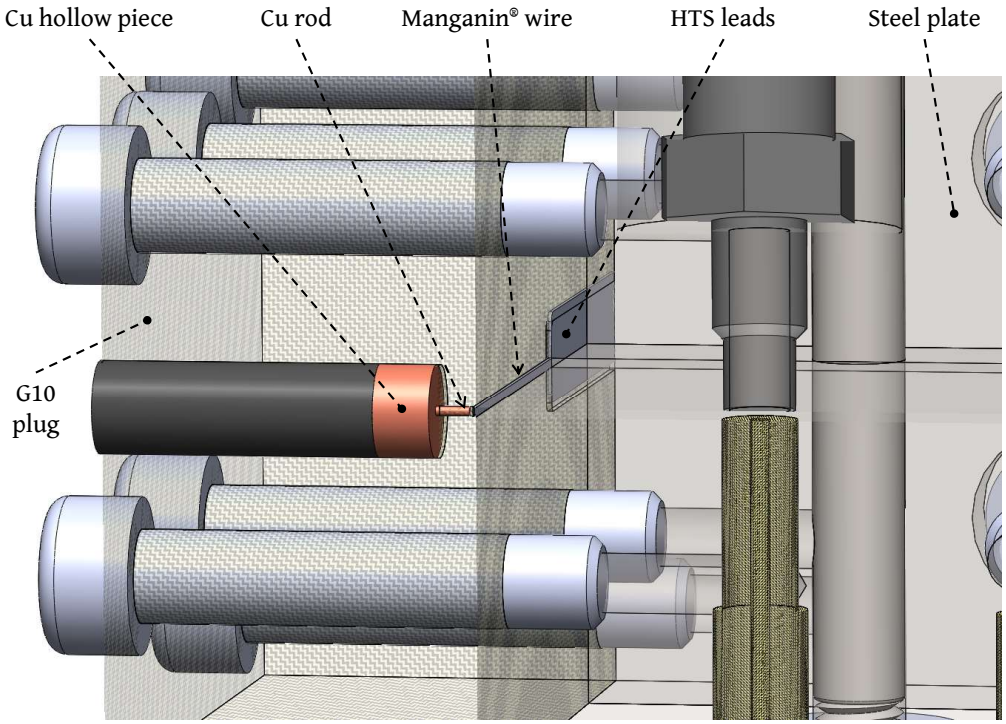

Figure 3.11: Temperature measurement design for the heating wire [9].

The nine bare chip Cernox® sensors are not provided by the constructor along with a calibration curve. Therefore, they were calibrated in absence of heat loads against a Cernox® CX-1050-SD temperature sensor installed in the insert and situated near the aperture of the channel. The calibration data was collected from 1.5 K up to ambient temperature with the channel in the horizontal position in order to minimize temperature stratification effects. Each bare chip is built-in with the 4-wire resistance-temperature-detector (RTD) technique, which ensures accurate measurements by fully compensating for the resistance error due to the wires. According to this technique, the current to power the resistor is delivered through one pair of wires, and the actual voltage drop is measured through the other pair of wires. The sensors are powered with 10 μA delivered by a battery system.

The two pressure sensors are mounted along the centerline of the other steel plate, facing the temperature sensors. One sensor is 1.5 cm far from the heater and the other sensor is 1.5 cm far from the aperture of the channel. Because of the cryogenic conditions of the experiments, the chosen sensors are Kulite® [90] cryogenic miniature ruggedized pressure transducers of the CTL-190 (M) series. The shape of the sensors' body allows to screw them directly into threaded holes inside the plate. As for the case of the temperature sensors, the sensitive surface of the sensors is located at the same level as the plate's internal edge. These Kulite® transducers are differential pressure sensors and, as such, are equipped with a small capillary to measure the pressure of the reference environment, which is the pressurized He II bath. The calibration curve of these pressure sensors was not

available and, thus, it was obtained by calibrating the sensors in superfluid helium against two MKS© Baratron® absolute pressure sensors in a smaller cryostat. The Kulite® sensors were tested at different pressures up to 7 bar with pressurized helium gas.

The analog signals of the sensors are transmitted to the data acquisition system and digitized with 16-bit A/D converter cards. The resulting measurements are visualized and acquired through a LabVIEW® [91] program.

Heat Leaks Despite this experimental setup is meant to provide information about the thermal response of He II, the interaction between helium and the various components surrounding it cannot be ignored. If He II undergoes phase transitions, its thermal time constant becomes comparable with one of the solid components and, thus, heat leaks from the channel through the materials start to be significant. In this paragraph, an analysis of the heat losses is presented to estimate the amount of energy that is not dissipated in helium. First off, the thermal time constant $\tau = L^2/\alpha$, defined as the ratio between the square of the characteristic length L and the thermal diffusivity α of the material, must be evaluated for the main leak paths of the setup. Components with a low time constant suffer fast temperature changes, which affect the steady-state temperature profile of helium. Fig. 3.12 reports τ as a function of the temperature for different components. The time

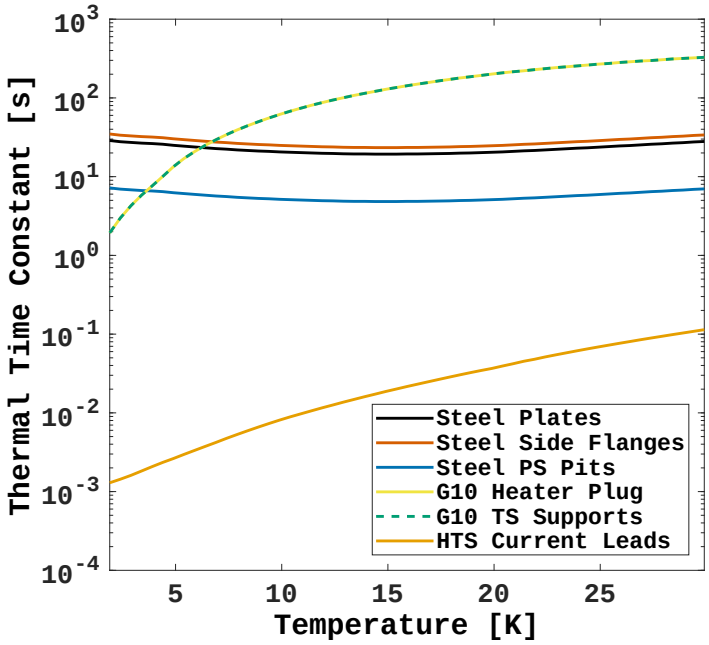

Figure 3.12: Thermal time constants of the experimental setup components.

constant of the HTS current leads is several orders of magnitude lower than the other materials because of its high thermal conductivity. On the other hand, the G10 components (temperature sensor supports and heater plug) have very high τ. Details on the time constant per material can be seen in Fig. B.1 in Annex B.1.

The heat losses Q are computed via one-dimensional integration of the thermal

conductivity of the material for different ranges of temperature starting from the reference value 1.9 K:

$$Q = \frac{A}{L} \int_{1.9}^{T} k(T)\, \mathrm{d}T\,, \tag{3.1}$$

where A is the area of contact with the helium in the channel. The heat leak per material can be found in Fig. B.2 in Annex B.1, while the total heat losses are presented in Fig. 3.13 for both channel thicknesses. More specifically, Fig. 3.13 shows the heat loss as a percentage

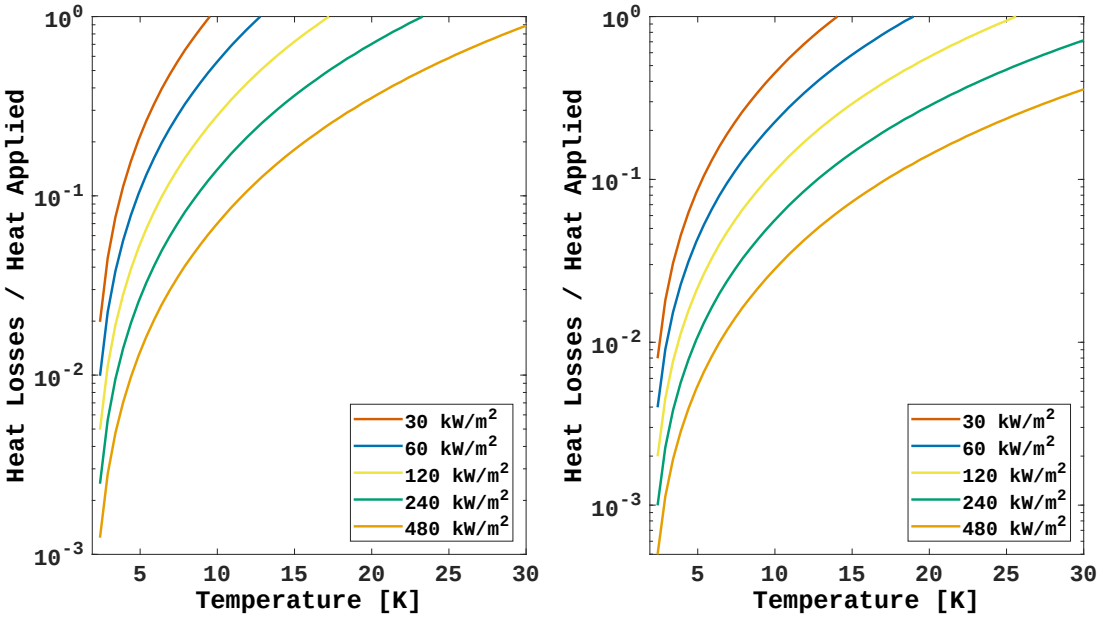

(a) 0.2 mm thick channel (b) 0.5 mm thick channel

Figure 3.13: Total heat losses estimation as a function of temperature for different representative heat fluxes.

with respect to the heat applied through the heater. Since the heat loss increases with the temperature, the zone that experiences the highest losses is the one nearby the heater. For this reason, the contact surface A of the steel parts is taken as the area from the heater to the first sensor. Taking into account that 10 % is an acceptable loss, the heat leaks become significant above 5 K for an applied heat flux equal to 30 kW/m^2 and 15 K for 480 kW/m^2. It must be borne in mind though, that these values refer to the steady state and hence have an actual impact only for test durations comparable with the thermal time constant of the materials.

As a last consideration, it is useful to compute what percentage of these losses is associated with which component. Table 3.1 reports such percentages for the same components and heat fluxes considered above. The percentages do not vary significantly in a wide range of heat fluxes. As it is clear, the steel components (plates and pressure sensor pits) represent the highest portion of losses together with the HTS current leads. In contrast, the percentage associated with the G10 plug appears very small as A in Eq. (3.1) corresponds to the cross-sectional area of the channel. However, since the plug

	q [kW/m^2]				
Leak Path	30	60	120	240	480
Steel Plates	70	70.5	71.2	72.1	72.9
Steel Sides	0.6	0.6	0.6	0.7	0.7
Steel PS Pit	16.5	16.6	16.8	17	17.2
G10 Plug	0.7	0.7	0.6	0.5	0.5
G10 TS Support	2	1.9	1.7	1.4	1.2
HTS Leads	10.2	9.7	9.1	8.3	7.5

Table 3.1: Heat loss percentage through the components of the experimental setup for different representative heat fluxes.

houses the heater, the effective area must be larger and thus the result is most certainly underestimated by the one-dimensionality of the analysis. This consideration will be relevant in the numerical modeling of the thermal events.

3.1.3 Data Elaboration and Error Estimation

Experimental measurements inevitably carry intrinsic uncertainties due to both the precision of the instrumentation, the instability of the experimental conditions, and the accuracy of the measurement method. It is essential to estimate the error made at each measurement in order to comprehend how accurate the experimental data is. Two different groups of errors can be distinguished: systematic and precision errors [149]. Systematic errors are associated with reproducible discrepancies with respect to the real value of a measured quantity, whereas precision errors yield results that change at every repetition of the measurement. Systematic errors are often difficult to recognize because of their nature. One typical example is the error associated with the calibration of a sensor. Normally, the calibration accuracy of a sensor is provided by the constructor and depends on the measurement conditions. The specifications of the temperature sensors and pressure transducers utilized in the present work are summarized in Table 3.2. Moreover, errors due to the acquisition system must be considered. The conversion error from analog to digital signals with a 16-bit A/D converter results to be lower than the residual noise of the A/D converter itself, which is about 20 μV. Since systematic errors are constant throughout the measurements, no information about their magnitude can be extrapolated from data samples. Therefore, the focus of the following paragraph is on precision errors.

If a quantity x is measured several times under the same conditions, fluctuations in the measured values can be observed. All the values scatter from a mean value $\overline{x}$ that can be

Sensor	Range of use	Accuracy
Cernox® CX-1050-SD	0.1 - 420 K	±5 mK (4.2 K) ±6 mK (10 K) ±10 mK (30 K) ±16 mK (77 K) ±40 mK (300 K)
MKS© Baratron® 627B	100 - 7×10^5 Pa	±0.12 %
Kulite® CTL-190	0 - 7×10^5 Pa	±0.1 %

Table 3.2: Accuracy and ranges of use of the temperature and pressure sensors.

calculated as

$$\overline{x} = \frac{1}{N} \sum_{i=1}^{N} x_i, \tag{3.2}$$

where N is the number of determinations of x. Let us imagine to subdivide these measurements into several groups, each of one associated with a certain range of values of x. If all the measurements are plotted in a histogram that shows how many values lie in each group, the resulting shape of the histogram will resemble the Gaussian probability distribution. This fact suggests that it is possible to apply statistical methods to analyze precision errors. In statistics, the average difference between the measurements and the mean of the sample distribution is generally calculated through the standard deviation σ:

$$\sigma_x = \left[\frac{1}{N-1} \sum_{i=1}^{N} (x_i - \overline{x})^2 \right]^{\frac{1}{2}}, \tag{3.3}$$

where $(N-1)$ is the number of degrees of freedom and it is equal to the number of measurements minus the number of intermediate parameters used, which, in this case, is just one — the mean of the sample distribution. The final value of the error is given by the standard deviation of the mean $\sigma_{\overline{x}}$:

$$\sigma_{\overline{x}} = \frac{\sigma_x}{\sqrt{N}}. \tag{3.4}$$

At this point, it is necessary to introduce a topic that needs to be addressed in the estimation of measurement uncertainties — the propagation of errors. If the measured quantity is not the final experimental result but rather serves the purpose of calculating another one, the error made to measure the first one propagates to the quantity of interest. The way this error propagates is regulated by statistical laws. Let us consider a variable y to be calculated through n measured quantities ($y = f(x_1, x_2, ..., x_n)$). If we assume that the mean $\overline{y}$ is a function of the mean of the measured quantities ($\overline{y} = f(\overline{x}_1, \overline{x}_2, ..., \overline{x}_n)$) and that

this is also true for the result associated with each measurement ($y_i = f(x_{1,i}, x_{2,i}, ..., x_{n,i})$), then the Taylor expansion can be used to express the deviation of each result:

$$y_i - \overline{y} \simeq (x_{1,i} - \overline{x}_1) \frac{\partial y}{\partial x_1} + (x_{2,i} - \overline{x}_2) \frac{\partial y}{\partial x_2} + ... \tag{3.5}$$

Therefore, the variance σ_y^2 of the variable y reads

$$\sigma_y^2 \simeq \sigma_{x_1}^2 \left(\frac{\partial y}{\partial x_1}\right)^2 + \sigma_{x_2}^2 \left(\frac{\partial y}{\partial x_2}\right)^2 + ... + 2\sigma_{x_1 x_2}^2 \left(\frac{\partial y}{\partial x_1}\right)\left(\frac{\partial y}{\partial x_2}\right) + ..., \tag{3.6}$$

where $\sigma_{x_1 x_2}^2$ is the covariance and tells how much the two measured quantities vary with respect to each other:

$$\sigma_{x_1 x_2}^2 = \frac{1}{N-1} \sum_{i=1}^{N} \left[(x_{1,i} - \overline{x}_1)(x_{2,i} - \overline{x}_2)\right]. \tag{3.7}$$

In this dissertation, there are some experimental results that derive from measured signals. For instance, the heat flux applied in the channel shown in the previous section is calculated as $q = IVA^{-1}$, where V, I, and A are respectively the voltage across the heater, the current provided, and the area of the heating surface. The error linked to the measurement of voltage and current propagates to the heat flux result. The standard deviation of the heat flux is evaluated with Eq. (3.6):

$$\sigma_q \simeq \frac{1}{A} \left(I^2 \sigma_V^2 + V^2 \sigma_I^2 + 2IV\sigma_{IV}^2\right)^{\frac{1}{2}}. \tag{3.8}$$

Another calculated parameter is the temperature, which is a function of the resistance R of the thermistors in temperature sensors. The way in which the temperature and the resistance relate to each other depends on the choice of the calibration function used to extrapolate the desired experimental result. In this dissertation, two cases are distinguished to partially simplify the calibration procedure. On the one hand, if the range of temperatures involved in an experiment is not too wide, such as in superfluid helium ($T < T_\lambda$), then a polynomial function can be satisfactorily utilized:

$$T = \sum_{j=0}^{m} a_j R^j, \tag{3.9}$$

where a_j refers to the polynomial coefficients. On the other hand, if helium vapour is generated following a high heat flux, the temperature is likely to cover a greater temperature range. In this case, the typical calibration curve resembles the shape of the inverse of the natural logarithm and hence the Steinhart-Hart equation is used [143]:

$$T^{-1} = a_0 + a_1 \ln(R) + a_2 \left[\ln(R)\right]^3. \tag{3.10}$$

For the experimental results of the present study, it was decided to adopt a generalized version of Eq. (3.10):

$$T^{-1} = \sum_{j=0}^{m} a_j \left[\ln(R)\right]^j. \tag{3.11}$$

The generalized Steinhart-Hart equation allows tailoring the number of terms ($m+1$) in Eq. (3.11) differently to each of the temperature sensors utilized in the experiments in order to optimize the fit. The calculation of the coefficients a_j in Eq. (3.11) is less trivial than the polynomial case. Therefore, they are computed in MATLAB® [104] by solving a system of equations of the form $[A][x] = [b]$, where $[A]$ is the matrix of the logarithms, $[x]$ is the array of the unknown coefficients, and $[b]$ is the array of the inverse of temperatures taken from the pre-calibrated sensors of the cryostat. It is known that $R = VI^{-1}$, where I in this case is the current provided to power the thermal sensors and V is the voltage signal from the sensors. If we consider that the current is constant for each sensor, then the standard deviation of the temperature can be computed through Eq. (3.6) by deriving Eqs. (3.9) and (3.11) for the voltage V:

$$\sigma_T \simeq \begin{cases} \sigma_V \sum_{j=1}^{m} \frac{j a_j}{I^j} V^{j-1}, & \text{for } T \approx T_\lambda, \quad (3.12a) \\ \sigma_V \frac{\sum_{j=1}^{m} j a_j V^{-1} \left[\ln\left(VI^{-1}\right)\right]^{j-1}}{\left\{\sum_{j=0}^{m} a_j \left[\ln(VI^{-1})\right]^j\right\}^2}, & \text{for } T \gg T_\lambda. \quad (3.12b) \end{cases}$$

For what concerns the Kulite® pressure sensors, the calculation is straightforward as the pressure difference is linearly proportional to the voltage signal. The standard deviation is then $\sigma_p \simeq a_1 \sigma_V$. It is important to underline that Eqs. (3.9) and (3.11) do not provide an exact value of the temperature. The calibration equations suffer, indeed, from a curve-fitting error. The error that results from the fitting process is evaluated with MATLAB® and must be considered in the total error of the measurement. The total error $\sigma_{\overline{y},tot}$ associated with the measured quantity y is computed by taking the 2-norm of the single standard deviations. If N is high enough (i.e., typically $N > 10$), it is common practice to roughly estimate the interval within which a measure is likely to lie with confidence of 95 %. This is obtained through the precision uncertainty $P_{\overline{y}} \simeq 2\sigma_{\overline{y},tot}$. A measurement y_i is then said to lie within the interval $\overline{y} \pm P_{\overline{y}}$ with 95 % probability. In this study, the precision uncertainty associated with the temperature measurements without the presence of boiling is roughly 0.12 % for all the sensors.

3.2 Numerical Toolbox

Nowadays, the usage of Computer-Aided Engineering (CAE) tools is widely spread in the prediction of physical phenomena that might be too costly to study via experimental investigations. Numerical simulations are used also if the analytical solution of a certain set of equations describing a phenomenon is impossible to obtain. In the vast majority of engineering applications, either the geometry of interest or the complexity of the equations does not allow the simplifications required to solve the problem analytically. The partial differential equations (PDEs) of fluid mechanics (i.e., the Navier-Stokes equations) represent one of those cases. Computational Fluid Dynamics (CFD) is the numerical tool

that gives access to an approximate solution of a wide range of fluid flow problems. The approximation is achieved through methods that reduce the problem to a system of algebraic equations by discretizing the PDEs in space and time. One of these discretization methods is the so-called Finite Volume Method (FVM) [51], which is also the method chosen for the present study. There are various commercial software packages available on the market that implement the FVM. However, often the numerical procedure is encrypted and difficult to adapt to specific needs required by the complexity of a problem. Due to the peculiar characteristics of superfluid helium, it was decided to utilize an open-source software known as OpenFOAM® (Open Source Field Operation and Manipulation) [119], which ensures versatility and freedom to modify the existing modules in order to overcome the difficulties of He II. In the following subsections, the main features of the FVM are presented along with the solution approach of OpenFOAM®. Subsequently, an overview of the numerical models used in heat transfer and multiphase flow applications is provided. The last part of this section focuses on the solution procedure of the solver chosen as a base for the He II modifications.

3.2.1 Finite Volume Method

In the FVM, the computational domain is subdivided into a pre-defined number of cells, called control volumes, that form the geometrical model. Each control volume is characterized by a centroid (P or N in Fig. 3.14) and a finite number of bounding faces that define the shape of the cell. The control volume faces can be either boundary or internal faces, whether they are part of the outer surfaces of the computational domain or not. Each internal face is shared between two adjacent control volumes. The centroids of the control volumes coincide with the computational locations where the governing equations are solved for the variables.

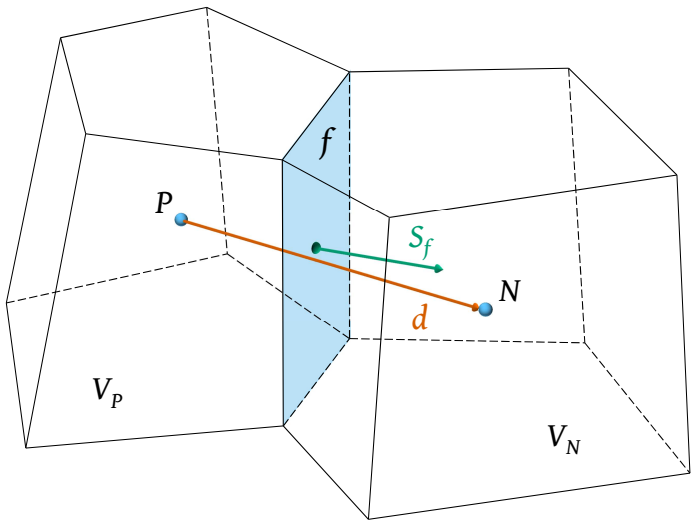

Figure 3.14: Representation of two adjacent control volumes with arbitrary shape.

The discretization procedure of the PDEs consists mainly of two steps: integration of the PDEs over the control volumes; interpolation of the variable values between cells. In order to break down these steps, let us consider a generic transport equation that needs to be solved for the scalar quantity ϕ:

$$\frac{\partial(\rho\phi)}{\partial t} + \boldsymbol{\nabla}\cdot(\rho\mathbf{v}\phi) = \boldsymbol{\nabla}\cdot(\Gamma_\phi\boldsymbol{\nabla}\phi) + Q_\phi(\phi), \tag{3.13}$$

where Γ_ϕ is the transport property associated with ϕ and $Q_\phi(\phi)$ is the net value between source and sink functions, which will be referred to simply as source function from now on. The terms in Eq. (3.13) represent from left to right the temporal term, advection term, diffusion term, and source term. For the sake of simplicity, let us drop the time derivative and consider a steady-state case. The integration of Eq. (3.13) over a control volume V_P yields

$$\int_{V_P}\boldsymbol{\nabla}\cdot(\rho\mathbf{v}\phi)\,\mathrm{d}V = \int_{V_P}\boldsymbol{\nabla}\cdot(\Gamma_\phi\boldsymbol{\nabla}\phi)\,\mathrm{d}V + \int_{V_P}Q_\phi(\phi)\,\mathrm{d}V\,. \tag{3.14}$$

At this point, the volume integrals involving differential operators can be transformed into surface integrals by applying the Gauss's theorem [159], which states that the integral of the divergence of a vector field over a volume V is equal to the surface integral of the flux through the closed surface S surrounding that volume:

$$\oint_{S_P}(\rho\mathbf{v}\phi)\,\mathrm{d}\mathbf{S} = \oint_{S_P}(\Gamma_\phi\boldsymbol{\nabla}\phi)\,\mathrm{d}\mathbf{S} + \int_{V_P}Q_\phi(\phi)\,\mathrm{d}V\,. \tag{3.15}$$

The vector fields $\rho\mathbf{v}\phi$ and $\Gamma_\phi\boldsymbol{\nabla}\phi$ are denoted as the advective and diffusive flux respectively. These fluxes represent the transport of the quantity ϕ throughout the computational domain by either the mass flow or the spatial differences of ϕ. The surface integrals over the closed surface must be discretized as a summation of surface integrals over all the faces f of the control volume:

$$\oint_{S_P}(\rho\mathbf{v}\phi)\,\mathrm{d}\mathbf{S} = \sum_{f=1}^{N_f(P)}\left[\int_f(\rho\mathbf{v}\phi)\,\mathrm{d}\mathbf{S}\right], \tag{3.16a}$$

$$\oint_{S_P}(\Gamma_\phi\boldsymbol{\nabla}\phi)\,\mathrm{d}\mathbf{S} = \sum_{f=1}^{N_f(P)}\left[\int_f(\Gamma_\phi\boldsymbol{\nabla}\phi)\,\mathrm{d}\mathbf{S}\right]. \tag{3.16b}$$

In order to calculate the exact value of the surface integral over a face of the control volume, the value of the flux at each point of the face would be necessary. However, the quantity ϕ is known at the centroid of the cell only. Therefore, the integrals need to be approximated with a quadrature formula. Various options are available in numerical science depending on the number of integration points considered on the cell face f [110]. Although multiple integration points are usually preferred, the gain in accuracy does not justify the increment in computational cost. Therefore, the most utilized formula is the mid-point rule, which

approximates the integral by considering the value of the flux at the center of the face f:

$$\int_f (\rho \mathbf{v}\phi)\, \mathrm{d}\mathbf{S} = (\rho \mathbf{v}\phi)_f \cdot \mathbf{S}_f, \tag{3.17a}$$

$$\int_f (\Gamma_\phi \boldsymbol{\nabla}\phi)\, \mathrm{d}\mathbf{S} = (\Gamma_\phi \boldsymbol{\nabla}\phi)_f \cdot \mathbf{S}_f, \tag{3.17b}$$

where $\mathbf{S}_f$ is a surface normal vector whose magnitude is equal to the area of the face (see Fig. 3.14). The centroid P in Fig. 3.14 refers to the cell from which $\mathbf{S}_f$ points outward, the so-called "owner" cell. From the point of view of the neighbour cell N, $\mathbf{S}_f$ will then point inward.

Similarly, the volume integral of the source term (last term on the RHS of Eq. (3.15)) can be approximated with a quadrature formula. In the case of one integration point, only the centroid of the cell is taken into account:

$$\int_{V_P} Q_\phi(\phi)\, \mathrm{d}V = Q_{\phi,P} V_P, \tag{3.18}$$

where the source term $Q_{\phi,P}$ is a constant term. The general steady-state transport equation after the first discretization step becomes then

$$\sum_{f=1}^{N_f(P)} \Big[(\rho \mathbf{v}\phi)_f \cdot \mathbf{S}_f - (\Gamma_\phi \boldsymbol{\nabla}\phi)_f \cdot \mathbf{S}_f \Big] = Q_{\phi,P} V_P. \tag{3.19}$$

The second discretization step consists of computing the flux values at the cell faces by interpolation between cell centroid values. Since the flux that enters a control volume through a face is equal to the one that exits the adjacent cell, the global conservation of the variable is intrinsically achieved for the whole domain. This is a key characteristic of the FVM, which is then able to satisfy exactly an approximate conservation law. Because of the different physical nature of the fluxes in the transport equation, diverse interpolation approaches are used for the terms. The interpolation schemes have distinctive properties, such as boundedness and stability. A scheme ensures boundedness if in the absence of sources the computed value of the unknown variable is bounded by the spatial and temporal conditions applied to the computational domain. An unbounded solution may result in the instability of the algorithm, which hence may not converge to a numerical solution of the PDEs. If the algorithm converges, the error due to the discretization of the PDEs should tend to zero as the number of cells tends to infinite. The discretization schemes have different orders of approximation, which can be evaluated by considering the truncation error of the Taylor series expansion of the discretized expression. The truncation error is proportional to a power n of the cell size and hence the scheme will be nth-order accurate [51]. The order of accuracy essentially indicates the rate at which the approximation error decreases with finer grids. Similar arguments can be made for the temporal discretization of the transport equation in terms of the time step instead of the cell size. In the next paragraphs, the main interpolation schemes are presented for each term of the equation for a Cartesian orthogonal grid (see Fig. 3.15).

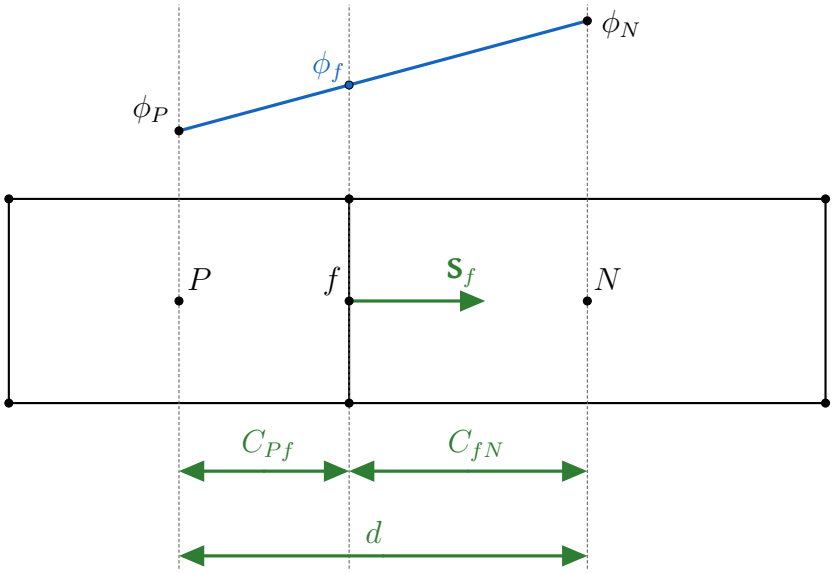

Figure 3.15: Schematic representation of two adjacent cells in a non-uniform orthogonal grid.

Gradient Computation Various methods are available in literature for the numerical computation of the gradient. The most popular one derives from a corollary of the Gauss's theorem stating that the integral of the gradient of a scalar quantity ϕ over a volume V is equal to the surface integral of the flux through the closed surface S surrounding that volume:

$$\int_V \boldsymbol{\nabla}\phi \, \mathrm{d}V = \oint_S \phi \, \mathrm{d}\mathbf{S} \,. \tag{3.20}$$

Eq. (3.20) can be numerically approximated as for the case of the divergence operator [110]:

$$(\boldsymbol{\nabla}\phi)_P = \frac{1}{V_P} \sum_{f=1}^{N_f(P)} \phi_f \mathbf{S}_f . \tag{3.21}$$

The value of the conserved quantity at the face center ϕ_f needs to be computed through linear interpolation between the centroid values of the cells sharing the face:

$$\phi_f = \lambda_f \phi_P + (1 - \lambda_f)\, \phi_N, \tag{3.22}$$

where the coefficient λ is a geometric factor that determines the weight of the cell center values depending on the shape of the cells:

$$\lambda_f = \frac{S_{f,N}}{S_{f,N} + S_{f,P}}, \tag{3.23}$$

where the factors S_f are scalars defined as

$$S_{f,P} = \|\mathbf{S}_f \cdot \mathbf{C}_{Pf}\|, \tag{3.24a}$$

$$S_{f,N} = \|\mathbf{S}_f \cdot \mathbf{C}_{fN}\|. \tag{3.24b}$$

The vectors **C** represent the distance between the face center and the centroid of a cell. It is easy to check that, for a uniform orthogonal grid, Eq. (3.22) provides the harmonic mean of ϕ_P and ϕ_N.

Diffusive Flux The most used interpolation scheme for the diffusion term is the central-difference scheme (CDS) [122], which is second-order accurate. It corresponds to a linear interpolation between the centroid values of ϕ of the cells sharing the face f:

$$\left(\Gamma_\phi \boldsymbol{\nabla}\phi\right)_f \cdot \mathbf{S}_f = \Gamma_{\phi,f} \|\mathbf{S}_f\| \frac{\phi_N - \phi_P}{\|\mathbf{d}\|}, \tag{3.25}$$

where **d** is the distance vector between the two centroids. The diffusion coefficient $\Gamma_{\phi,f}$ is evaluated at the face location with the same procedure as the calculation of ϕ_f in the previous paragraph dedicated to the gradient term.

Advective Flux The advection term can be addressed through various schemes depending on the magnitude of the velocity field. Applying the CDS to the advective flux yields

$$\left(\rho \mathbf{v} \phi\right)_f \cdot \mathbf{S}_f = \dot{m}_f \phi_f, \tag{3.26}$$

where $\dot{m}_f$ represents the mass flux through the face f. The value of the conserved variable at the face ϕ_f is computed as previously shown. The CDS involves both the ϕ values of the owner and neighbour cells equally in the calculation of the flux at the face. This fact makes the CDS particularly suitable for isotropic transport phenomena such as the diffusion term. However, for highly anisotropic phenomena such as advection-dominated problems, the CDS may lead to unphysical solutions due to its unboundedness [78].

A possible solution to this issue is represented by the upwind scheme (US) [36], which is first-order accurate but unconditionally bounded. This scheme simply sets the face value to the centroid one of either the owner or neighbour cell according to the flow direction:

$$\phi_f = \begin{cases} \phi_P, & \text{for } \dot{m}_f \geq 0, \quad \text{(3.27a)} \\ \phi_N, & \text{for } \dot{m}_f < 0. \quad \text{(3.27b)} \end{cases}$$

The US truncation error shows a typical diffusive character that makes the scheme stable but also less accurate than the CDS.

There exist also blended versions of different schemes that try to reach an optimal trade-off between accuracy and stability [51].

Boundary Conditions If the face under consideration is not internal (i.e., it belongs to the domain boundaries), the flux cannot be evaluated in terms of neighbouring cells. In this case, the conserved quantity ϕ must be either set to a known value or computed in terms of internal centroid values only. There are many possible boundary conditions depending on the nature of ϕ and on the boundary type. Two boundary conditions are particularly used regardless of the transported quantity: the Dirichlet and Neumann boundary conditions [110]. The latter specifies a known value for the flux, while the first one specifies ϕ_f, and the flux is derived consequently.

3.2.1.1 Transient Problems

If the problem requires a transient solution, a PDE including the time derivative must be considered. The temporal term has to be integrated over the control volume similarly to the constant source term:

$$\int_t^{t+\Delta t} \int_{V_P} \frac{\partial (\rho\phi)}{\partial t} \, \mathrm{d}V \, \mathrm{d}t = \int_t^{t+\Delta t} \frac{\partial (\rho\phi)_P}{\partial t} V_P \, \mathrm{d}t \, . \tag{3.28}$$

Introducing the discretized temporal term into Eq. (3.19) and integrating over an interval of time Δt yields

$$\begin{aligned} \int_t^{t+\Delta t} \frac{\partial (\rho\phi)_P}{\partial t} V_P \, \mathrm{d}t = & \int_t^{t+\Delta t} \left\{ \sum_{f=1}^{N_f(P)} \left[(\Gamma_\phi \boldsymbol{\nabla}\phi)_f \cdot \mathbf{S}_f - (\rho \mathbf{v}\phi)_f \cdot \mathbf{S}_f \right] \right\} \mathrm{d}t \\ & + \int_t^{t+\Delta t} Q_{\phi,P} V_P \, \mathrm{d}t \, . \end{aligned} \tag{3.29}$$

The discretization of the time integral of the temporal term takes the following general form:

$$\int_t^{t+\Delta t} \frac{\partial (\rho\phi)_P}{\partial t} V_P \, \mathrm{d}t = \frac{(\rho\phi)_P^{t+\Delta t} - (\rho\phi)_P^t}{\Delta t} V_P, \tag{3.30}$$

where the superscripts on the RHS indicate which instant of the discretized timeline the field ϕ is associated with. The discretization of the time integral of the other terms in Eq. (3.29) depends on the instant at which the fluxes are evaluated. The temporal discretization methods can be distinguished between explicit and implicit methods [51]. In an explicit method, the fluxes are evaluated at instants at which the variable field is already known, while in an implicit method the fluxes are part of the unknowns of the equation since they refer to the successive instant $t + \Delta t$. The solution algorithm of explicit methods is much simpler and faster since the equation at each control volume has one unknown only. However, the stability of these methods is limited by the Courant number $Co = \mathbf{v}_f \cdot \mathbf{d}/\Delta t$, which must be lower than 1 for the algorithm to converge to a solution [35]. In implicit methods, a coefficient matrix must be inverted to solve the system of equations. This binds the solution of all the control volumes together and makes the algorithm stable. The most used implicit method is the Euler implicit scheme, which is first-order accurate and expresses the equation as

$$\frac{(\rho\phi)_P^{t+\Delta t} - (\rho\phi)_P^t}{\Delta t} V_P = \sum_{f=1}^{N_f(P)} \left[(\Gamma_\phi \boldsymbol{\nabla}\phi)_f^{t+\Delta t} \cdot \mathbf{S}_f - (\rho \mathbf{v}\phi)_f^{t+\Delta t} \cdot \mathbf{S}_f \right] + Q_{\phi,P} V_P. \tag{3.31}$$

A more accurate method is the Crank-Nicolson scheme (CNS) [37], which is second-order accurate in time. It is a blend of both the implicit and explicit versions of the Euler scheme. The CNS aims at combining the stability of an implicit method with the accuracy

of a second-order accurate scheme. The discretized transport equation becomes then

$$\frac{(\rho\phi)_P^{t+\Delta t} - (\rho\phi)_P^t}{\Delta t} V_P = \frac{1}{2} \sum_{f=1}^{N_f(P)} \left[(\Gamma_\phi \boldsymbol{\nabla}\phi)_f^{t+\Delta t} \cdot \mathbf{S}_f - (\rho \mathbf{v}\phi)_f^{t+\Delta t} \cdot \mathbf{S}_f \right] + \frac{1}{2} \sum_{f=1}^{N_f(P)} \left[(\Gamma_\phi \boldsymbol{\nabla}\phi)_f^{t} \cdot \mathbf{S}_f - (\rho \mathbf{v}\phi)_f^{t} \cdot \mathbf{S}_f \right] + Q_{\phi,P} V_P. \tag{3.32}$$

Since the CNS may be unstable in certain problems, it is common to stabilize it through a blending coefficient that determines how close the scheme has to be to a pure implicit Euler method [119].

After expressing the face values in function of the centroid ones, Eqs. (3.31) and (3.32) may be summarized by the following form:

$$a_P^\phi \phi_P = \sum_{c=1}^{N_{nb}(P)} a_{nb}^\phi \phi_{nb} + b^\phi, \tag{3.33}$$

where a^ϕ represents multiplying coefficients, ϕ_{nb} are the centroid values of the neighbouring cells, and b^ϕ contains the source terms. Setting up Eq. (3.33) for each control volume of the computational domain yields a system of linear algebraic equations of the form $[A][\phi] = [b]$, where $[A]$ is the matrix of the coefficients multiplying the unknowns, $[\phi]$ is the array of the unknown variables, and $[b]$ is the array of source terms and constants. This system can be solved with several methods, which are usually subdivided into direct and iterative methods [127]. Direct methods invert the matrix $[A]$ to solve the system directly at once. For this reason, if the matrix is large (i.e., the mesh is very fine) the operation becomes computationally too costly to handle. A valid alternative is represented by the iterative methods, which are widely used in CFD for their computational cost-efficiency. They iteratively get closer to a solution that satisfies a pre-defined convergence tolerance starting from an initial guess. The iterative methods were also chosen for the simulations of this dissertation.

3.2.1.2 Segregated Approach on Colocated Grids

When the general transport equation treated so far is applied to fluid mechanics, a complication arises in the solution procedure of the momentum equations. Since the pressure is not used as a state variable despite it drives the flow, an additional equation is introduced to anticipate the pressure effect on the flow. This issue is usually addressed via a pressure-velocity coupling equation that is assembled by rearranging together the momentum and continuity equations. The resulting system of equations may be solved with semi-direct methods [27], which solve the equations simultaneously. However, the number of numerical operations necessary for these methods increases drastically with the mesh size. Another group of methods utilizes rather a segregated solution approach, which solves the equations sequentially in an uncoupled manner. More specifically, the procedure consists of: solving implicitly the momentum equation using the pressure

field of the previous step; assembling and solving the coupling equation for the pressure; updating the mass flux and the velocity with the new pressure field. In order to ensure mass conservation, the procedure must be iterated until the continuity error is below a certain pre-defined value.

Before deriving the pressure equation, it is useful to specify where the conserved variables are stored in the domain. The choice of the locations should not be underestimated as it may affect positively or negatively the solution procedure. One possibility is the staggered arrangement proposed by Harlow and Welsh [66]. In a staggered grid, the velocity field is stored at cell faces in the form of vector components, while all other variables are located at cell centroids. This arrangement makes the interpolation of the advective fluxes superfluous, as the face values are already available. The disadvantage of this approach appears when the problem requires more than one dimension. Since each face accommodates a single velocity component, in the case of multi-dimensional domains a separate grid system for each vector component would be needed [110]. This imposes severe memory requirements on the hardware. A more affordable solution is the colocated arrangement, which is also adopted in OpenFOAM®. In a colocated grid all the variables are stored at cell centroids, simplifying considerably the arrangement. However, a typical issue that may arise in a colocated grid is the so-called checkerboard problem. It can be shown that the discretization via CDS of the pressure gradient in the momentum equation yields a term that depends on the pressure values of non-consecutive cell centroids (i.e., spaced of $2\|\mathbf{d}\|$) [51]. If the pressure field is non-uniform and distributed in such a way its values are equal at alternate cells (i.e., checkerboard pressure field), the CDS will interpret it as a uniform field instead. This implies that, for an incompressible fluid, the wrong uniform pressure field causes a stagnant flow because of the pressure-velocity interaction in the momentum equation. A solution to this problem was proposed by Rhie and Chow [130], who constructed an interpolation method that overcomes the issue by introducing a dissipation term into the linear interpolation of the velocity field. This additional term derives from a staggered-like momentum equation and it forces the velocity interpolation to depend on the pressure gradient too.

The Rhie-Chow interpolation is at the base of the colocated formulation of the most popular segregated method — the SIMPLE (Semi Implicit Method for Pressure Linked Equations) algorithm [121]. Over the years, numerous variants of SIMPLE were born in order to improve different aspects of the original method [40]. This subsection reports a general version of the pressure equation, which represents the starting point of all the variants. Applying Eq. (3.33) to the case of the momentum equation and rearranging for the unknown yields

$$\mathbf{v}_P = \frac{\sum_{c=1}^{N_{nb}(P)} a_{nb}^{\mathbf{v}} \mathbf{v}_{nb} + b^{\mathbf{v}}}{a_P^{\mathbf{v}}} - \frac{V_P}{a_P^{\mathbf{v}}} \left(\boldsymbol{\nabla} p\right)_P , \tag{3.34}$$

where the pressure gradient term has not been discretized yet. Eq. (3.34) can be expressed in a more readable way as $\mathbf{v}_P = \mathbf{H}(\mathbf{v})_P - \mathbf{D}(p)_P$, with $\mathbf{H}(\mathbf{v})_P$ and $\mathbf{D}(p)_P$ being the first and second terms on the RHT of Eq. (3.34) respectively. As explained at the beginning of this

subsection, a segregated algorithm consists mainly of two steps: a predictor step, in which a preliminary value for the velocity is estimated, and a corrector step, in which a corrected value of the velocity is computed using the new pressure field. It is then useful to express the variables as

$$p = p^* + p', \tag{3.35a}$$

$$\mathbf{v} = \mathbf{v}^* + \mathbf{v}', \tag{3.35b}$$

$$\rho = \rho * + \rho', \tag{3.35c}$$

where the superscript $*$ stands for the value of a new iteration and $'$ indicates the contribution due to the correction. For compressible flows, the pressure-velocity coupling involves also the density ρ, which appears in the equation of state of the fluid. The continuity equation for compressible fluids can be discretized by following the same principles presented in the previous subsection:

$$\frac{\rho_P^{t+\Delta t} - \rho_P^t}{\Delta t} V_P + \sum_{f=1}^{N_f(P)} (\rho \mathbf{v})_f \cdot \mathbf{S}_f = 0, \tag{3.36}$$

where the time discretization of the second term is omitted as it depends on the scheme utilized. The mass flux $\rho\mathbf{v}$ can be linearized as

$$\rho\mathbf{v} = \rho\mathbf{v}^* + \rho^*\mathbf{v} - \rho^*\mathbf{v}^* + \rho'\mathbf{v}' \tag{3.37}$$

by means of Eqs. (3.35b) and (3.35c). Eq. (3.36) becomes then

$$\begin{aligned} \frac{\rho_P^{t+\Delta t} - \rho_P^t}{\Delta t} V_P = & \sum_{f=1}^{N_f(P)} \left[(\rho^*\mathbf{v}^*)_f \cdot \mathbf{S}_f \right] - \sum_{f=1}^{N_f(P)} \left[(\rho'\mathbf{v}')_f \cdot \mathbf{S}_f \right] \\ & - \sum_{f=1}^{N_f(P)} \left[(\rho\mathbf{v}^* + \rho^*\mathbf{v})_f \cdot \mathbf{S}_f \right], \end{aligned} \tag{3.38}$$

where the second term on the RHS is negligible [40]. Eq. (3.38) can be written more conveniently as

$$\begin{aligned} \frac{\rho_P^{t+\Delta t}}{\Delta t} V_P + \sum_{f=1}^{N_f(P)} (\rho v^*)_f - \sum_{f=1}^{N_f(P)} \left[(\rho^*\mathbf{D}(p))_f \cdot \mathbf{S}_f \right] = & \frac{\rho_P^t}{\Delta t} V_P + \sum_{f=1}^{N_f(P)} (\rho^* v^*)_f \\ & - \sum_{f=1}^{N_f(P)} \left[(\rho^*\mathbf{H}(\mathbf{v}))_f \cdot \mathbf{S}_f \right]. \end{aligned} \tag{3.39}$$

The pressure equation is finally derived by expressing the density as a function of the pressure through the compressibility $\psi(T,p)$ of the fluid ($\rho = \psi p$). A solver for compressible fluids needs to solve an energy equation in order to update at each time step the thermodynamic properties and hence $\psi(T,p)$. The vector field $\mathbf{H}(\mathbf{v})$ can be decomposed into $\mathbf{H}(\mathbf{v}^*) + \mathbf{H}(\mathbf{v}')$. This helps in the characterization of the variants of the SIMPLE algorithm, as their differences reside mainly on how they treat the term $\mathbf{H}(\mathbf{v}')$ [110]. The

SIMPLE algorithm, for example, neglects this term. This is because SIMPLE was originally designed for steady-state problems and, since a correction term by definition tends to 0 at convergence, the term $\mathbf{H}(\mathbf{v}')$ does not influence the solution of the problem. The exclusion of this term has consequences on the convergence stability of the algorithm though, which is what gave rise to the variants of the SIMPLE method. Probably the most important one is the PISO (Pressure-Implicit with Splitting of Operators) algorithm [76], which is suitable for transient problems as it takes advantage of the fact that an event that is discretized in time can be addressed via an iterative procedure. In fact, in PISO the computed variables at each iteration refer to a specific instant of the discretized timeline. PISO is characterized by a predictor step and multiple corrector steps included in an internal pressure correction loop that ensures mass conservation at each time step. The term $\mathbf{H}(\mathbf{v}')$ is taken into account in this internal loop. The convergence stability of the PISO algorithm can be controlled by adjusting the time interval Δt between one iteration and the successive one.

For transient problems, OpenFOAM® gives the possibility to utilize the PIMPLE algorithm [119], which is a combination of SIMPLE and PISO. It consists of three loops: an inner pressure correction loop; an outer loop that includes the predictor step and the energy equation; the time-marching loop. The opportunity to repeat the sequence within a time-step after solving the energy equation (thus updating the thermophysical properties) facilitates the solution procedure in problems that lack convergence stability, even when the Courant number is greater than 1. If the outer loop is run just once, a pure PISO algorithm is obtained. In this study, the PIMPLE method is adopted with different settings on the number of outer and inner iterations depending on the problem under investigation.

3.2.2 Heat Transfer and Multiphase Flow Solvers

The need to simulate the phase transitions of superfluid helium requires multiphase flow numerical techniques. The focus of this dissertation is on compressible liquid/gas phases. A two-phase mixture is constituted by a continuous phase and a dispersed phase. The continuous phase is always treated with an Eulerian approach, while the dispersed one can be addressed via either an Eulerian or Lagrangian approach depending on its nature [51]. The various numerical models for multiphase phenomena are then distinguished between Euler-Euler [75] and Euler-Lagrange methods [38]. In the latter, the dispersed phase is considered as an aggregation of individual particles that are tracked throughout the computational domain. These methods are appropriate when the dispersed phase is low in volume percentage with respect to the continuous phase (e.g., dust or sprays), which is not the case in the present study. In Euler-Euler methods, both phases are considered as continua and a phase fraction parameter determines the volume percentage occupied by each phase in a control volume. Many Euler-Euler solvers have been developed over the years. Below, a brief explanation of the most popular ones is given.

The most complex one is the two-phase model, which treats the phases separately and thus solves a distinct set of governing equations per phase. Due to this distinction, additional terms describing the momentum transfer between the phases are needed. This

transfer mechanism is regulated by the drag, lift, and virtual mass forces [133]. If the problem involves also phase change events such as boiling, the inter-phase heat transfer due to bubble agitation must be taken into account as well [74]. These additional terms require a large number of empirical inputs which heavily depend on the nature of the multiphase phenomenon under investigation. The two-phase model is typically chosen when the interaction surface between phases is very large, which usually happens for turbulent flows in macro-scale systems (e.g., bubble columns). In micro-channels, as in the context of this study, the flow is mainly laminar and the dispersed phase is for the most part markedly separated from the continuous one [170].

Another family of multiphase flow numerical methods is generally referred to as interface tracking methods [72], which can be further subdivided into surface, moving, and volume tracking methods. These methods aim at resolving accurately the interface between the phases. The surface tracking methods are the simplest and least accurate since the interface is considered as a sharp front whose position is computed by interpolating between markers lying on it [56]. The moving tracking methods are the most expensive in terms of computational cost as the location of the interface is tracked by modifying the mesh at each iteration in order to follow the shape of the front [152]. In volume tracking methods the interface is smooth rather than sharp since it is constructed from the volume fraction field [71], [144]. Unlike the two-phase model, in volume tracking methods a single set of governing equations is solved for all the phases. The thermophysical and transport properties are averaged at each computational cell using the volume fraction of each phase. A separate transport equation for the volume fraction is solved at each iteration in order to advect the front and track its location. The interface tracking methods are commonly utilized for immiscible phases (e.g., water-air mixture), when the motion of the free-surface is a key aspect.

For the simulations of this study, it was decided to treat the helium mixture as a whole and hence solve a single set of equations. Since in this case the formation of helium vapour in a liquid helium channel is a result of a heat-driven phase change, the volume fraction is explicitly calculated from the mixture enthalpy and density instead of solving a transport equation. This allows circumventing the additional implicit PDE for the volume fraction, thus decreasing the computational effort. This approach is possible owing to an energy equation expressed in terms of a conserved quantity (i.e., enthalpy) instead of temperature. In a sense, this approach is similar to the Voller's enthalpy method for melting phase change problems [164], in which a mushy region grows as a consequence of enthalpy changes. In the case of boiling, the mushy region is constricted and thinned by the surface tension forces acting on the interface. Moreover, due to the relevance of solid-helium coupling phenomena such as the Kapitza heat transfer (see Section 2.3), solid components are also included in the solution procedure by solving an energy equation per solid part in a segregated fashion. To sum up, the simulations are conducted with a conjugate heat transfer solver for compressible fluids and transient problems. Details about the equations solved in the numerical algorithm will be given in the next chapters.

CHAPTER 4

He II Investigations

4.1 Experiments

This section reports the data from the experimental sessions conducted with the channel setup described in Sec. 3.1.2. In the following figures, the temperature sensors are labeled as "TSX", where X is a digit that is proper of a specific sensor. TS9 is the sensor situated in the heater plug, behind the Manganin® strip, while for the sensors installed in the steel plate (see Fig. 3.5) X goes from 1 (closest sensor to the heater) to 8 (closest sensor to the channel exit). Similarly, the two pressure sensors are labeled PS1 and PS2. Various tests were carried out with different heat fluxes, bath temperatures, and orientations of the channel. The bath temperature was maintained either at 1.8 K, 1.9 K, or 2.0 K. The channel was tested in three orientations: horizontal; vertical with the heater above the helium zone (i.e., downward heat flux); vertical with the heater below the helium zone (i.e., upward heat flux). The experiments consisted of the so-called clamped flux tests, where a constant heat flux is applied on the closed side of the channel by providing electric current to the resistive strip (i.e., the heater). The energy produced by the heater via Joule effect divided by the contact area with the helium contained in the channel determines the equivalent heat flux applied.

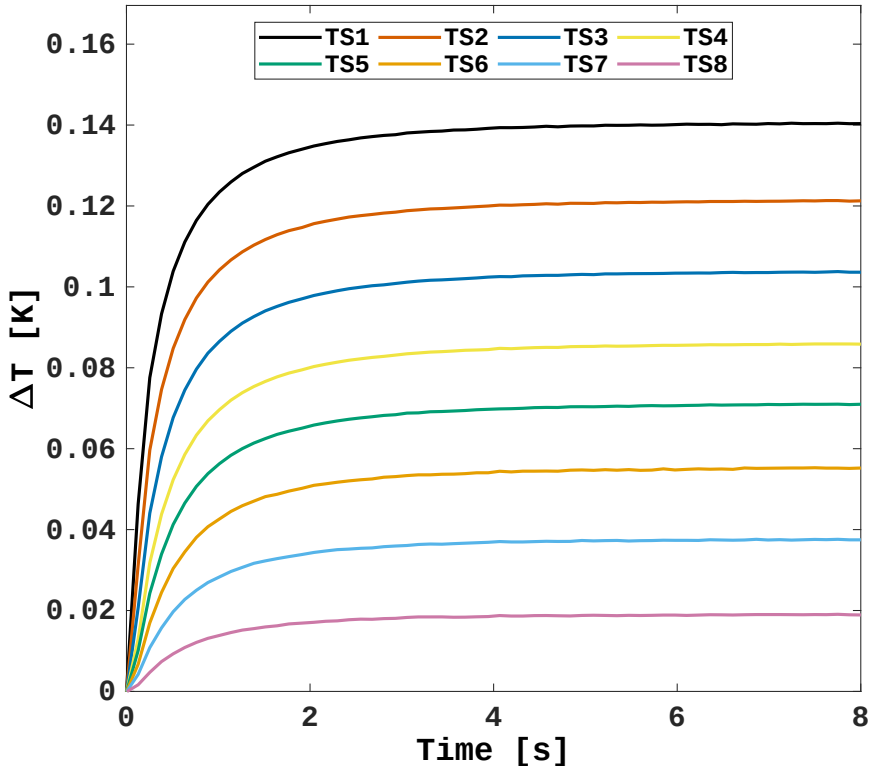

Figure 4.1: Temperature evolution in the horizontal 0.2 mm thick channel at a bath temperature $T_b = 1.8$ K and a heat flux $q = 22.5$ kW/m^2.

4.1.1 Clamped Flux Tests

An example of the typical outcome of the clamped flux tests is displayed in Fig. 4.1, which shows the temperature difference evolution at the sensors' locations with respect to the bath temperature (1.8 K). In particular, Fig. 4.1 refers to a test conducted in the 0.2 mm thick channel in horizontal position with a heat flux of 22.5 kW/m^2. The time 0 corresponds to the application of the heat flux, which can be considered constant since the beginning of the test given the size of the heater. The latter assumption will be verified at the end of Sec. 4.3.4. The helium temperature rises until a steady gradient settles along the channel after about 6 s. As it is clear from the temperature variations at steady state, the measurements suffer from negligible disturbances. The precision uncertainties computed with the methodology presented in Sec. 3.1.3 result to be approximately 0.12% for all the sensors. Such uncertainties will be reported in the form of error bars in figures exhibiting the temperature distribution against the length of the channel. TS9 measured a much lower steady-state temperature than expected (see Fig. A.1 in Annex A.1). Its maximum temperature is more than one order of magnitude smaller than the one recorded by TS1. This is probably due to the measurement location — inside a copper piece at 2.8 mm far from the actual heater (see Fig. 3.11). However, a one-dimensional finite difference analysis of the copper piece showed a temperature increase at the interface with the heater inconsistent with the heat generated (see Fig. B.6 in Annex B.3). Different sources reported higher temperature jumps with much smaller heat fluxes than the present one [158]. Therefore, this evidence indicates the presence of a significant Kapitza resistance between the copper piece and the heating wire in the superfluid helium temperature range.

Fig. 4.2 shows other tests in the same configuration as before at different bath temperatures and two heat fluxes. Each row of plots refers to a certain bath temperature, while each column refers to a certain heat flux. First, let us focus on the left column. Even though the disturbances seem more pronounced compared to Fig. 4.1, the measurement uncertainties were not found to change significantly with either the heat flux or the bath temperature. The reason for this appearance is simply due to the scale of the plot: the lower the maximum temperature, the higher the visual impact of the uncertainty. More interestingly, it is visible how the maximum temperature difference reached by the sensors is lower at 1.9 K compared to the other bath temperatures. This effect is clearly due to the temperature dependence of the heat conductivity function (see Fig. 2.11), whose peak is at around 1.95 K. Beyond the peak, the function decreases sharply. Since the temperature gradient is inversely proportional to this function (see Eq. (2.44)), at $T_b = 1.8$ K and 2 K the temperature rise is larger. This evidence was also observed during experiments in the 0.5 mm thick channel (see Fig. A.2 in Annex A.1). For the same reason, the temperature difference between TS1 and TS2 in Fig. 4.2e is greater than in farther sensors as the helium close to the heater has a lower equivalent thermal conductivity than downstream. Similar arguments can be made at a higher heat flux (right column of graphs). The effect is even more marked in Fig. 4.2f, where the temperature at TS1 is distinctly greater than the other

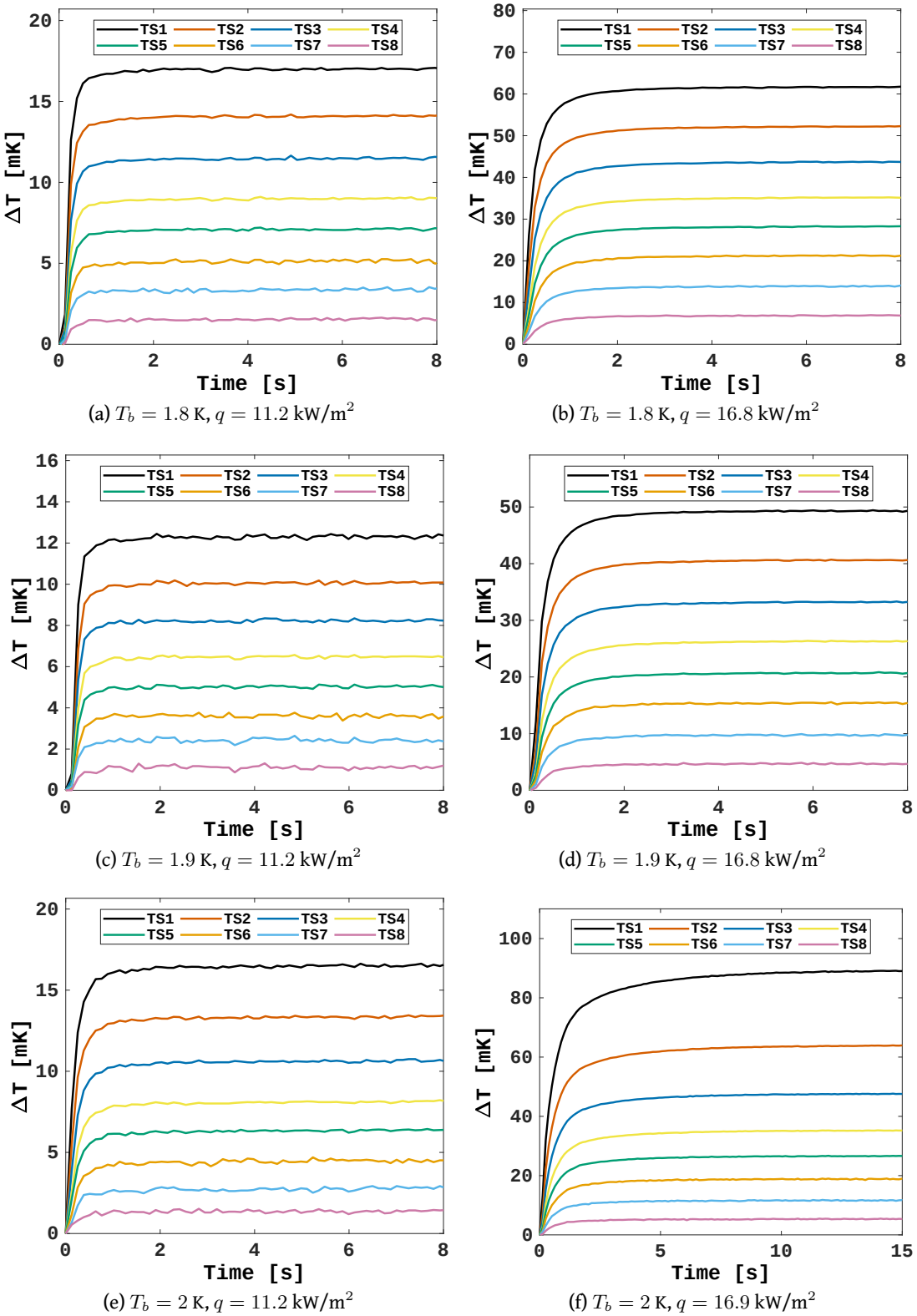

(a) $T_b = 1.8$ K, $q = 11.2$ kW/m^2

(b) $T_b = 1.8$ K, $q = 16.8$ kW/m^2

(c) $T_b = 1.9$ K, $q = 11.2$ kW/m^2

(d) $T_b = 1.9$ K, $q = 16.8$ kW/m^2

(e) $T_b = 2$ K, $q = 11.2$ kW/m^2

(f) $T_b = 2$ K, $q = 16.9$ kW/m^2

Figure 4.2: Temperature evolution in the horizontal 0.2 mm thick channel at different bath temperatures T_b and heat fluxes q.

sensors. This fact, together with the much longer time to achieve the steady state, suggests that there could be another reason for this diverging behaviour. Computing via Eq. (2.58) the minimum heat flux needed to reach the lambda temperature for a $L = 14$ cm long channel reveals that the heat flux in Fig. 4.2f is actually higher than q_{min}. This means that the second-order phase transition occurs nearby the heater but remains undetected by TS1. In order to prove it, the same experiment is conducted with the channel in vertical position (see Fig. A.3 in Annex A.1). Since the thermal expansivity of helium changes sign across T_λ (see Fig. 2.5), if the heat flux direction is opposite to gravity, the generated He I rises and disturbs the signal at the TS1 location. The temperature variations of TS1 in Fig. A.3b support thus the hypothesis. Table 4.1 reports the minimum heat fluxes computed via numerical integration at different bath temperatures with $n = 3.4$ and Sato's empirical heat conductivity function (Eq. (2.46)).

T_b [K]	q_{min} [kW/m^2]
1.7	28.08
1.8	26.35
1.9	22.79
2.0	16.50
2.1	7.12
2.15	1.69

Table 4.1: Minimum heat flux q_{min} to reach the lambda temperature T_λ for a 14 cm long channel at different bath temperatures T_b. The heat flux is computed through Eq. (2.58) with $n = 3.4$ and Sato's empirical heat conductivity function (Eq. (2.46)).

4.1.1.1 Effect of the Channel Thickness and Orientation

The figures presented so far referred to the horizontal 0.2 mm thick channel only. In order to investigate the effect of the channel orientation and thickness on the temperature evolution, tests in the three channel orientations at similar conditions of bath temperature and heat flux are compared with each other. Fig. 4.3 shows such comparison. The left column of graphs corresponds to tests run in the 0.2 mm thick channel at 1.9 K and 22.6 kW/m^2, while the right one to the 0.5 mm thick channel at 1.8 K and 23.6 kW/m^2. In both cases, the orientation does not seem to affect either the temperature gradient established along the channel or its evolution. Moreover, the temperature evolution in the 0.5 mm channel presents a comparable behaviour to the thinner one (see Fig. 4.1).

The transient temperature profiles corresponding to the left column of Fig. 4.3 are shown in Fig. 4.4 to better visualize the differences between the three orientations. The markers indicate the temperature difference with respect to the bath temperature at different moments since the application of the heat flux. Since the data points are not

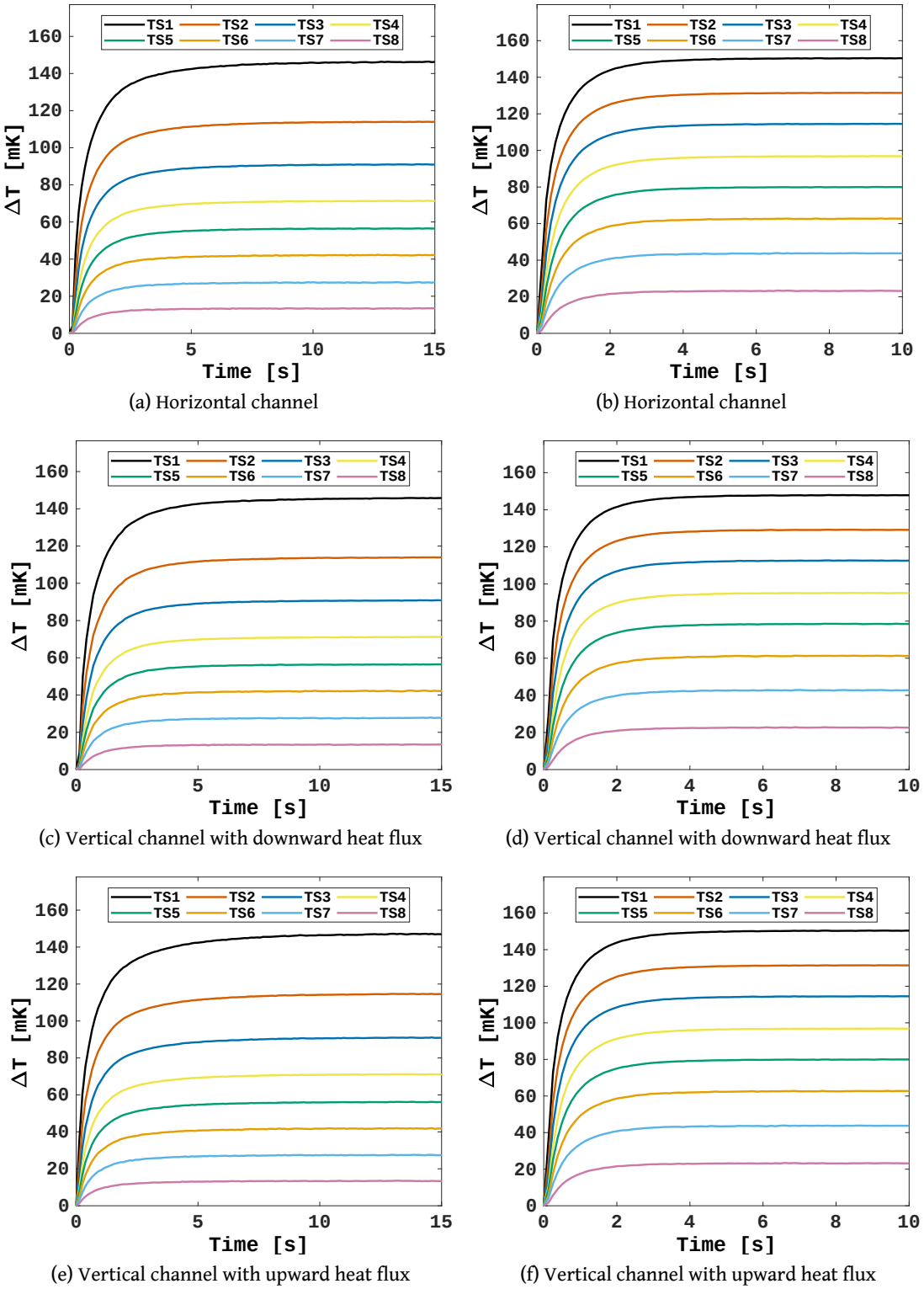

(a) Horizontal channel

(b) Horizontal channel

(c) Vertical channel with downward heat flux

(d) Vertical channel with downward heat flux

(e) Vertical channel with upward heat flux

(f) Vertical channel with upward heat flux

Figure 4.3: Temperature evolution with different channel orientations: in the 0.2 mm thick channel [(a), (c), (e)] at $T_b = 1.9$ K and $q = 22.6$ kW/m^2; in the 0.5 mm thick channel [(b), (d), (f)] at $T_b = 1.8$ K and $q = 23.6$ kW/m^2.

always available at the exact time desired for plotting, the values are linearly interpolated between the measured ones. The lines depicted in Fig. 4.4 are obtained by interpolating

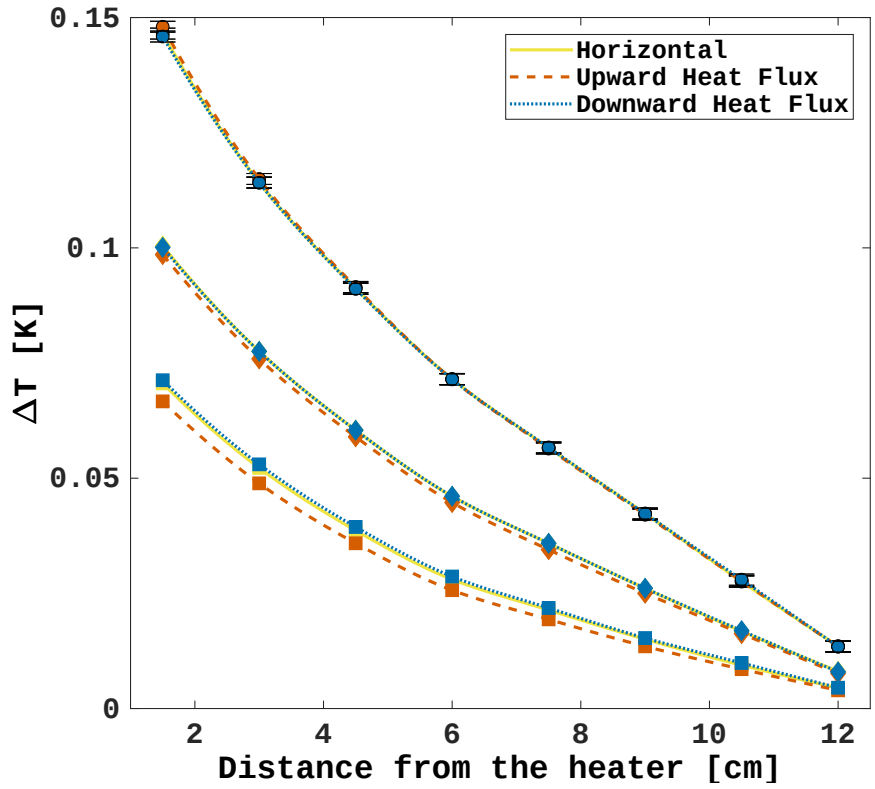

Figure 4.4: Temperature profiles comparison between different orientations of the 0.2 mm thick channel at a bath temperature $T_b = 1.9$ K and a heat flux $q = 22.6$ kW/m^2. The profiles are presented for different moments of the transient: 0.3 s (squares), 0.7 s (diamonds), steady state (circles). The lines are computed through the piecewise cubic Hermite interpolation.

between the marker points with a cubic Hermite spline. The steady-state profiles are almost identical for every orientation. The minor differences in the early transient are most likely due to both the interpolation, measurement unsteadiness, and calibration curves. Such a comparison was produced as well for two cases of the 0.5 mm thick channel (see Fig. A.15 in Annex A.2), which confirm the randomness of the minor differences.

The author wants to stress that the various orientations were tested during different experimental sessions as the channel needed to be relocated and secured to the frame in the new position. This means that the experimental conditions had to be re-established twice following the entire preparation process of the cryostat described in Sec. 3.1. Bearing this in mind, the consistency of the results proves the repeatability of the measurements.

4.1.1.2 Pressure Measurements

The heat flux range of this chapter's results was determined such that He II does not undergo phase transitions. Since no helium gas is generated, the density changes of the fluid are negligible and hence the pressure perturbations are not expected to be

significant. Unfortunately, the power released by the pressure sensors due to their impedance appeared to affect systematically and unquestionably the temperature inside the channel (see Fig. A.4 in Annex A.1). Because of this additional power, if the heat flux and the bath temperature are close enough to q_{min} and T_λ respectively, the helium nearby the pressure sensors changes phase and alters the pressure. The impact is even stronger when the pressure plate is closer to the temperature one (i.e., 0.2 mm thick channel). For this reason, the temperature measurements previously reported were recorded with the pressure sensors turned off. Moreover, in order to avoid this undesired effect, the pressure was measured in tests with low bath temperature and moderate heat fluxes.

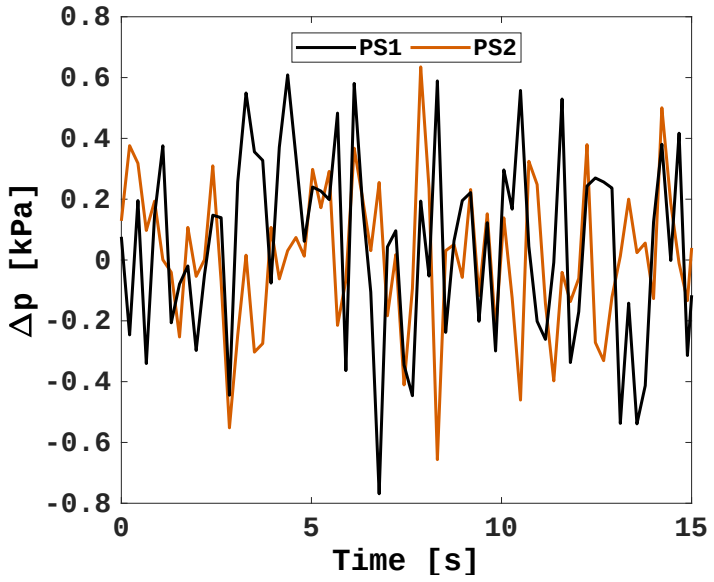

(a) $q = 7.2$ kW/m^2

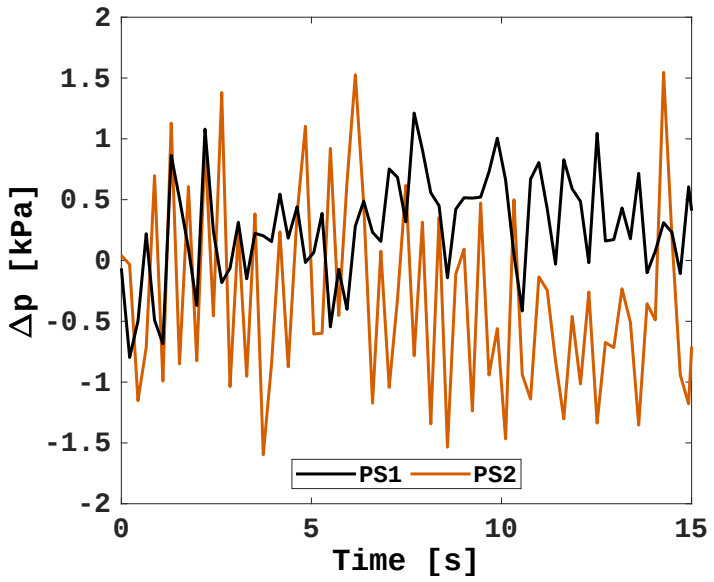

(b) $q = 21.9$ kW/m^2

Figure 4.5: Pressure evolution in the 0.5 mm thick channel at $T_b = 1.8$ K and different heat fluxes.

Fig. 4.5 shows the pressure difference evolution with respect to the bath pressure in the horizontal 0.5 mm thick channel at 1.8 K and two different heat fluxes. In both cases, the pressure variations are so small that the sensors' sensitivity hardly catches any relevant change since the beginning of the test. At low heat currents (Fig. 4.5a), the signal fluctuates around the initial value without any visible trend. The sensor far from the heater (i.e., PS2) seems to maintain the same behaviour regardless of the extent of power injected into the channel. At the location of PS1, instead, at a high heat flux (Fig. 4.5b) the pressure slightly increases after an initial drop. This trend will be more apparent and further discussed in Sec. 4.3.4.

4.2 Numerical Model

As seen in Ch. 2, the HVBK equations represent an appropriate tool to describe the heat and mass transfer in He II. Because of the difficulty to solve the equations analytically, various authors used numerical methods to obtain steady-state and transient solutions for different problems [113], [129], [146], [148]. However, the numerical solution of a set of governing equations involving two momentum equations may result in high computational time depending on the size of the mesh. If a pressure-correction method is used, the complexity of the model increases even further because of the necessity to modify the segregated algorithm [140]. Since one of the aims of this work is programming a code capable of simulating He II in multi-dimensional domains, it was decided to simplify the two-fluid model to obtain a single-fluid momentum equation that considers He II as a whole fluid. Over the years, some authors faced the problem with a similar approach. Kashani et al. modified the energy equation to take the counterflow into account in one-dimensional forced flow problems [81]. Ramadan and Witt derived a total fluid equation for natural convection problems by neglecting the thermo-mechanical and mutual friction terms, the effect of which was included in the energy equation [128]. Bottura derived a set of one-dimensional compressible equations for liquid helium in terms of primitive variables instead of conserved quantities [19] and he later generalized it to He II by including the counterflow mechanism [21]. Kitamura et al. found a way to neglect the superfluid momentum equation by including additional terms in the total fluid equation [89]. In this dissertation, the latter approach is adopted along with the proper modifications required by the present study. Before doing so, it is necessary to understand the weight of the various terms in the momentum equation of the superfluid component under different thermodynamic conditions. This can be done through the non-dimensionalization of the equation.

4.2.1 Non-Dimensionalization of the Superfluid Momentum Equation

The procedure requires all the dimensional variables to be transformed into non-dimensional ones by means of characteristic quantities. The parameters chosen in this study are selected to take advantage of a couple of equations valid for superfluid helium, as it

will be clear later in this section. Let us consider the steady-state form of Eq. (2.38) under the influence of a gravitational field and substitute the variables with the following dimensionless parameters:

$$\mathbf{v}_s^* = \frac{\mathbf{v}_s}{v_{s,0}}, \tag{4.1a}$$

$$\boldsymbol{\nabla}^* = D\boldsymbol{\nabla}, \tag{4.1b}$$

$$p^* = \frac{p}{\Delta p_0}, \tag{4.1c}$$

$$T^* = \frac{T}{\Delta T_0}, \tag{4.1d}$$

$$\mathbf{v}_{ns}^* = \frac{\mathbf{v}_{ns}}{v_{ns,0}}, \tag{4.1e}$$

$$\mathbf{g}^* = \frac{\mathbf{g}}{g_0}, \tag{4.1f}$$

where $v_{s,0}$, D, Δp_0, ΔT_0, g_0 and $v_{ns,0}$ are characteristic parameters. In particular, D is the characteristic dimension of the channel filled with helium, Δp_0 is the pressure drop along the channel, ΔT_0 is the temperature difference with respect to the bath, g_0 is the acceleration of gravity. The dimensionless form of the equation becomes then

$$\begin{aligned}\frac{v_{s,0}^2}{D}\left(\mathbf{v}_s^* \cdot \boldsymbol{\nabla}^*\right)\mathbf{v}_s^* = \frac{s\Delta T_0}{D}\boldsymbol{\nabla}^* T^* - \frac{\Delta p_0}{\rho D}\boldsymbol{\nabla}^* p^* + \frac{\rho_n}{2\rho}\frac{v_{ns,0}^2}{D}\boldsymbol{\nabla}^*\mathbf{v}_{ns}^{*2} \\ + A_{GM}\rho_n v_{ns,0}^3 \mathbf{v}_{ns}^{*3} + g_0\mathbf{g}^*\end{aligned} \tag{4.2}$$

Let us now multiply every term by the characteristic dimension D and divide by the square of the superfluid velocity $v_{s,0}$:

$$\begin{aligned}\left(\mathbf{v}_s^* \cdot \boldsymbol{\nabla}^*\right)\mathbf{v}_s^* = \frac{s\Delta T_0}{v_{s,0}^2}\boldsymbol{\nabla}^* T^* - \frac{\Delta p_0}{\rho v_{s,0}^2}\boldsymbol{\nabla}^* p^* + \frac{\rho_n}{2\rho}\frac{v_{ns,0}^2}{v_{s,0}^2}\boldsymbol{\nabla}^*\mathbf{v}_{ns}^{*2} \\ + A_{GM}\rho_n D\frac{v_{ns,0}^3}{v_{s,0}^2}\mathbf{v}_{ns}^{*3} + \frac{g_0 D}{v_{s,0}^2}\mathbf{g}^*\end{aligned} \tag{4.3}$$

If we consider the total velocity of the fluid v_0 and the heat flux having the same direction, we can relate $v_{s,0}$ to $v_{ns,0}$ and v_0 through Eq. (2.6) and the definition of $v_{ns,0}$:

$$v_{s,0} = v_0 - \frac{\rho_n}{\rho}v_{ns,0}. \tag{4.4}$$

Also, $v_{ns,0}$ can be expressed in function of a characteristic heat flux q_0 through Eq. (2.19):

$$v_{s,0} = v_0 - \frac{\rho_n q_0}{\rho\rho_s s T_b}, \tag{4.5}$$

where T_b is the bath temperature. This trick allows us to determine the dimensionless numbers in terms of parameters that are more familiar (i.e., the total velocity of the fluid and the heat flux applied). Substituting Eq. (4.5) into Eq. (4.3) yields the final form of the non-dimensionalized equation:

$$\left(\mathbf{v}_s^* \cdot \boldsymbol{\nabla}^*\right)\mathbf{v}_s^* = \mathcal{A}\boldsymbol{\nabla}^* T^* - \mathcal{E}\boldsymbol{\nabla}^* p^* + \mathcal{B}\boldsymbol{\nabla}^*\mathbf{v}_{ns}^{*2} + \mathcal{C}\mathbf{v}_{ns}^{*3} + \mathcal{F}^{-2}\mathbf{g}^*, \tag{4.6}$$

where $\mathcal{A}$, $\mathcal{E}$, $\mathcal{B}$, $\mathcal{C}$, and $\mathcal{F}$ are the dimensionless numbers of the equation. In particular, $\mathcal{E}$ and $\mathcal{F}$ are the equivalent superfluid versions of the Euler and Froude numbers in the classical Navier-Stokes equations, whereas $\mathcal{A}$, $\mathcal{B}$, and $\mathcal{C}$ are associated with terms that are proper of He II. The dimensionless numbers read as follows:

$$\mathcal{A} = \frac{\Delta T_0 \rho^2 \rho_s^2 s^3 T_b^2}{\left(\rho\rho_s s T_b v_0 - \rho_n q_0\right)^2}, \tag{4.7a}$$

$$\mathcal{E} = \frac{\Delta p_0 \rho \rho_s^2 s^2 T_b^2}{\left(\rho\rho_s s T_b v_0 - \rho_n q_0\right)^2}, \tag{4.7b}$$

$$\mathcal{B} = \frac{\rho\rho_n q_0^2}{2\left(\rho\rho_s s T_b v_0 - \rho_n q_0\right)^2}, \tag{4.7c}$$

$$\mathcal{C} = \frac{A_{GM}\rho_n \rho^2 q_0^3 D}{\rho_s s T_b \left(\rho\rho_s s T_b v_0 - \rho_n q_0\right)^2}, \tag{4.7d}$$

$$\mathcal{F} = \frac{\rho\rho_s s T_b v_0 - \rho_n q_0}{\rho\rho_s s T_b \sqrt{g_0 D}}. \tag{4.7e}$$

It is interesting to notice that, in absence of heat currents, $\mathcal{E}$ and $\mathcal{F}$ become their respective numbers for ordinary fluids ($Eu = \Delta p_0/\rho {v_0}^2$, $Fr = v_0/\sqrt{g_0 D}$). This result is obtained for very low temperatures (i.e., $\rho_n \to 0$) too, which suggests that, for He II tending to be constituted mainly by the superfluid component, He II experiences the pressure drop and gravitational force similarly to ordinary fluids. The condition $\rho_n q_0 = 0$ nullifies the dimensionless numbers that originate directly from the relative motion of the He II components (i.e., $\mathcal{B}$ and $\mathcal{C}$). On the contrary, the $\mathcal{A}$ number becomes $\mathcal{A}\big|_{\rho_n q_0 = 0} = s\Delta T_0/{v_0}^2$, which looks much like the Euler number. This similarity provides an additional insight into Eq. (2.20) and indicates that the $\mathcal{A}$ number represents the relationship between the thermo-mechanical force and the superfluid stream inertial force.

At zero net mass flow, the superfluid component may still move because of the counterflow mechanism, which is confirmed by setting $v_0 = 0$ in the dimensionless numbers. In particular, it might be interesting to highlight the relation found between $\mathcal{C}$ and the dimensionless number of Dimotakis [42], who non-dimensionalized a general momentum equation at zero net mass flow accounting for both components of He II. He obtained a number associated with the mutual friction term equal to $Di = \rho_s A_{GM} v_{ns,0} D$, which can be written as well as

$$Di = \alpha_s \left(1 - \alpha_s\right) \mathcal{C}\big|_{v_0 = 0}, \tag{4.8}$$

where α_s is the superfluid density fraction and $\mathcal{C}$ is calculated at zero net mass flow. Computing the roots of α_s for $\mathcal{C}\big|_{v_0=0} = Di$ reveals that there exists no real value of α_s that allows this condition. This is due to the nature of the two numbers: Di is related to He II, while $\mathcal{C}$ is specifically associated with the superfluid component. Moreover, when He II is equally constituted by the two components (i.e., $\alpha_s = 0.5$), Di is one fourth of $\mathcal{C}$.

It is now possible to compare the dimensionless numbers among each other by varying the characteristic parameters. Since some thermophysical properties appear in Eqs. (4.7), the dimensionless numbers must depend on the pressure as well. However, since no major

difference has been observed in their behaviour in the range of pressures of helium cooling applications, the pressure is simply set to the saturated vapour one and the properties are evaluated at T_b. Moreover, it has to be mentioned that, above a certain critical heat flux, He II undergoes a phase transition and the equation becomes meaningless. Nevertheless, since this critical heat flux depends significantly on the fluid velocity and on the length of the channel - the latter of which does not appear in the dimensionless numbers (D is rather the hydraulic diameter of the channel) - then this upper limit is disregarded in the following study that is meant to be an analysis of the general behaviour of the terms in Eq. (2.38).

As explained in Section 2.2.2, in the range of heat currents that this investigation is mainly focused on, He II is certainly in the Gorter-Mellink regime and hence the mutual friction force is expected to be one of the dominant terms. For this reason, the following considerations are made with respect to Eq. (4.7d). Each of the following figures shows

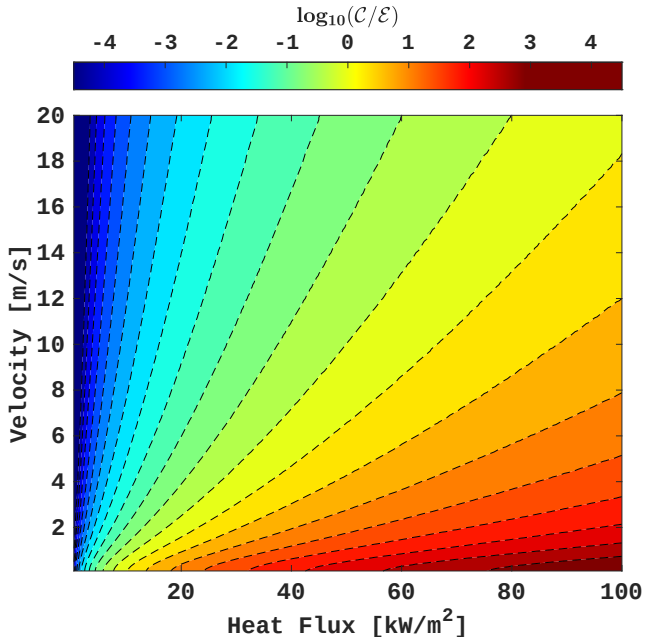

Figure 4.6: Relative magnitude between $\mathcal{C}$ and $\mathcal{E}$ as a function of the total velocity v_0 and heat flux q_0 at 1.9 K and $D = 1$ cm.

the relative importance of a dimensionless number with respect to $\mathcal{C}$ as a function of two characteristic parameters. The range of colors conveys information about how many orders of magnitude a dimensionless number is higher (or lower) than the other. This is obtained by calculating the common logarithm of the ratio between the two dimensionless numbers under investigation. If a ratio contains more than two characteristic parameters, the other ones are kept constant at values specified in the caption of the figure. As a first example, Fig. 4.6 shows the relevance of the pressure drop term in the momentum equation as a function of the characteristic heat flux q_0 and velocity v_0. The characteristic pressure drop Δp_0 is expressed as a function of v_0 through an empirical equation derived from data collected by Fuzier [55]. Fuzier et al. conducted He II forced flow experiments in a 1 m

long tube with an internal diameter of 1 cm [53], [54]. They proved the importance of the pressure drop term in the He II heat transport for non-negligible flow velocities and a 100 kW/m^2 heat flux. Fig. 4.6 confirms this outcome with regards to the superfluid mass transport as well. Since the experiments of this study are conducted in confined channels

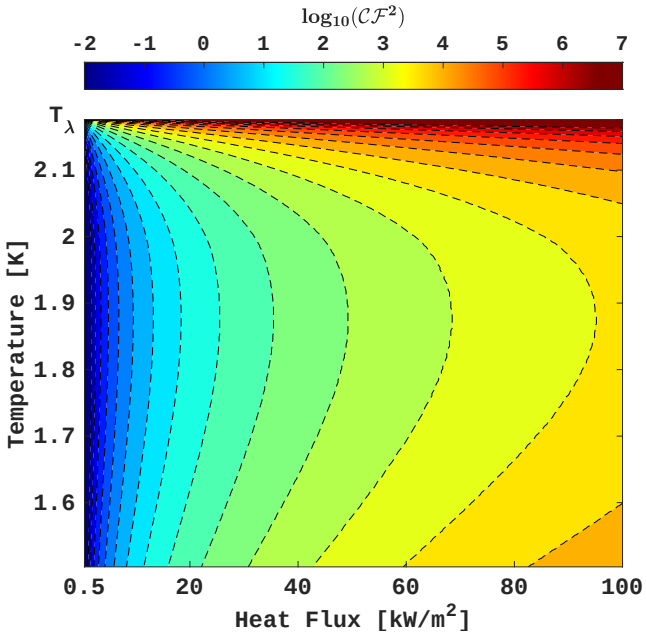

Figure 4.7: Relative magnitude between $\mathcal{C}$ and $\mathcal{F}$ as a function of the temperature T_b and heat flux q_0.

in a stagnant bath, the fluid velocity is quite low and the pressure drop is negligible. For this reason, the pressure drop term is neglected in Eq. (2.38).

It is easy to evaluate the entity of the number associated with the thermo-mechanical effect by using the definition of the heat conductivity function (Eq. (2.45)). Combining the $\mathcal{A}$ and $\mathcal{C}$ numbers yields then

$$\mathcal{A} = \frac{\Delta T_0}{f(T,p) q_0^3 D} \mathcal{C}. \tag{4.9}$$

If we consider again Eq. (2.43), it is clear from Eq (4.9) that the $\mathcal{A}$ and $\mathcal{C}$ numbers tend to equal each other for high heat fluxes, that is, when the viscous contribution can be neglected in Eq. (2.43). This evidence reveals that, for sufficiently high heat fluxes, the thermo-mechanical effect counts as much as the mutual friction force in the dynamics of the superfluid component. This result will be particularly helpful in the construction of the numerical model.

Since both the $\mathcal{C}$ and $\mathcal{F}$ numbers depend on the characteristic length D, their ratio is not affected by this parameter. Fig. 4.7 shows their relation as a function of the temperature and heat flux. It is clear that, apart from very low heat fluxes, the acceleration of gravity plays a little role in the superfluid dynamics. It also appears that the $\mathcal{F}$ number is most significant at around 1.876 K. The presence of peak values is due to the heat

conductivity function (see Fig. 2.11). However, the temperature at which the maximum occurs is modified by the other parameters appearing in the numbers ratio. It is important to notice how the mutual friction force is by far the most dominant term in the vicinity of the lambda temperature, which is clearly due to the combination of both the steep rise of the Gorter-Mellink coefficient A_{GM} and the diminishing ρ_s as the temperature approaches T_λ.

The energy diffusion term associated with the $\mathcal{B}$ number is often neglected in the two-fluid model [58], [167], [158], [140], as its contribution is considered to be a small part in the total effect deriving from the relative motion of the He II fluid components. This is

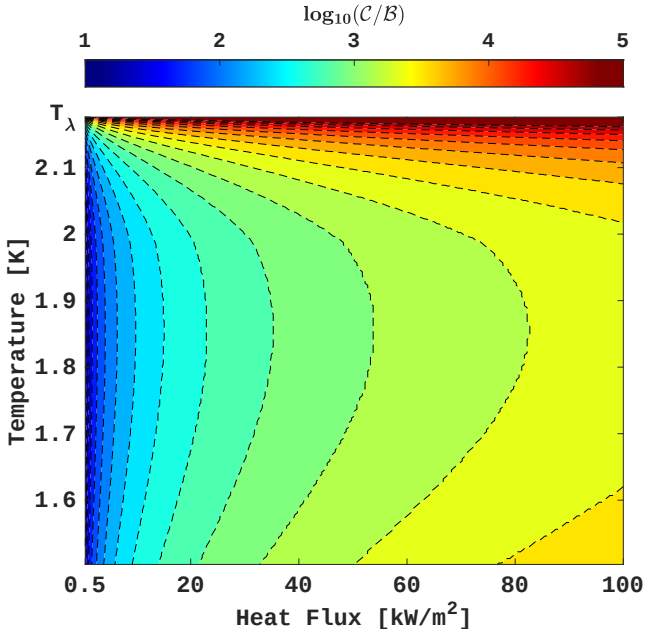

Figure 4.8: Relative magnitude between $\mathcal{C}$ and $\mathcal{B}$ as a function of the temperature T_b and heat flux q_0 for $D = 1$ cm.

confirmed by Fig. 4.8, which shows that the contribution of the mutual friction grows with the heat flux value and distinctly dominates. Obviously, since $\mathcal{B}$ does not depend on the characteristic length, the mutual friction becomes less influential for small geometries. However, unlike in the mutual friction term, the relative velocity v_{ns} is involved in the energy diffusion term only through a differential operator and, as such, the mutual friction is expected to prevail in the majority of the heat transport applications. The $\mathcal{B}$ number appears to be most significant at around 1.855 K, which is independent of D. Moreover, it is again noticeable the steep rise of the $\mathcal{C}$ value towards T_λ. This observation is important with regards to the present study as it legitimizes and extends the necessary assumption made to construct the single-fluid model to a context that involves the lambda phase transition. This assumption together with the single-fluid model will be presented in the next section.

4.2.2 Single-Fluid Governing Equations

The dimensional analysis of the previous section provides an important conclusion about the extent of the terms appearing in the superfluid momentum equation: for sufficiently high heat fluxes, the superfluid dynamics is largely determined by the mutual friction force and the thermo-mechanical effect, which prevail over the other terms by several orders of magnitude. This conclusion allows us to neglect from Eq. (2.38) all terms except the ones associated with the dimensionless numbers $\mathcal{C}$ and $\mathcal{A}$. Similarly to what was done by Kitamura et al. [89], Eq. (2.38) then becomes

$$A_{GM}\rho_n \mathbf{v}_{ns}^n = -s\boldsymbol{\nabla} T, \tag{4.10}$$

which can be rearranged into

$$\mathbf{v}_{ns} = -\left(\frac{s}{A_{GM}\rho_n \|\boldsymbol{\nabla} T\|^{n-1}}\right)^{\frac{1}{n}} \boldsymbol{\nabla} T, \tag{4.11}$$

where the temperature gradient has been linearized. Substituting Eq. (4.11) into Eq. (4.4) yields

$$\mathbf{v}_s = \mathbf{v} + \left(\frac{s\rho_n^{n-1}}{A_{GM}\rho^n \|\boldsymbol{\nabla} T\|^{n-1}}\right)^{\frac{1}{n}} \boldsymbol{\nabla} T. \tag{4.12}$$

Similarly, for $\mathbf{v}_n$:

$$\mathbf{v}_n = \mathbf{v} - \left(\frac{s\rho_s^{n}}{A_{GM}\rho^n \rho_n \|\boldsymbol{\nabla} T\|^{n-1}}\right)^{\frac{1}{n}} \boldsymbol{\nabla} T. \tag{4.13}$$

Let us write the total fluid momentum equation (Eq. (2.15)) in its compressible form:

$$\begin{aligned}\frac{\partial}{\partial t}\left(\rho_n \mathbf{v}_n + \rho_s \mathbf{v}_s\right) = & -\boldsymbol{\nabla}\cdot\left(\rho_n \mathbf{v}_n \otimes \mathbf{v}_n + \rho_s \mathbf{v}_s \otimes \mathbf{v}_s\right) \\ & + \mu\left[\nabla^2 \mathbf{v}_n + \frac{1}{3}\boldsymbol{\nabla}\left(\boldsymbol{\nabla}\cdot\mathbf{v}_n\right)\right] - \boldsymbol{\nabla} p + \rho\mathbf{g}.\end{aligned} \tag{4.14}$$

By substituting Eqs. (4.12) and (4.13) into Eq. (4.14) and rearranging we obtain

$$\begin{aligned}\frac{\partial}{\partial t}\left(\rho\mathbf{v}\right) = & -\boldsymbol{\nabla}\cdot\left(\rho\mathbf{v}\otimes\mathbf{v}\right) + \mu\left[\nabla^2\mathbf{v} + \frac{1}{3}\boldsymbol{\nabla}\left(\boldsymbol{\nabla}\cdot\mathbf{v}\right)\right] - \boldsymbol{\nabla} p + \rho\mathbf{g} \\ & - \frac{\mu\rho_s}{\rho} M\left[\nabla^2\left(\boldsymbol{\nabla} T\right) + \frac{1}{3}\boldsymbol{\nabla}\left(\nabla^2 T\right)\right] \\ & - \boldsymbol{\nabla}\cdot\left[\frac{\rho_n\rho_s}{\rho} M^2 \boldsymbol{\nabla} T \otimes \boldsymbol{\nabla} T\right],\end{aligned} \tag{4.15}$$

where

$$M \equiv \left(\frac{s}{A_{GM}\rho_n \|\boldsymbol{\nabla} T\|^{n-1}}\right)^{\frac{1}{n}}, \tag{4.16}$$

which may be considered a momentum diffusivity per unit of temperature increase. As such, it is a measure of the rate of mass transfer due to a temperature gradient. Under the

assumption of (4.10), Eq. (4.15) has the great advantage of modelling He II fluid dynamics without taking into account singularly the velocity field of each fluid component. This is achieved because of the last two terms on the RHS of Eq. (4.15), which are additional contributions to the ordinary Navier-Stokes equations. The last term was referred to as a convectional acceleration resulting from the net motion of the He II components, while the second to last (two terms in square brackets) as a viscous stress contribution due to the thermo-mechanical effect [89]. Since these two additional terms are not velocity dependent, they are computed explicitly by taking the temperature field of the previous time step.

A complete set of governing equations requires also the equations of continuity and energy. The continuity Eq. (2.7) of the two-fluid model can be simply written as

$$\frac{\partial \rho}{\partial t} + \boldsymbol{\nabla} \cdot (\rho \mathbf{v}) = 0. \tag{4.17}$$

The energy equation can be expressed in terms of the enthalpy as [70]

$$\frac{\partial}{\partial t}(\rho h) + \boldsymbol{\nabla} \cdot (\rho \mathbf{v} h) + \frac{\partial}{\partial t}(\rho K) + \boldsymbol{\nabla} \cdot (\rho \mathbf{v} K) = \frac{\partial p}{\partial t} - \boldsymbol{\nabla} \cdot \mathbf{q} + \rho \mathbf{v} \cdot \mathbf{g}, \tag{4.18}$$

where h is the specific enthalpy and K is the kinetic energy. Combining Eq. (2.19) with Eq. (4.11) and substituting the temperature gradient with the enthalpy gradient provides an expression for the heat flux $\mathbf{q}$ in Eq. (4.18):

$$\mathbf{q} = \frac{k_{eff}}{c_p} \boldsymbol{\nabla} h, \tag{4.19}$$

where the pressure dependence of the thermophysical properties has been neglected. The property k_{eff} can be considered as the effective thermal conductivity of He II and reads

$$k_{eff} \equiv \left(\frac{1}{f(T,p) \| \boldsymbol{\nabla} T \|^{n-1}} \right)^{\frac{1}{n}}, \tag{4.20}$$

where the heat conductivity function is equal to either Eq. (2.45) or Eq. (2.46), depending on the value chosen for the exponent n.

Eqs. (4.17), (4.15), and (4.18) constitute the set of single-fluid governing equations of the present He II numerical model, which, for simplicity, will be addressed as *heliumChtFoam* from now on. This set of equations differs from Kitamura's one essentially in the value of n and in the variable of the energy equation. In the derivation of their model, Kitamura et al. set $n = 3$ in the main assumption (Eq. (4.10)), as this is the value that emerges from the theoretical formulation of the two-fluid model. However, as explained in Section 2.2.2, the value of n varies according to the temperature. It is worth observing that the condition $n \neq 3$ has been applied in the past to the He II heat transport but never to the fluid transport [2], [97], [17]. Nevertheless, the exponent n originates from the mutual friction term in the superfluid momentum equation and, as such, it must influence the fluid transport too. Therefore, in this work, the derivation of the single-fluid equations has been generalized for an arbitrary exponent n, whose usage has been extended to the

momentum equation as well as the energy equation. Moreover, the energy equation has been formulated in terms of a conserved quantity in place of the temperature.

Unless otherwise specified, the simulations of this study were carried out with $n = 3.4$ and Sato's empirical heat conductivity function (Eq. (2.46)). Nevertheless, *heliumChtFoam* has been programmed by the author in such a way the user is able to choose in pre-processing $n = 3$ and the theoretical heat conductivity function (Eq. (2.45)).

4.2.3 He II Boundary Conditions

The peculiar physics of He II has impacts also on the conditions that must be set at the boundaries of a computational domain. In particular, two especially useful conditions pertain to the conjugate heat transfer at the interface with a solid part and the velocity of the fluid at the walls. These boundary conditions will be presented in the next subsections.

4.2.3.1 Kapitza Heat Transfer

As introduced in Section 2.3, establishing a heat current across He II and a solid generates a thermal boundary resistance at their interface. The heat exchange between the two media is strongly affected by the resulting Kapitza conductance h_K. Numerically, the thermal resistance can be imposed by considering a virtual layer between the He II and solid regions with a thermal resistance $1/h_K$. Equating the heat fluxes through the virtual layer and He II regions leads to the following temperature boundary condition for a generic computational cell with centroid P in the helium domain:

$$T_f = \frac{h_K C_{Pf}}{h_K C_{Pf} + k_{eff}} T_{f,nb} + \frac{k_{eff}}{h_K C_{Pf} + k_{eff}} T_P, \tag{4.21}$$

where $T_{f,nb}$ is the temperature at the interface between the solid and virtual layer regions, while the other parameters may be interpreted using Fig. 3.15 as a reference. The Kapitza conductance h_K is derived from Eq. (2.54) similarly to [57]:

$$h_K = \max\left(a_{II} T_b^{m_{II}}, a_I \frac{T_{f,nb}^{m_I} - T_b^{m_I}}{T_{f,nb} - T_b} \right). \tag{4.22}$$

4.2.3.2 Superfluid Slip

The common velocity boundary condition for an ordinary viscous fluid in contact with a wall is the no-slip condition, which simply sets the velocity of the fluid equal to zero. However, there exist fluids that were observed manifesting wall slip phenomena such as polymers and die materials [50]. Superfluid helium exhibits a wall slip behaviour to a certain extent. Indeed, as seen in Section 2.1, the superfluid component of He II is inviscid and hence able to move tangentially to the walls. On the other hand, the normal component behaves like an ordinary fluid and remains static at the walls. This situation may be represented by a partial-slip condition of the total fluid. The total fluid velocity at

the walls is determined by imposing Eq. (4.13) equal to zero:

$$\mathbf{v}_{\parallel} = \frac{\rho_s}{\rho} M \boldsymbol{\nabla} T_{\parallel}. \tag{4.23}$$

The velocity component $\mathbf{v}_{\perp}$ normal to the wall is obviously set to zero. The tangential component $\mathbf{v}_{\parallel}$ is obtained by removing the normal component from the temperature gradient:

$$\boldsymbol{\nabla} T_{\parallel} = \boldsymbol{\nabla} T - (\boldsymbol{\nabla} T \cdot \mathbf{n})\mathbf{n}, \tag{4.24}$$

where $\mathbf{n}$ is the normal vector with respect to the wall. Eq. (4.23) is in agreement with the theory of He II, stating that the superfluid component is oppositely directed with respect to the heat flux.

4.3 Model Benchmarking

A numerical model requires a validation process in order to ensure the reliability of its solutions. The validation process usually consists of the comparison of the model solution to the analytical one. If the latter is not available, the comparison may also be performed with respect to either experimental data or previously established numerical models. The severe non-linearity of the He II equations excludes the possibility to obtain analytical solutions for problems in which the impact of the temperature dependence of the properties is significant. For this reason, it was decided to validate *heliumChtFoam* against other models and data from both literature and experiments conducted for this study [162]. This section reports such comparisons.

All the simulations of this section were obtained with the PISO algorithm (i.e., single outer loop iteration) and three inner-loop iterations. The transient problem was solved using the CNS with a blending factor of 0.9. As the following study cases are not advection dominated, both the divergence and gradient terms were discretized with the CDS. The interpolated values between cell centroids were computed linearly. The simulations were run in parallel utilizing 36 CPUs.

4.3.1 Srinivasan and Hoffman's Tube Experiment

A typical benchmark experiment for He II is the one from Srinivasan and Hoffman [141]. They conducted steady-state experiments in a 1 m long tube with an inner diameter of 3 mm. The He II is heated up at the center of the tube. The temperature is recorded at eight locations, which are 10 cm far from each other (starting at 10 cm from both sides of the tube). The tests that are within the interest of this study were carried out in stagnant conditions with a power deposition of 0.145 W and 0.205 W.

In order to compare *heliumChtFoam* to other models at even conditions, a one-dimensional uniform mesh constituted by 200 cells was chosen as the computational domain for this validation, in accordance with the simulations of Bottura and Rosso [21]. The time step

was set to be adaptive such that the Courant number was always less than the unit. Since the experiment was originally conceived for forced flow tests, the apparatus was unable to maintain a stable temperature at the inlet and outlet of the tube at stagnant conditions. Therefore, it was decided to simulate only the region between the first and last sensors. Consequently, the temperature at the domain boundaries was set to the one measured by those sensors at steady state. The initial temperature was assumed to be uniform in the whole domain and equal to the lowest boundary temperature. The pressure was fixed to the experimental one (i.e., atmospheric pressure). Since the domain boundaries do not correspond to physical confines for the fluid, a possible backflow must be taken into account and hence two different conditions are imposed on the velocity depending on the flux direction: zero gradient if the flux points outward; pressure dependent if the flux points inward. Since this boundary condition is quite common in the present study, it is convenient to refer to it as the inlet-outlet velocity condition from now on. The fluid was assumed to be initially static. The heat load was applied as a volumetric heat generation in the two central cells of the domain. The steady state was reached after 80 s and 150 s of simulated time for 0.205 W and 0.145 W respectively.

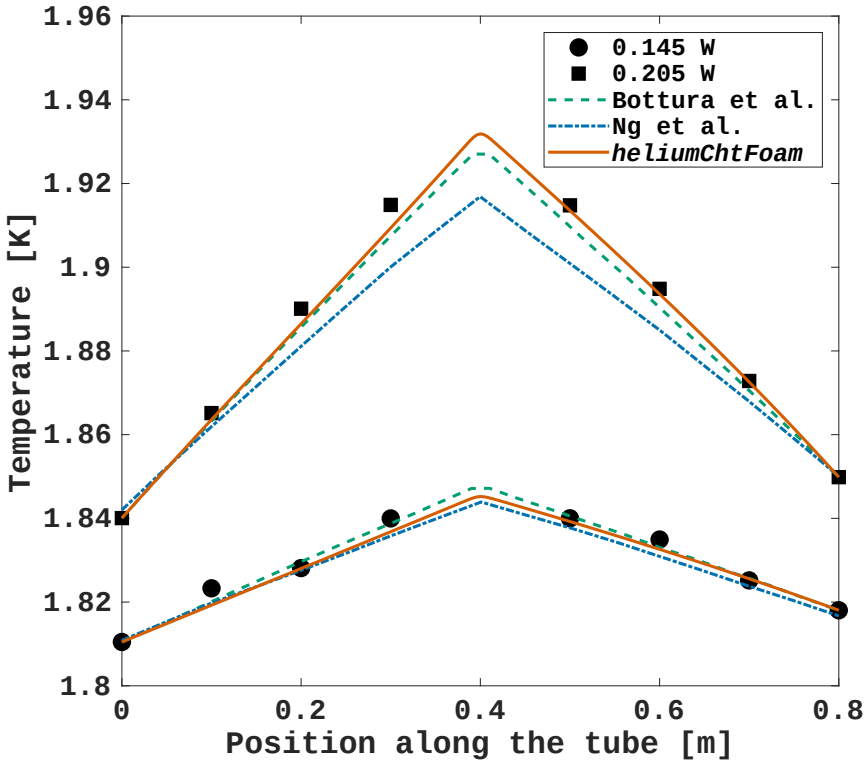

Figure 4.9: He II temperature profiles comparison between *heliumChtFoam* (solid line) and data from Srinivasan and Hoffman's tube experiment (markers) [141]. The simulations by Bottura and Rosso [21], and Ng et al. [113] are also shown as dashed and dash-dotted line respectively.

Fig. 4.9 shows the comparison between the computed temperature distribution along the tube by the present code and the data of the aforementioned experiments by Srinivasan

and Hoffman [141]. The temperature profiles obtained by Bottura and Rosso [21], and Ng et al. [113] are also displayed in the figure. The set of governing equations of Bottura and Rosso's model is in terms of pressure, velocity, and temperature. They utilized a friction factor to model the viscous force, and the theoretical derivation of the heat conductivity function. Ng et al. used the classic two-fluid model with a double momentum equation. As it is clear from the figure, *heliumChtFoam* is in very good agreement with the experiments.

4.3.2 Rectangular Duct Experiment of Shiotsu et al.

Shiotsu et al. conducted transient experiments in a rectangular vertical duct submerged in a pressurized He II bath to study the critical heat flux needed to trigger the second-order phase transition [137]. In particular, they studied the dependence of the time required to reach T_λ (i.e., lambda time t_λ) on the heat flux applied. The duct is 10 cm high, 1 cm wide, and 4 cm deep. The subcooled helium is heated up at the bottom side of the duct, while the upper side is open to the bath. The temperature is measured at the center of the heated surface.

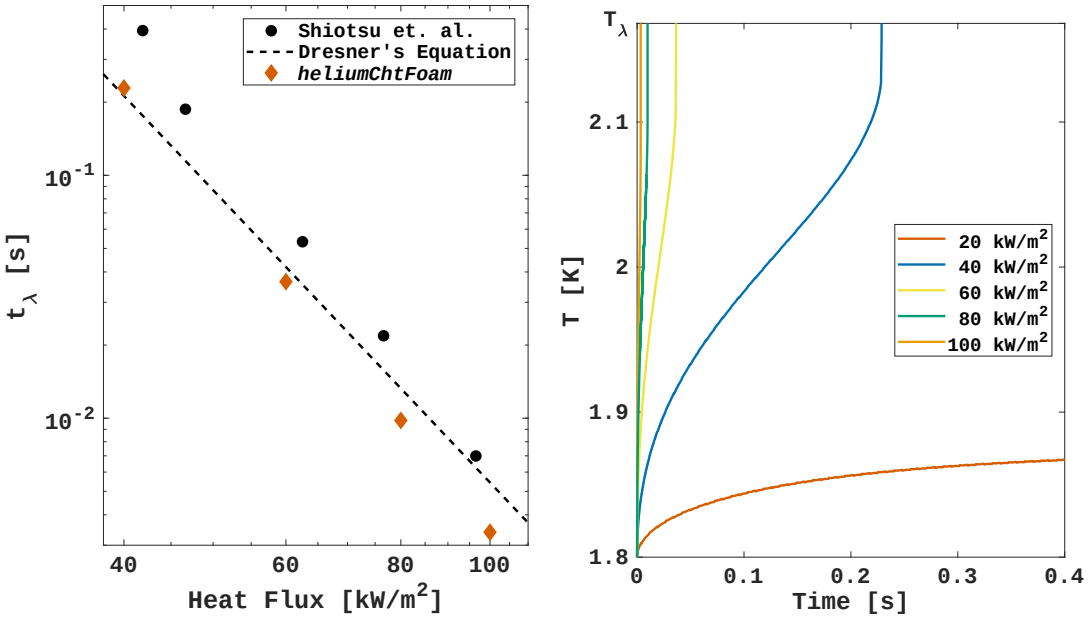

(a) Relation between the lambda time t_λ and heat flux q in logarithmic scale

(b) Temperature evolution at the closest cell to the heated surface on the symmetry boundary

Figure 4.10: Lambda time comparison between *heliumChtFoam* (red diamonds) and data from the duct experiment by Shiotsu et al. (circles) [137]. The theoretical Eq. 2.59 by Dresner is also shown (dashed line) [44]. On the right, the simulated temperature evolutions until the lambda time for different heat fluxes.

The depth of the duct allows simplifying the problem by considering a two-dimensional computational domain. Moreover, since the duct is symmetrical with respect to a central vertical line, only half region of the domain is considered for this simulation. As previously done by Tatsumoto et al. [147], the domain is split into 8000 orthogonal cells (20

horizontally) of the same size. The time step was fixed to 10^{-6} s. The temperature of the upper boundary was fixed to the bath one (1.8 K), which was also the initial temperature in the whole domain. The heat flux was applied at the bottom wall, while the lateral wall was considered adiabatic. The velocity at the walls was computed with the superfluid slip condition (Eq. (4.23)), while the inlet-outlet velocity condition was used for the upper boundary. The fluid was assumed to be initially static. The pressure of the bath was fixed to the atmospheric one. At the walls, the pressure gradient is velocity dependent and it is derived by inverting the semi-discretized momentum equation (Eq. (3.34)). Since the latter pressure boundary condition is commonly used for walls, where the velocity is defined, it will be referred to as the fixed flux pressure condition from now on. At the symmetry boundary, all the variables were assumed to be varying with a gradient equal to zero.

Fig. 4.10 shows the result of five simulations run with different heat fluxes. In particular, Fig. 4.10b displays the simulated temperature evolutions at the location of the closest cell to the heated surface on the symmetry boundary. Fig. 4.10a is a log-log graph that compares the measured lambda time with the simulated one and the equation derived by Dresner (Eq. 2.59). Despite the model predicts lower t_λ values, the agreement between the model and the empirical fourth power law of the heat flux reciprocal is satisfactory.

4.3.3 Pool Simulation of Kitamura et al.

In order to uncover the differences between the original model by Kitamura et al. [89] and *heliumChtFoam*, their numerical test case was taken under study. The computational domain represents a 6 cm by 6 cm two-dimensional pressurized He II pool. The pool is open to the bath on the upper boundary and closed by walls on the others. The fluid is initially static and at 1.8 K. The pool is heated up through a 30 kW/m^2 heat flux applied on a 1.5 cm long section at the center of the bottom wall. As the pool is symmetrical with respect to a central vertical line, only the left half of the domain is resolved. The grid is uniform and constituted by 2016 elements (32 horizontally). The time step of the transient simulation is 10^{-6} s. It must be mentioned that Kitamura's simulation was carried out in a staggered grid with the Finite Difference Method.

Same initial settings and mesh characteristics were adopted for the present study as well. The inlet-outlet and superfluid slip velocity boundary conditions were utilized for the upper boundary and the walls respectively. The pressure was set to the atmospheric one at the upper boundary and computed through the fixed flux pressure condition at the walls. The heat flux was applied at the bottom wall on a 7.5 mm long section adjacent to the symmetry plane. A zero gradient condition was used at the symmetry boundary for all the variables.

Figs. 4.11 and 4.12 compare the results of the two models in terms of the velocity and temperature fields respectively. In Fig. 4.11, iso-temperature difference lines with respect to the bath are shown for both Kitamura's model (Fig. 4.11a) and *heliumChtFoam* (Figs. 4.11b, 4.11c, 4.11d) at three different moments of the transient, namely, at 0.01 s, 0.1 s, and 2 s. Kitamura et al. found that the maximum temperature reached was 1.8159 K, which is close

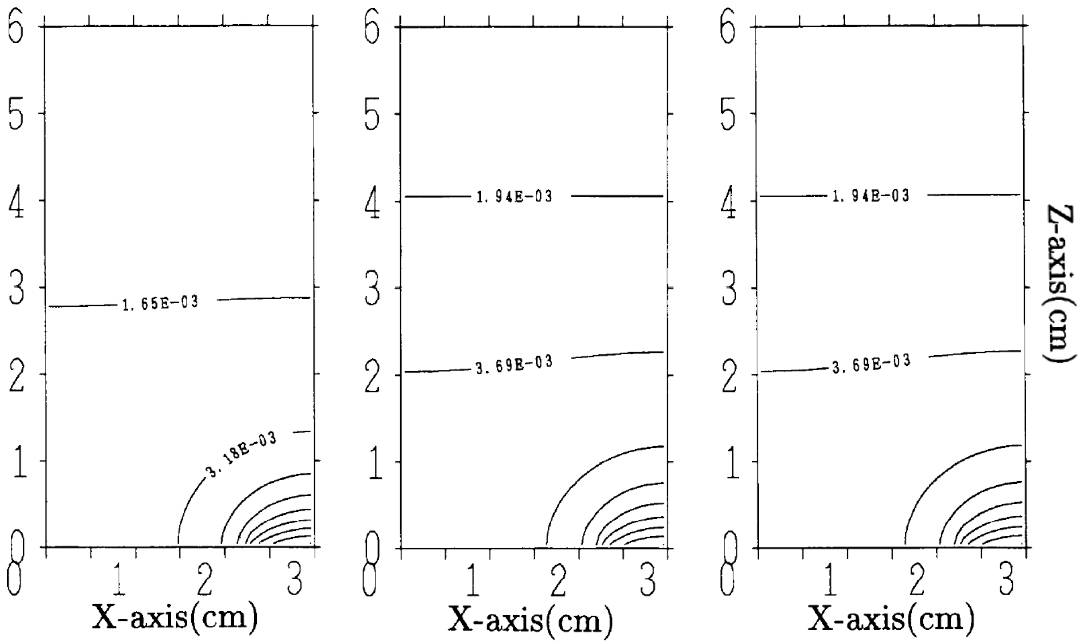

(a) Kitamura's simulation

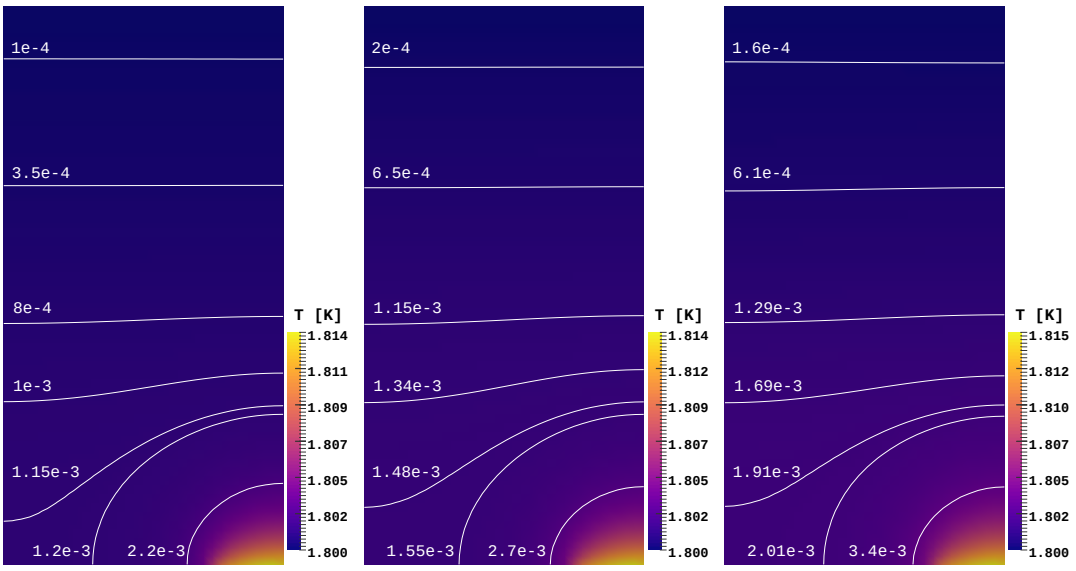

(b) 0.01 s (c) 0.1 s (d) 2 s

Figure 4.11: Temperature field comparison between *heliumChtFoam* and the model of Kitamura et al. [89]. The lines represent iso-temperature difference lines with respect to the bath temperature.

to the present one. However, in 4.11a the steady state seems to be achieved already at 0.1 s, while in *heliumChtFoam* the temperature relaxation time is longer. Overall, the temperature field obtained with *heliumChtFoam* appears to be lower than 4.11a throughout the whole transient. By comparing 4.11c and the central graph in 4.11a, it is interesting to notice that in the present model, despite the higher heat power law (see Eq. (2.44)), the temperature gradient across the pool is less pronounced. This could be related to the velocity field, as

explained in the next paragraph.

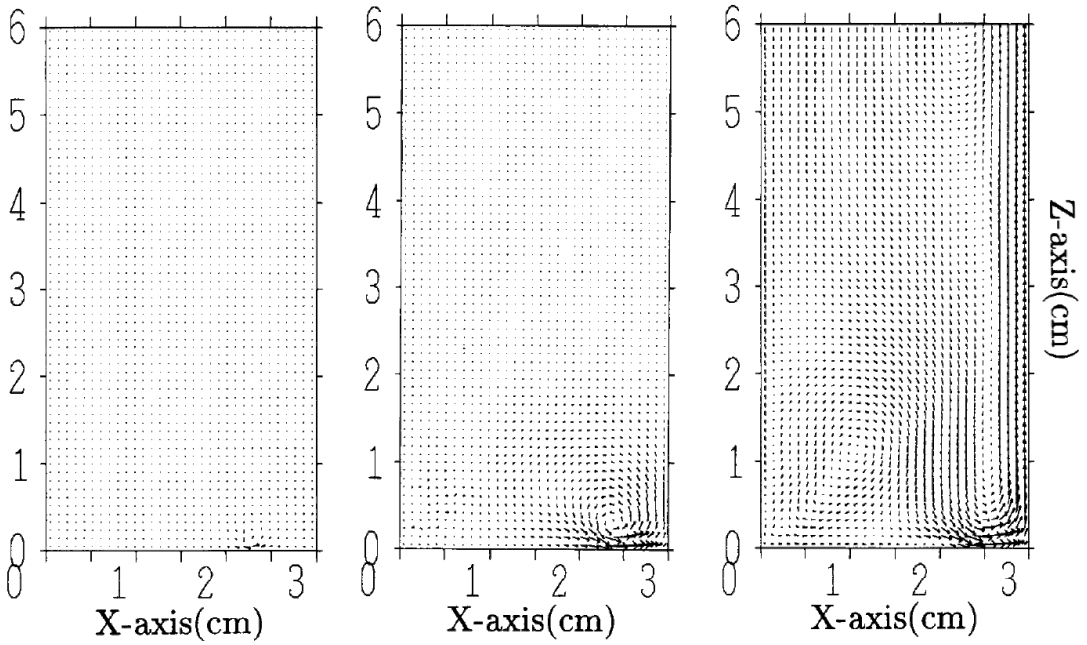

(a) Kitamura's simulation

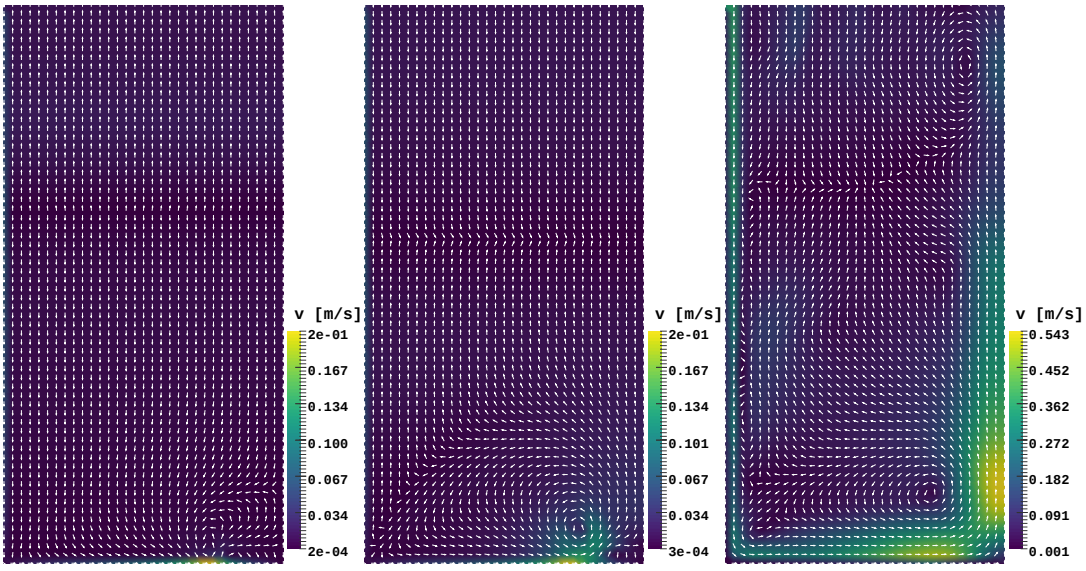

(b) 0.01 s (c) 0.1 s (d) 2 s

Figure 4.12: Velocity field comparison between *heliumChtFoam* and the model of Kitamura et al. [89]. The arrows represent the velocity vectors, whose magnitude is indicated by either their size (a) or the color scheme [(b), (c), (d)].

Figs. 4.12b, 4.12c, and 4.12d show the total fluid velocity vector orientation (arrows) and magnitude (color scale) at each cell of the domain for the same time instants as before. Firstly, it is important to underline how the direction of the velocity vectors at the solid boundaries matches the predicted one: since the superfluid is the only component that moves along the walls, the vectors were expected to be directed towards higher

temperature areas. The velocity field obtained by Kitamura et al. is presented in Fig. 4.11a, where the vectors magnitude is qualitatively indicated by the size of the arrows. In both simulations, a velocity vortex begins at the bottom wall in correspondence to the end of the heating surface. Later in the transient, the vortex seems to develop farther from the bottom wall. This is probably due to a higher velocity magnitude with respect to 4.11a. In fact, the maximum total fluid velocity reported by Kitamura et al. is 11.6 cm/s, which is much lower than the one found with *heliumChtFoam*. The higher velocity may be due to the effect of n on the temperature gradient magnitude. Since $\|\boldsymbol{\nabla} T\| \ll 1$, using $n > 3$ in Eq. (4.16) raises M, which, in turn, enhances the superfluid slip velocity (Eq. (4.23)). This could also explain the lower temperature gradient: the stronger advection homogenizes the temperature field throughout the pool. It is interesting to notice that, since the density of He II increases with temperature, the upward mass flow next to the symmetry plane is not due to natural convection but rather to fluid streams converging at the center of the heating area.

4.3.4 Channel Experiment

At last, *heliumChtFoam* is validated against the channel experiments conducted by the author for this study. In order to prove the feasibility of the multi-dimensionality with *heliumChtFoam*, the simulations were run in a three-dimensional domain. Convergence studies were carried out to assess the independence of the results from the mesh size and time step adopted for the PISO loop.

Convergence Studies The reference case for the convergence studies is an experimental test conducted in the 0.5 mm thick horizontal channel at a bath temperature of 1.8 K and a 23.6 kW/m^2 heat flux (see Fig. 4.3b). The computational geometry is a rectangular slab that resembles the shape of the channel filled with He II. The walls of the slab that correspond to the helium in contact with the stainless steel plates and flanges are kept adiabatic, while at the heater location the Neumann boundary condition is applied with the value of the heat flux. The superfluid slip and fixed flux pressure conditions are applied to all the walls for the velocity and pressure respectively. The temperature and pressure at the open side of the channel are fixed to the bath one, while the velocity is computed through the inlet-outlet condition.

Grids with different cell sizes were produced to check the convergence behaviour of the relative error of the simulated steady-state temperature profiles with respect to data. All the grids are structured, orthogonal, and uniform. The simulations were run with a fixed time step of 10^{-5} s. Fig. 4.13a shows the dependency of the relative error to the number of mesh control volumes. The relative error is computed through the 2-norm and involves the simulated temperature at the locations of the sensors in the channel and the measured values. The error decreases with the increasing number of cells until the variation becomes negligible and convergence is reached. The mesh chosen for the

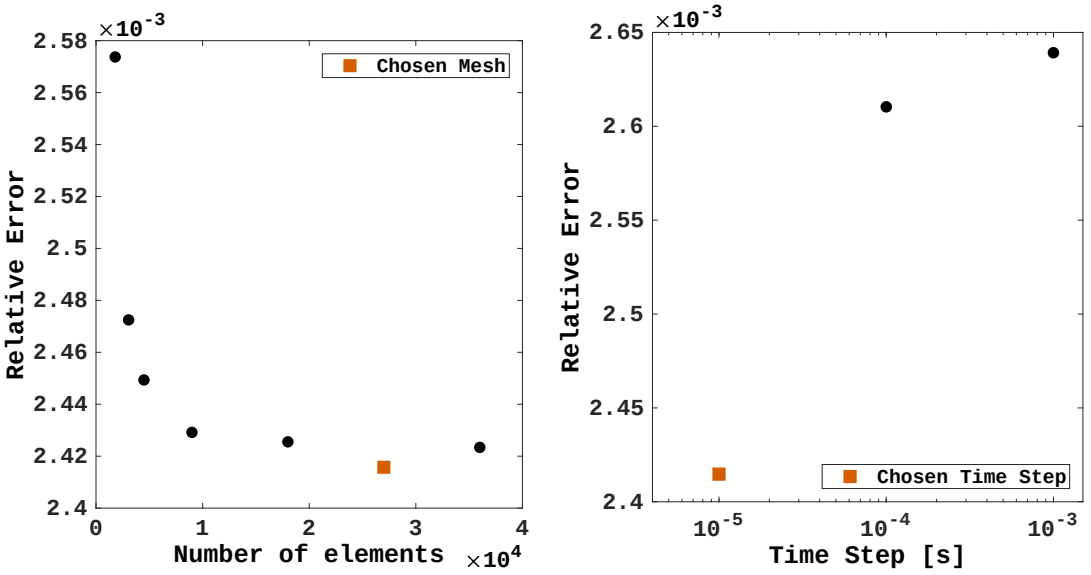

(a) Grid Convergence

(b) Time Convergence

Figure 4.13: Relative error of the simulated temperature profile for different grids and time steps with respect to the experimental measurements in the 0.5 mm thick horizontal channel at a bath temperature of 1.8 K and a 23.6 kW/m^2 heat flux.

following studies is indicated in Fig. 4.13a and it is constituted by 27×10^3 cells (150 along the channel length and 36 along its width) (see Fig. B.3 in Annex B.2).

The time convergence is investigated by utilizing different fixed time steps with the mesh chosen in Fig. 4.13a. Similar to the grid convergence study, Fig. 4.13b shows the relative error of the simulations with respect to data. As expected, the error decreases along with the time step. However, the relative error variations are very small despite the difference in orders of magnitude of the time step. Taking into account the three-dimensionality of the problem, the increasing computational cost that would derive from a further decrease of the time step was then considered unworthy. The time step chosen for the following studies is indicated in Fig. 4.13b and equal to 10^{-5} s.

Validation Against Data The validation process was realized with the grid and time settings chosen in the convergence study. At first, steady-state temperature profiles are compared to measurements in the horizontal 0.5 mm thick channel for four tests at different heat fluxes and bath temperatures. The profiles are presented as temperature differences with respect to the bath temperature. Fig. 4.14 shows such comparisons for simulations obtained with both conductive heat power laws: $n = 3$ and the derived heat conductivity function f_t (see Eq. (2.45)); $n = 3.4$ and the empirical heat conductivity function f_S (see Eq. (2.46)). The simulated profiles with the empirical settings are in good agreement with the experiments. It is clear from both Figs. 4.14a and 4.14b that the theoretical law performs better at low heat fluxes. The discrepancy becomes significant for heat fluxes close to the critical value. For this reason, the empirical power law is adopted

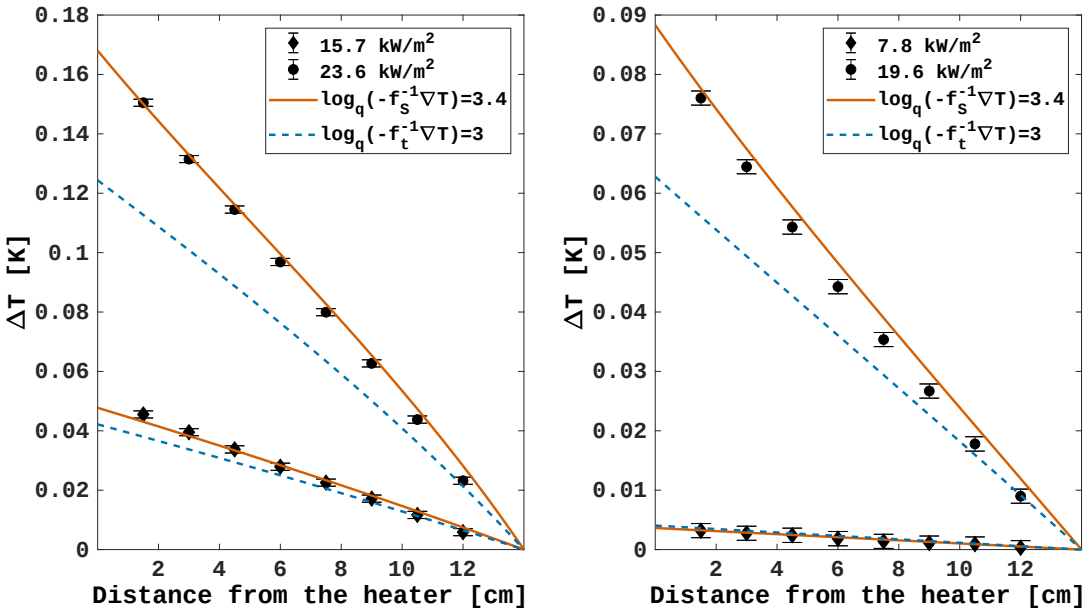

(a) $T_b = 1.8$ K (b) $T_b = 1.9$ K

Figure 4.14: Steady-state temperature profiles comparison between *heliumChtFoam* and data from experimental tests in the horizontal 0.5 mm thick channel at different bath temperatures T_b and heat fluxes. The simulated profiles for both the theoretical conductive heat power law (dashed lines) and the empirical law (solid lines) are presented.

for the subsequent simulations.

Fig. 4.15 shows the transient evolution of the temperature profile since the application of a clumped heat flux of 23.6 kW/m^2, which corresponds to the case in Fig. 4.14a at 1.8 K. The simulations agree satisfactorily to the data with a discrepancy of 0.38%, 0.21%, and 0.15% at 0.3 s, 0.7 s, and steady state respectively. The slightly higher error at an early transient stage could be due to the interpolation of the experimental data at the time instants requested for comparison.

Because of the low bath temperature and heat flux of the test in Fig. 4.15, the temperature profiles are almost linear along the channel. In order to prove that the correct temperature gradient distribution is captured by *heliumChtFoam*, another case study with higher bath temperature and a heat flux closer to the critical value was considered. Fig. 4.16 displays the transient profiles for the 0.2 mm thick channel at 1.9 K and 22.6 kW/m^2. The channel was simulated in its vertical position with an upward heat flux to diversify the study cases. The high heat flux applied causes a significant temperature gradient close to the heater, which brings the nearby He II close to T_λ. In spite of the vicinity to the critical heat flux, the steady state is achieved smoothly and entirely in He II. Experimentally, the temperature gradients seem to be more pronounced than numerically. With this regard, it is important to recall that the conductive heat exponent $n = 3.4$ is just a fit to the heat conductivity function over a wide range of temperatures (see Sec. 2.2.2), which is probably the reason for this discordance. Anyway, the overall agreement is satisfactory

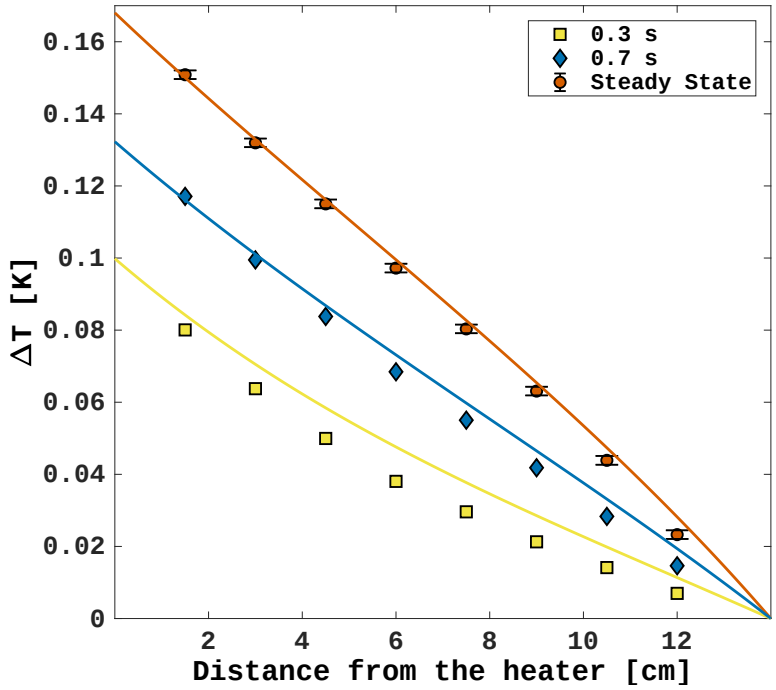

Figure 4.15: Transient temperature profiles comparison between *heliumChtFoam* and data from an experiment in the horizontal 0.5 mm thick channel at a bath temperature $T_b = 1.8$ K and a heat flux $q = 23.6$ kW/m^2.

with a maximum relative error within the 0.35%.

In order to confirm that the orientation of the channel does not affect majorly the physical phenomena happening in He II, the same test of Fig. 4.16 is simulated for the reversed orientation (i.e., downward heat flux), which did not show significant differences (see Fig. B.7 in Annex B.3).

It is interesting to plot the transient profiles of other variables for the case of Fig. 4.16. Fig. 4.17 displays the profiles of the velocity magnitude and pressure drop along the centerline of the channel. Fig. 4.17a shows that the fluid in contact with the heater is almost static: since this is the farthest spot from both adiabatic sides of the domain, the superfluid slip streams, which head towards the warmest area, converge to this point with opposite directions. The velocity increases sharply close to the heater, where the fluid is pushed upward. Since He II has negative thermal expansivity (see Fig. 2.5), the liquid close to the heater gets depressurized at the beginning of the transient, when the heater starts dissipating energy. As a result, helium from the bath is pulled into the channel, and the velocity at the exit increases. As the transient evolves, the pressure drop relaxes and the backflow ceases. At steady state, the pressure profile is almost linear with a maximum value just above the bath pressure, while the maximum velocity decreases down to almost 5 cm/s.

Fig. 4.18 shows the transient profiles of the effective thermal conductivity k_{eff} and the momentum diffusive-like parameter M. Both properties depend on the temperature gradient and hence present similar behaviour. At an early stage of the transient, the

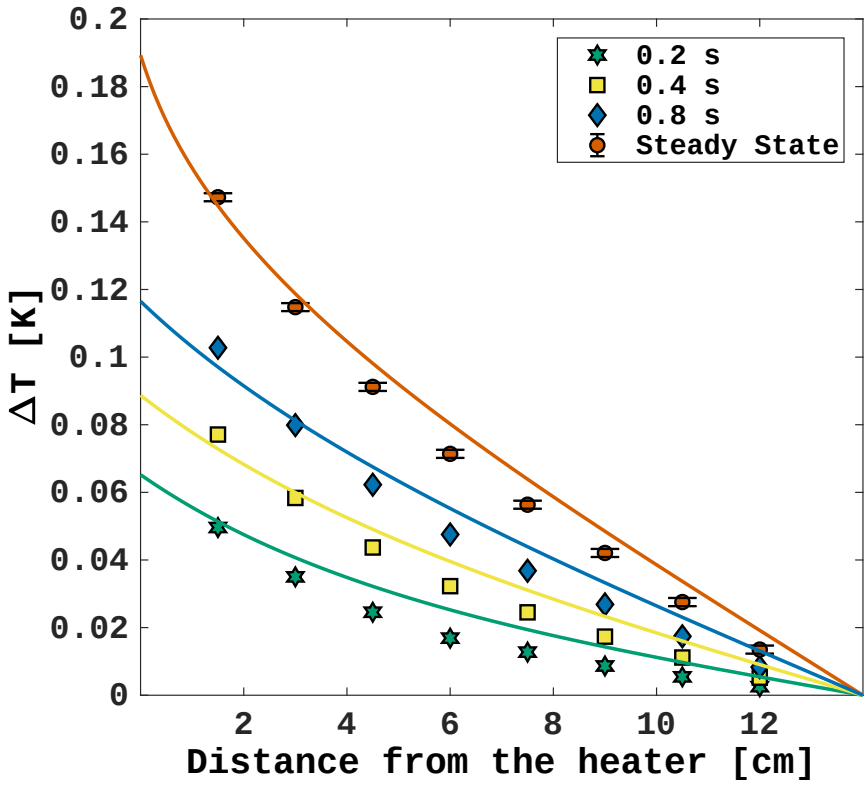

Figure 4.16: Transient temperature profiles comparison between *heliumChtFoam* and data from an experiment in the vertical 0.2 mm thick channel at a bath temperature $T_b = 1.9$ K and an upward heat flux $q = 22.6$ kW/m^2.

thermal gradient is very low far from the heater. This implies greater values of k_{eff} and M close to the channel exit as both properties are proportional to the inverse of the temperature gradient. The profiles gradually relax throughout the simulation until steady state, when the thermal gradient is homogenized along the channel and both properties reach lower values.

Conjugate Heat Transfer As already mentioned at the end of Sec. 3.2.2, *heliumChtFoam* is capable of simulating the conjugate heat transfer between helium and other media. In order to demonstrate it, the case study of Fig. 4.15 is taken into consideration one more time. This time, an additional region corresponding to the Manganin® heater is modeled and joined to the original He II slab, whose number of cells remains unchanged. The heater region is subdivided into 8 cells in the direction of the channel length (see Fig. B.4 in Annex B.2). The boundary conditions are unchanged with the exception of the patch at the heater, where Eq. (4.21) is now applied. Unfortunately, no Kapitza conductance measurements for Manganin® were found in literature. By testing various parameters in Eq. (4.22) starting from the as-received copper values [158], it appeared that $a_I = a_{II} = 400$, $m_{II} = 3$, and $m_I = 2$ allow a good representation of the temperature evolution at the heater interface. The heater boundaries that are not exposed to helium are kept adiabatic, since in the experiment they are in contact with the insulating G10 plug. The energy dissipated during

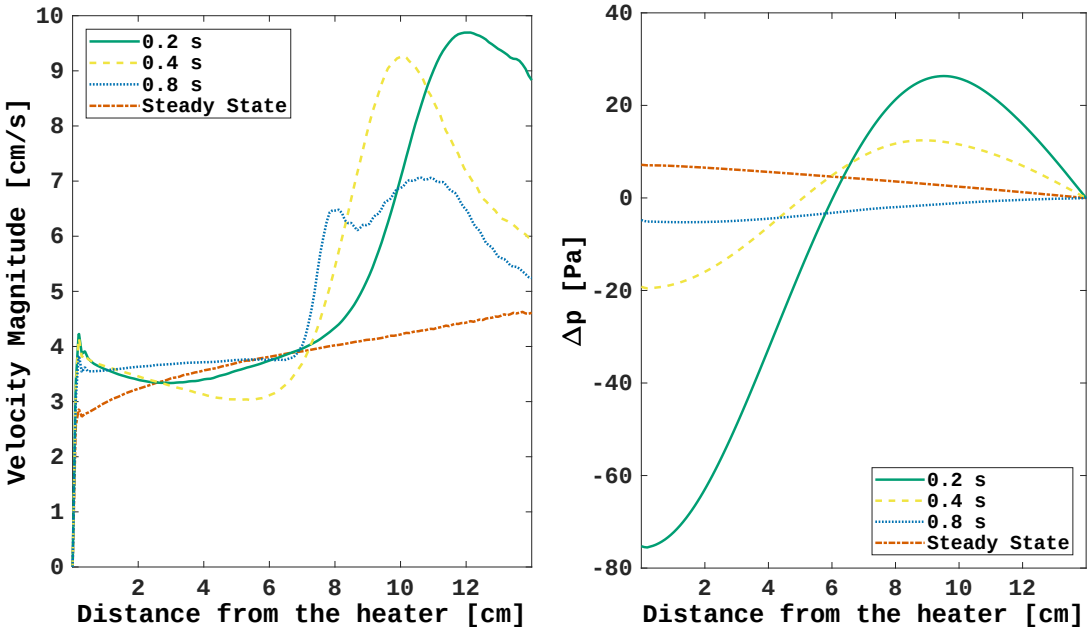

(a) Velocity Magnitude (b) Pressure Difference

Figure 4.17: Simulated velocity and pressure profiles at the centerline of the vertical 0.2 mm thick channel at a bath temperature $T_b = 1.9$ K and an upward heat flux $q = 22.6$ kW/m^2.

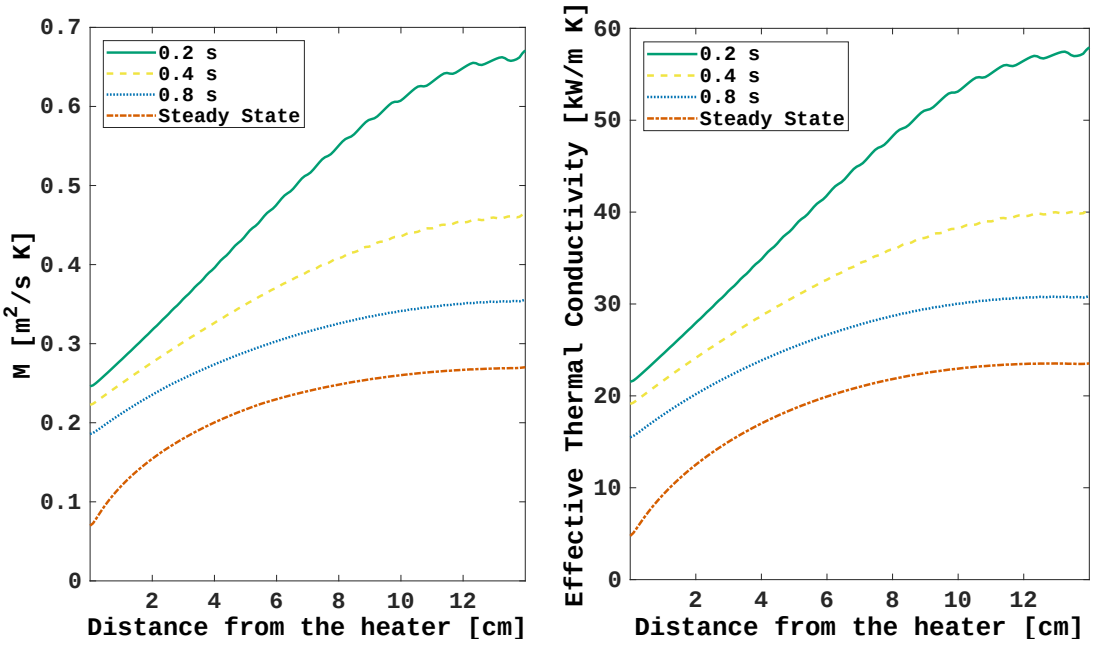

(a) Momentum Diffusive-like Parameter (b) Effective Thermal Conductivity

Figure 4.18: Simulated M and k_{eff} profiles at the centerline of the vertical 0.2 mm thick channel at a bath temperature $T_b = 1.9$ K and an upward heat flux $q = 22.6$ kW/m^2.

the experiment is exerted via a volumetric heat generation Q in the solid part. The thermal behaviour of the heater is described by the ordinary energy equation for solids:

$$\rho \frac{\partial h}{\partial t} = \rho \boldsymbol{\nabla} \cdot (\alpha \boldsymbol{\nabla} h) + Q, \tag{4.25}$$

where α is the thermal diffusivity of the solid. The thermophysical properties of Manganin® are obtained from METALPAK© [107].

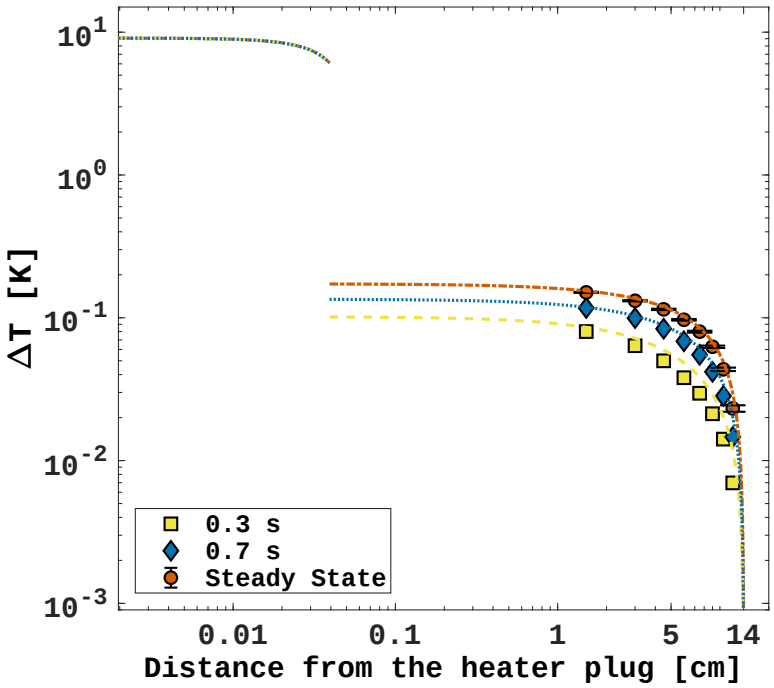

Figure 4.19: Transient temperature profiles of the heater strip and He II with respect to data from an experiment in the horizontal 0.5 mm thick channel at a bath temperature $T_b = 1.8$ K and a heat flux $q = 23.6$ kW/m^2.

Fig. 4.19 shows the transient temperature profiles simulated for both the helium and heater domains in a log-log graph. The temperature drop of about 6 K at the interface between the two media at steady state is clearly due to the Kapitza resistance. Because of both the high thermal diffusivity of Manganin® and the small dimensions of the strip, the thermal time constant of the heater is very low. As a result, the steady state is reached much earlier than in helium.

CHAPTER 5

Phase Transitions Study

5.1 Experiments

If the heat flux applied in the channel overcomes the minimum value q_{min} reported in Table 4.1, He II undergoes λ-transition. In this section, the experimental results obtained with greater heat fluxes than q_{min} are reported and discussed. The sensors' nomenclature used in Ch. 4 is maintained. The results of the clamped flux tests are presented in the form of temperature evolution graphs against the time of the test. Since often the temperature gradient in the channel is significant in experiments involving helium phase transitions, some graphs are supported by insets that show a close-up view of the temperature evolution in the early moments of the transients in the He II range of temperatures.

The effect of different experimental conditions is dealt with in-depth in specific subsections thereafter. In particular, the data is analyzed for the three channel orientations and two thicknesses already presented in Sec. 4.1. In addition to the bath temperatures chosen for the superfluid tests, the phase transitions experiments were conducted at 2.15 K as well. Each graph is labeled with the equivalent heat flux computed at the heater-helium interface from the product between the voltage and induced electric current. It must be borne in mind, though, that heat losses through the solid materials surrounding the helium zone are inevitable and become significant when He I and helium vapour are generated. Since their thermal conductivities are comparable to the materials of the setup, the thermal time constant of the helium fluids with respect to the solids' one cannot be considered negligible any longer (see the final paragraph of Sec. 3.1.2). The temperature gradient that is established along the channel at steady state is then strongly affected by both the solid-helium interaction and surface tension forces acting on the vapour-He I interface. The gradient cannot be described solely by the heat flux applied like in the case of He II. Despite the difficulty to dissipate energy just in the helium zone at this level of geometrical confinement, the analysis of the data reveals interesting aspects of the three-phase phenomena occurring in the early moments of the clamped flux tests.

5.1.1 Clamped Flux Tests

Fig. 5.1 shows the temperature evolution of helium following the application of a clamped flux in the horizontal 0.2 mm thick channel for different heat fluxes and a bath temperature of 1.9 K. At a heat flux moderately above q_{min} (Fig. 5.1a), the lambda transition does not occur beyond 3 cm from the heater. After the initial temperature increase at the TS1 location, the second time derivative of the temperature changes sign before reaching the steady state because of the increasing temperature gradient close to the heater. Once the λ-point is reached, the temperature rises sharply as He II turns into He I. The distinct change in slope of the temperature evolution can be explained by considering the temporal partial derivative of the temperature from the one-dimensional diffusion equation ($\partial T/\partial t = (\rho c_p)^{-1}\partial q/\partial x$). In fact, the specific heat c_p of helium at the λ-point at atmospheric pressure is more than seven times higher than at 2.2 K [158]. The steady state is reached after 20 s, when the temperature at TS1 is stable in He I with temperature oscillations within 0.2 K.

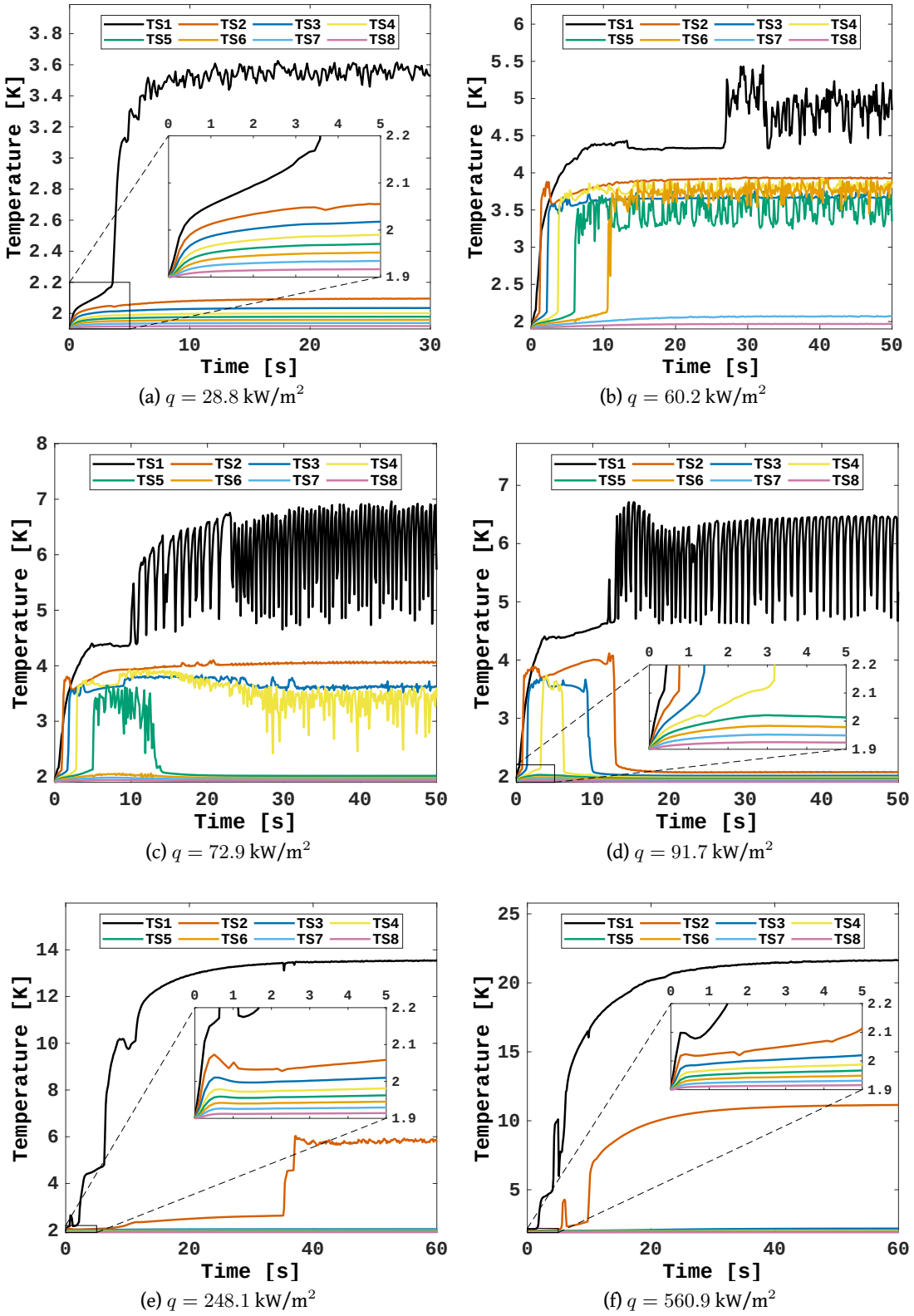

(a) $q = 28.8\ \mathrm{kW/m^2}$ (b) $q = 60.2\ \mathrm{kW/m^2}$

(c) $q = 72.9\ \mathrm{kW/m^2}$ (d) $q = 91.7\ \mathrm{kW/m^2}$

(e) $q = 248.1\ \mathrm{kW/m^2}$ (f) $q = 560.9\ \mathrm{kW/m^2}$

Figure 5.1: Temperature evolution in the horizontal 0.2 mm thick channel at $T_b = 1.9$ K and different heat fluxes q.

As the heat flux applied is raised (Fig. 5.1b), the λ-front propagates downstream and stops at around 4 cm far from the channel aperture. It is clear that helium vapour is generated close to the heater, as the temperature at TS1 fluctuates around 4.7 K after overcoming a plateau at the boiling point. The He I region seems to extend over a great portion of the channel, which grows with the heat flux covering an increasing number of sensors (see Fig. A.5 in Annex A.1). It can be noticed that in the early moments of the transient the temperature at TS2 is higher than at TS1. This is not a heat diffusion phenomenon as it would be witnessed also without phase transitions (e.g., Sec. 4.1). It is rather caused by the distribution of the vapour and He I phases in the channel. It must be taken into account, indeed, that the channel is 5 cm wide and hence the expanding phases are likely to be distributed non-uniformly in the horizontal configuration of the channel. When the bubbles are produced in the vicinity of the heater, they develop downstream heterogeneously and end up being confined in certain regions by the surface tension forces and thickness of the channel. Eventually, their proximity to the sensors determines the irregular temperature gradient.

At higher heat fluxes (Figs. 5.1c and 5.1d), the temperature fluctuates markedly between 7 K and values just above the saturation one. Remarkably, increasing the energy dissipated does not cause the λ-front to propagate farther in the channel. The temperature crosses the λ-point within 10 s since the application of the clamped flux and returns to the superfluid range after a few seconds. This is observed at multiple sensor locations with greater heat fluxes (see Fig. A.6 in Annex A.1). Moreover, the λ-front reaches fewer sensors as the heat flux rises. This phenomenon is the consequence of a vapour film generated quickly at the heater surface. The higher the heat dissipated, the sooner the onset of the film boiling regime. Since the thermal conductivity of helium vapour is considerably low, the film acts as an insulator and interrupts the heat diffusion towards the He II bath. For the same reason, the steady-state temperature at TS1 in Fig. 5.1d is lower than in Fig. 5.1c.

At very high heat fluxes (Figs. 5.1e and 5.1f), the amount of vapour generated is such that, after the initial increase, even at TS1 the temperature decreases almost below the λ-point before rising again. Moreover, the temperature at TS2 is no longer higher than the one recorded by TS1 in the early transient, as the vapour region occupies a greater portion of the channel and develops homogeneously throughout it. The He I region is now limited to a small portion of the channel (i.e., less than 1.5 cm), as the temperature at TS3 remains in the He II range until steady state. The inset in Fig. 5.1e reveals the temporary increment of the temperature due to diffusion in the whole channel at the very beginning of the transient. Once the vapour film is generated, the temperature drops before starting a slow growth that will bring helium at TS2 to change phase twice at a much later stage of the test — after 10 s. A bump that reaches 10 K happening above the boiling point is observable in both Figs. 5.1e, 5.1f, and other graphs in the same range of heat fluxes (see Fig. A.6 in Annex A.1). A similar bump is also present in Fig. 5.1f at TS2, which occurs right after the one recorded at TS1. This might be due to a vapour region propagating quickly after the heat impulse and collapsing as it travels through the channel.

5.1.1.1 Effect of the Bath Temperature

The clamped flux tests were conducted as well at a bath temperature T_b very close to the λ-point. Fig. 5.2 shows the temperature evolution of experiments at $T_b = 2.15$ K. At this initial temperature, the minimum heat flux to trigger a phase transition is much lower compared to the previous case. A heat flux of 8 kW/m^2 is enough to produce a λ-front propagating until TS1 (Fig. 5.2a). Unlike the results at low fluxes (above q_{min}) at $T_b = 1.9$ K (Fig. 5.1a), the steady-state temperature at TS1 is lower than the maximum value reached during the transient, which suggests the presence of helium vapour close to the heater. Increasing slightly the flux results in a steady presence of He I at TS1 (Fig. 5.2b), although the temperature is lower than the peak in Fig. 5.2a. This was also observed in Fig. 5.1 and represents another indication of first-order phase change occurring before TS1.

At higher fluxes, the boiling front crosses TS1 (Fig. 5.2c), where a steady temperature is experienced at the boiling point because of the latent heat of vaporization. In a certain range of heat fluxes, the vapour region reaching TS1 seems to recede after the initial propagation and before becoming stable at that location (see Fig. A.7 in Annex A.1). This phenomenon is absent at higher energy (Fig. 5.2d), where the plateau at the boiling point becomes steeper.

It is interesting to highlight the behaviour of the temperature evolution at farther sensors from the heater. A sharp change in slope takes place at a lower temperature than the saturation one at ambient pressure (Figs. 5.2d, 5.2e, 5.2f). As it will be clear later in this chapter, possible explanations due to pressure changes are to be excluded, since no major pressure drop was detected. The reason could be attributed to advection prevailing on diffusion. In other words, at high heat fluxes, the temporal derivative of the temperature at a certain location in the channel is strongly affected by advective phenomena arising due to the expansion of the vapour phase, which disturbs the diffusive character of heat transport.

In contrast to the tests at a lower bath temperature, the insets in Fig. 5.2 do not reveal any temporary increment of the temperature. This is probably because at $T_b = 2.15$ K the time needed to reach the λ-transition is very small and, thus, there is no moment in the transient in which the temperature evolution is entirely determined by the effective thermal conductivity of He II in the whole channel. The temperature increases then because of the propagation of the double front, as is proved by the much slower process that characterizes the phase change at farther sensors (see Fig. 5.2f).

The insets show a systematic temperature drop at TS2 (and TS4 in Fig. 5.2f) that lasts less than a second. A possible explanation for this short event relies on a pressure increase that weakens fast in the upstream portion of the channel. This would justify a small temperature drop of about 5 mK by considering that, at this temperature and pressure, the Joule-Thomson coefficient is about -7.4×10^{-7} K/Pa. It is also worth noticing that the bump above the boiling point occurs at this bath temperature as well and reaches almost 10 K regardless of the heat flux applied (see Fig. A.8 in Annex A.1), even though the time

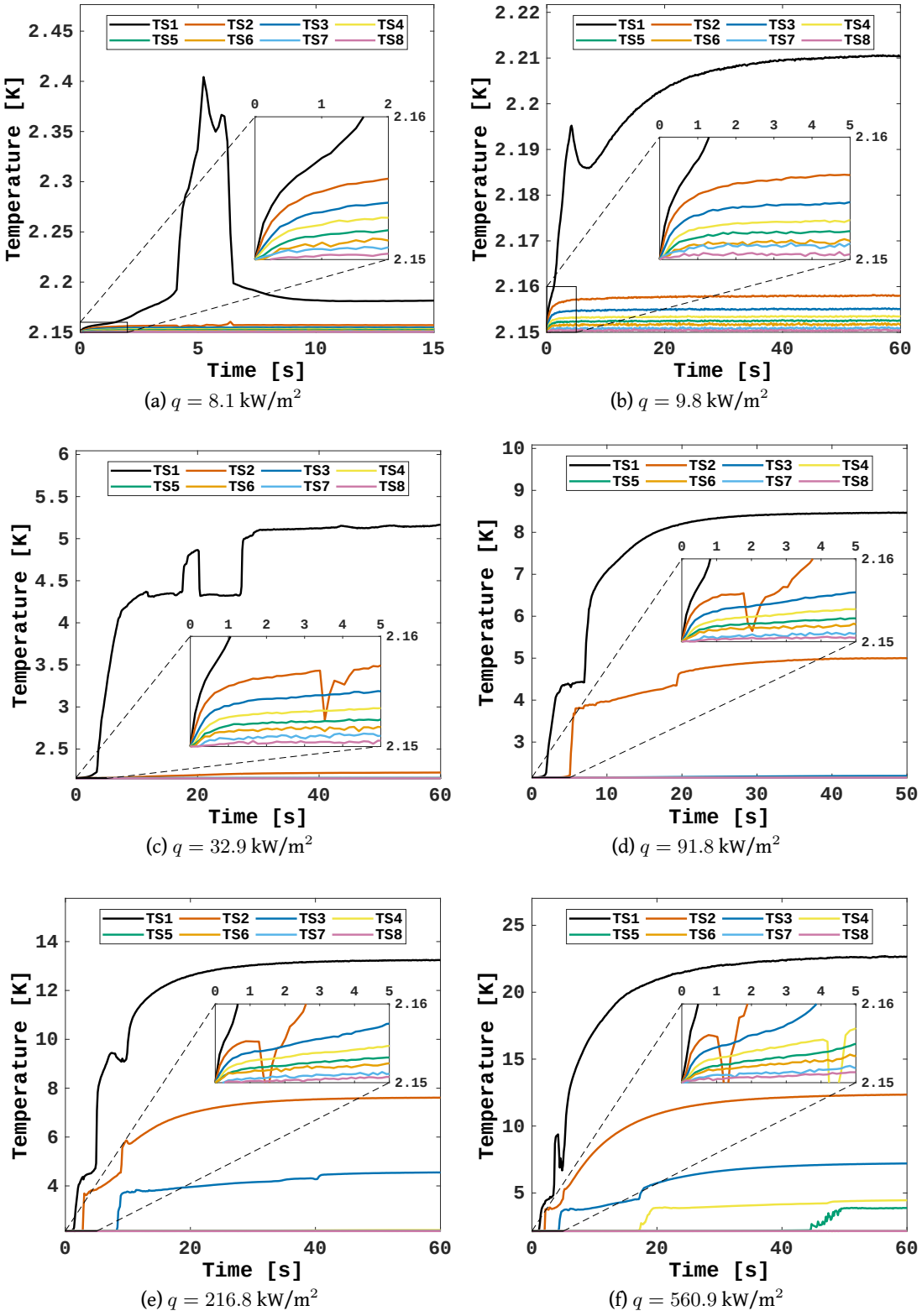

(a) $q = 8.1\ \mathrm{kW/m^2}$ (b) $q = 9.8\ \mathrm{kW/m^2}$

(c) $q = 32.9\ \mathrm{kW/m^2}$ (d) $q = 91.8\ \mathrm{kW/m^2}$

(e) $q = 216.8\ \mathrm{kW/m^2}$ (f) $q = 560.9\ \mathrm{kW/m^2}$

Figure 5.2: Temperature evolution in the horizontal 0.2 mm thick channel at $T_b = 2.15$ K and different heat fluxes q.

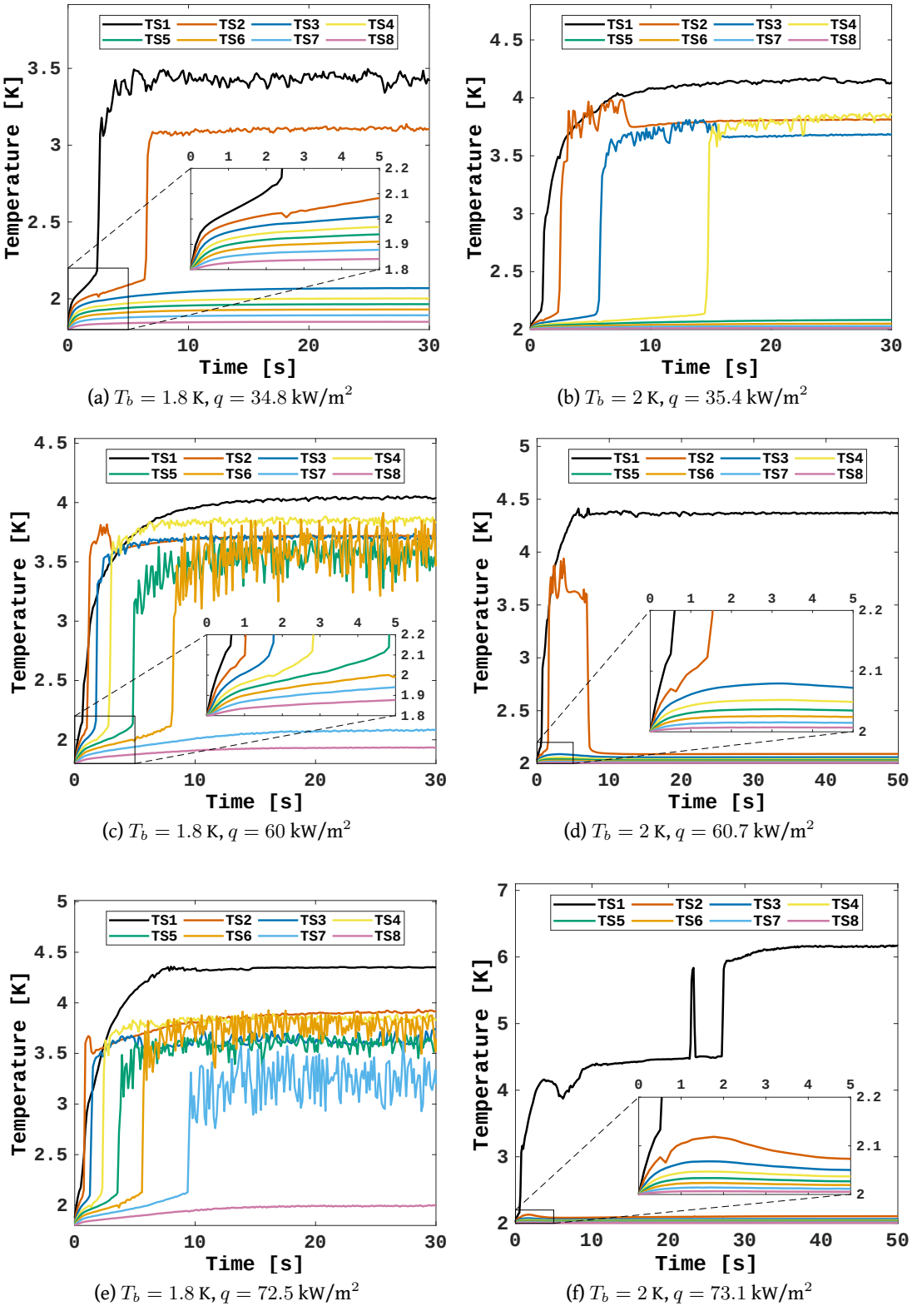

(a) $T_b = 1.8$ K, $q = 34.8$ kW/m^2

(b) $T_b = 2$ K, $q = 35.4$ kW/m^2

(c) $T_b = 1.8$ K, $q = 60$ kW/m^2

(d) $T_b = 2$ K, $q = 60.7$ kW/m^2

(e) $T_b = 1.8$ K, $q = 72.5$ kW/m^2

(f) $T_b = 2$ K, $q = 73.1$ kW/m^2

Figure 5.3: Temperature evolution in the horizontal 0.2 mm thick channel at different bath temperatures T_b and heat fluxes q.

span shortens.

The differences between the results at high and low He II bath temperatures can be summarized with Fig. 5.3. This figure compares tests at $T_b = 1.8$ K (left column of plots) and 2 K (right column of plots) with similar heat fluxes. At a low heat flux (Figs. 5.3a and 5.3b), the temperature evolves in a similar way with He I covering a larger region when the initial temperature is closer to the λ-point. At a moderate heat flux (Figs. 5.3c and 5.3d), while at 1.8 K the channel is still mainly constituted by He I, at 2 K the helium close to the heater undergoes double phase change and the temperature in the channel decreases down below the λ-point. At a high heat flux (Figs. 5.3e and 5.3f), the q_{min} value at 1.8 K allows a stable and large He I region, with the λ-front reaching almost the channel aperture. At 2 K, the temperature rises at the beginning of the transient in the entire channel because of heat diffusion. At the onset of film boiling, the temperature drops, and the majority of the channel remains in He II at a temperature slightly higher than the initial one. The λ-front develops with time but stops right after TS1 followed by the boiling front. In this case, the He I region is much smaller and constricted between the vapour film and the superfluid region.

5.1.1.2 Effect of the Channel Orientation

The experiments were conducted also with different orientations of the 0.2 mm thick channel. Fig. 5.4 shows representative temperature evolutions at $T_b = 1.9$ K (left column of plots) and 2.15 K (right column of plots) for different downward heat fluxes. Unlike in the horizontal configuration, the transition fronts do not reach many sensors regardless of the energy dissipated into the channel. Since the slope of the density as a function of temperature changes sign across the λ-point, a temperature increase in He I and helium vapour results in upstream natural convection flows. Consequently, once He II undergoes phase transitions, the fluid tends to remain on top of the channel if the heater is situated above the helium zone.

At 1.9 K, the temporary diffusion-driven temperature increment is again found in the early moments of the transients (Figs. 5.4a and 5.4c). This is responsible for the first sharp temperature increase at TS1. Soon after, the slope decreases while still being positive. Since this event does not occur at a temperature characterized by phase transitions, the change in slope is probably due to the vapour expansion, which leads to either a steady value (Fig. 5.4a) or, at a higher heat flux, to a peak followed by a temperature drop (Fig. 5.4c). In the latter case, the heat flux is sufficient to build up a homogeneous vapour region that facilitates the heat extraction from the cool bath. Raising the heat flux applied decreases the peak maximum (Fig. 5.4e), which can be clearly seen at gradual flux increments in Fig. A.9 of Annex A.1. Thereafter, a second λ-transition develops within 4.5 cm from the heater, and the temperature grows proportionally to the heat flux. It is important to notice that, with respect to the horizontal orientation at a comparable heat flux (Fig. 5.1b), the He I region appears very small, similar to a higher range of heat fluxes in the horizontal case. This happens because the enhancement of the vapour region is

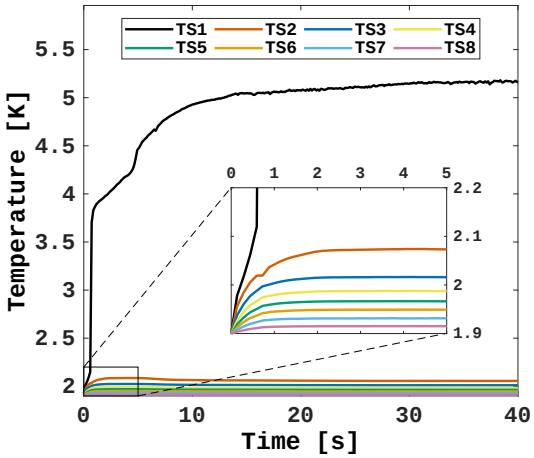

(a) $T_b = 1.9$ K, $q = 48.1$ kW/m^2

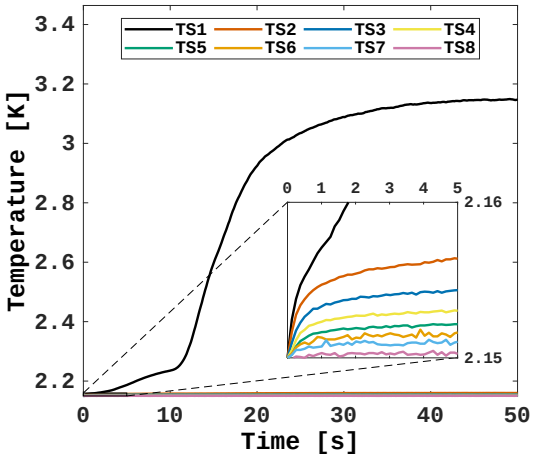

(b) $T_b = 2.15$ K, $q = 17.6$ kW/m^2

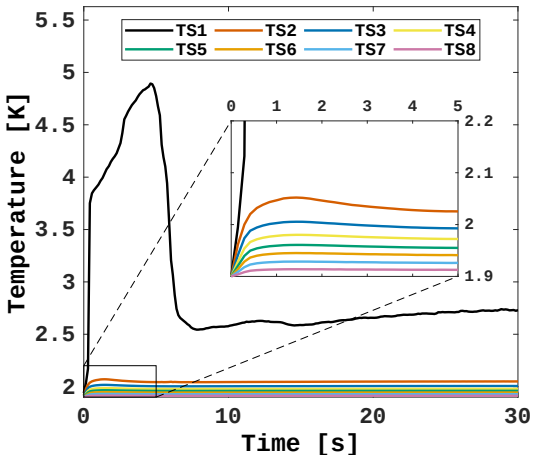

(c) $T_b = 1.9$ K, $q = 73.1$ kW/m^2

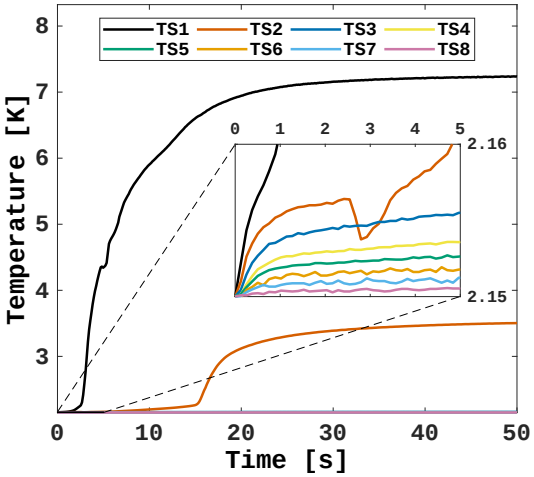

(d) $T_b = 2.15$ K, $q = 73.1$ kW/m^2

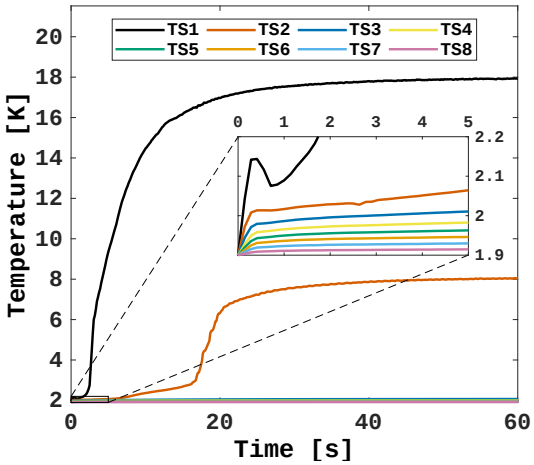

(e) $T_b = 1.9$ K, $q = 373.4$ kW/m^2

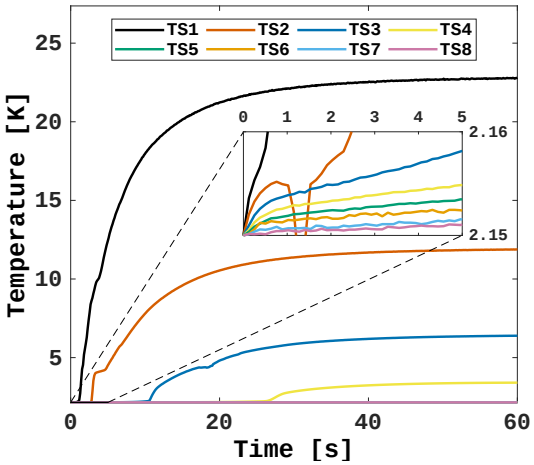

(f) $T_b = 2.15$ K, $q = 560.9$ kW/m^2

Figure 5.4: Temperature evolution in the vertical 0.2 mm thick channel at different bath temperatures T_b and downward heat fluxes q.

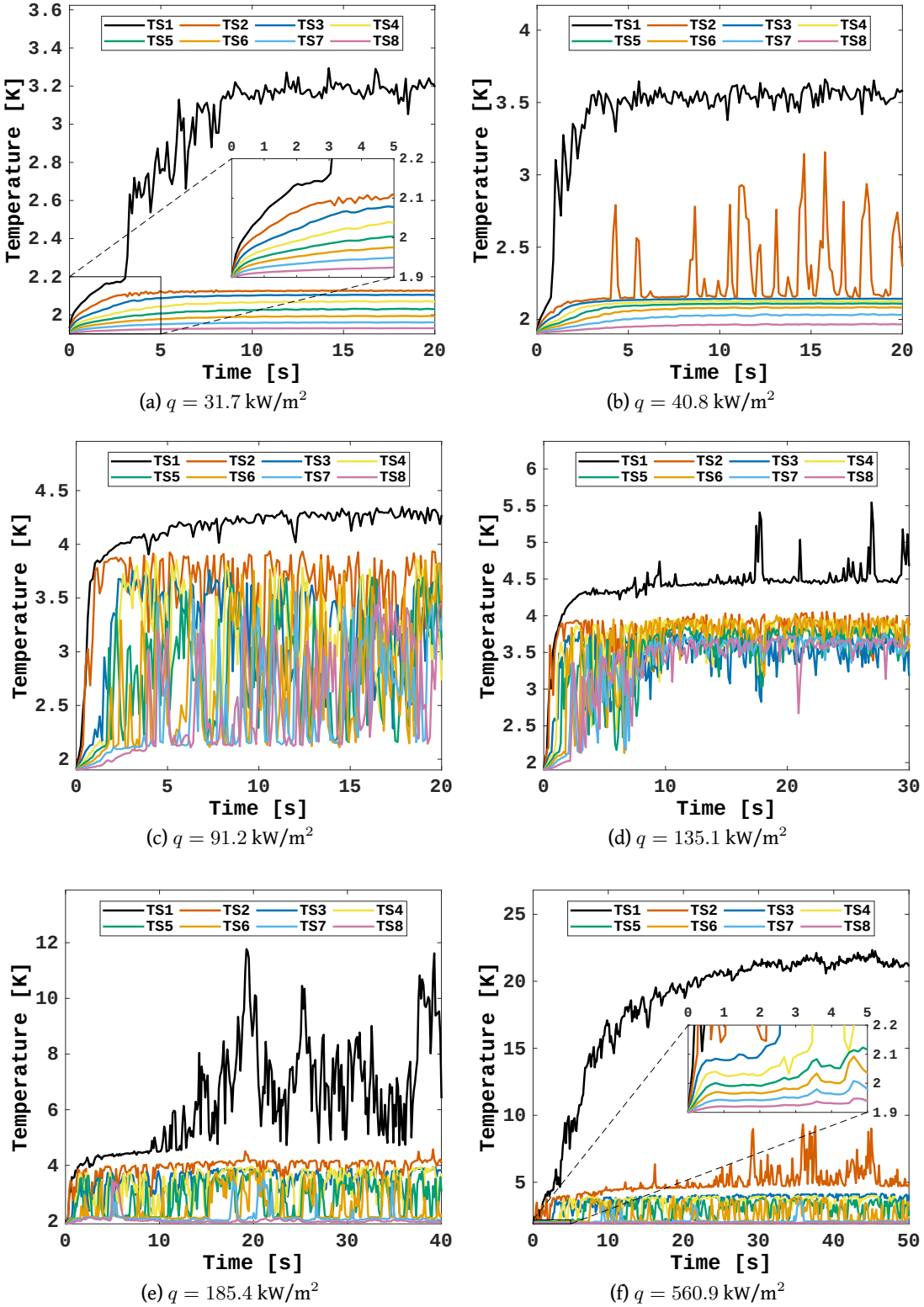

(a) $q = 31.7\ \mathrm{kW/m^2}$ (b) $q = 40.8\ \mathrm{kW/m^2}$

(c) $q = 91.2\ \mathrm{kW/m^2}$ (d) $q = 135.1\ \mathrm{kW/m^2}$

(e) $q = 185.4\ \mathrm{kW/m^2}$ (f) $q = 560.9\ \mathrm{kW/m^2}$

Figure 5.5: Temperature evolution in the vertical 0.2 mm thick channel at $T_b = 1.9$ K and different upward heat fluxes q.

gravity assisted and, thus, a lower heat flux is sufficient to generate a stable insulating film.

At 2.15 K, because of the low q_{min}, vapour is soon generated. Therefore, the heat diffusion from the heater in He II is almost immediately interrupted, and the λ-transition is mostly determined by the propagation of the boiling front. This is demonstrated by the long time needed by the λ-front to reach the farthest sensors from the heater (Fig. 5.4f). The small temperature drop at the beginning of the transient is visible in this orientation as well.

Fig. 5.5 presents the results for the vertical channel with upward heat fluxes (i.e., helium zone above the heater). With this orientation, He I and helium vapour tend to rise towards the aperture of the channel assisted by gravity. As a consequence, the steady state is achieved earlier than in other configurations. Moreover, the steady-state temperature ends up being lower because of the natural convection that builds up throughout the channel. At low heat fluxes (Figs. 5.5a and 5.5b), most of the sensors remain in He II, whereas TS1 measures oscillating values in He I. The signal at TS2 is greatly disturbed, with values ranging from just below T_λ to almost the temperature at TS1 (Fig. 5.5b). Increasing the heat flux results in large fluctuations along the entire channel (Fig. 5.5c), suggesting hence an ongoing boiling process with bubbles rising to the bath. The fluctuations diminish considerably at a higher heat flux (Fig. 5.5d), when the temperature is stable in the He I range in the whole channel. TS1 appears to reach the saturation temperature, with occasional peaks in vapour. From Figs. 5.5e and 5.5f it is possible to identify a phenomenon already observed in other channel configurations: higher heat fluxes cause the temperature to drop down below the λ-point. This is again due to the vapour film, which is sustained by the extent of the energy dissipated. The film hinders the heat extraction and induces a substantial temperature increase in the vicinity of the heater, as shown by TS1. At 2.15 K, a similar behaviour was observed (see Fig. A.10 in Annex A.1).

5.1.1.3 Effect of the Channel Thickness

The clamped flux tests were repeated in the 0.5 mm thick channel in order to see the effect of a bigger geometry on the phase change phenomena. Before presenting the results, it is useful to make a few considerations through the usage of the confinement number Co, which is a measure of the restrictive effect of the confining geometry on the boiling flow. The Co number is defined as the square root of the Bond number (Bo) reciprocal:

$$Co = \frac{1}{\sqrt{Bo}} = \frac{1}{D}\sqrt{\frac{\sigma}{g(\rho_l - \rho_v)}}, \tag{5.1}$$

where D is the hydraulic diameter, σ is the surface tension coefficient, g is the gravitational acceleration, and ρ_l and ρ_v are the densities at saturation of the liquid and vapour phase respectively. The hydraulic diameter for rectangular channels is computed as $D = 4A/p$, where A and p are respectively the area and perimeter of the channel cross-section. Calculating the Co number at atmospheric pressure gives as result approximately the

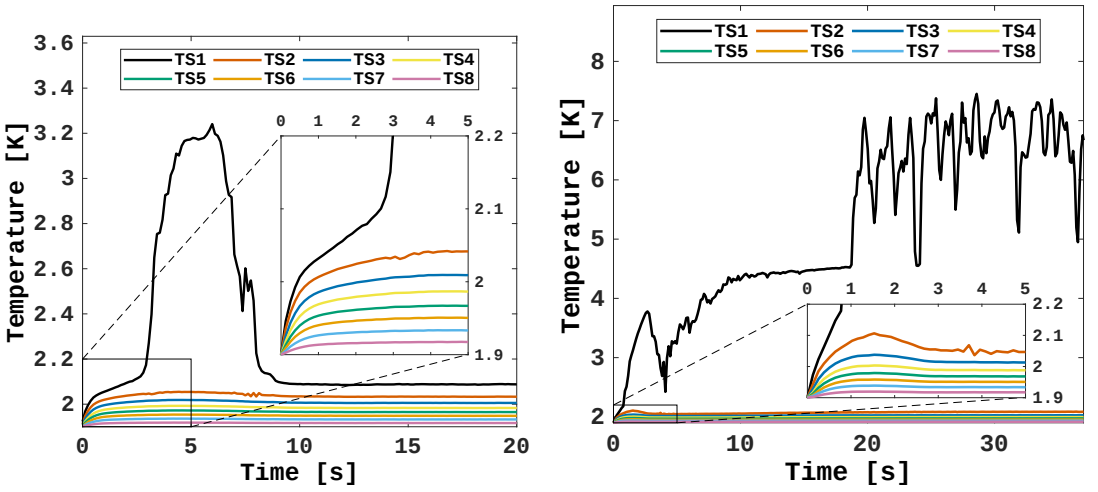

(a) $q = 29.3\ \mathrm{kW/m^2}$ (b) $q = 60\ \mathrm{kW/m^2}$

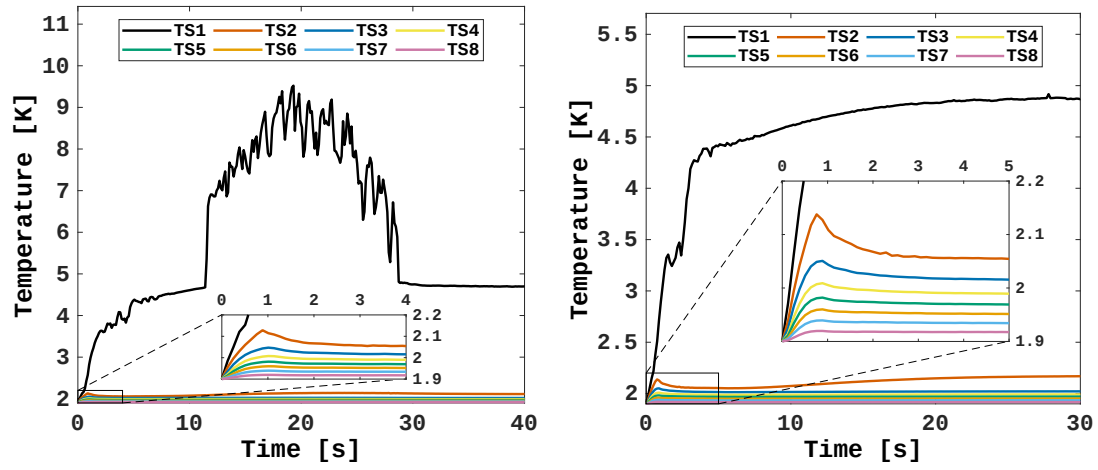

(c) $q = 86.2\ \mathrm{kW/m^2}$ (d) $q = 112.6\ \mathrm{kW/m^2}$

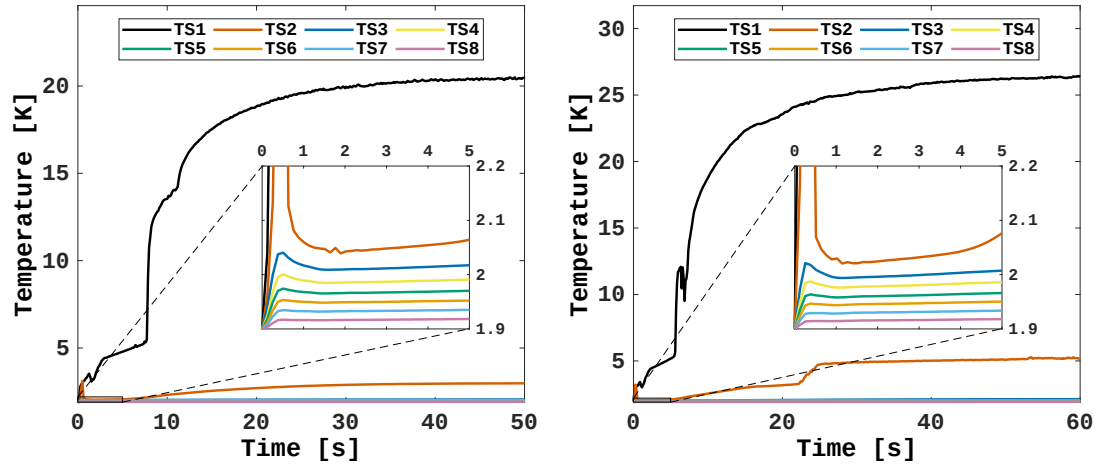

(e) $q = 261.3\ \mathrm{kW/m^2}$ (f) $q = 392.1\ \mathrm{kW/m^2}$

Figure 5.6: Temperature evolution in the horizontal 0.5 mm thick channel at $T_b = 1.9$ K and different heat fluxes q.

values 0.72 and 0.29 for the 0.2 mm and 0.5 mm thick channels respectively. Cornwell and Kew identified $Co = 0.5$ as the threshold that differentiates between confined and non-confined two-phase flows [34]. Above this value, the boiling flow is affected by the restricting geometry. Therefore, the propagation of the phase change fronts is expected to differ significantly in the 0.5 mm thick channel compared to the smaller one.

Fig. 5.6 shows the temperature evolution in the horizontal 0.5 mm thick channel at $T_b = 1.9$ K. It is immediately clear from a comparison between Figs. 5.6a, 5.6b and Figs. 5.1a, 5.1b that the He I region is much thinner in the bigger channel. In fact, with a heat flux moderately above q_{min}, the λ-front reaches TS1 before receding close to the heater. In Fig. 5.6b, the vapour-He I interface oscillates nearby TS1, while TS2 remains in He II until steady state. The He I phase is, thus, confined between the vapour and He II phases in a portion that is less than 1.5 cm long. All the other sensors register temperatures in the He II range of values. In contrast, in the same range of heat fluxes in the 0.2 mm thick channel, the λ-front crosses multiple sensors before receding close to the heater. This dissimilarity with respect to the smaller channel lies in the expansion of the liquid-vapour mixture, which occurs mostly horizontally because of the lacking space in the gravity direction.

At a higher heat flux (Fig. 5.6c), the maximum temperature at TS1 is greater than the steady-state one, which indicates a growing vapour film. This is confirmed by Fig. 5.6d, where the vapour phase is stable at TS1 at a temperature just above the saturation value and hence much lower than in Figs. 5.6b and 5.6c. After the first diffusion-driven increment, the λ-front develops slowly and approaches TS2. Raising further the heat flux (Figs. 5.6e and 5.6f) does not cause major differences in the temperature evolution. The heat diffusion is such that the λ-front passes TS2 within 1 s since the application of the flux. After dropping down below T_λ, the temperature at TS2 starts a slow growth with a resulting first-order phase change after 20 s (Fig. 5.6f).

It is important to underline a subtle distinction in comparison to the smaller channel. While in the 0.2 mm thick channel the first temperature increment seems to attenuate as the heat flux increases (Figs. 5.1e and 5.1f), in this case the time at which the temperature reaches T_λ appears constant (Figs. 5.6e and 5.6f). This appearance will be confirmed by studying the front speed, which is presented later in this chapter. It is also interesting to notice that, unlike in the smaller channel, the temperature at a sensor is always above the one at the next sensor (e.g., TS1 > TS2). This confirms that the overlapping evolution seen in Fig. 5.1 is due to the size of the channel, which obstructs the homogeneous distribution of the vapour and He I phases.

Fig. 5.7 shows representative results for the two vertical orientations of the 0.5 mm thick channel at 1.9 K. The temperature evolutions for downward heat fluxes are presented on the left column of plots, while the right column refers to upward fluxes. Let us focus at first on the left column. At a low heat flux above q_{min} (Fig. 5.7a), the temperature rises by heat diffusion in the whole channel before slightly dropping towards steady state. Although all the sensors remain in He II for the entire test, it is clear from this behaviour that a phase transition occurs near the heater. At a higher heat flux (Fig. 5.7c),

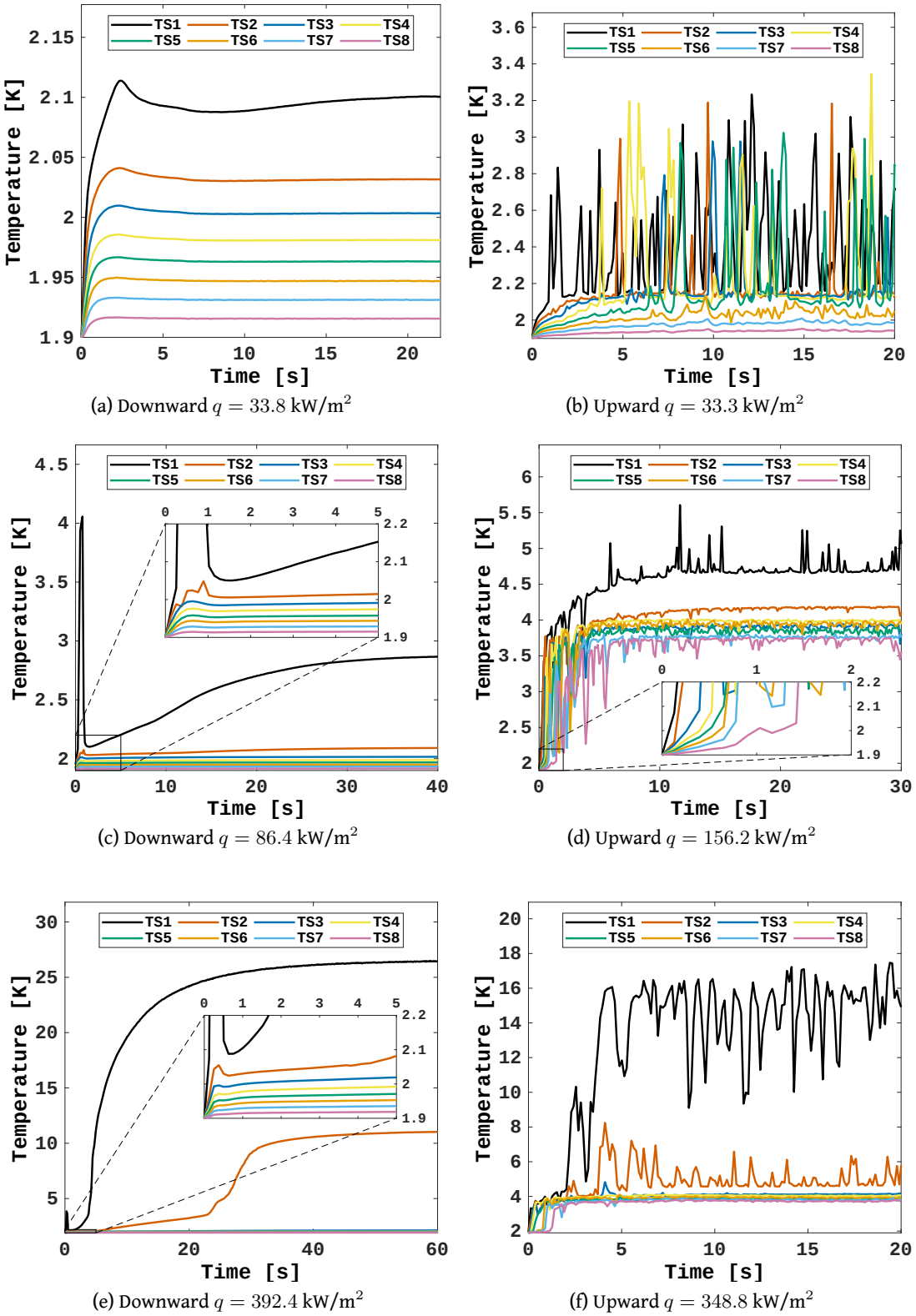

(a) Downward $q = 33.8$ kW/m^2

(b) Upward $q = 33.3$ kW/m^2

(c) Downward $q = 86.4$ kW/m^2

(d) Upward $q = 156.2$ kW/m^2

(e) Downward $q = 392.4$ kW/m^2

(f) Upward $q = 348.8$ kW/m^2

Figure 5.7: Temperature evolution in both vertical orientations of the 0.5 mm thick channel at $T_b = 1.9$ K and different heat fluxes q.

the evolution does not change significantly except at TS1, where a peak approaches the saturation temperature within the first second of the test. In comparison to the smaller channel at a similar heat flux (Fig. 5.4c), the peak resolves itself much faster (roughly $1/5$ of the time span) and reaches a lower temperature. This is again due to the different extent of flow confinement between the two geometries. Interestingly, increasing the heat flux shortens the time span of the peak but does not affect its maximum value (Fig. 5.7e). This evidence differs from what experienced in the 0.2 mm thick channel, where both parameters decrease as clearly exhibited by Fig. A.11 in Annex A.1. After the peak, the temperature grows slowly proportionally to the heat flux applied.

Contrary to the smaller channel (Fig. 5.5a and 5.5b), a low upward heat flux above q_{min} causes fluctuations in most of the sensors' locations (Fig.5.7b). Since the vapour and He I phases are relatively free to flow in this channel, no minimum heat impulse is necessary for them to rise the channel. At higher heat fluxes (Figs. 5.7d and 5.7f), the fluctuations diminish and the temperature settles just below the saturation value at almost all locations. The heat extraction due to the ongoing boiling process ensures a small temperature increase at the heater and a nearly constant value throughout the channel because of the rising bubbles. It should be noted that, with respect to this case, in the smaller channel above a certain heat flux the temperature goes back to a fluctuating behaviour along a large portion of the channel (Figs. 5.5e and 5.5f). On the other hand, the size of the larger channel, together with the action of gravity, delays the onset of the vapour film, which is responsible for interrupting the thermal connection between the He II bath and the heater.

5.1.1.4 Pressure Measurements

Due to the first-order phase transition and consequent high variations in density, pressure changes of some extent were expected. Unfortunately, no major pressure variations were detected. Moreover, the results seem to be independent of the heat flux, as indicated by Fig. 5.8. The figure shows the pressure evolution recorded by the two sensors, which, as a reminder, are located at 1.5 cm far from each longitudinal margin of the channel. Despite the large difference in energy dissipated, the maximum pressure increase does not exceed 4 kPa, which is measured by the sensor close to the heater. This peak occurs at the beginning of the tests, which suggests a connection with the vapour expanding quickly after the application of the heat flux. Shortly after, the pressure drops down below the atmospheric value and reaches the steady state. This is probably due to the pressure jump occurring across the boiling front because of the surface tension forces, as it will be clear later in this chapter. In contrast, the pressure close to the bath does not vary significantly. It increases until almost 2 kPa with a sudden step that occurs earlier for high heat fluxes.

The reason for such low variations in pressure can be attributed to the open bath the channel setup is submerged in. The free surface of the bath allows the vapour phase to expand undisturbed. In order to achieve pressure bursts as high as the ones that

characterize quench phenomena, it will be necessary to obstruct the channel aperture or confine the bath volume to maintain isochoric conditions.

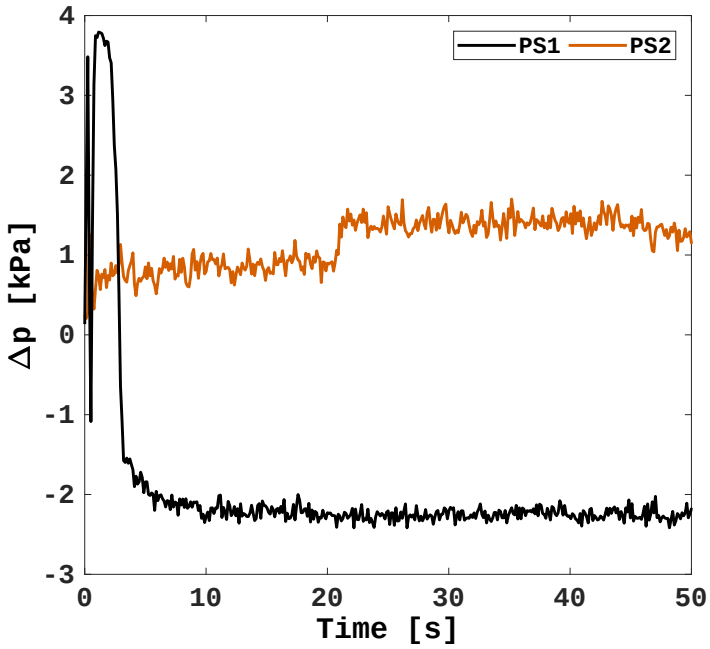

(a) $q = 88.6$ kW/m^2

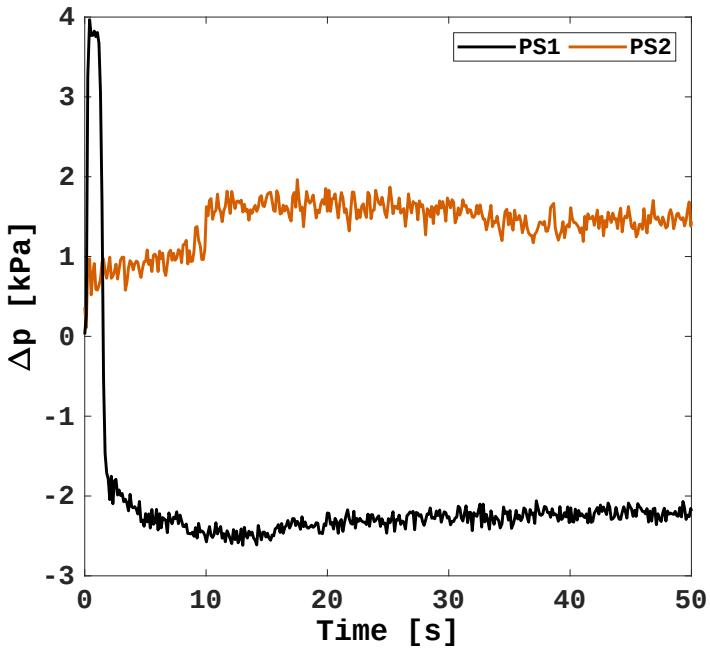

(b) $q = 536.6$ kW/m^2

Figure 5.8: Pressure evolution in the 0.5 mm thick channel at $T_b = 2.15$ K and different heat fluxes.

5.1.2 Double-Front Propagation

The data collected from the clamped flux tests in the horizontal 0.2 mm thick channel provides information on the propagation speed of the λ-front. The speed is computed as the ratio between the distance from the heater to a certain sensor and a time difference. The latter is the difference between the time at which a sensor measures T_λ and the time at which the heater reaches the same temperature. Fig. 5.9 is a comparison of the λ-front speed at four different bath temperatures among four heat fluxes in the range between 35 kW/m^2 and 73 kW/m^2. The solid, dashed, dotted, and dash-dotted lines refer to the speed profiles obtained respectively at 1.8 K, 1.9 K, 2 K, and 2.15 K. As predicted by various

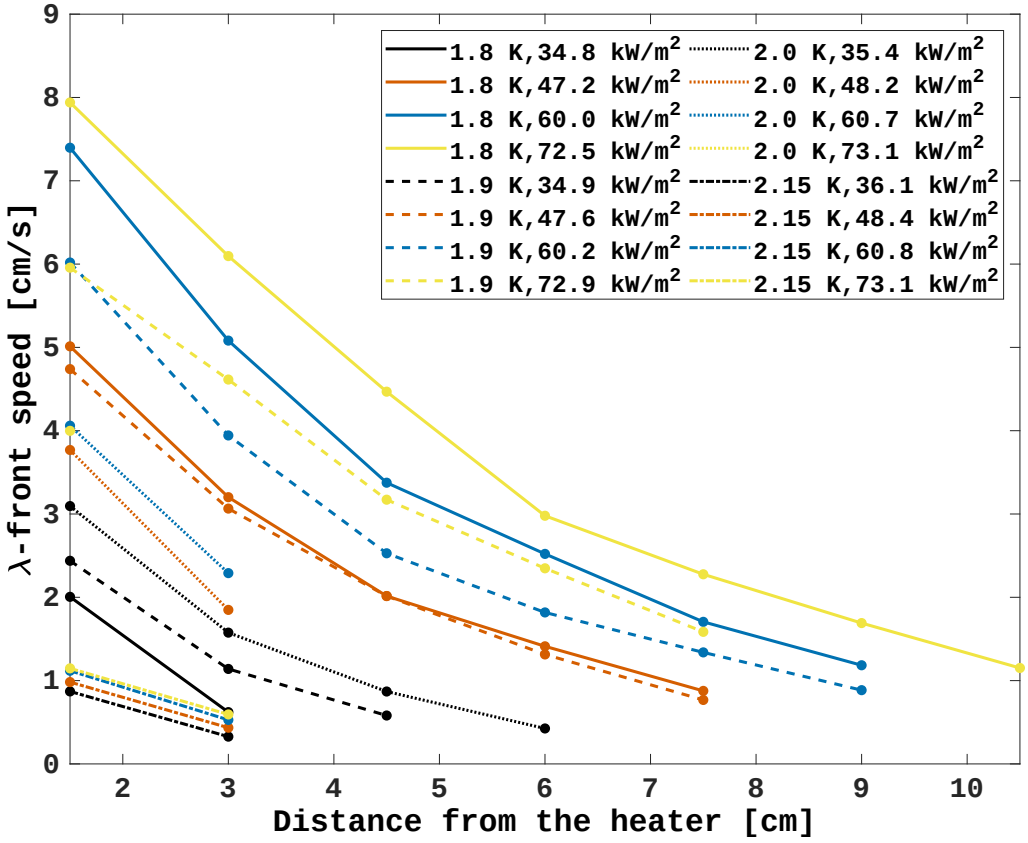

Figure 5.9: Lambda front propagation along the horizontal 0.2 mm thick channel for different heat fluxes and bath temperatures. The circle markers indicate the position of the sensors.

authors [45], [26], [138], the speed is inversely proportional roughly to the cubic root of the front position. It is immediately clear that the lower the bath temperature, the wider the range of speeds covered in the same interval of heat fluxes. Both the speed and the path traversed by the front increase with the heat flux. However, as the bath temperature approaches T_λ, the path shortens with the heat flux. At 2 K, the front barely reaches TS1 at the upper heat flux. This evidence can be explained by considering the onset of film boiling. This is confirmed by the speed profiles at 2.15 K, which diverge from the other results: lower speed and slope; covered path independent from the heat flux in the current range.

The initial temperature is evidently too close to T_λ for the He I phase to develop before the latent heat of vaporization is matched by the energy dissipated. It is legitimate to think, thus, that the λ-front propagation is affected by the vapour phase growth.

Fig. 5.10 shows the speed profiles for a larger range of heat fluxes at 1.9 K. As seen in the previous graph, the speed increases with the heat flux. This trend stops being valid at a certain heat flux (roughly 10^5 W/m^2), above which the speed starts decreasing with the heat flux. This effect is particularly clear beyond TS1 as indicated by the speed computed at TS2, where the value drops drastically above the aforementioned heat flux. Moreover, the path traversed by the front appears unchanged for a wide range of heat flux: it is only at very high values that the front approaches TS3. Increasing the heat flux above 10^5 W/m^2 results in a gradual change in the slope of the profiles, which tends to resemble the behaviour already observed in Fig. 5.9 at 2.15 K. In this case, since the bath temperature is lower, more energy is required to trigger the first-order phase change in order to obtain this particular slope.

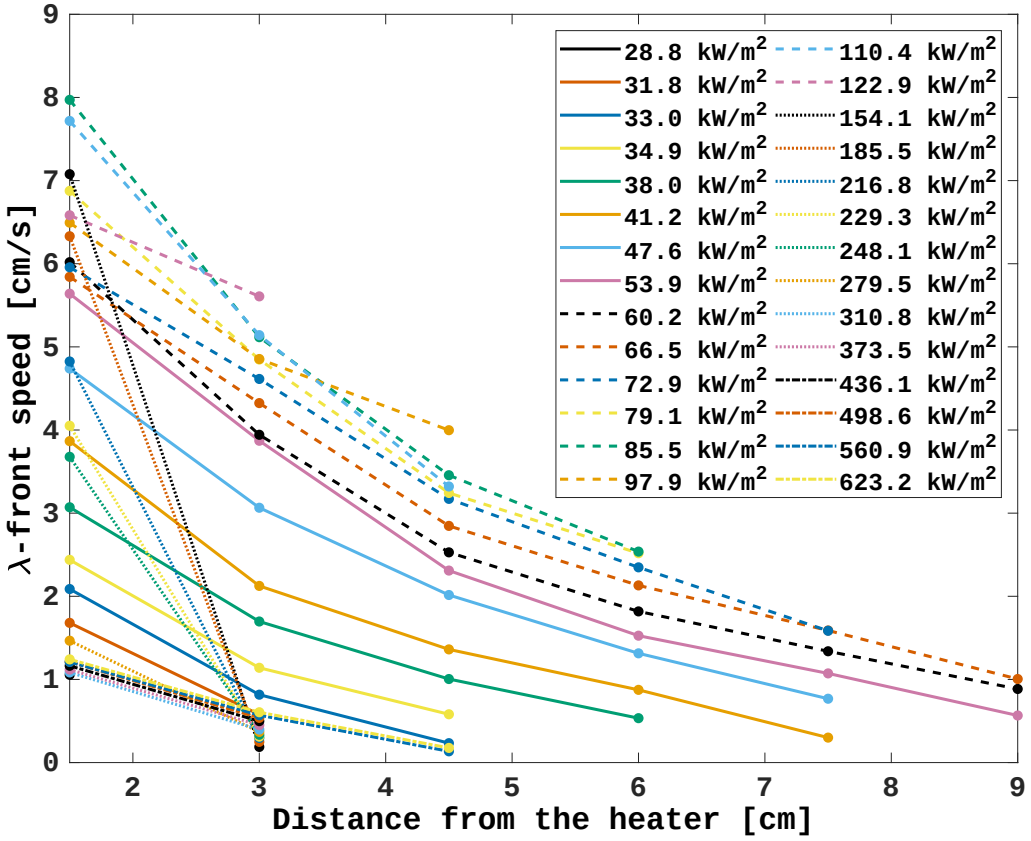

Figure 5.10: λ-front propagation along the horizontal 0.2 mm thick channel for different heat fluxes at $T_b = 1.9$ K.

This variation of the front propagation is better visualized in Fig. 5.11, which shows the front speed as a function of the temperature difference between the heater and the He II bath for different heat fluxes. The results obtained at 1.9 K (Fig. 5.11a) and 2.15 K (Fig. 5.11b) are compared. The temperature dependence of the speed at a constant location in

the channel is roughly linear at low and high temperatures (Fig. 5.11a). However, the function is much steeper for low differences in temperature. In the intermediate range of temperatures (i.e., between the two distinguishable linear trends for a specific sensor), the front appears to reach TS1 only, where the slope becomes negative and the function ceases to be linear. At locations from TS2 on, after the first linear function, the front is again detected at a much higher heater temperature, indicating that the phenomenologic change of the propagation occurs nearby the heater.

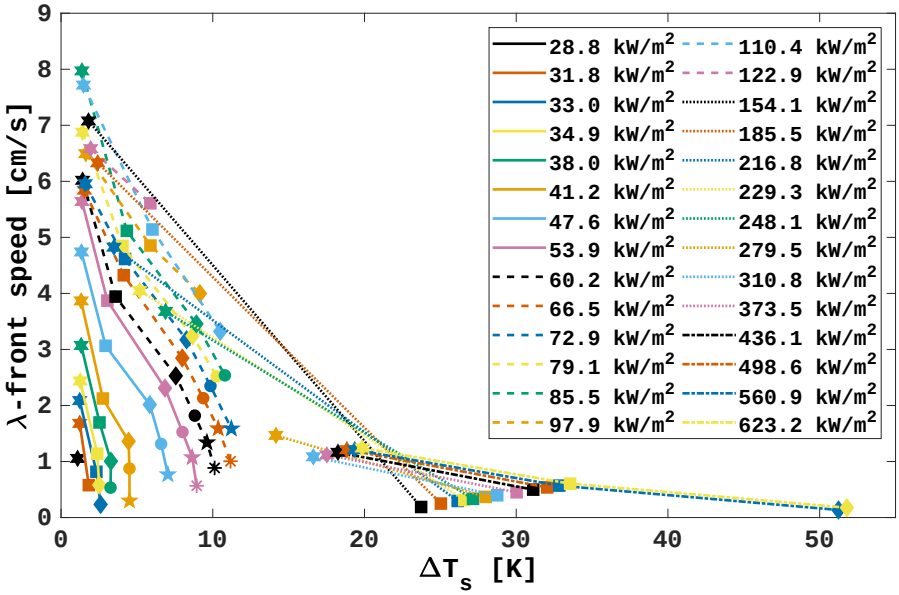

(a) $T_b = 1.9\,\mathrm{K}$

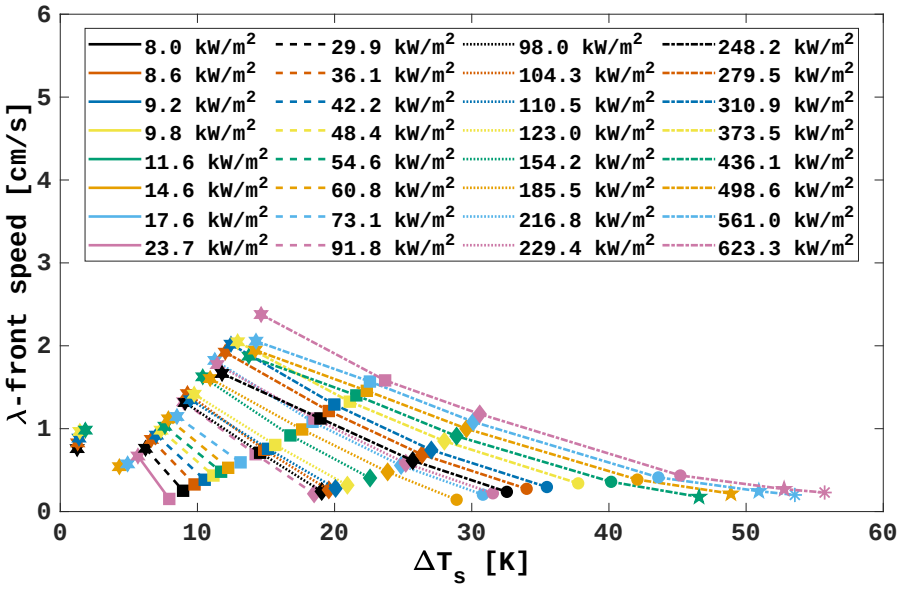

(b) $T_b = 2.15\,\mathrm{K}$

Figure 5.11: λ-front speed with respect to the temperature difference between the heater and bath for different heat fluxes. Each sensor location along the channel is referred to with a different marker: from TS1 to TS6 the markers are respectively hexagrams, squares, diamonds, circles, pentagrams, and asterisks.

At 2.15 K (Fig. 5.11b), the differentiation can be identified for TS1 only. The steep function is visible just for very low temperatures, whereas above around 10^4 W/m^2 the speed increases at a slope similar to the high-temperature region of Fig. 5.11a. It appears clear at this point that the λ-front speed is greatly affected by the growing vapour film and boiling front.

The data of the front speed was utilized to study Eq. (2.61), which was derived by Dresner to approximate the λ-front speed [45]. For this purpose, a proportionality factor K is introduced and defined as

$$K = \frac{v_\lambda \overline{\rho c_p}\,(T_s - T_\lambda)}{\left(x_\lambda^{-1} \int_{T_b}^{T_\lambda} f_S^{-1}(T)\,\mathrm{d}T\right)^{\frac{1}{3.4}}}, \tag{5.2}$$

where v_λ and x_λ are the speed and position of the front, T_s is the heater temperature, and density and specific heat are averaged in the temperature range between T_λ and T_s. In Dresner's formula, which is applicable to He II-He I multiphase cases, the factor K would equal 1 assuming that using averaged properties is a correct assumption. Any deviation from unity would then indicate either the inaccuracy of the assumption or a different multiphase regime (e.g., presence of helium vapour at the heating surface). Computing K at every sensor location with the present data reveals that K depends on the heat flux. Fig. 5.12 shows that K varies from 0 to 3 below 10^5 W/m^2. Above this value, when the vapour phase is stable at the heater, K drops down below 1. In this region, K depends markedly on the front position and varies weakly with the heat flux. Averaging the properties represents no longer a correct assumption as the density lies between the values of vapour

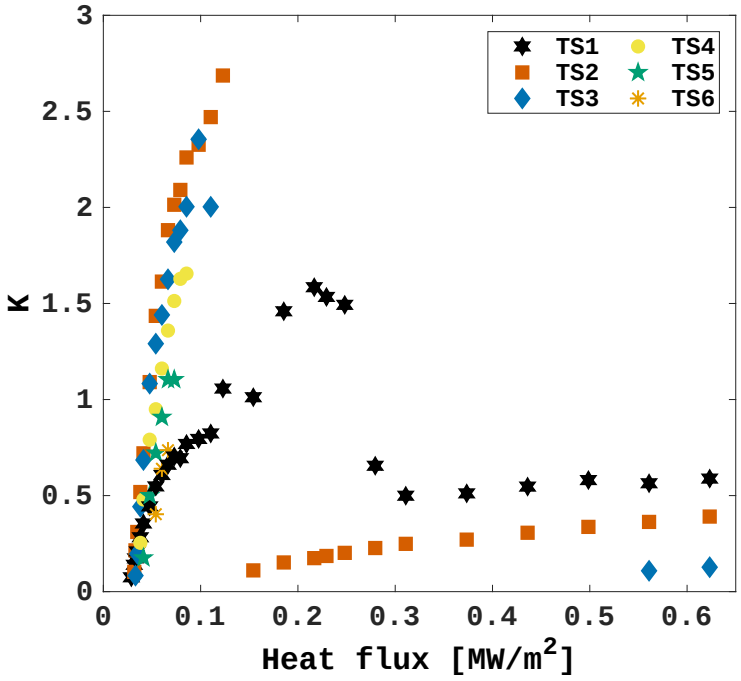

Figure 5.12: Proportionality factor K as a function of the heat flux for different positions of the λ-front.

and He I, decreasing considerably the value of K.

At last, it is interesting to compare the lambda and boiling fronts with each other at the location where the most data is available (i.e., TS1). Fig. 5.13 presents this comparison as a function of the heat flux for both horizontal channels, which are labeled according to their confinement number. In the 0.2 mm thick channel (Fig. 5.13a), three different regions are clearly distinguishable for the λ-front speed. In the first one, the speed increases sharply with the heat flux until around 10^5 W/m^2, where a peak is reached. In the second region, the speed drops at a similar rate down to the value of the first detectable front. Thereafter, the speed becomes weakly proportional to the heat flux. On the other hand, the boiling front travels at a much lower speed and never overcomes 1 cm/s. Its speed increases slowly until 10^5 W/m^2, after which a small drop occurs. Then, the speed rises at the same rate of the λ-front. To sum up, this figure clarifies the mechanism of double front propagation in He II. The λ-front travels at a speed that is proportional to the heat flux until the boiling front reaches its maximum value. As the heat flux increases, the time to achieve the film boiling regime diminishes and the heat diffusion in He II is interrupted sooner. As a result, the He II-He I transformation rate decreases, and thus the He I phase thins. The λ-front speed is then determined by the vapour phase growth, with the two fronts propagating at the same rate.

In the 0.5 mm thick channel (Fig. 5.13b), the boiling front presents similar characteristics. However, only two regions can be distinguished for the λ-front. The first one is comparable to the case of the smaller channel. The second region resembles the third one

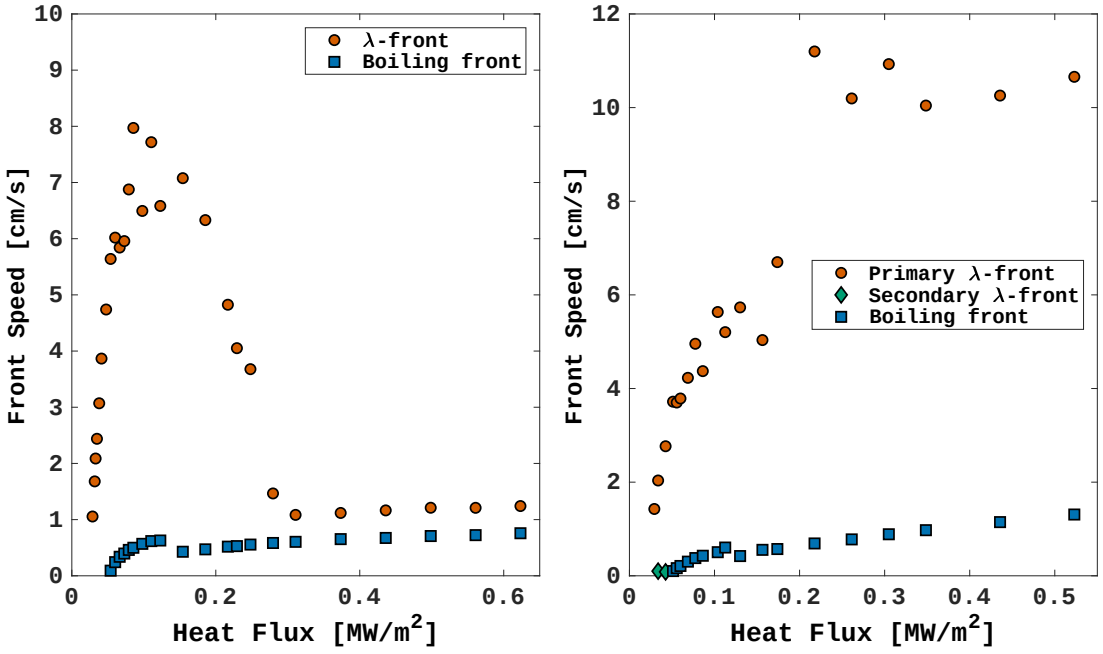

(a) $Co > 0.5$ (b) $Co < 0.5$

Figure 5.13: Speed of the lambda and boiling fronts at 1.5 cm far from the heater as a function of the heat flux applied.

in Fig. 5.13a, where the speed rate looks like the boiling front one. Nevertheless, the speed is greater than in the previous case. The intermediate region characterized by a speed drop is no longer present, which explains the absence of attenuation in the first temperature increment (see Sec. 5.1.1.3). Since the confinement number is lower than the critical value, the vapour and He I phases expand more easily, ensuring a relatively high λ-front speed in the last region. Another difference lies in the number of times the λ-front travels through the same spot. Because of the early peaks detected in multiple tests (see Fig. 5.6), it is possible to identify two λ-fronts. The primary front is the diffusion-driven one, similarly to the smaller channel. The secondary one is associated with speeds in the range of the boiling front. This result confirms that the nature of slow λ-fronts is mainly due to the vapour-He I transformation process, which is also responsible for preventing the λ-front speed to increase with the heat flux for non-confined channels.

5.2 Phase Change Modeling

The numerical modeling of the He II phase transitions in multi-dimensional domains is a rarely approached subject in scientific research. The change in several orders of magnitude of the thermophysical properties between the different phases of helium represents a severe obstacle for the convergence stability of numerical simulations. For this reason, not many sources with regards to this topic can be found in literature. Some authors attempted at simulating one or both phase transitions with different assumptions to simplify the problem. Hama and Shiotsu constructed a two-dimensional model to simulate film boiling on a vertical plate [65]. They assumed the solid surface temperature as uniform, negligible thickness of the vapour film, and steady convection mechanism in the vapour phase. Noda et al. developed a one-dimensional model for forced flow applications using empirical formulae for the friction force and zero heat conduction in the two-phase region [115]. Okamura et al. developed a two-dimensional finite element model to simulate the lambda transition in natural convection [117]. The models implementing also conjugate heat transfer with solids are even scarcer. Mao et al. utilized an adaptive mesh algorithm to resolve the lambda front in one-dimensional cable-in-conduit conductors [102]. They neglected convection effects, gravity, He I heat conduction, and solid heat conduction in the He II region.

In the present study, both the second and first-order phase transitions that helium undergoes when subject to high heat fluxes are dealt with. Taking into account the complexity associated with a double phase transition, it was decided to partly simplify the problem by working just with fixed orthogonal numerical grids. This choice is also dictated by the intention to carry out simulations in multi-dimensions while avoiding the extra computational time that an adaptive mesh code would require to refine high gradient areas. In the first part of this section, the problems related to the lambda transition are tackled, while the second part concerns the He I-vapour transition.

5.2.1 Second-Order Phase Transition

As described in Sec. 2.4, the phase transition between He II and He I is of second-order and hence it is not associated with latent heat. Therefore, the change from one phase to the other occurs instantaneously once T_λ is reached. The superfluid volume fraction α_{II}, thus, takes the form of a Boolean parameter that defines exactly the presence of either He II or another phase. Moreover, since the density is continuous across the lambda transition (see Fig. 2.5), no additional tension force is required at the interface. The critical subject about the lambda transition pertains, instead, to the discontinuity of the specific heat and thermal conductivity at the λ-point. In this subsection, a novel algorithm designed to face this issue in fixed grids is formulated and discussed. The algorithm is constructed specifically for the finite volume method, in alignment with the structure of *heliumChtFoam*.

5.2.1.1 Effective Thermal Conductivity Correction Algorithm

As seen in Sec. 4.2.2, the effective thermal conductivity of He II k_{eff} depends also on the temperature gradient (see Eq. (4.20)). This dependency is valid as long as the local temperature is below the λ-point. If the second-order phase transition occurs though, a front separating the two phases appears in the computational domain. Due to the considerable difference in the thermal conductivity between the two phases (compare Figs. 2.7b and 4.18b), the temperature gradient changes drastically at the location of the lambda front. The gradient calculation in the mesh cells located across the front carries an intrinsic error due to the way the gradient is numerically approximated. The source of the error can be identified with the linear interpolation of the temperature at the face separating the cells, which will be described later in this section. In this case, a correction of k_{eff} is needed to take into account this error.

The approach presented here is based on the interfacial heat transfer between He I and He II at the lambda front. The main goal is to identify the actual location of the front in order to correct the temperature gradient field and consequently k_{eff}. As a reference for the equations, let us consider the case displayed in Fig. 5.14, in which the lambda front is situated in an arbitrary location between the centers of two adjacent cells in the computational domain. The first step is to define the heat flux q_{II} through the He II phase from Eq. (2.44):

$$q_{II} = -\left(\frac{1}{f(T,p)}\frac{T_\lambda - T_P}{\gamma\|\mathbf{d}\|}\right)^{\frac{1}{n}}, \tag{5.3}$$

where $\mathbf{d}$ is the distance vector between the two cell centers, and γ is a coefficient whose value is between 0 and 1. As a reminder from Sec. 3.2, the subscript P refers to the "owner" cell. Let us consider a fictitious heat flux $q_{II,fict}$ between the cell centers that does not take into account the change in temperature steepness across the front like it would be computed without correction:

$$q_{II,fict} = -\left(\frac{1}{f(T,p)}\frac{T_N - T_P}{\|\mathbf{d}\|}\right)^{\frac{1}{n}}, \tag{5.4}$$

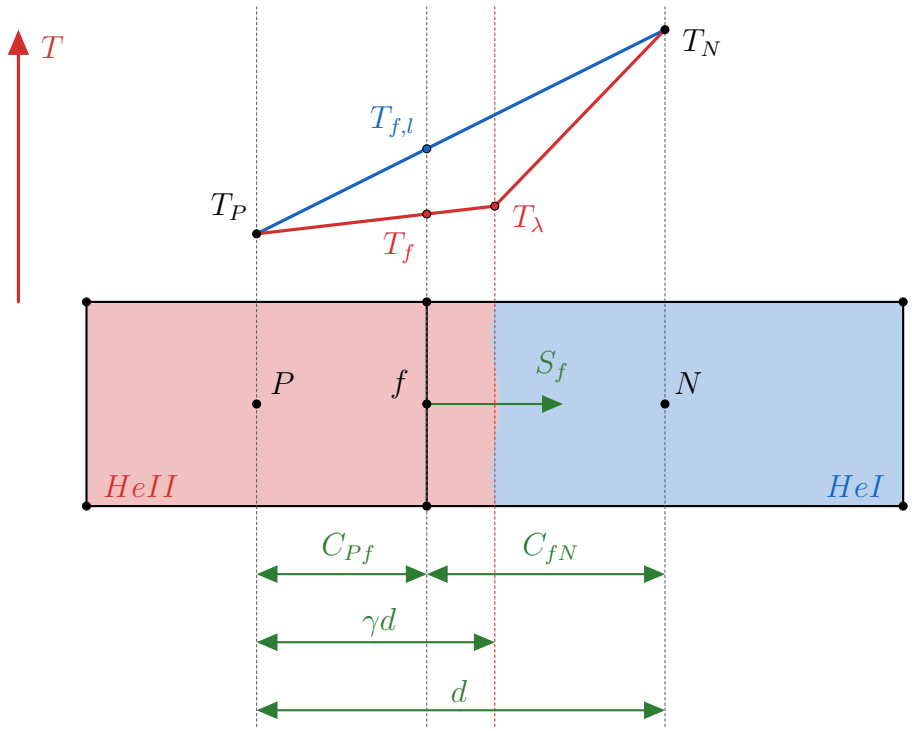

Figure 5.14: Schematic representation of the lambda front in a two-dimensional grid.

where the subscript N refers to the center of the neighbour cell. The heat flux q_{II} can be expressed in function of $q_{II,fict}$ as

$$q_{II} = \gamma^{-\frac{1}{n}} q_{II,fict} \left(\frac{T_\lambda - T_P}{T_N - T_P} \right)^{\frac{1}{n}}, \tag{5.5}$$

which has to be equal to the heat flux through the He I phase q_I, defined as

$$q_I = -k_I \frac{T_\lambda - T_N}{(1-\gamma)\,\|\mathbf{d}\|}, \tag{5.6}$$

where k_I is the thermal conductivity of He I. Equating (5.5) and (5.6) yields

$$\frac{1-\gamma}{\gamma^{\frac{1}{n}}} = \frac{k_I}{q_{II,fict}\|\mathbf{d}\|} (T_N - T_\lambda) \left(\frac{T_N - T_P}{T_\lambda - T_P} \right)^{\frac{1}{n}}. \tag{5.7}$$

Eq. (5.7) is a nonlinear equation that can be solved numerically for the parameter γ. A simplified version of this approach was formulated by Noda et al. [114], who obtained an expression for $n = 3$ suitable for the finite difference method.

In order to correct the temperature gradient, it is useful to recall how the gradient field is computed numerically. From Eq. (3.21) it follows that the gradient calculation requires the value of the flux through the cell face. Eq. (3.22) tells us that the value of the temperature at the face center $T_{f,l}$ can be computed via linear interpolation between the center values of the cells sharing the face:

$$T_{f,l} = \lambda_{f,l} T_P + (1 - \lambda_{f,l})\, T_N, \tag{5.8}$$

where the subscript l refers to the way the face center value is calculated (i.e., linearly interpolated), and the coefficient $\lambda_{f,l}$ is the geometric factor computed with Eq. (3.23). Therefore, the temperature at the face center has to be modified to properly calculate the flux. For this purpose, let us make a further adjustment to Eq. (5.7). Since the gradients use the linear interpolation scheme, the heat flux $q_{II,fict}$ can be computed as well as

$$q_{II,fict} = -k_{eff,fict} \frac{T_{f,l} - T_P}{\|\mathbf{C}_{Pf}\|}, \tag{5.9}$$

where $k_{eff,fict}$ is calculated using the temperature gradient before the application of the correction algorithm. Substituting Eq. (5.9) into (5.7) yields

$$\frac{1-\gamma}{\gamma^{\frac{1}{n}}} = \begin{cases} \dfrac{\|\mathbf{C}_{Pf}\|}{\|\mathbf{d}\|} \dfrac{k_I}{k_{eff,fict}} \dfrac{T_N - T_\lambda}{T_{f,l} - T_P} \left(\dfrac{T_N - T_P}{T_\lambda - T_P} \right)^{\frac{1}{n}}, & \text{for } T_P < T_\lambda < T_N, \quad (5.10a) \\ \dfrac{\|\mathbf{C}_{fN}\|}{\|\mathbf{d}\|} \dfrac{k_I}{k_{eff,fict}} \dfrac{T_P - T_\lambda}{T_{f,l} - T_N} \left(\dfrac{T_N - T_P}{T_N - T_\lambda} \right)^{\frac{1}{n}}, & \text{for } T_N < T_\lambda < T_P. \quad (5.10b) \end{cases}$$

Eq. (5.10a) refers to the case of the example in Fig. 5.14, whereas Eq. (5.10b) refers to the case in which the neighbour cell is in He II. These equations are solved iteratively using the Newton-Raphson method for nonlinear equations [127]. The coefficient γ ranges always between 0 and 1 for any value of the RHS of Eq. (5.10). The convergence of the Newton-Raphson method applied to Eq. (5.10) is always guaranteed for any value of the RHS and any arbitrary positive initial guess. The tolerance selected for the method is 10^{-5}, which is also chosen as the initial guess value. Moreover, due to the structure of Eq. (5.10), the method converges in few iterations regardless of the sought value of γ. These statements are demonstrated via calculus analysis, which can be found in Annex B.4.

Once obtained γ, the exact location of the lambda front is known too, and it is possible to compute the corrected face center temperature. The idea consists in interpolating between temperature values within the liquid phase that crosses the face location, so that the numerical approximation involves just a region where the gradient is pretty much constant. Therefore, Eqs. (5.8) and (3.23) must be updated. For the case in which $T_P < T_\lambda < T_N$ (see Fig. 5.14), the updated factors S_f that determine the new λ_f read:

$$S_{f,P} = \begin{cases} \|\mathbf{S}_f \cdot \mathbf{C}_{Pf}\|, & \text{for } \gamma\|\mathbf{d}\| > \|\mathbf{C}_{Pf}\|, \quad (5.11a) \\ \|\mathbf{S}_f \cdot (\mathbf{C}_{Pf} - \gamma\mathbf{d})\|, & \text{for } \gamma\|\mathbf{d}\| < \|\mathbf{C}_{Pf}\|, \quad (5.11b) \end{cases}$$

and

$$S_{f,N} = \begin{cases} \|\mathbf{S}_f \cdot (\gamma\mathbf{d} - \mathbf{C}_{Pf})\|, & \text{for } \gamma\|\mathbf{d}\| > \|\mathbf{C}_{Pf}\|, \quad (5.12a) \\ \|\mathbf{S}_f \cdot \mathbf{C}_{fN}\|, & \text{for } \gamma\|\mathbf{d}\| < \|\mathbf{C}_{Pf}\|. \quad (5.12b) \end{cases}$$

The face center temperature is finally computed as

$$T_f = \begin{cases} \lambda_f T_P + (1-\lambda_f) T_\lambda, & \text{for } \gamma\|\mathbf{d}\| > |\mathbf{C}_{Pf}|, \quad (5.13a) \\ \lambda_f T_\lambda + (1-\lambda_f) T_N, & \text{for } \gamma\|\mathbf{d}\| < |\mathbf{C}_{Pf}|. \quad (5.13b) \end{cases}$$

It is easily verifiable that, for $\gamma\|\mathbf{d}\|$ that tends to $\|\mathbf{c}_{Pf}\|$, T_f tends to T_λ from both sides of the face. Similarly it is done for the case in which $T_N < T_\lambda < T_P$. At last, the temperature gradient is updated using Eq. (3.21), and the He II properties (Eqs. (4.16) and (4.20)) are corrected accordingly.

5.2.1.2 Specific Heat Cell Face Interpolation

Another characteristic of the lambda transition is the discontinuity of the specific heat capacity at the λ-point (see Fig. 2.6b). As known, the specific heat appears as part of the thermal diffusivity in the energy equation. The flux associated with the diffusion term in the energy equation requires the value of the diffusivity at the face shared by two adjacent cells (see Eq. (3.25)). The face value is computed via linear interpolation between the cell centroids value. Let us consider again the case in Fig. 5.14. If the lambda front is located between the two cells, the interpolation of the specific heat at the face shared by those cells would result in an incorrect value due to the lambda discontinuity. Depending on the location of the front, interpolating between two values before and beyond the "λ" diverging peak may greatly underestimate the face value. Therefore, the specific heat interpolation must be corrected in those faces. Since these faces are the same ones treated in the previous subsection, the correction is simply achieved by using the algorithm presented before. Once the face temperature T_f (Eq. (5.13)) is updated, the specific heat is re-computed as a function of T_f.

Since the main variable in the energy equation herein presented is the enthalpy, the temperature must be derived consequently by means of the specific heat capacity. In OpenFOAM®, a Newton-based iterative algorithm is utilized for this purpose. However, the convergence of this method is strongly affected by the temperature dependence of the specific heat. In the case of He II, the algorithm diverges once T_λ is reached because of the specific heat discontinuity. Therefore, this algorithm was substituted with a method that interpolates values from an enthalpy-temperature table.

5.2.2 First-Order Phase Transition

The first-order phase transition between subcooled He I and helium vapour is an ordinary phase change associated with boiling/condensation. As such, it involves a latent heat of vaporization at the saturation point and interface phenomena due to high gradients in density across the two media. As it was preannounced at the end of Sec. 3.2.2, the present model deals with this event through an enthalpy-based method for fixed grids [165], [163]. The usage of the enthalpy as the variable for the energy equation allows to take on convection-diffusion problems even at saturation conditions.

5.2.2.1 Thermophysical Properties Calculation

In isothermal problems, the common approach for the calculation of the thermophysical properties of a mixture consists of evaluating the portion of a volume occupied by a phase

in order to weigh the property value among all the phases present in that volume. This requires the implicit solution of an additional transport equation to obtain the evolution of the mixture front over time. The problem under investigation, instead, involves unsteady thermodynamic conditions of the same fluid, which can be advantageously exploited to derive volume and mass fractions. Rather than tracking the front location, thus, *heliumChtFoam* computes explicitly the volume fraction α_I of the vapour-He I mixture as a function of the density

$$\alpha_I = \min\left[\max\left(\frac{\rho - \rho_v}{\rho_l - \rho_v}, 0\right), 1\right], \tag{5.14}$$

where the subscripts v and l stand for the saturated conditions of vapour and liquid respectively. The total fluid density ρ is computed through the empirical compressibility factor Z:

$$\rho = \frac{p}{Z(h)RT}, \tag{5.15}$$

where R is the specific gas constant. The compressibility factor Z is extracted as a function of the enthalpy from the database HEPAK© [68]. Since the two phases can coexist at saturation, α_I ranges from 0 (saturated vapour) to 1 (saturated liquid) depending on the vicinity to the saturated states. However, the total density of the fluid ρ does not always lie between the saturation values. The "min" and "max" functions are then necessary to ensure that α_I is bounded between physical quantities. The mass fraction Y_I is simply calculated as

$$Y_I = \min\left[\max\left(\frac{h - h_v}{h_l - h_v}, 0\right), 1\right]. \tag{5.16}$$

The temperature for $h_l \leq h \leq h_v$ is fixed to the saturation value T_{sat}.

The thermophysical properties at T_{sat} are weighed between the values at saturation as a function of α_I and Y_I. In particular, the transport properties (i.e., viscosity and thermal conductivity) are computed as

$$\mu_{sat} = \alpha_I \mu_l + (1 - \alpha_I)\, \mu_v, \tag{5.17a}$$

$$k_{sat} = \alpha_I k_l + (1 - \alpha_I)\, k_v, \tag{5.17b}$$

while the specific heat capacity as

$$c_{p,sat} = Y_I c_{p,l} + (1 - Y_I)\, c_{p,v}. \tag{5.18}$$

Since α_I and Y_I are derived explicitly, the code is provided with pre-weighed properties that are interpolated at run time depending on the local enthalpy. At $T \neq T_{sat}$, the properties take the values corresponding to the only phase present in the control volume.

5.2.2.2 Surface Tension

Molecules in bulk liquids are subject to cohesion forces that are evenly distributed and cancel each other, resulting in a zero net force. If a liquid is in contact with gas though, the liquid molecules at the interface are attracted by the cohesion force towards the bulk fluid only. The adhesion force acting between molecules of a different phase is usually much lower than the cohesion force, leaving a net inward force that tends to contract the liquid. Because of the liquid contraction, a pressure jump arises across the interface. The surface, thus, experiences a tension force $\mathbf{F}_\sigma$ that is proportional to the pressure jump. In this work, the continuum surface force (CSF) model proposed by Brackbill et al. [22] is adopted for the calculation of $\mathbf{F}_\sigma$. Under the assumption of a constant surface tension coefficient σ, the CSF model estimates the pressure jump as

$$\Delta p = \sigma\kappa, \tag{5.19}$$

where κ is the curvature of the interface and is defined as the divergence of the interface unit normal vector:

$$\kappa = -\boldsymbol{\nabla} \cdot \left(\frac{\boldsymbol{\nabla}\alpha_I}{\|\boldsymbol{\nabla}\alpha_I\|} \right). \tag{5.20}$$

The surface tension force is then

$$\mathbf{F}_\sigma = \frac{\rho}{\overline{\rho}_{sat}} \sigma\kappa\boldsymbol{\nabla}\alpha_I, \tag{5.21}$$

where $\overline{\rho}_{sat}$ is the density averaged between the liquid and vapour saturation values. The condition $\mathbf{F}_\sigma \neq 0$ is satisfied just on the surface, where the volume fraction varies depending on the enthalpy. Moreover, the CSF model interprets the surface tension as a continuous volumetric force acting across the entire interface proportionally to the local total density. This proportionality allows thinning the interface without further numerical treatment of the front.

5.2.3 Multiphase Governing Equations

The governing equations presented in Sec. 4.2.2 must be modified to account for multiphase phenomena. The continuity equation (Eq. (4.17)) remains essentially unchanged. The momentum equation (Eq. (4.15)) must include the surface tension force (Eq. (5.21)). Moreover, the parameter M must be updated with the corrected temperature gradient $\boldsymbol{\nabla}T^*$ (see Sec. 5.2.1.1), where * identifies the corrected field. At T_λ, the superfluid terms in the momentum equation simply vanish as they all are proportional to the superfluid density, which becomes zero at the lambda transition. The energy equation (Eq. (4.18)) must comprise the conductive heat flux of He I and helium vapour too. Eq. (4.19) becomes then

$$\mathbf{q} = \frac{k_{He}}{c_p^*} \boldsymbol{\nabla} h, \tag{5.22}$$

where c_p^* is the corrected specific heat capacity (see Sec. 5.2.1.2) and the thermal conductivity of helium k_{He} is defined as

$$k_{He} = \begin{cases} k_{eff}^*, & \text{for } T < T_\lambda, \quad (5.23a) \\ k_I, & \text{for } T_\lambda \leq T < T_{sat}, \quad (5.23b) \\ k_{sat}, & \text{for } T = T_{sat}, \quad (5.23c) \\ k_{vap}, & \text{for } T > T_{sat}, \quad (5.23d) \end{cases}$$

where k_I and k_{vap} are the thermal conductivities of subcooled He I and superheated helium vapour respectively, whereas k_{sat} is computed with Eq. (5.17b). The effective thermal conductivity of He II k_{eff}^* is updated with the corrected temperature gradient field $\boldsymbol{\nabla} T^*$ (see Sec. 5.2.1.1). The other thermophysical properties are set up similarly to Eq. (5.23).

Boundary Conditions Within the temperature range of helium vapour at ambient pressure, the fluid and solids are fully in thermal contact, and the Kapitza heat transfer mechanism is negligible. Furthermore, a viscous fluid without superfluid traits such as He I does not experience wall slip on solid surfaces. Nevertheless, the boundary conditions implemented in *heliumChtFoam* that are proper of He II do not require any modification. More specifically, Eq. (4.22) allows the Kapitza resistance to fade away as the solid surface temperature gradually increases. This fade-out process starts when the Kapitza conductance for high differences in temperature (see Eq. (2.54b)) overcomes the one for low differences (see Eq. (2.54a)), which does not depend on the solid temperature. As the heater temperature increases because of the volumetric heat generation, the Kapitza resistance diminishes until the resulting temperature jump with helium is negligible. By the time the helium in contact with the heater turns into vapour, a perfect thermal contact between the two media is achieved. The superfluid wall slip simply ceases to exist at T_λ, when the superfluid density becomes zero (see Eq. (4.23)) and hence a no-slip condition is imposed at the boundary. Moreover, the parameter M, which is also present in the superfluid slip equation, is automatically updated with the corrected temperature gradient field, resulting in the right value also at the boundaries where the lambda front intersects a wall. Consequently, the boundary conditions presented in Sec. 4.2.3 adjust accordingly to represent the appropriate circumstances even in presence of phase changes.

Solution Algorithm The updated governing equations for multiphase helium are solved in a novel solution algorithm for transient conjugate heat transfer problems in multi-dimensional domains. Fig. 5.15 represents the flow chart of *heliumChtFoam* with the modifications implemented for superfluid helium and its phase transitions. With respect to the ordinary PIMPLE algorithm described in Sec. 3.2, the modified and added steps are highlighted and referenced in the legend of Fig. 5.15. The solution algorithm starts by updating the current time and variables from the previous time step. The first outer loop iteration is then initiated by computing explicitly the superfluid and normal volume fractions. For the first iteration, the continuity equation is solved to compute the new

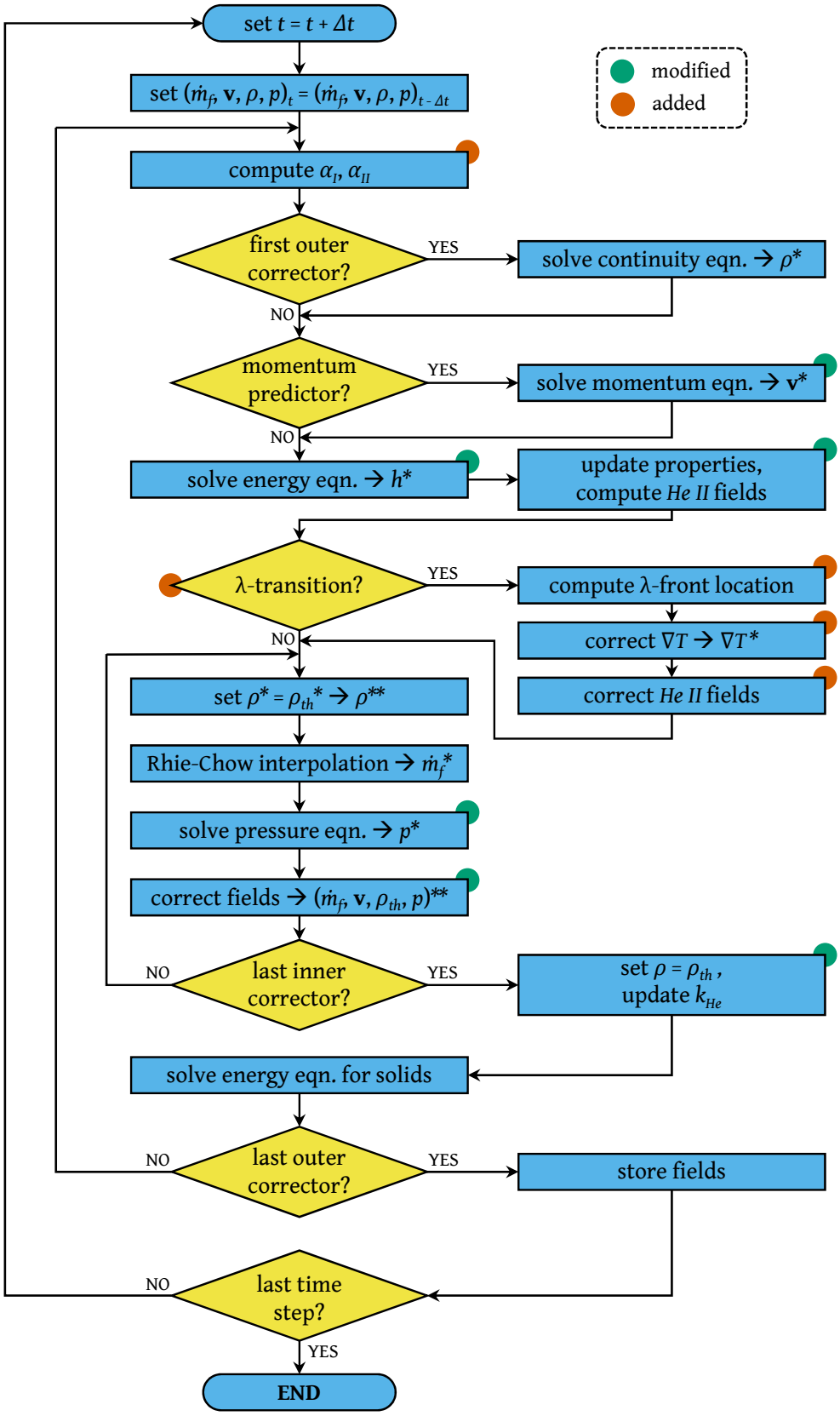

Figure 5.15: *heliumChtFoam* PIMPLE algorithm.

density field. If the momentum predictor step is requested, the momentum equation is solved before the pressure correction loop. In the present work, the latter step is skipped as the physical phenomena involved are not advection driven. The energy equation is then solved and the resulting enthalpy is used to update the thermophysical properties and the superfluid helium parameters. At this point, if the temperature reaches the λ-point anywhere in the domain, the correction algorithm presented in Sec. 5.2.1.1 is activated in order to identify the exact location of the lambda front. As described previously, the front location is utilized to correct the temperature gradient and, consequently, the superfluid fields k^*_{eff} and M^*. If He II does not undergo λ-transition, the correction algorithm is skipped and the inner loop is initiated. This loop is the classic pressure correction loop, where the pressure and momentum equations are solved iteratively until attainment of velocity and pressure fields that satisfy the mass conservation. The subscript th in ρ_{th} serves to differentiate the thermodynamic density computed as a function of the enthalpy (Eq. (5.15)) from the one obtained by solving the continuity equation. After the last corrector iteration, the final density field is stored and the thermal conductivity field k_{He} is assembled. A diffusion equation (Eq. (4.25)) is then solved sequentially for each solid part present in the domain. The solution of the diffusion equations marks the end of an outer loop iteration, which, in the case of a PIMPLE algorithm, is repeated to facilitate the convergence stability and strengthen the coupling between fluids and solids. After the last outer loop, the fields are stored and the time marches forward. The whole sequence is repeated until steady state.

5.3 Numerical Case Study

The algorithm just presented was validated against some experimental data of this study. Due to the diverse phenomena occurring in the experiments, it was decided to simplify partially the problem by taking into account only the thicker channel at moderate downward and horizontal heat fluxes. Avoiding the thinner channel and the upward orientation allows to neglect respectively confinement effects and the prediction of nucleation sites, which usually are artificially induced via suitable computational domains that resemble the imperfections of the heating surface. Applying moderate heat fluxes is justified by the need for stability of the solution algorithm, which was observed diverging across the phase transitions above a certain heat flux because of the abrupt change in thermophysical properties of the different helium phases.

Since the thermal time constant of helium vapour is comparable to the one of the components of the experimental setup, it is essential for predicting the correct thermal behaviour to include in the computation the solid parts surrounding the helium slab. However, considering the size of the steel plates with respect to the channel, a three-dimensional model of the setup would require a substantial computational effort and long simulations. Therefore, despite the algorithm can be applied to three-dimensional problems, the phase change modules were tested in a two-dimensional domain that

represents the cross-section of the setup at its centerline (i.e., 2.5 cm from the steel side flanges). The two-dimensional assumption is legitimized by the high aspect ratio of the channel.

To strengthen the coupling between the solid and helium solutions of the segregated-like algorithm and withstand the strong density variations associated with the first-order phase transition, the PIMPLE algorithm (Fig. 5.15) is chosen here instead of the simple PISO loop. The setting comprises three inner-loop and ten outer-loop iterations. Like in Ch. 4, the transient problem was solved using the CNS with a blending factor of 0.9. Both the divergence and gradient terms were discretized with the CDS, and the interpolated values between cell centroids were computed linearly. The linear systems of algebraic equations were solved with different methods depending on the unknown variable [110]: preconditioned conjugate gradient (PCG) method for the continuity equation; generalized geometric-algebraic multi-grid (GAMG) solver for the pressure equation; Gauss-Seidel for the momentum and energy equations. The solid diffusion equations were solved with the PCG method for symmetric matrices.

5.3.1 Mesh Tests

The mesh utilized for the simulations is a two-dimensional structured non-uniform grid with fully orthogonal control volumes. Since the mesh is fixed, it is of interest to investigate how the simulated steady-state location of the λ-front varies with the grid size. The domain created for these tests is shown in Fig. 5.16 with the real relative proportions of the sub-domains. The geometrical model includes both stainless steel plates, the G10 heater plug, the Manganin® heater, and the helium channel. The thermophysical properties of these materials were taken from METALPAK© [107] and CryoComp© [39]. The initial temperature

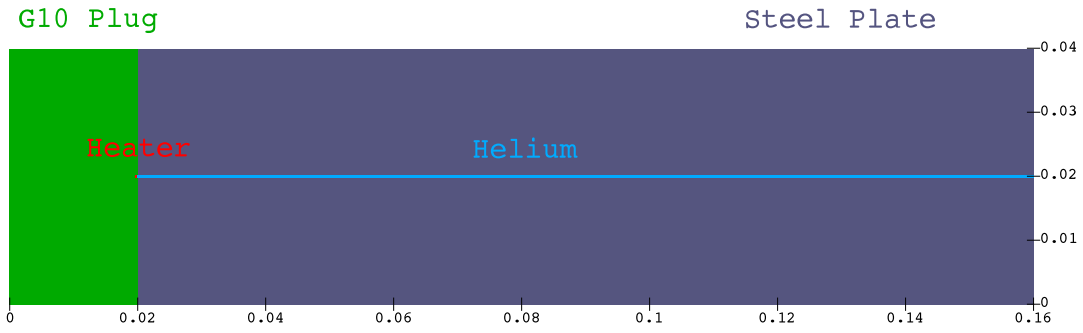

Figure 5.16: Computational domain for the phase transitions simulations. The length coordinates are in meters.

of the entire system was set to 2.15 K, while the pressure of the fluid was set to the atmospheric one. As for the boundary conditions, at the walls the pressure is determined by the fixed flux condition, whereas the velocity is either computed through the superfluid slip condition for He II or zero for the other helium phases. The temperature at the bath and all external solid walls is fixed to the initial value. At the interfaces between helium

and solids, the Kapitza condition is applied. As explained earlier in this chapter, the resistance tends naturally to zero as the temperature of the solid increases. Therefore, helium vapour results in perfect thermal contact with the solid. At relatively high heat fluxes, the Kapitza resistance between solids (e.g., heater and plug) is negligible and hence neglected. A volumetric heat generation was applied in the heater domain and equivalent to 5 kW/m^2 at the interface with the helium channel. An adaptive time step was used to ensure that the Courant number was always below the unit. The latter choice is particularly helpful in multiphase problems involving stagnant fluids as it shortens the time step only when needed, that is, in case a phase change associated with high variations in density occurs. In this case, a large time step is maintained as long as He II is the only fluid present in the channel. When vapour is generated, the significant density change causes a velocity increment, which shortens the time step to stabilize the computation.

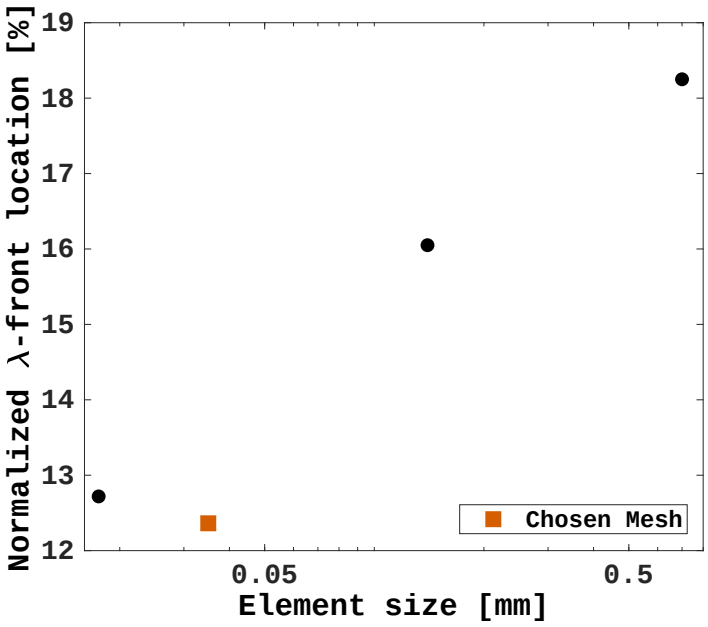

Figure 5.17: Normalized λ-front position with respect to the channel length for grids of different cell longitudinal sizes.

With the exception of the heater, the grids of the solid components of the domain are all non-uniform with increasing cell size from the helium interface to the external boundaries, where the cells get as large as 5 mm for the steel plates and 2 mm for the G10 plug. Close to the helium slab, the cell size is 20 µm. The heater domain is constituted by uniform cells of around 23 µm. The channel thickness is subdivided into 11 cells, while the number of cells along its length is the varying parameter of this study. Four different grids were tested at the aforementioned conditions. Fig. 5.17 shows the cell size dependence of the λ-front position at steady state as a normalized value with respect to the channel length. Despite the finest grid is forty times smaller than the coarsest one, the front position varies only within few percentage points, indicating that the correction algorithm for fixed grids (see 5.2.1.1) performs adequately.

The cell size chosen for the following simulations, which is indicated in Fig. 5.17, seemed to be a good compromise between accuracy and computational cost. To further decrease the numerical effort, it was decided to split the channel domain into two parts. The half next to the heater is discretized with the cell size chosen in this section, while the other half is non-uniform with increasing cell size towards the bath. Moreover, the channel thickness is split into 30 non-uniform cells. The final mesh is constituted by more than 67×10^3 hexahedra in the helium domain and more than 3×10^5 hexahedra in total. A close-up picture of the mesh refinement is shown in Fig. B.5 in Annex B.2.

5.3.2 Model Validation

Because of the two-dimensional assumption, some components of the setup such as the HTS current leads and the steel side flanges had to be disregarded. The computational domain misses then some heat leak paths that might affect the overall temperature distribution in long transients. Therefore, it was decided to replace the volumetric heat generation in the

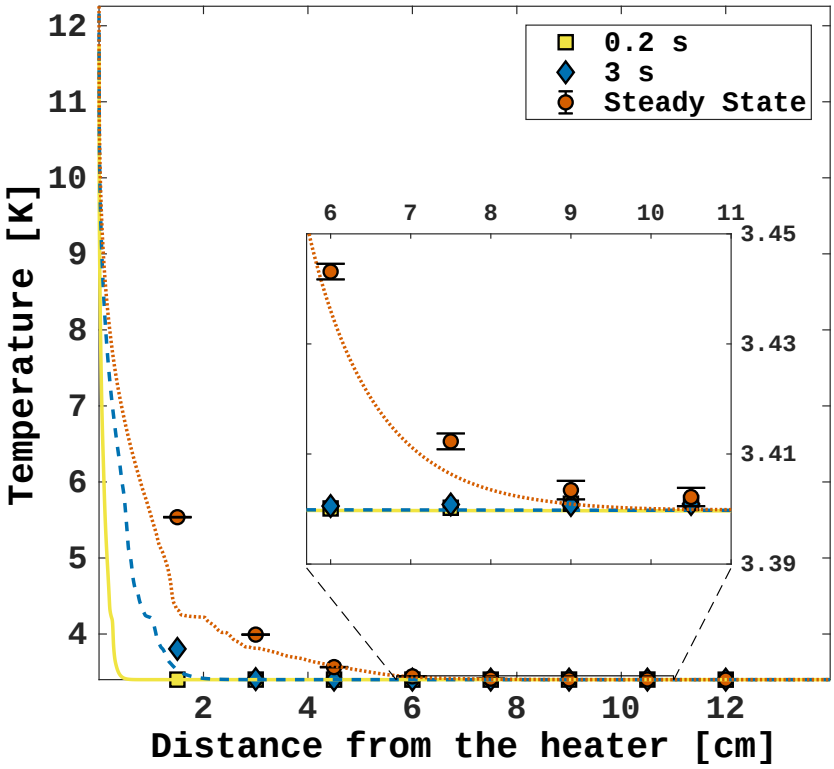

Figure 5.18: Transient temperature profiles comparison between *heliumChtFoam* and data from an experiment in the downward vertical 0.5 mm thick channel at a bath temperature $T_b = 3.4$ K and the heater at 13.4 K.

heater with a fixed temperature boundary condition at the interface between the G10 plug and the heater. The driving source is thus this temperature, which is taken from the value measured at steady state by the sensor installed in the plug. As the thermal time constant of the heater is very low, fixing the temperature of the heater to its peak value since the beginning of the transient is a reasonable assumption. All the simulation results presented

in this section use such boundary condition settings and the mesh chosen in the previous sub-section.

Before simulating the double phase change, it is useful to focus at first on the first-order phase transition only. For this purpose, an experiment was conducted in the vertical 0.5 mm thick channel with the helium bath above the λ-point (see Fig. A.12 in Annex A.1). In this experiment, the heater reaches a temperature of 13.4 K, while the bath is maintained at 3.4 K. Fig. 5.18 shows the comparison between the simulated temperature profiles and data. The temperature rises sharply next to the heater and reaches almost instantaneously the peak value, which is slightly lower than the heater temperature for two reasons: the profile is probed along the interface with the steel plate that houses the sensors, where the temperature is less than the centerline of the channel; the fixed temperature is imposed behind the heater. The increase is so abrupt that any effect of the latent heat of vaporization is barely visible at the beginning of the transient. The boiling front advances slowly and, as it moves downstream, a plateau at the saturation temperature arises. Eventually, the front stops just below the location of TS1. Although the

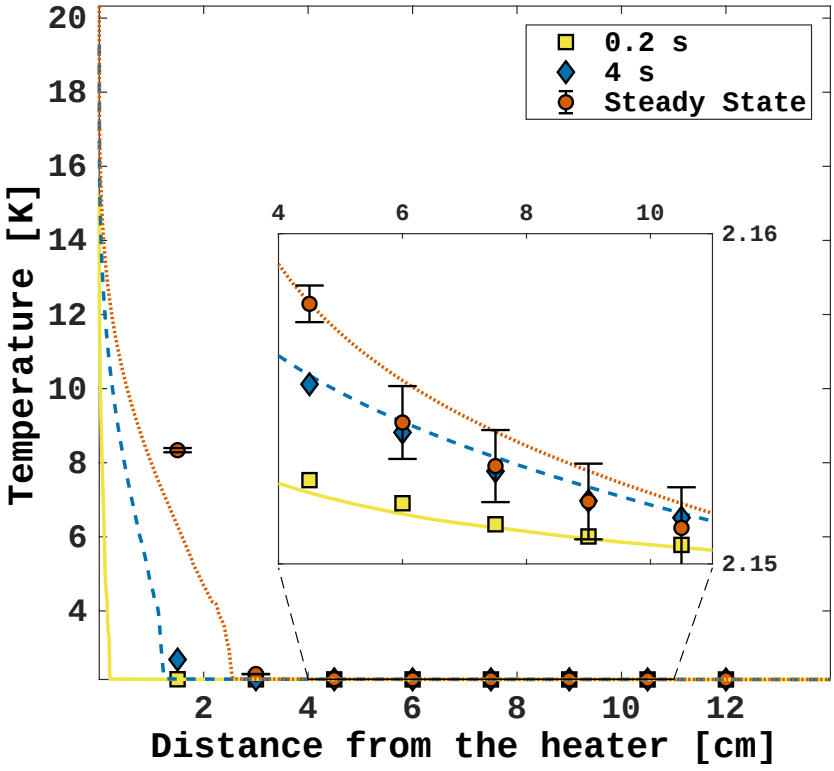

Figure 5.19: Transient temperature profiles comparison between *heliumChtFoam* and data from an experiment in the downward vertical 0.5 mm thick channel at a bath temperature $T_b = 2.15$ K and the heater at 21.6 K.

temperature profile achieves the steady state after 50 s, the considerable gradient nearby the heater persists. The inset in Fig. 5.18 zooms in on the zone far from the heating surface, where the gradient is much lower. Although the simulated profile underestimates the temperature increment in helium vapour, it predicts satisfactorily the overall distribution

with a relative error of 11.3 %.

A similar experiment was carried out in He II, with the bath at 2.15 K and the heater reaching 21.6 K at steady state (see Fig. A.13 in Annex A.1). The comparison with *heliumChtFoam* is displayed in Fig. 5.19. The temperature rises immediately above the saturation and lambda points. The resulting profiles share some features with the previous case. The temperature gradient is very high close to the heater, while it drops significantly beyond the λ-front. Both fronts develop slowly until a stable configuration is reached after 50 s. However, the plateau at the boiling point is almost absent in this case, indicating that the presence of the λ-front thins the boiling front. The inset shows a good agreement

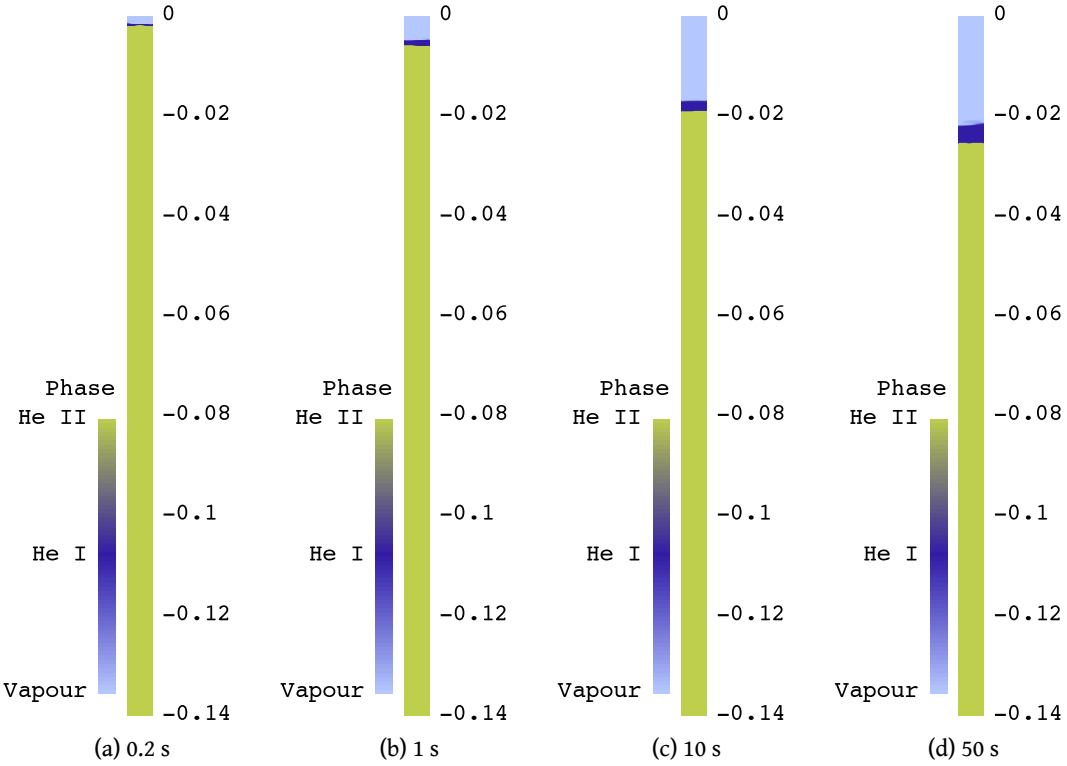

Figure 5.20: Helium three-phase evolution in the downward vertical 0.5 mm thick channel at a bath temperature $T_b = 2.15$ K and the heater at 21.6 K. The length coordinates are in meters.

with the data downstream in the channel. The simulation underestimates once again the steady-state profile. Considering the temperature measured by TS1 and TS2, the λ-front must lie between these sensors, indicating an acceptable estimation of its position by the model. Fig. 5.20 shows the volume fraction distribution in the channel at four moments of the simulation. The channel was magnified ten times in its thickness to favour a better visualization of the results in post-processing. It is clear how the vapour phase arises quickly at the beginning of the transient and expands downstream. The He I phase thickens in time but constitutes always a small portion of the channel between the vapour and He II phases. This was already observed in the experimental results, where a fast onset of film

boiling appeared to reduce the He II-He I transformation rate, limiting then the He I phase portion.

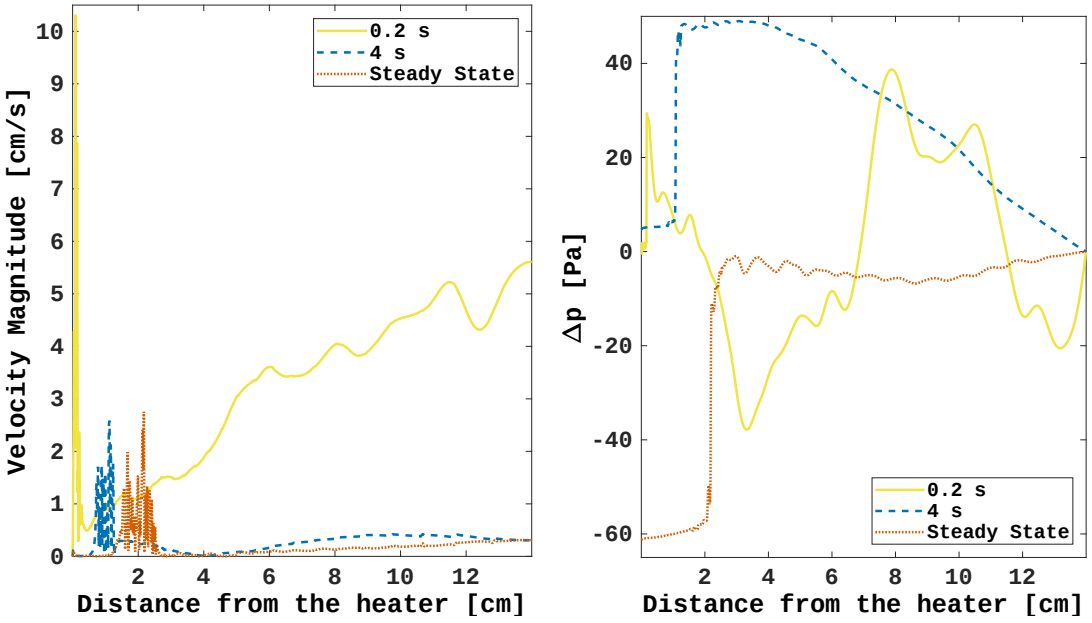

(a) Velocity Magnitude (b) Pressure Difference

Figure 5.21: Simulated velocity and pressure profiles at the centerline of the downward vertical 0.5 mm thick channel at a bath temperature $T_b = 2.15$ K and the heater at 21.6 K.

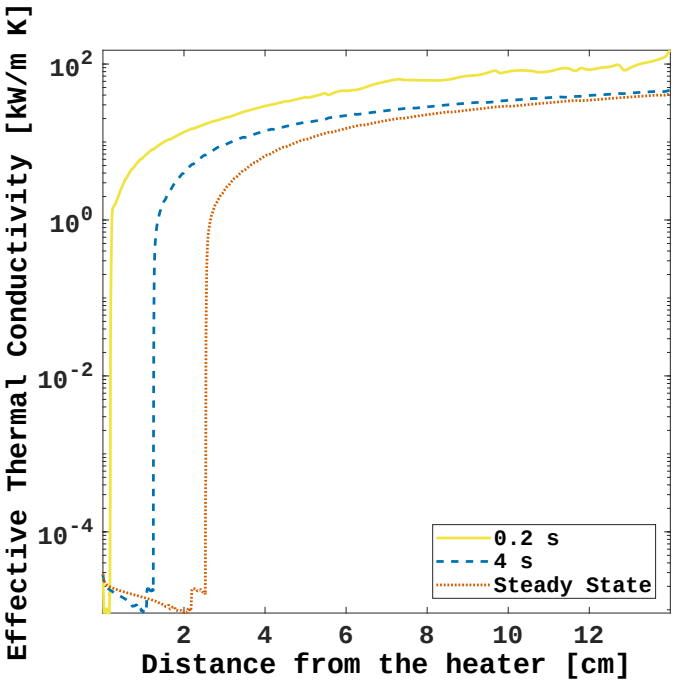

Figure 5.22: Simulated thermal conductivity at the centerline of the downward vertical 0.5 mm thick channel at a bath temperature $T_b = 2.15$ K and the heater at 21.6 K.

It is interesting to plot the velocity magnitude and pressure at the centerline of the channel (Fig. 5.21). Fig. 5.21a shows that the velocity reaches a peak as soon as the temperature is prescribed at the heating wall because of the fast expansion of the vapour. Beyond the two fronts, the velocity is one order of magnitude lower than the peak and increases weakly towards the bath. Later in the transient, the velocity drops in the whole channel, although some peaks are still present around the boiling front (see also Fig. B.8a), where the surface tension forces act. In the rest of the channel, the velocity remains low below half a centimeter per second. The pressure difference with respect to the atmospheric value is displayed in Fig. 5.21b. At the beginning of the transient, the pressure drop is irregular with no major variations. As the vapour phase expands, the boiling front settles and a pressure drop across it becomes evident (see also Fig. B.8b). This pressure jump is predicted by Eq. (5.19) and caused by the surface tension forces acting on the interface between He I and vapour. Since the fluid is free to flow at the bath boundary, the pressure decreases as the vapour phase grows.

Fig. 5.22 shows the thermal conductivity (Eq. (5.23)) of the fluid in the same simulation as above. The change of several orders of magnitude within the same substance is

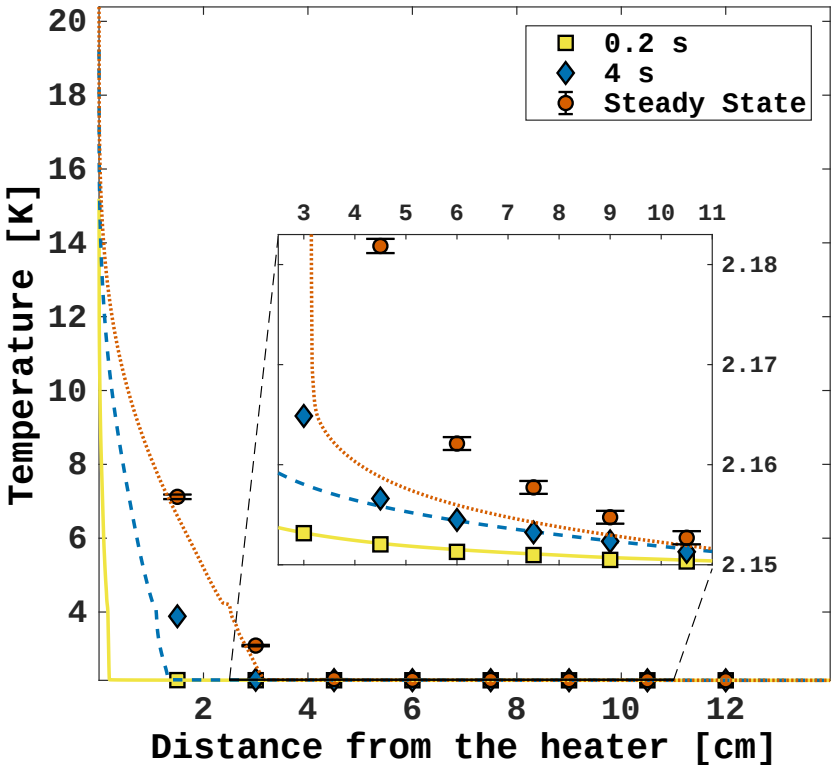

Figure 5.23: Transient temperature profiles comparison between *heliumChtFoam* and data from an experiment in the horizontal 0.5 mm thick channel at a bath temperature $T_b = 2.15$ K and the heater at 22.7 K.

impressive and proper of the triple-phase phenomenon in helium. The value is maximum in He II next to the bath boundary, where the temperature gradient is minimum. It mildly decreases towards the λ-front, where the value drops significantly down to the He I range.

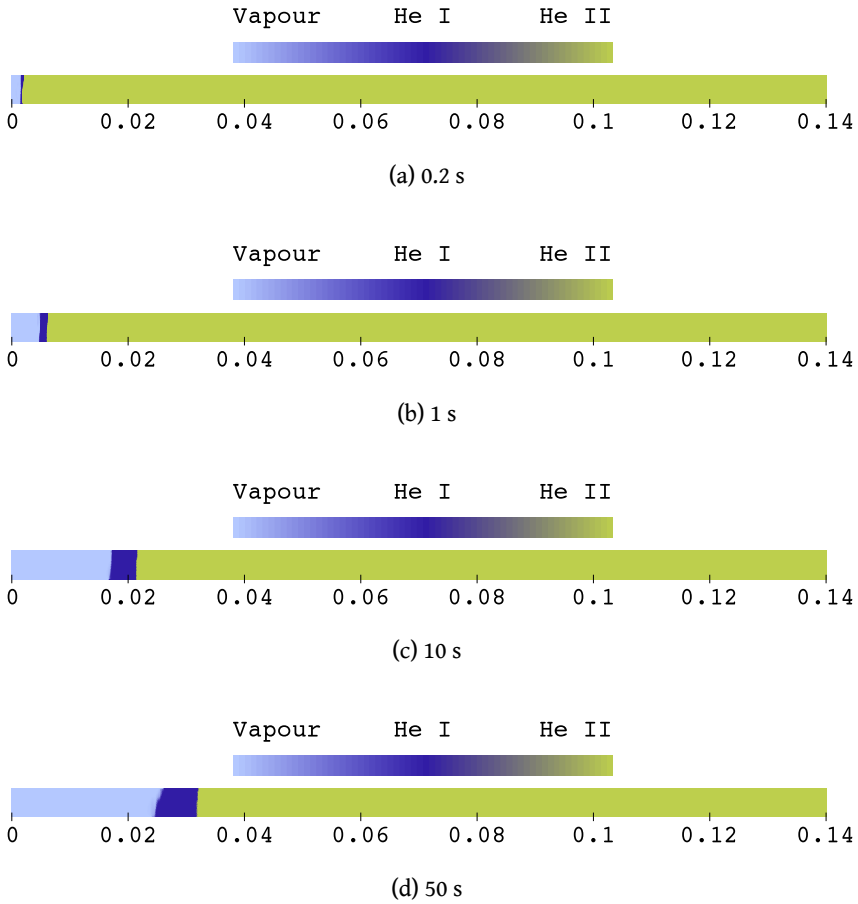

(a) 0.2 s

(b) 1 s

(c) 10 s

(d) 50 s

Figure 5.24: Helium three-phase evolution in the horizontal 0.5 mm thick channel with the heater at 22.7 K. The length coordinates are in meters.

Another small temperature reduction characterizes the phase change to helium vapour, where the minimum value is reached. The thermal conductivity of vapour increases towards the heater as a function of the temperature.

Another experiment in similar conditions was conducted with the channel in its horizontal orientation (see Fig. A.14 in Annex A.1). In this case, the heater reaches a temperature of 22.7 K. Fig. 5.23 shows the comparison of the simulated temperature profiles with the data. The profiles are quite similar to the vertical orientation case, except the gradient is lower in vapour and He I. Since the lighter phase is no longer gravity-driven towards the heater, the vapour expands further towards the bath. As a consequence, the λ-front propagates farther and exceeds TS1 at steady state. As the inset shows, the profiles in He II are well predicted, particularly in the early moments of the test and despite the presence of the vapour phase. The overall temperature is slightly underestimated, with a satisfactory relative error of 7.9 %. The volume fraction fields of this simulation are presented in Fig. 5.24, where the channel thickness is again magnified ten times. As in the previous case, the vapour is soon generated and grows slowly throughout the channel. However, the He I phase is visibly thicker than the vertical case. Another difference

pertains to the shape of the boiling front, which appears tilted due to the effect of gravity. The same phenomenon is not observable, instead, for the λ-front, where the density gradient is very small and hence the interface is unaffected by buoyancy forces.

CHAPTER 6

Conclusions

6.1 Summary

The present study investigates heat and mass transfer phenomena in superfluid helium in two rectangular cross-section channels of high aspect ratios. Both channels are 14 cm long and 5 cm wide, whereas their thicknesses are 0.5 mm and 0.2 mm. Experiments were conducted at atmospheric pressure in a superfluid helium bath, where the channel setup was submerged. One aperture of the channels is closed with a heater, while the other one is kept open to the bath. Thick steel components surrounding the setup are meant to insulate the helium contained in the channel from the bath. The experiments consisted of clamped heat flux tests, in which the heater releases a heat load into the channel. The helium temperature was recorded at eight equally spaced locations along the channel centerline. The tests were carried out at different bath temperatures (i.e., 1.8 K, 1.9 K, 2 K, 2.15 K) and channel orientations (i.e., horizontal, downward, upward). The applied heat flux ranged from few thousands to several hundred thousands of watts per square meter, in order to study the thermal behaviour of He II in the Gorter-Mellink regime as well as the first and second-order phase transitions. The difference in thickness between the two channels allowed exploring the effect of the geometrical confinement on the propagation of the phase change fronts in the presence of helium vapour. Unlike the 0.5 mm thick channel, the confinement number Co associated with the thinner channel is above a certain value that is known to be the threshold beyond which confinement effects influence the dynamics of multiphase flows.

A transient FVM-based numerical model for multi-dimensional grids was developed to simulate the thermo-fluid dynamics of He II. The equations of the classic two-fluid model were investigated in-depth to formulate novel dimensionless numbers associated with the superfluid component of He II. These numbers helped in the validation of the assumption that underlies the governing equations implemented in the code. These equations constitute an advanced version of an existing single-fluid model, which is herein derived again with a more generalized conductive heat power law. The numerical model is also intended to simulate the conjugate heat transfer between helium and solids, which required the implementation of customized boundary conditions to replicate the Kapitza resistance and superfluid partial slip. This He II model was enriched with novel modules for the simulation of phase change phenomena. For this purpose, an algorithm for fixed non-uniform orthogonal grids was conceptualized to deal with the lambda transition. The first-order phase transition was addressed through an explicit calculation of the volume fractions of the helium mixture and by introducing surface tension forces.

6.2 Conclusions

The experimental and numerical work of this study allows drawing some conclusions that are summarized in the following list.

He II Experiments

1. The maximum temperature increase recorded in the clamped flux tests varies clearly with the bath temperature. Specifically, the increment at 1.9 K is less than the one measured at both higher and lower bath temperatures. This represents an experimental confirmation of the temperature dependence of the He II heat conductivity function, which is known to peak at around 1.95 K.

2. Integrating the heat conductivity function with the empirical exponent (i.e., 3.4) from a certain bath temperature to the λ-point over the length of the channel predicts quite accurately the value of the critical heat flux necessary to trigger the lambda transition.

3. Regardless of the channel thickness, the orientation of channels with high aspect ratios does not affect significantly either the temperature gradient or evolution.

He II Numerical Model and Simulations

1. By manipulating the fluid dynamic equations of superfluid helium under the hypothesis of Gorter-Mellink regime, it is possible to derive dimensionless numbers (associated with the superfluid component of He II) that are expressed in terms of the heat flux, total velocity, and thermophysical properties only, without taking into account singularly the fluid components' velocities.

2. The analysis of the dimensionless numbers associated with the superfluid component of He II revealed that the mutual friction force and thermo-mechanical effect tend to equal each other for high heat fluxes, legitimizing the assumption at the basis of the single-fluid governing equations.

3. A numerical model benchmarking validated a modified version of the single-fluid model for He II with a typical relative error of the transient temperature profiles below 1 %. This model, which is a FVM-based multi-dimensional code, comprises a generalized conductive heat power law, whose usage is extended to the momentum equation as well as the energy equation. The model includes also a customized superfluid partial slip boundary condition that captures the correct thermo-fluid dynamic behaviour of He II at the walls.

4. A segregated-like conjugate heat transfer module linked to the He II model enables simulating properly the thermal relationship between He II and solids through the usage of a customized Kapitza resistance boundary condition, which smoothly switches from a regime characterized by low helium-solid temperature differences to a regime where the temperature difference is comparable to the bath temperature.

Phase Transition Experiments

1. Applying clamped heat fluxes above the lambda critical value triggers the second-order phase transition, which causes a sudden temperature increase due to the abrupt drop in specific heat capacity from He II to He I.

2. From the majority of the experiments it can be deduced that, at almost all bath temperatures, in thin channels of high aspect ratios the minimum heat flux needed to trigger the second-order phase transition is sufficiently large to initiate boiling too. At the saturation temperature, the fluid mixture temperature experiences a steady evolution due to the latent heat of vaporization. The duration and slope of this evolution are affected by the heat flux: the higher the heat flux, the shorter and steeper the evolution at a certain location.

3. Considerably different steady-state temperature profiles can be distinguished in the horizontal confined channel depending on the heat flux applied. By qualitatively subdividing the heat fluxes into low, moderate, and high values, three different phenomenologic zones can be distinguished. Increasing the heat flux has different effects within each zone (see Fig. 6.1): the He I phase occupies an increasing portion of the channel, while helium vapour is confined next to the heater (low zone); the He I region progressively shortens after an initial expansion and He II returns to occupy the majority of the channel (intermediate zone); the He I phase occupies a small portion of the channel between He II and the expanding vapour phase (high zone). These opposing behaviours are due to different multiphase regimes. At low heat fluxes, the vapour phase is heterogeneously constituted by small regions that allow maintaining a direct thermal link between the heater and He II. As a consequence, the He II-He I transformation rate grows proportionally to the heat flux and, hence, the He I phase expands quickly. At moderate heat fluxes, the vapour regions slowly coalesce into a homogeneous insulating film that blankets the heater (i.e., film boiling) and interrupts the heat transfer to He II. It follows that the λ-front propagation slows down and stops earlier before receding because of the heat removal from the He II bath. At high heat fluxes, the onset of film boiling takes place so rapidly that the He II-He I transformation is hindered since the beginning of the transient. The vapour phase expands then proportionally to the heat flux.

4. At high heat fluxes, a bump-like temporary temperature increment is always observed at the beginning of the clamped flux tests. This increment decreases towards the bath but occurs at the same instant at every location of the channel. As such, it has been attributed to a diffusion-driven temperature rise that stops at the onset of film boiling, when the temperature drops back within the He II range. The peak of the bump decreases with larger heat fluxes until it disappears. Moreover, the phenomenon is absent at higher bath temperatures (i.e., close to the λ-point), where

(a) Low Heat Flux

(b) Moderate Heat Flux

(c) High Heat Flux

Figure 6.1: Representation of different multiphase regimes according to the extent of the heat flux applied.

the onset of film boiling occurs almost immediately after the application of the heat flux.

5. At high heat fluxes and a bath temperature close to the λ-point, the temperature evolution at locations far from the heater experiences a sharp rise in slope occurring at no meaningful temperature (i.e., between the lambda and saturation points). As boiling starts at the heater, the vapour phase expands and the consequent large differences in density cause advective phenomena that alter the diffusive character of the heat transport in the channel.

6. The orientation of the channel has a significant impact on the temperature evolution if He II undergoes phase transitions during the test. Since the thermal expansivity of liquid helium changes sign across the λ-point, a temperature increase in He I and vapour results in upstream natural convection flows. Consequently, in vertical channels, the lighter fluid phases tend to either remain on top of the channel in the case of downward heat fluxes or rise the channel towards the bath in the case of upward heat fluxes. In the latter case, the heat extraction due to boiling resulted in a lower temperature increase of the heater.

7. Unlike in the horizontal orientation, in downward vertical channels the He I region never extends to a large portion of the channel. Since the enhancement of the vapour film is gravity-assisted, even low heat fluxes are sufficiently large to generate a stable

insulating film. As explained before, this results in a thin He I phase restricted between He II and vapour.

8. The temperature evolution in upward channels reaches the steady state in fewer seconds than in the horizontal orientation. In this configuration, at low and moderate heat fluxes the temperature fluctuates vividly in the He I range in most of the channel. The fluctuations diminish with increasing heat fluxes. This unsteady behaviour is associated with an ongoing boiling process, which is attenuated by the onset of the film boiling regime. When the energy dissipated is sufficiently high to sustain the vapour film, the heat transfer drops and the temperature far from the heater goes back to the He II range.

9. The thickness of the channels determines the relative proportion between the different phases of helium. In contrast to the 0.2 mm thick channel, in the thicker channel the He I phase does not cover a large portion of the channel regardless of the heat flux (see Fig. 6.2). Therefore, the thinner the channel, the more the He I phase expands longitudinally. It can be concluded that the thickness of the He I region decreases with increasing characteristic dimensions of the geometry until it reaches a minimum value determined by He II and vapour.

(a) $Co > 0.5$

(b) $Co < 0.5$

Figure 6.2: Representation of different multiphase configurations according to the confinement number Co.

10. In the non-confined downward channel (i.e., 0.5 mm thick), the diffusion-driven temporary temperature increment at the beginning of the transients resolves itself much faster compared to the confined channel. Moreover, increasing the heat flux shortens the time span of the peak but does not affect its maximum value.

11. In the non-confined upward channel, the larger heating surface in comparison to the confined channel together with the action of gravity delays the onset of film boiling, which is responsible for interrupting the thermal connection between the

heater and He II. As a consequence, it was not identified any heat flux above which the temperature far from the heater returns below the λ-point, like in the case of the thinner channel.

Double-Front Propagation

1. If the temperature is sufficiently lower than T_λ and the heat flux is moderately low (i.e., below 10^5 W/m^2), the λ-front speed is inversely proportional roughly to the cubic root of the front position in the channel. However, if the temperature is in close proximity to T_λ or the heat flux is too large, the slope of the speed profile changes, altered by the growing vapour phase.

2. In the confined channel, at a constant location not far from the heating surface, the λ-front speed varies differently according to the heat flux range. With reference to the categorization introduced in point 3 of the previous paragraph, it is possible to distinguish three main zones: the speed increases sharply with the heat flux (low zone); the speed decreases with increasing heat flux (intermediate zone); the speed increases weakly with the heat flux (high zone). Since in the moderate zone the λ-front propagation slows down and stops earlier, this zone is absent at locations farther from the heater. Because of the change in behaviour from the low zone to the intermediate one, there exists a top speed and a maximum length covered by the front.

3. The boiling front travels much more slowly than the λ-front. Unlike the latter, the boiling front shows two behavioural zones only: the speed increases with the heat flux with a negative second derivative until a maximum value (first zone); the speed increases weakly with the heat flux at the same rate as the λ-front (second zone). The first zone matches roughly the λ-front low zone. Since the second zone corresponds to both the moderate and high λ-front zones, the similar growth rate in the second zone indicates that the λ-front propagation is mainly determined by the expansion of the vapour phase and hence of the boiling front propagation.

4. Different levels of geometrical confinement affect significantly the relationship between the λ-front speed and heat flux. In the non-confined channel, only two zones are distinguishable: the speed increases sharply with the heat flux (low zone); the speed varies weakly with the heat flux (high zone). Since the level of confinement is lower, the vapour and He I phases expand more easily and, thus, the λ-front speed in the high zone is greater than the top value reached in the confined channel.

5. Because of the diffusion-driven temperature increase in the early moments of the transients (see point 4 in the previous paragraph), the λ-front may cross the same location in the channel twice. The primary front is diffusion-driven and travels at a typical λ-front speed, while the secondary front is due to the vapour expansion and travels at a typical boiling front speed.

Phase Change Modeling and Simulations

1. The comparison of data collected during He I experiments at moderate heat flux with a multiphase numerical model for boiling phenomena revealed good accuracy of the model with a relative error of the transient temperature profiles around 10 %. This model exploits the enthalpy dependence of the thermophysical properties to derive mass and volume fractions explicitly without tracking the vapour-He I interface. The model also implements a continuum surface force module for the calculation of the surface tension forces acting on the mixture interface.

2. By combining the heat transfer equations of He I and He II, it is possible to derive a nonlinear equation for the λ-front position in fixed non-uniform orthogonal computational grids. The solution of this equation via the iterative Newton-Raphson method showed consistent and fast results.

3. The comparison of data collected during He II experiments at moderate heat flux with a multiphase numerical model for triple-phase phenomena revealed good accuracy of the model with a relative error of the transient temperature profiles around 10 %. The model is based on a modified PIMPLE algorithm, which includes the module for the identification of the λ-front location. This additional module allows to correct at the λ-front the He II fields that depend on the temperature gradient. The predicted λ-front position varies weakly with the size of the control volumes.

4. The triple-phase numerical model simulates satisfactorily the propagation of the phase change fronts. The channel portion occupied by the He I phase resembles the one observed in the experiments of the non-confined channel. The simulations revealed that the saturation interface between vapour and He I is thinner if boiling occurs in an environment initially constituted by He II only.

6.3 Future Work

The present study is not exempt from potential improvements both experimentally and numerically. Due to the comparable thermophysical properties between helium vapour and the solid materials constituting the setup, the experiments suffered from inevitable losses of energy. Moreover, the pressure sensors did not measure any relevant variation during the tests. To solve this kind of issues, the channel setup may be improved under different aspects, which are listed below:

- In order to ensure the exclusive contact of the heating surface with helium, the heater could be rather installed at the mid-point of the channel, which would be kept open to the bath in both apertures.

- The channel could be further insulated to minimize the heat losses by conducting the experiments in vacuum, with the bath connected to the apertures only.

- Since the pressure sensors appeared to disturb the temperature measurements, the configuration of the probes could be changed to maximize the space among them.
- In order to measure significant pressure changes, it could be necessary to close the aperture of the channel for maintaining isochoric conditions like in the case of the stagnant bath surrounding the magnet dipoles of the LHC.
- The use of visualization techniques would unravel more information about the propagation of the double-front in three-dimensional environments.

The numerical model presented in this work may represent a useful tool in the prediction of quench phenomena in combination with magnet solvers. For this purpose though, the model must be improved in several ways, a few of which are listed below:

- The He II governing equations could be modified to include the pressure drop term for forced flow applications.
- By changing the discretization schemes and matrix solvers, and introducing different levels of relaxation factors, it could be possible to improve the robustness of the code, allowing to run simulations at higher heat fluxes.
- The temperature gradient correction algorithm could be generalized to make it applicable to non-orthogonal or unstructured grids.
- The interpolating tables of the thermophysical properties of helium could be substituted by two-variable tables to include the pressure dependence.
- The polynomial calculation of the thermophysical properties of solids could be substituted by interpolating tables to speed up the solver and increase accuracy.

Bibliography

[1] I. N. Adamenko and E. K. Nemchenko. “Heat Flow from Solid to Liquid He II Due to Inelastic Processes of Phonons Interaction”. In: *Journal of Low Temperature Physics* 171.3 (May 2013), pp. 266–272. ISSN: 0022-2291, 1573-7357. DOI: 10.1007/s10909-012-0754-9.

[2] G. Ahlers. “Mutual Friction in He II Near the Superfluid Transition”. In: *Physical Review Letters* 22.2 (Jan. 13, 1969), pp. 54–56. ISSN: 0031-9007. DOI: 10.1103/PhysRevLett.22.54.

[3] H. Allain et al. “Upscaling of superfluid helium flow in porous media”. In: *International Journal of Heat and Mass Transfer* 53.21 (Oct. 2010), pp. 4852–4864. ISSN: 00179310. DOI: 10.1016/j.ijheatmasstransfer.2010.06.007.

[4] J. F. Allen and H. Jones. “New Phenomena Connected with Heat Flow in Helium II”. In: *Nature* 141.3562 (Feb. 1938), pp. 243–244. ISSN: 0028-0836, 1476-4687. DOI: 10.1038/141243a0.

[5] J. F. Allen and A. D. Misener. “Flow of Liquid Helium II”. In: *Nature* 141.3558 (Jan. 1938), pp. 75–75. ISSN: 0028-0836, 1476-4687. DOI: 10.1038/141075a0.

[6] AMI©. *Standard AMI liquid helium sensors*. 112 Flint Rd Oak Ridge, TN 37830: American Magnetics, Inc.

[7] E. Andronikashvili. “A direct observation of two kinds of motion in helium II”. In: *Journal of Physics, USSR* 10 (1946), p. 201.

[8] V. Arp. “Heat transport through helium II”. In: *Cryogenics* 10.2 (Apr. 1970), pp. 96–105. ISSN: 00112275. DOI: 10.1016/0011-2275(70)90078-0.

[9] G. Authelet. *Channel technical drawing*. DACM/IRFU, CEA Saclay, Gif-sur-Yvette 91191.

[10] U. Ayachit. *The ParaView guide: updated for ParaView version 4.3*. Ed. by L. Avila. In collab. with B. Geveci. Full color version. OCLC: 944221263. Los Alamos: Kitware, 2015. 261 pp. ISBN: 978-1-930934-30-6.

[11] S. Balibar. “The discovery of superfluidity”. In: *Journal of Low Temperature Physics* 146.5 (Feb. 13, 2007), pp. 441–470. ISSN: 0022-2291, 1573-7357. DOI: 10.1007/s10909-006-9276-7. arXiv: physics/0611119.

[12] B. Baudouy et al. “He II heat transfer through superconducting cables electrical insulation”. In: *Cryogenics* 40.2 (Feb. 2000), pp. 127–136. ISSN: 00112275. DOI: 10.1016/S0011-2275(00)00015-1.

[13] B. Baudouy. “Heat-balance integral method for heat transfer in superfluid helium”. In: *Thermal Science* 13.2 (2009), pp. 121–132. ISSN: 0354-9836. DOI: 10.2298/TSCI0902121B.

[14] I. L. Bekarevich and I. M. Khalatnikov. “Phenomenological derivation of the equations of vortex motion in He II”. In: *Sov. Phys. JETP* 13 (1961), p. 643.

[15] F. Bertinelli et al. “Production of Austenitic Steel for the LHC Superconducting Dipole Magnets”. In: *IEEE Transactions on Applied Superconductivity* 16.2 (June 2006), pp. 1773–1776. ISSN: 1051-8223. DOI: 10.1109/TASC.2006.873244.

[16] D. Bocian, B. Dehning, and A. Siemko. “Modeling of Quench Limit for Steady State Heat Deposits in LHC Magnets”. In: *IEEE Transactions on Applied Superconductivity* 18.2 (June 2008), pp. 112–115. ISSN: 1051-8223, 1558-2515. DOI: 10.1109/TASC.2008.921338.

[17] G. Bon Mardion, G. Claudet, and P. Seyfert. “Practical data on steady state heat transport in superfluid helium at atmospheric pressure”. In: *Cryogenics* 19.1 (Jan. 1979), pp. 45–47. ISSN: 00112275. DOI: 10.1016/0011-2275(79)90109-7.

[18] S. N. Bose. “Plancks Gesetz und Lichtquantenhypothese”. In: *Zeitschrift fuer Physik* 26.1 (Dec. 1924), pp. 178–181. ISSN: 1434-6001, 1434-601X. DOI: 10.1007/BF01327326.

[19] L. Bottura. “A Numerical Model for the Simulation of Quench in the ITER Magnets”. In: *Journal of Computational Physics* 125.1 (Apr. 1996), pp. 26–41. ISSN: 00219991. DOI: 10.1006/jcph.1996.0077.

[20] L. Bottura, M. Calvi, and A. Siemko. “Stability analysis of the LHC cables”. In: *Cryogenics* 46.7 (July 2006), pp. 481–493. ISSN: 00112275. DOI: 10.1016/j.cryogenics.2006.01.012.

[21] L. Bottura and C. Rosso. “Finite element simulation of steady state and transient forced convection in superfluid helium”. In: *International Journal for Numerical Methods in Fluids* 30.8 (1999), pp. 1091–1108. DOI: 10.1002/(SICI)1097-0363(19990830)30:8<1091::AID-FLD882>3.0.CO;2-I. eprint: https://onlinelibrary.wiley.com/doi/pdf/10.1002/%28SICI%291097-0363%2819990830%2930%3A8%3C1091%3A%3AAID-FLD882%3E3.0.CO%3B2-I.

[22] J. Brackbill, D. Kothe, and C. Zemach. “A continuum method for modeling surface tension”. In: *Journal of Computational Physics* 100.2 (June 1992), pp. 335–354. ISSN: 00219991. DOI: 10.1016/0021-9991(92)90240-Y.

[23] S. Breon and S. Van Sciver. “Boiling phenomena in pressurized He II confined to a channel”. In: *Cryogenics* 26.12 (Dec. 1986), pp. 682–691. ISSN: 00112275. DOI: 10.1016/0011-2275(86)90169-4.

[24] D. F. Brewer, D. O. Edwards, and K. Mendelssohn. “CXIV. The onset of friction in helium II”. In: *Philosophical Magazine* 1.12 (Dec. 1956), pp. 1130–1132. ISSN: 0031-8086. DOI: 10.1080/14786435608238196.

[25] M. Buckingham and W. Fairbank. “Chapter III The Nature of the λ-Transition in Liquid Helium”. In: *Progress in Low Temperature Physics*. Vol. 3. Elsevier, 1961, pp. 80–112. ISBN: 978-0-444-53309-8. DOI: 10.1016/S0079-6417(08)60134-1.

[26] O. Capatina. “Lambda Front Propagation in the Superfluid Helium Contained in the External Auxiliary Bus-Bar Line of the LHC”. In: *AIP Conference Proceedings*. ADVANCES IN CRYOGENIC ENGEINEERING: Transactions of the Cryogenic Engineering Conference - CEC. Vol. 710. ISSN: 0094243X. Anchorage, Alaska (USA): AIP, 2004, pp. 1068–1078. DOI: 10.1063/1.1774791.

[27] L. Caretto, R. Curr, and D. Spalding. “Two numerical methods for three-dimensional boundary layers”. In: *Computer Methods in Applied Mechanics and Engineering* 1.1 (June 1972), pp. 39–57. ISSN: 00457825. DOI: 10.1016/0045-7825(72)90020-5.

[28] S. Caspi and T. Frederking. “Triple-phase phenomena during quenches of superconductors cooled by pressurized superfluid helium II”. In: *Cryogenics* 19.9 (Sept. 1979), pp. 513–516. ISSN: 00112275. DOI: 10.1016/0011-2275(79)90003-1.

[29] Cernox®. *Cernox Sensors Catalog*. 575 McCorkle Blvd, Westerville, OH 43082: Lake Shore Cryotronics, Inc.

[30] L. J. Challis. “Heat transfer between solids and liquid helium II”. In: *Proceedings of the Royal Society of London. Series A. Mathematical and Physical Sciences* 260.1300 (Feb. 7, 1961), pp. 31–46. ISSN: 0080-4630, 2053-9169. DOI: 10.1098/rspa.1961.0011.

[31] C. E. Chase. “Thermal Conduction in Liquid Helium II. I. Temperature Dependence”. In: *Physical Review* 127.2 (July 15, 1962), pp. 361–370. ISSN: 0031-899X. DOI: 10.1103/PhysRev.127.361.

[32] M. Chorowski, S. Pietrowicz, and R. v. Weelderen. “Towards a better understanding of the physics of the two-volume model of accelerator magnet quench thermohydraulics”. In: *Cryogenics* 46.7 (July 2006), pp. 581–588. ISSN: 00112275. DOI: 10.1016/j.cryogenics.2006.01.013.

[33] G. Claudet and R. Aymar. “Tore Supra and He II Cooling of Large High Field Magnets”. In: *Advances in Cryogenic Engineering*. Ed. by R. W. Fast. Boston, MA: Springer US, 1990, pp. 55–67. ISBN: 978-1-4612-7904-4 978-1-4613-0639-9. DOI: 10.1007/978-1-4613-0639-9_8.

[34] K. Cornwell and P. A. Kew. “Boiling in Small Parallel Channels”. In: *Energy Efficiency in Process Technology*. Ed. by P. A. Pilavachi. Dordrecht: Springer Netherlands, 1993, pp. 624–638. ISBN: 978-1-85861-019-1 978-94-011-1454-7. DOI: 10.1007/978-94-011-1454-7_56.

[35] R. Courant, K. Friedrichs, and H. Lewy. "Ueber die partiellen Differenzengleichungen der mathematischen Physik". In: *Mathematische Annalen* 100.1 (Dec. 1928), pp. 32–74. ISSN: 0025-5831, 1432-1807. DOI: 10.1007/BF01448839.

[36] R. Courant, E. Isaacson, and M. Rees. "On the solution of nonlinear hyperbolic differential equations by finite differences". In: *Communications on Pure and Applied Mathematics* 5.3 (Aug. 1952), pp. 243–255. ISSN: 00103640, 10970312. DOI: 10.1002/cpa.3160050303.

[37] J. Crank and P. Nicolson. "A practical method for numerical evaluation of solutions of partial differential equations of the heat-conduction type". In: *Advances in Computational Mathematics* 6.1 (Dec. 1996), pp. 207–226. ISSN: 1019-7168, 1572-9044. DOI: 10.1007/BF02127704.

[38] C. T. Crowe et al. *Multiphase Flows with Droplets and Particles*. 1st ed. CRC Press, Aug. 26, 2011. ISBN: 978-0-429-10639-2. DOI: 10.1201/b11103.

[39] CryoComp©. *version 5.3*. Florence, SC 29501-8006: Eckels Engineering Inc.

[40] F. M. Darwish M. "A unified formulation of the segregated class of algorithms for fluid flow at all speeds". In: *Numerical Heat Transfer, Part B: Fundamentals* 37.1 (Jan. 2000), pp. 103–139. ISSN: 1040-7790, 1521-0626. DOI: 10.1080/104077900275576.

[41] J. G. Daunt and K. Mendelssohn. "Zero Point Diffusion in Liquid Helium II". In: *Nature* 157.3999 (June 1946), pp. 839–840. ISSN: 0028-0836, 1476-4687. DOI: 10.1038/157839b0.

[42] P. E. Dimotakis. "Gorter-Mellink scale, and critical velocities in liquid—helium-II counterflow". In: *Physical Review A* 10.5 (Nov. 1, 1974), pp. 1721–1723. ISSN: 0556-2791. DOI: 10.1103/PhysRevA.10.1721.

[43] R. J. Donnelly and C. F. Barenghi. "The Observed Properties of Liquid Helium at the Saturated Vapor Pressure". In: *Journal of Physical and Chemical Reference Data* 27.6 (Nov. 1998), pp. 1217–1274. ISSN: 0047-2689, 1529-7845. DOI: 10.1063/1.556028.

[44] L. Dresner. "Transient Heat Transfer in Superfluid Helium". In: *Advances in Cryogenic Engineering*. Vol. 27. San Diego, CA, 1982, pp. 411–419.

[45] L. Dresner. "Transient Heat Transfer in Superfluid Helium — Part II". In: *Advances in Cryogenic Engineering*. Ed. by R. W. Fast. Boston, MA: Springer US, 1984, pp. 323–333. ISBN: 978-1-4613-9867-7 978-1-4613-9865-3. DOI: 10.1007/978-1-4613-9865-3_37.

[46] P. Ehrenfest. *Phasenumwandlungen im ueblichen und erweiterten Sinn, classifiziert nach den entsprechenden Singularitaeten des thermodynamischen Potentiales*. N. V. Noord-Hollandsche Uitgevers Maatschappij, 1933.

[47] A. Einstein. "Quantentheorie des einatomigen idealen Gases". In: *Sitz. Ber. Preuss. Akad. Wiss.* 22 (1924), p. 261.

[48] C. Enss and S. Hunklinger. *Low-Temperature Physics*. Berlin/Heidelberg: Springer-Verlag, 2005. ISBN: 978-3-540-23164-6. DOI: 10.1007/b137878.

[49] L. Evans. "The Large Hadron Collider". In: *Philosophical Transactions of the Royal Society A: Mathematical, Physical and Engineering Sciences* 370.1961 (Feb. 28, 2012), pp. 831–858. ISSN: 1364-503X, 1471-2962. DOI: 10.1098/rsta.2011.0453.

[50] C. Fernandes et al. "Implementation of partial slip boundary conditions in an open-source finite-volume-based computational library". In: *Journal of Polymer Engineering* 39.4 (Mar. 26, 2019), pp. 377–387. ISSN: 2191-0340, 0334-6447. DOI: 10.1515/polyeng-2018-0343.

[51] J. H. Ferziger and M. Perić. *Computational Methods for Fluid Dynamics*. Berlin, Heidelberg: Springer Berlin Heidelberg, 2002. ISBN: 978-3-540-42074-3 978-3-642-56026-2. DOI: 10.1007/978-3-642-56026-2.

[52] R. Feynman. "Chapter II Application of Quantum Mechanics to Liquid Helium". In: *Progress in Low Temperature Physics*. Vol. 1. Elsevier, 1955, pp. 17–53. ISBN: 978-0-444-53307-4. DOI: 10.1016/S0079-6417(08)60077-3.

[53] S. Fuzier, B. Baudouy, and S. Van Sciver. "Steady-state pressure drop and heat transfer in He II forced flow at high Reynolds number". In: *Cryogenics* 41.5 (May 2001), pp. 453–458. ISSN: 00112275. DOI: 10.1016/S0011-2275(01)00090-X.

[54] S. Fuzier and S. Van Sciver. "Experimental measurements and modeling of transient heat transfer in forced flow of He II at high velocities". In: *Cryogenics* 48.3 (Mar. 2008), pp. 130–137. ISSN: 00112275. DOI: 10.1016/j.cryogenics.2008.02.004.

[55] S. Fuzier. "Heat Transfer and Pressure Drop in Forced Flow Helium II at High Reynolds Numbers". In: *PhD Thesis* (2004).

[56] J. Glimm, D. Marchesin, and O. McBryan. "A numerical method for two phase flow with an unstable interface". In: *Journal of Computational Physics* 39.1 (Jan. 1981), pp. 179–200. ISSN: 00219991. DOI: 10.1016/0021-9991(81)90144-3.

[57] M. B. Gorbounov et al. "Finite Element Code for Quench and Stability Analysis of Superconducting Magnets Cooled by He II". In: *Advances in Cryogenic Engineering*. Ed. by P. Kittel. Vol. 41. Series Title: A Cryogenic Engineering Conference Publication. Boston, MA: Springer US, 1996, pp. 335–342. ISBN: 978-1-4613-8022-1 978-1-4613-0373-2. DOI: 10.1007/978-1-4613-0373-2_43.

[58] C. Gorter and J. Mellink. "On the irreversible processes in liquid helium II". In: *Physica* 15.3 (May 1949), pp. 285–304. ISSN: 00318914. DOI: 10.1016/0031-8914(49)90105-6.

[59] P. P. Granieri. "Heat transfer through cable insulation of Nb–Ti superconducting magnets operating in He II". In: *Cryogenics* 53 (Jan. 2013), pp. 61–71. ISSN: 00112275. DOI: 10.1016/j.cryogenics.2012.06.007.

[60] P. P. Granieri et al. "Stability Analysis of the LHC Cables for Transient Heat Depositions". In: *IEEE Transactions on Applied Superconductivity* 18.2 (June 2008), pp. 1257–1262. ISSN: 1051-8223, 1558-2515. DOI: 10.1109/TASC.2008.922543.

[61] P. P. Granieri et al. “Steady-State heat transfer through micro-channels in pressurized He II”. In: ADVANCES IN CRYOGENIC ENGINEERING: Transactions of the Cryogenic Engineering Conference - CEC, Volume 57. Spokane, Washington, USA, 2012, pp. 231–238. DOI: 10.1063/1.4706925.

[62] H. E. Hall. “The rotation of liquid helium II”. In: *Advances in Physics* 9.33 (Jan. 1960), pp. 89–146. ISSN: 0001-8732, 1460-6976. DOI: 10.1080/00018736000101169.

[63] H. E. Hall and W. F. Vinen. “The rotation of liquid helium II I. Experiments on the propagation of second sound in uniformly rotating helium II”. In: *Proceedings of the Royal Society of London. Series A. Mathematical and Physical Sciences* 238.1213 (Dec. 18, 1956), pp. 204–214. ISSN: 0080-4630, 2053-9169. DOI: 10.1098/rspa.1956.0214.

[64] H. E. Hall and W. F. Vinen. “The rotation of liquid helium II II. The theory of mutual friction in uniformly rotating helium II”. In: *Proceedings of the Royal Society of London. Series A. Mathematical and Physical Sciences* 238.1213 (Dec. 18, 1956), pp. 215–234. ISSN: 0080-4630, 2053-9169. DOI: 10.1098/rspa.1956.0215.

[65] K. Hama and M. Shiotsu. “Film boiling on a vertical plate in subcooled helium II”. In: *Cryogenics* 47.4 (Apr. 2007), pp. 209–219. ISSN: 00112275. DOI: 10.1016/j.cryogenics.2006.12.004.

[66] F. H. Harlow and J. E. Welch. “Numerical Calculation of Time-Dependent Viscous Incompressible Flow of Fluid with Free Surface”. In: *Physics of Fluids* 8.12 (1965), p. 2182. ISSN: 00319171. DOI: 10.1063/1.1761178.

[67] D. G. Henshaw and A. D. B. Woods. “Modes of Atomic Motions in Liquid Helium by Inelastic Scattering of Neutrons”. In: *Physical Review* 121.5 (Mar. 1, 1961), pp. 1266–1274. ISSN: 0031-899X. DOI: 10.1103/PhysRev.121.1266.

[68] HEPAK©. *version 3.4*. P.O. Box 173, Louisvile, CO 80027: Cryodata Inc.

[69] M. Hilal. “Analytical study of laminar free convection heat-transfer to supercritical helium”. In: *Cryogenics* 18.9 (Sept. 1978), pp. 545–551. ISSN: 00112275. DOI: 10.1016/0011-2275(78)90158-3.

[70] C. Hirsch. *Numerical computation of internal and external flows: fundamentals of computational fluid dynamics*. 2nd ed. OCLC: ocn148277909. Oxford ; Burlington, MA: Elsevier/Butterworth-Heinemann, 2007. 656 pp. ISBN: 978-0-7506-6594-0.

[71] C. Hirt and B. Nichols. “Volume of fluid (VOF) method for the dynamics of free boundaries”. In: *Journal of Computational Physics* 39.1 (Jan. 1981), pp. 201–225. ISSN: 00219991. DOI: 10.1016/0021-9991(81)90145-5.

[72] J. M. Hyman. “Numerical methods for tracking interfaces”. In: *Physica D* 12.1 (1984), pp. 396–407.

[73] E. A. Ibrahim, R. W. Boom, and G. E. McIntosh. "Heat Transfer to Subcooled Liquid Helium". In: *Advances in Cryogenic Engineering*. Ed. by K. D. Timmerhaus. Boston, MA: Springer US, 1978, pp. 333–339. ISBN: 978-1-4613-4041-6 978-1-4613-4039-3. DOI: 10.1007/978-1-4613-4039-3_41.

[74] M. Ilic, M. Petrovic, and V. Stevanovic. "Boiling heat transfer modelling: A review and future prospectus". In: *Thermal Science* 23.1 (2019), pp. 87–107. ISSN: 0354-9836, 2334-7163. DOI: 10.2298/TSCI180725249I.

[75] M. Ishii and T. Hibiki. *Thermo-fluid dynamics of two-phase flow*. 2nd ed. OCLC: ocn690084123. New York: Springer, 2011. 518 pp. ISBN: 978-1-4419-7984-1 978-1-4419-7985-8.

[76] R. Issa. "Solution of the implicitly discretised fluid flow equations by operator-splitting". In: *Journal of Computational Physics* 62.1 (Jan. 1986), pp. 40–65. ISSN: 00219991. DOI: 10.1016/0021-9991(86)90099-9.

[77] G. Jaeger. "The Ehrenfest Classification of Phase Transitions: Introduction and Evolution". In: *Archive for History of Exact Sciences* 53.1 (May 1, 1998), pp. 51–81. ISSN: 1432-0657. DOI: 10.1007/s004070050021.

[78] H. Jasak. "Error Analysis and Estimation for the Finite Volume Method with Applications to Fluid Flows". In: *PhD Thesis* (June 1996).

[79] P. L. Kapitza. "Heat Transfer and Superfluidity of Helium II". In: *Physical Review* 60.4 (Aug. 15, 1941), pp. 354–355. ISSN: 0031-899X. DOI: 10.1103/PhysRev.60.354.

[80] P. L. Kapitza. "Viscosity of Liquid Helium below the λ-Point". In: *Nature* 141.3558 (Jan. 1938), pp. 74–74. ISSN: 0028-0836, 1476-4687. DOI: 10.1038/141074a0.

[81] A. Kashani, S. W. Van Sciver, and J. C. Strikwerda. "Numerical Solution of Forced Convection Heat Transfer in He II". In: *Numerical Heat Transfer, Part A: Applications* 16.2 (Sept. 1989), pp. 213–228. ISSN: 1040-7782, 1521-0634. DOI: 10 . 1080 / 10407788908944714.

[82] W. Keesom and K. Clusius. In: *Commun. Leiden 219e, Proc. Roy. Acad. Amsterdam* 35 (1932), p. 307.

[83] W. Keesom and A. Keesom. "On the heat conductivity of liquid helium". In: *Physica* 3.5 (May 1936), pp. 359–360. ISSN: 00318914. DOI: 10.1016/S0031-8914(36)80312-7.

[84] W. Keesom and M. Wolfke. "Two Different Liquid States of Helium". In: *Helium 4*. Elsevier, 1971, pp. 65–71. ISBN: 978-0-08-015816-7. DOI: 10.1016/B978-0-08-015816-7.50006-7.

[85] W. H. Keesom and J. N. van der Ende. In: *Proceedings of the Royal Academy of Amsterdam* 33 (1930), p. 24.

[86] W. Keller and E. Hammel. "Heat conduction and fountain pressure in liquid He II". In: *Annals of Physics* 10.2 (June 1960), pp. 202–231. ISSN: 00034916. DOI: 10.1016/0003-4916(60)90022-1.

[87] I. M. Khalatnikov. *An introduction to the theory of superfluidity*. Advanced book classics. Redwood City, Calif: Addison-Wesley Pub. Co, 1988. 206 pp. ISBN: 978-0-201-09505-0.

[88] J. E. Kilpatrick and M. F. Kilpatrick. "Discrete Energy Levels Associated with the Lennard-Jones Potential". In: *The Journal of Chemical Physics* 19.7 (July 1951), pp. 930–933. ISSN: 0021-9606, 1089-7690. DOI: 10.1063/1.1748408.

[89] T. Kitamura et al. "A numerical model on transient, two-dimensional flow and heat transfer in He II". In: *Cryogenics* 37.1 (Jan. 1997), pp. 1–9. ISSN: 00112275. DOI: 10.1016/S0011-2275(96)00096-3.

[90] Kulite®. *CTL-190(M) Cryogenic Miniature Ruggedized Pressure Transducer*. Leonia, New Jersey: Kulite Semiconductor Products, Inc.

[91] LabVIEW®. *Software Configuration Management and LabVIEW*. Austin, Texas: National Instruments Corporation.

[92] LakeShore®. *Model 336 Cryogenic Temperature Controller*. 575 McCorkle Blvd, Westerville, OH 43082: Lake Shore Cryotronics, Inc.

[93] L. D. Landau. "Theory of the Superfluidity of Helium II". In: *Physical Review* 60.4 (Aug. 15, 1941), pp. 356–358. ISSN: 0031-899X. DOI: 10.1103/PhysRev.60.356.

[94] L. D. Landau and E. M. Lifshitz. *Fluid mechanics*. OCLC: 881165478. London; Reading, Mass.: Pergamon Press ; Addison-Wesley Pub. Co., 1959. ISBN: 978-1-4831-4050-6.

[95] P. Lebrun and L. Tavian. "Cooling with Superfluid Helium". In: (2014). Publisher: CERN. DOI: 10.5170/CERN-2014-005.453.

[96] P. Lebrun et al. "Cooling Strings of Superconducting Devices Below 2 K: The Helium II Bayonet Heat Exchanger". In: *Advances in Cryogenic Engineering*. Ed. by P. Kittel. Boston, MA: Springer US, 1998, pp. 419–426. ISBN: 978-1-4757-9049-8 978-1-4757-9047-4. DOI: 10.1007/978-1-4757-9047-4_50.

[97] P. Leiderer and F. Pobell. "Critical currents in superfluid helium near T_λ". In: *Zeitschrift für Physik A Hadrons and nuclei* 223.4 (Aug. 1969), pp. 378–384. ISSN: 0939-7922. DOI: 10.1007/BF01392867.

[98] F. London. "On the Bose-Einstein Condensation". In: *Physical Review* 54.11 (Dec. 1, 1938), pp. 947–954. ISSN: 0031-899X. DOI: 10.1103/PhysRev.54.947.

[99] F. London. "The λ-Phenomenon of Liquid Helium and the Bose-Einstein Degeneracy". In: *Nature* 141.3571 (Apr. 1938), pp. 643–644. ISSN: 0028-0836, 1476-4687. DOI: 10.1038/141643a0.

[100] D. N. Lyon. "Boiling heat transfer and peak nucleate boiling fluxes in saturated liquid helium between the lambda and critical temperatures". In: *Advances in Cryogenic Engineering* 10 (Jan. 1965), p. 371.

[101] Manganin®. *Manganin - Resistance Alloy*. 125 Hookstown Grade Road, Coraopolis, PA 15108-9302: Goodfellow Corporation.

[102] S. Mao, C. A. Luongo, and D. A. Kopriva. “Numerical simulation of the He II/He I phase transition in superconducting magnets”. In: *International Journal of Heat and Mass Transfer* 49.25 (Dec. 2006), pp. 4786–4794. ISSN: 00179310. DOI: 10.1016/j.ijheatmasstransfer.2006.06.004.

[103] S. P. Martin. “A supersymmetry primer”. In: *Perspectives on supersymmetry II*. World Scientific, 2010, pp. 1–153.

[104] MATLAB®. *version R2018b*. Natick, Massachusetts: The MathWorks, Inc.

[105] J. McLennan, H. Smith, and J. Wilhelm. “XIV. The scattering of light by liquid helium”. In: *The London, Edinburgh, and Dublin Philosophical Magazine and Journal of Science* 14.89 (July 1932), pp. 161–167. ISSN: 1941-5982, 1941-5990. DOI: 10.1080/14786443209462044.

[106] P. H. E. Meijer and J. S. J. Peri. “New Kapitza heat-transfer model for liquid ^{4}He ”. In: *Physical Review B* 22.1 (July 1, 1980), pp. 195–205. ISSN: 0163-1829. DOI: 10.1103/PhysRevB.22.195.

[107] METALPAK©. *version 1.10*. Boulder, CO 80027: Vincent Arp.

[108] C. Meuris et al. “Heat transfer in electrical insulation of LHC cables cooled with superfluid helium”. In: *Cryogenics* 39.11 (Nov. 1999), pp. 921–931. ISSN: 00112275. DOI: 10.1016/S0011-2275(99)00115-0.

[109] MKS©. *Compact Pressure Transducers and Switches*. Andover, Massachusetts: MKS Instruments, Inc.

[110] F. Moukalled, L. Mangani, and M. Darwish. *The Finite Volume Method in Computational Fluid Dynamics: An Advanced Introduction with OpenFOAM® and Matlab*. Vol. 113. Fluid Mechanics and Its Applications. Cham: Springer International Publishing, 2016. ISBN: 978-3-319-16873-9 978-3-319-16874-6. DOI: 10.1007/978-3-319-16874-6.

[111] A. Münster. *Classical thermodynamics*. Chichester, New York: Wiley-Interscience, 1970. 387 pp. ISBN: 978-0-471-62430-1.

[112] T. Nakayama. “The Kapitza thermal resistance and tunnelling states of helium atoms”. In: *Journal of Physics C: Solid State Physics* 10.17 (Sept. 14, 1977), pp. 3273–3286. ISSN: 0022-3719. DOI: 10.1088/0022-3719/10/17/011.

[113] Y. S. Ng, J. H. Lee, and W. F. Brooks. “Numerical modeling of Helium-II in forced flow conditions”. In: *Journal of Thermophysics and Heat Transfer* 3.2 (Apr. 1989), pp. 203–212. ISSN: 0887-8722, 1533-6808. DOI: 10.2514/3.149.

[114] T. Noda et al. “Basic Studies on Two-dimensional Heat Transfer Characteristics of He II with Phase Changes (in Japanese)”. In: *Technology Reports of Kyushu University* 73 (Jan. 2000), pp. 53–61.

[115] T. Noda et al. “NUMERICAL STUDY ON HEAT TRANSFER CHARACTERISTICS OF HELIUM II WITH PHASE TRANSITIONS”. In: *Proceeding of International Heat Transfer Conference 11*. International Heat Transfer Conference 11. Kyongju, Korea: Begellhouse, 1998, pp. 219–224. ISBN: 978-1-56032-797-4. DOI: 10.1615/IHTC11.3710.

[116] M. Okabe and K. Ito. “Color Universal Design (CUD) - How to make figures and presentations that are friendly to Colorblind people”. In: *https://jfly.uni-koeln.de/color/* (Nov. 20, 2002).

[117] T. Okamura et al. “Heat transport in He II channel with phase transition”. In: *Cryogenics* 34.3 (Mar. 1994), pp. 187–193. ISSN: 00112275. DOI: 10.1016/0011-2275(94)90168-6.

[118] L. Onsager. “Statistical hydrodynamics”. In: *Il Nuovo Cimento* 6 (S2 Mar. 1949), pp. 279–287. ISSN: 0029-6341, 1827-6121. DOI: 10.1007/BF02780991.

[119] OpenFOAM®. *version 3.0.1*. London, United Kingdom: The OpenFOAM Foundation Ltd.

[120] D. V. Osborne. “The Rotation of Liquid Helium II”. In: *Proceedings of the Physical Society. Section A* 63.8 (Aug. 1, 1950), pp. 909–912. ISSN: 0370-1298. DOI: 10.1088/0370-1298/63/8/315.

[121] S. Patankar and D. Spalding. “A calculation procedure for heat, mass and momentum transfer in three-dimensional parabolic flows”. In: *International Journal of Heat and Mass Transfer* 15.10 (Oct. 1972), pp. 1787–1806. ISSN: 00179310. DOI: 10.1016/0017-9310(72)90054-3.

[122] S. Patankar. *Numerical Heat Transfer and Fluid Flow*. OCLC: 1140143078. 2018. ISBN: 978-1-4822-3421-3 978-1-315-27513-0 978-1-351-99151-3.

[123] V. Peshkov. “Determination of the velocity of propagation of the second sound in helium II”. In: *J. Phys. USSR* 10.1 (1946), pp. 389–398.

[124] J. M. Pfotenhauer and R. J. Donnelly. “Heat transfer in liquid helium”. In: *Advances in heat transfer* 17 (1985), pp. 65–158.

[125] A. B. Pippard. *Elements of classical thermodynamics: for advanced students of physics*. Repr. OCLC: 22321936. Cambridge: Univ. Pr, 1981. 165 pp. ISBN: 978-0-521-09101-5.

[126] S. J. Putterman. *Superfluid hydrodynamics*. North-Holland series in low temperature physics v. 3. Amsterdam : New York: North-Holland Pub. Co. ; American Elsevier Pub. Co, 1974. 443 pp. ISBN: 978-0-444-10681-0.

[127] A. Quarteroni, F. Saleri, and P. Gervasio. *Scientific computing with MATLAB and Octave*. Fourth edition. Texts in computational science and engineering v. 2. Heidelberg: Springer, 2014. 442 pp. ISBN: 978-3-642-45366-3.

[128] N. Ramadan and R. Witt. “Natural convection in large He II baths”. In: *Cryogenics* 34.7 (Jan. 1994), pp. 563–577. ISSN: 00112275. DOI: 10.1016/0011-2275(94)90182-1.

[129] V. F. Rao, K. Fukuda, and H. Horie. “A two-fluid-model analysis on transient, internal-convection heat transfer of He II in a vertical Gorter-Mellink duct heated at the bottom surface”. In: *Cryogenics* 36.6 (June 1996), pp. 457–464. ISSN: 00112275. DOI: 10.1016/0011-2275(96)00003-3.

[130] C. M. Rhie and W. L. Chow. “Numerical study of the turbulent flow past an airfoil with trailing edge separation”. In: *AIAA Journal* 21.11 (Nov. 1983), pp. 1525–1532. ISSN: 0001-1452, 1533-385X. DOI: 10.2514/3.8284.

[131] D. Richter et al. “Evaluation of the Transfer of Heat From the Coil of the LHC Dipole Magnet to Helium II”. In: *IEEE Transactions on Applied Superconductivity* 17.2 (June 2007), pp. 1263–1268. ISSN: 1051-8223. DOI: 10.1109/TASC.2007.898030.

[132] B. Rollin and F. Simon. “On the ”film” phenomenon of liquid helium II”. In: *Physica* 6.2 (Feb. 1939), pp. 219–230. ISSN: 00318914. DOI: 10.1016/S0031-8914(39)80013-1.

[133] H. Rusche. “Computational Fluid Dynamics of Dispersed Two-Phase Flows at High Phase Fractions”. In: *PhD Thesis* (Dec. 2002).

[134] A. Sato, M. Maeda, and Y. Kamioka. “Normalized representation for steady state heat transport in a channel containing He II covering pressure range up to 1.5 MPa”. In: *Proceedings of the Twentieth International Cryogenic Engineering Conference (ICEC20)*. Elsevier, 2005, pp. 849–852. ISBN: 978-0-08-044559-5. DOI: 10.1016/B978-008044559-5/50204-0.

[135] C. Schmidt. “Review of steady-state and transient heat transfer in pool boiling helium I”. In: *Stability of Superconductors in Helium I and Helium II, Proc.of the Workshop, held at Saclay, F, November 16-19, 1981 Paris: Institut International du Froid 1981*. 1981, pp. 17–31.

[136] P. Seyfert, J. Lafferranderie, and G. Claudet. “Time dependent heat transport in subcooled superfluid helium”. In: *Cryogenics* 22.8 (Aug. 1982), pp. 401–408. ISSN: 00112275. DOI: 10.1016/0011-2275(82)90084-4.

[137] M. Shiotsu et al. “Transient Heat Transfer Produced by a Stepwise Heat Input to a Flat Plate on One End of a Rectangular Duct Containing Pressurized Helium II”. In: *Advances in Cryogenic Engineering*. Ed. by Q.-S. Shu. Boston, MA: Springer US, 2000, pp. 1065–1072. ISBN: 978-1-4613-6892-2 978-1-4615-4215-5. DOI: 10.1007/978-1-4615-4215-5_14.

[138] M. Sitko and B. Skoczeń. “Modelling He I–He II phase transformation in long channels containing superconductors”. In: *International Journal of Heat and Mass Transfer* 52.1 (Jan. 2009), pp. 9–16. ISSN: 00179310. DOI: 10.1016/j.ijheatmasstransfer.2008.06.009.

[139] N. Snyder. “Heat transport through helium II: Kapitza conductance”. In: *Cryogenics* 10.2 (Apr. 1970), pp. 89–95. ISSN: 00112275. DOI: 10.1016/0011-2275(70)90077-9.

[140] C. Soulaine et al. “A PISO-like algorithm to simulate superfluid helium flow with the two-fluid model”. In: *Computer Physics Communications* 187 (Feb. 2015), pp. 20–28. ISSN: 00104655. DOI: 10.1016/j.cpc.2014.10.006.

[141] R. Srinivasan and A. Hofmann. “Investigations on cooling with forced flow of He II. Part 1”. In: *Cryogenics* 25.11 (Nov. 1985), pp. 641–651. ISSN: 00112275. DOI: 10.1016/0011-2275(85)90120-1.

[142] H. E. Stanley. *Introduction to phase transitions and critical phenomena*. New York: Oxford University Press, 1987. 308 pp. ISBN: 978-0-19-505316-6.

[143] J. S. Steinhart and S. R. Hart. “Calibration curves for thermistors”. In: *Deep Sea Research and Oceanographic Abstracts* 15.4 (Aug. 1968), pp. 497–503. ISSN: 00117471. DOI: 10.1016/0011-7471(68)90057-0.

[144] M. Sussman, P. Smereka, and S. Osher. “A Level Set Approach for Computing Solutions to Incompressible Two-Phase Flow”. In: *Journal of Computational Physics* 114.1 (Sept. 1994), pp. 146–159. ISSN: 00219991. DOI: 10.1006/jcph.1994.1155.

[145] E. T. Swartz and R. O. Pohl. “Thermal boundary resistance”. In: *Reviews of Modern Physics* 61.3 (July 1, 1989), pp. 605–668. ISSN: 0034-6861. DOI: 10.1103/RevModPhys.61.605.

[146] K. Takamatsu et al. “Numerical study of flow and heat transfer of superfluid helium in capillary channels”. In: *Cryogenics* 37.12 (Dec. 1997), pp. 829–835. ISSN: 00112275. DOI: 10.1016/S0011-2275(97)00136-7.

[147] H. Tatsumoto, K. Fukuda, and M. Shiotsu. “Numerical analysis for steady-state two-dimensional heat transfer from a flat plate at one side of a duct containing pressurized He II”. In: *Cryogenics* 42.1 (Jan. 2002), pp. 9–17. ISSN: 00112275. DOI: 10.1016/S0011-2275(01)00155-2.

[148] H. Tatsumoto, K. Fukuda, and M. Shiotsu. “Numerical analysis for two-dimensional transient heat transfer from a flat plate at one-side of a duct containing pressurized He II”. In: *Cryogenics* 42.1 (Jan. 2002), pp. 19–28. ISSN: 00112275. DOI: 10.1016/S0011-2275(01)00156-4.

[149] J. R. Taylor. *An introduction to error analysis: the study of uncertainties in physical measurements*. 2nd ed. Sausalito, Calif: University Science Books, 1997. 327 pp. ISBN: 978-0-935702-42-2 978-0-935702-75-0.

[150] R. D. Taylor and J. G. Dash. “Hydrodynamics of Oscillating Disks in Viscous Fluids: Viscosities of Liquids He 3 and He 4”. In: *Physical Review* 106.3 (May 1, 1957), pp. 398–403. ISSN: 0031-899X. DOI: 10.1103/PhysRev.106.398.

[151] Tektronix®. *Bench Power and DC Power Supply*. Beaverton, Oregon: Tektronix, Inc.

[152] J. L. Thé, G. D. Raithby, and G. D. Stubley. “Surface-adaptive finite-volume method for solving free surface flows”. In: *Numerical Heat Transfer, Part B: Fundamentals* 26.4 (1994), pp. 367–380. DOI: 10.1080/10407799408914935.

[153] L. Tisza. In: *C. r. hebd. séances Acad. sci. Paris* 207 (1938), pp. 1035, 1186.

[154] L. Tisza. "Transport Phenomena in Helium II". In: *Nature* 141.3577 (May 1938), pp. 913–913. ISSN: 0028-0836, 1476-4687. DOI: 10.1038/141913a0.

[155] L. Tisza. "The thermodynamics of phase equilibrium". In: *Annals of Physics* 13.1 (1961), pp. 1–92.

[156] M. Tsubota, T. Araki, and S. K. Nemirovskii. "Dynamics of vortex tangle without mutual friction in superfluid 4 He". In: *Physical Review B* 62.17 (Nov. 1, 2000), pp. 11751–11762. ISSN: 0163-1829, 1095-3795. DOI: 10.1103/PhysRevB.62.11751.

[157] C. Van den Meijdenberg, K. Taconis, and R. De Bruyn Ouboter. "The entropy of helium II under pressure from measurements on the fountain effect". In: *Physica* 27.2 (Feb. 1961), pp. 197–218. ISSN: 00318914. DOI: 10.1016/0031-8914(61)90042-8.

[158] S. W. Van Sciver. *Helium Cryogenics*. New York, NY: Springer New York, 2012. ISBN: 978-1-4419-9978-8 978-1-4419-9979-5. DOI: 10.1007/978-1-4419-9979-5.

[159] H. K. Versteeg and W. Malalasekera. *An introduction to computational fluid dynamics: the finite volume method*. 2nd ed. OCLC: ocm76821177. Harlow, England ; New York: Pearson Education Ltd, 2007. 503 pp. ISBN: 978-0-13-127498-3.

[160] W. F. Vinen. "Mutual friction in a heat current in liquid helium II III. Theory of the mutual friction". In: *Proceedings of the Royal Society of London. Series A. Mathematical and Physical Sciences* 242.1231 (Nov. 19, 1957), pp. 493–515. ISSN: 0080-4630, 2053-9169. DOI: 10.1098/rspa.1957.0191.

[161] W. F. Vinen. "Mutual friction in a heat current in liquid helium II. II. Experiments on transient effects". In: *Proceedings of the Royal Society of London. Series A. Mathematical and Physical Sciences* 240.1220 (Apr. 24, 1957), pp. 128–143. ISSN: 0080-4630, 2053-9169. DOI: 10.1098/rspa.1957.0072.

[162] A. Vitrano, R. Bruce, and B. Baudouy. "Transient Conjugate Heat Transfer Numerical Simulation in Superfluid Helium". In: *IOP Conference Series: Materials Science and Engineering* 755 (June 30, 2020), p. 012068. ISSN: 1757-899X. DOI: 10.1088/1757-899X/755/1/012068.

[163] V. R. Voller, C. R. Swaminathan, and B. G. Thomas. "Fixed grid techniques for phase change problems: A review". In: *International Journal for Numerical Methods in Engineering* 30.4 (Sept. 1990), pp. 875–898. ISSN: 0029-5981, 1097-0207. DOI: 10.1002/nme.1620300419.

[164] V. Voller. "An implicit enthalpy solution for phase change problems: with application to a binary alloy solidification". In: *Applied Mathematical Modelling* 11.2 (Apr. 1987), pp. 110–116. ISSN: 0307904X. DOI: 10.1016/0307-904X(87)90154-5.

[165] V. Voller and C. Prakash. “A fixed grid numerical modelling methodology for convection-diffusion mushy region phase-change problems”. In: *International Journal of Heat and Mass Transfer* 30.8 (Aug. 1987), pp. 1709–1719. ISSN: 00179310. DOI: 10.1016/0017-9310(87)90317-6.

[166] S. van der Walt and N. Smith. “A Better Default Colormap for Matplotlib”. In: *https://www.youtube.com/watch?v=xAoljeRJ3lU* (July 8, 2015).

[167] J. Wilks. *The Properties of Liquid and Solid Helium*. International series of monographs on physics. Clarendon P., 1967.

[168] M. Wilson. *Cryogenics and Practical Matters*. Joint Universities Accelerator School 2015.

[169] M. Wolfke and W. H. Keesom. “On the Change of the Dielectric Constant of Liquid Helium with the Temperature”. In: *Koninklijke Akad. van Wetenschappen* (1928).

[170] M. Wörner. “Numerical modeling of multiphase flows in microfluidics and micro process engineering: a review of methods and applications”. In: *Microfluidics and Nanofluidics* 12.6 (May 2012), pp. 841–886. ISSN: 1613-4982, 1613-4990. DOI: 10.1007/s10404-012-0940-8.

Appendix

APPENDIX A

He II Experiments

A.1 Temperature Evolutions

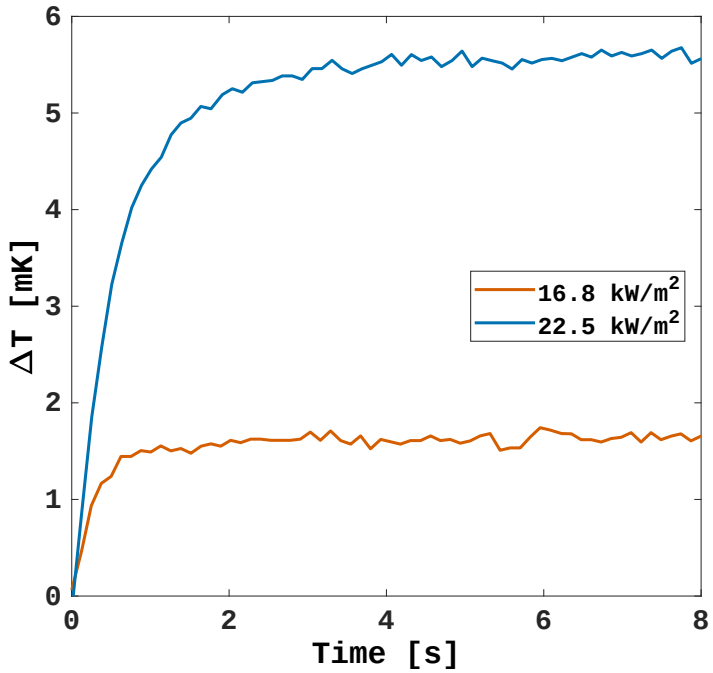

Figure A.1: Temperature evolution of the sensor behind the heater in the 0.2 mm thick channel at a bath temperature $T_b = 1.8$ K and two different heat fluxes.

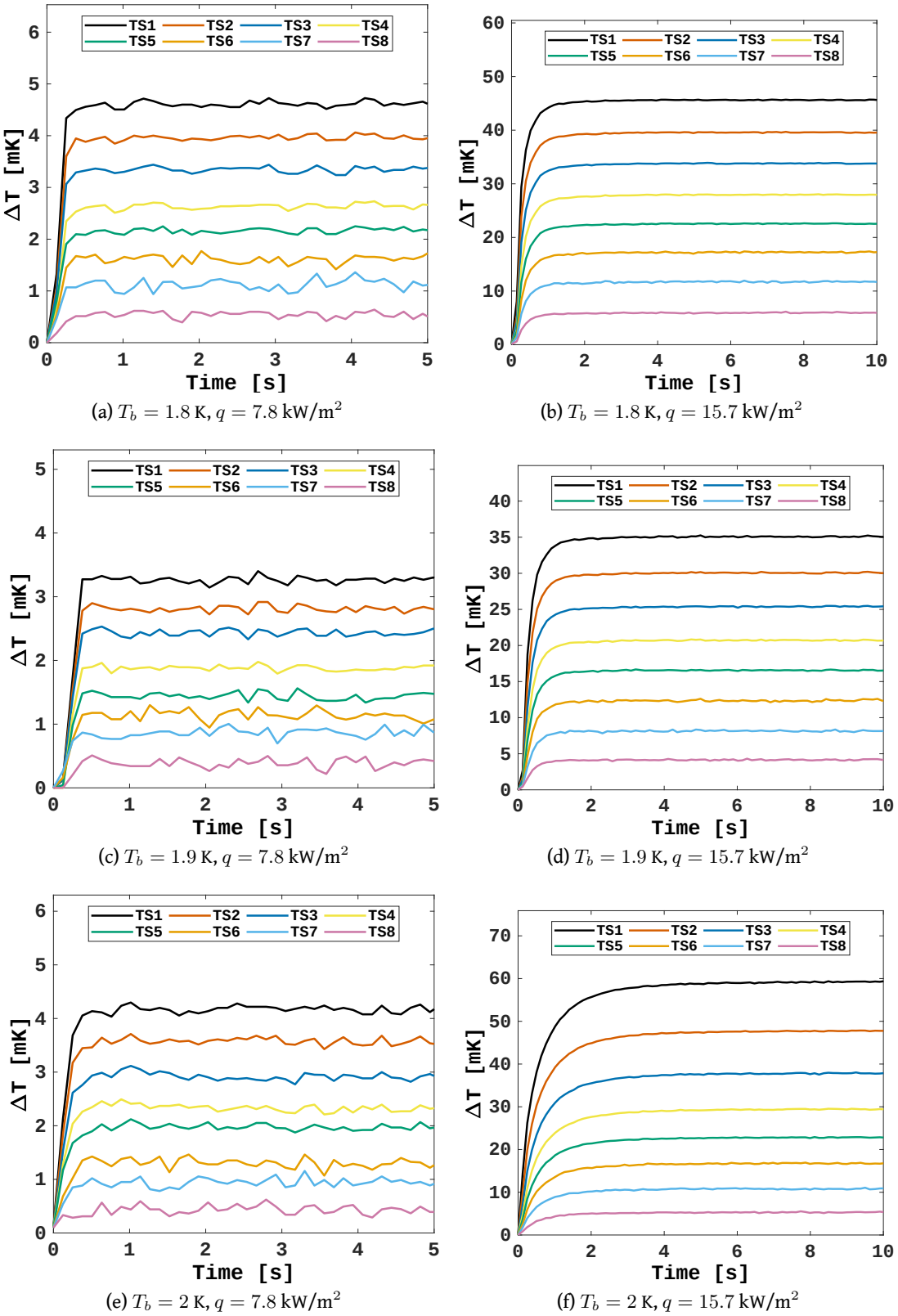

(a) $T_b = 1.8\,\mathrm{K}$, $q = 7.8\,\mathrm{kW/m^2}$

(b) $T_b = 1.8\,\mathrm{K}$, $q = 15.7\,\mathrm{kW/m^2}$

(c) $T_b = 1.9\,\mathrm{K}$, $q = 7.8\,\mathrm{kW/m^2}$

(d) $T_b = 1.9\,\mathrm{K}$, $q = 15.7\,\mathrm{kW/m^2}$

(e) $T_b = 2\,\mathrm{K}$, $q = 7.8\,\mathrm{kW/m^2}$

(f) $T_b = 2\,\mathrm{K}$, $q = 15.7\,\mathrm{kW/m^2}$

Figure A.2: Temperature evolution in the horizontal 0.5 mm thick channel at different bath temperatures T_b and heat fluxes q.

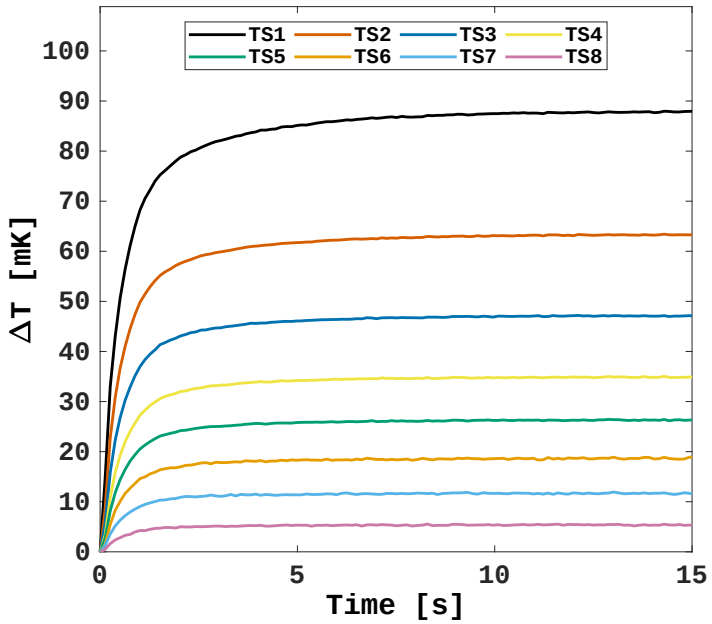

(a) Downward Heat Flux

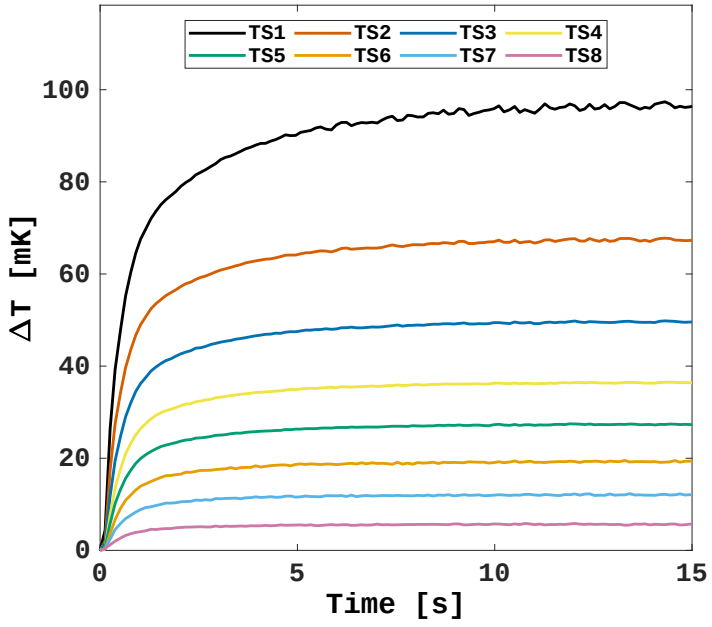

(b) Upward Heat Flux

Figure A.3: Temperature evolution comparison between the two orientations of the vertical 0.2 mm thick channel at a bath temperature $T_b = 2$ K and a heat flux $q = 16.9$ kW/m^2.

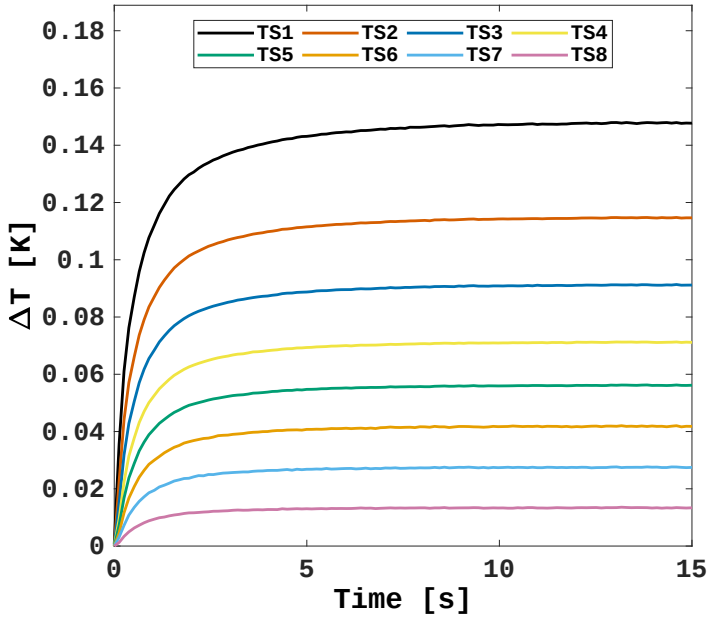

(a) Without pressure sensors

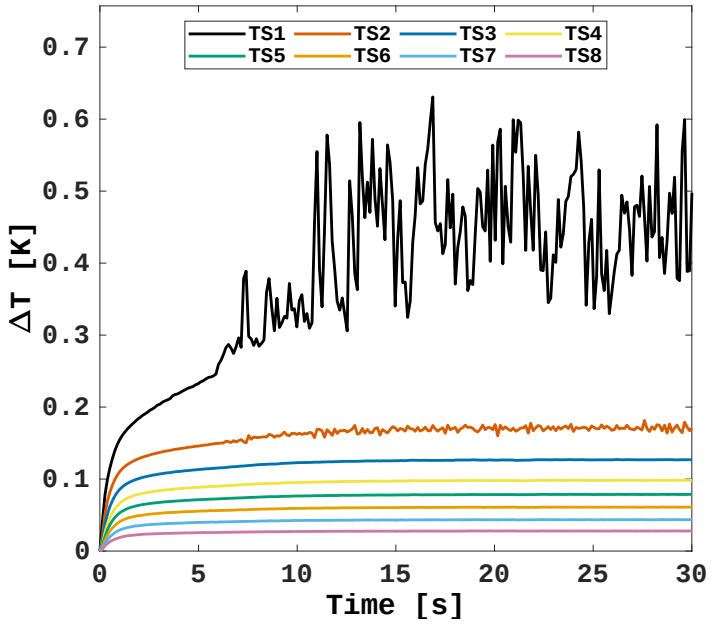

(b) With pressure sensors

Figure A.4: Temperature evolution comparison between two tests run in the 0.2 mm thick channel at a bath temperature $T_b = 1.9\,\mathrm{K}$ and a heat flux $q = 22.6\,\mathrm{kW/m^2}$ with the pressure sensors switched off (a) and on (b).

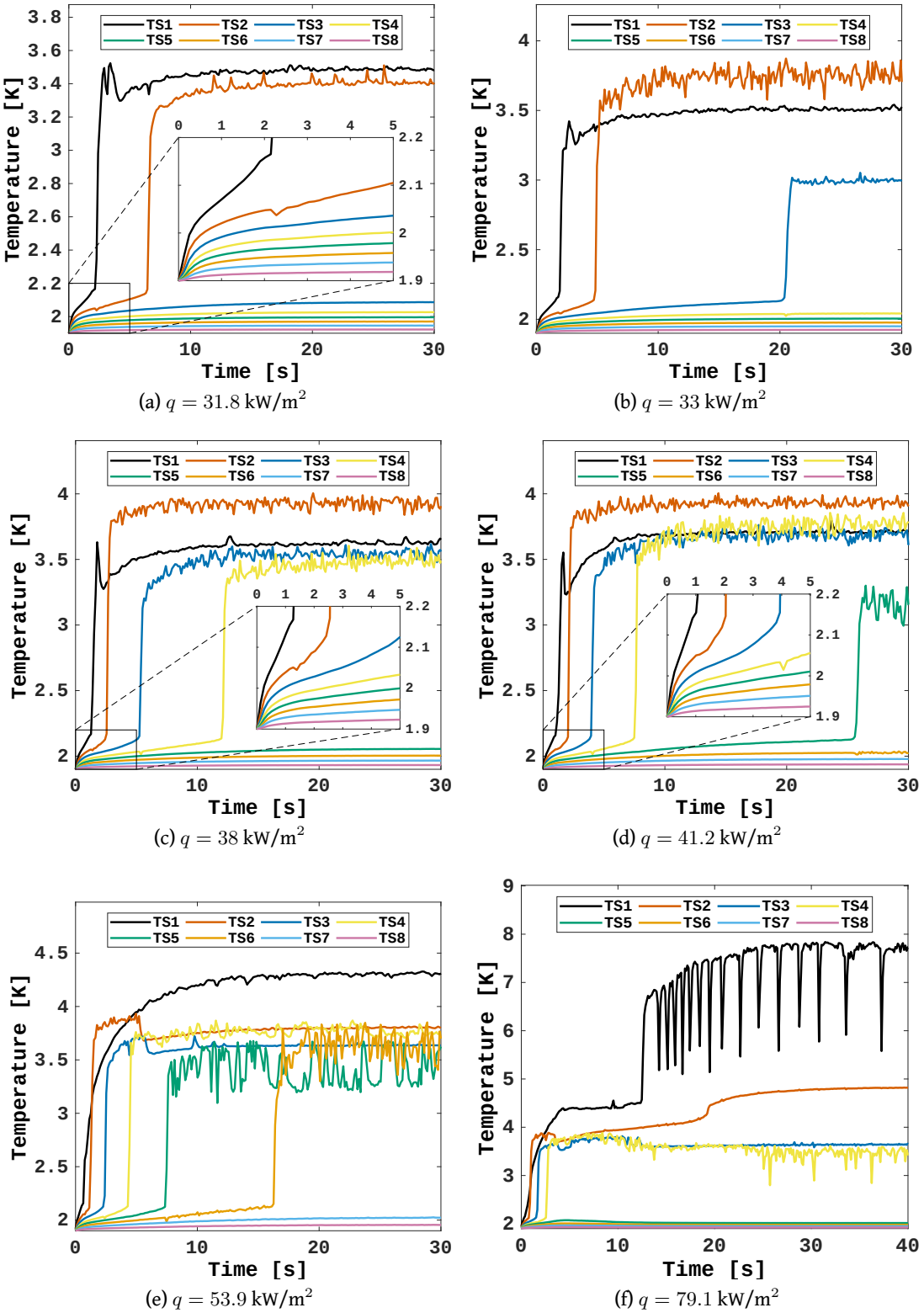

(a) $q = 31.8\ \mathrm{kW/m^2}$ (b) $q = 33\ \mathrm{kW/m^2}$

(c) $q = 38\ \mathrm{kW/m^2}$ (d) $q = 41.2\ \mathrm{kW/m^2}$

(e) $q = 53.9\ \mathrm{kW/m^2}$ (f) $q = 79.1\ \mathrm{kW/m^2}$

Figure A.5: Temperature evolution in the horizontal 0.2 mm thick channel at $T_b = 1.9$ K and different heat fluxes q.

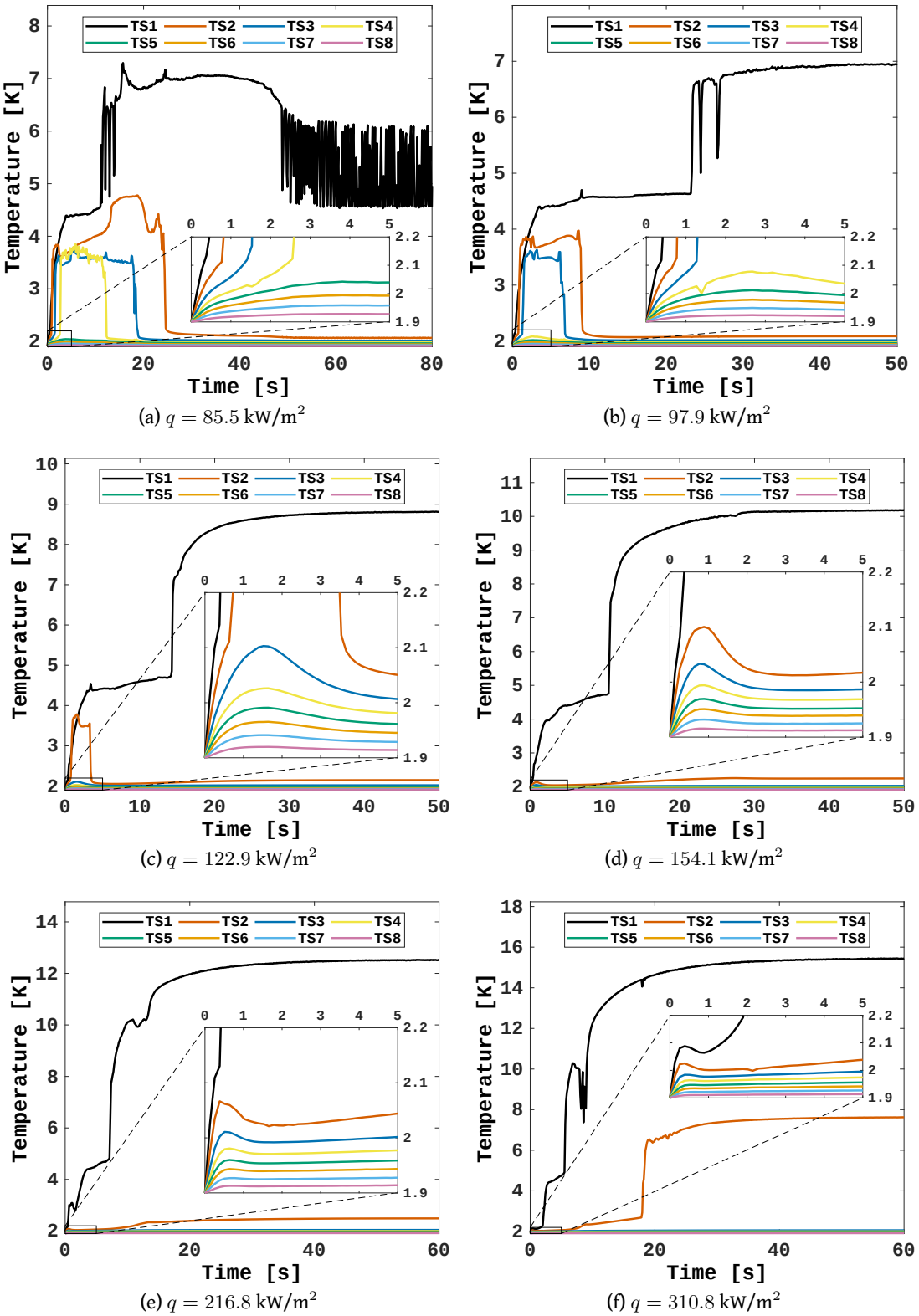

(a) $q = 85.5\ \mathrm{kW/m^2}$ (b) $q = 97.9\ \mathrm{kW/m^2}$

(c) $q = 122.9\ \mathrm{kW/m^2}$ (d) $q = 154.1\ \mathrm{kW/m^2}$

(e) $q = 216.8\ \mathrm{kW/m^2}$ (f) $q = 310.8\ \mathrm{kW/m^2}$

Figure A.6: Temperature evolution in the horizontal 0.2 mm thick channel at $T_b = 1.9$ K and different heat fluxes q.

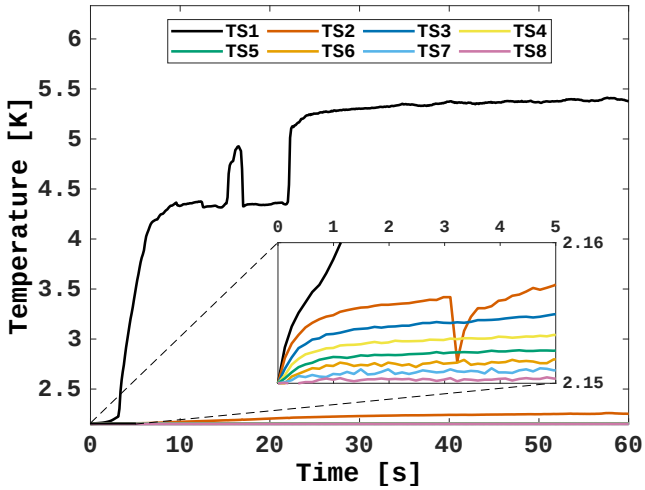

(a) $q = 36.1\ \mathrm{kW/m^2}$

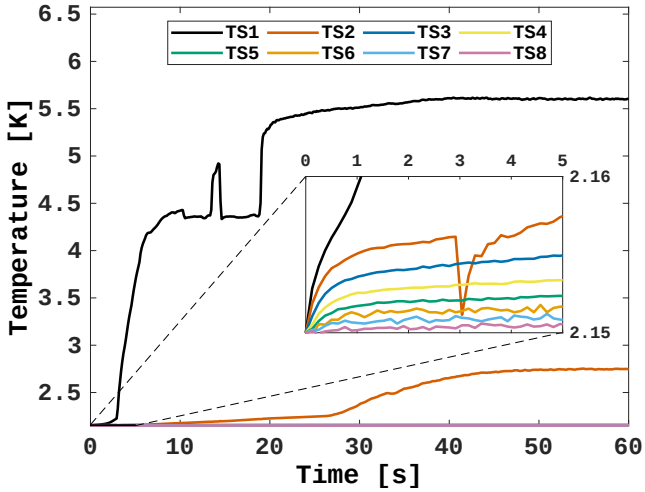

(b) $q = 39.2\ \mathrm{kW/m^2}$

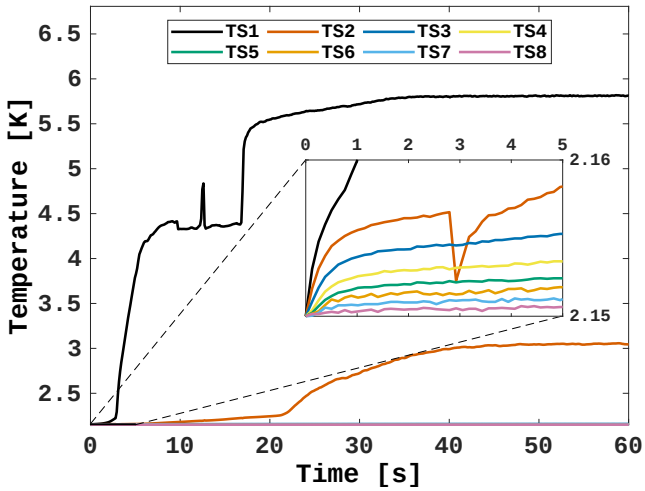

(c) $q = 42.2\ \mathrm{kW/m^2}$

Figure A.7: Temperature evolution in the horizontal 0.2 mm thick channel at $T_b = 2.15$ K and different heat fluxes q. The temperature bump around the saturation temperature occurs systematically in a certain range of heat currents.

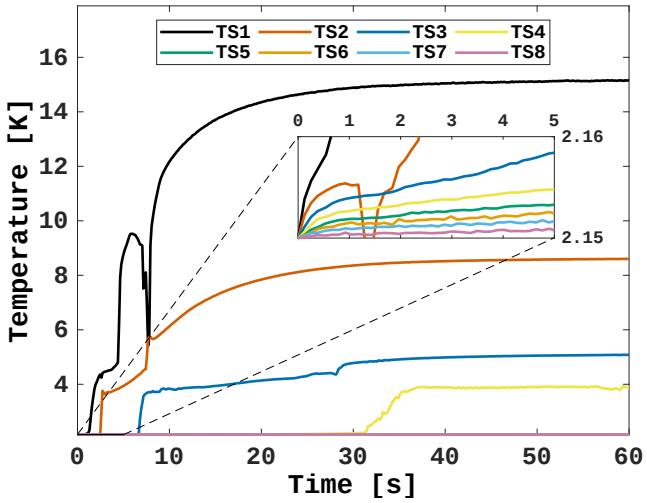

(a) $q = 279.5\ \mathrm{kW/m^2}$

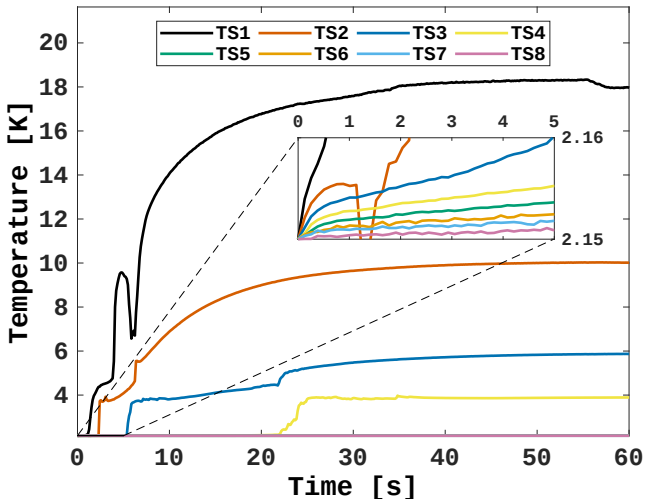

(b) $q = 373.5\ \mathrm{kW/m^2}$

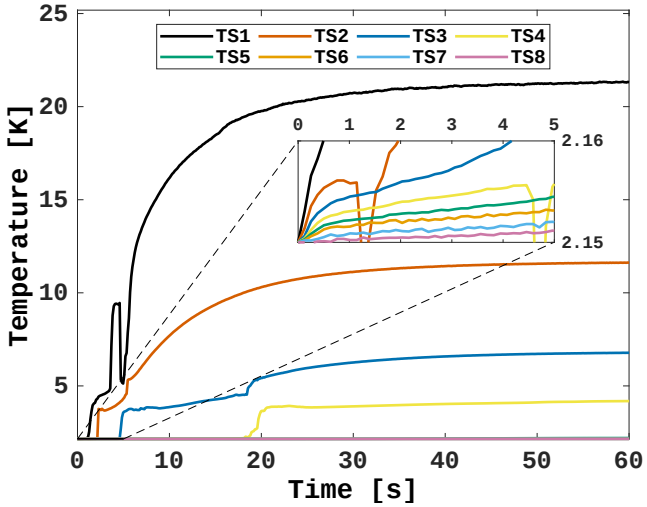

(c) $q = 498.6\ \mathrm{kW/m^2}$

Figure A.8: Temperature evolution in the horizontal 0.2 mm thick channel at $T_b = 2.15$ K and different heat fluxes q. The temperature bump after the saturation temperature occurs systematically in a certain range of heat currents.

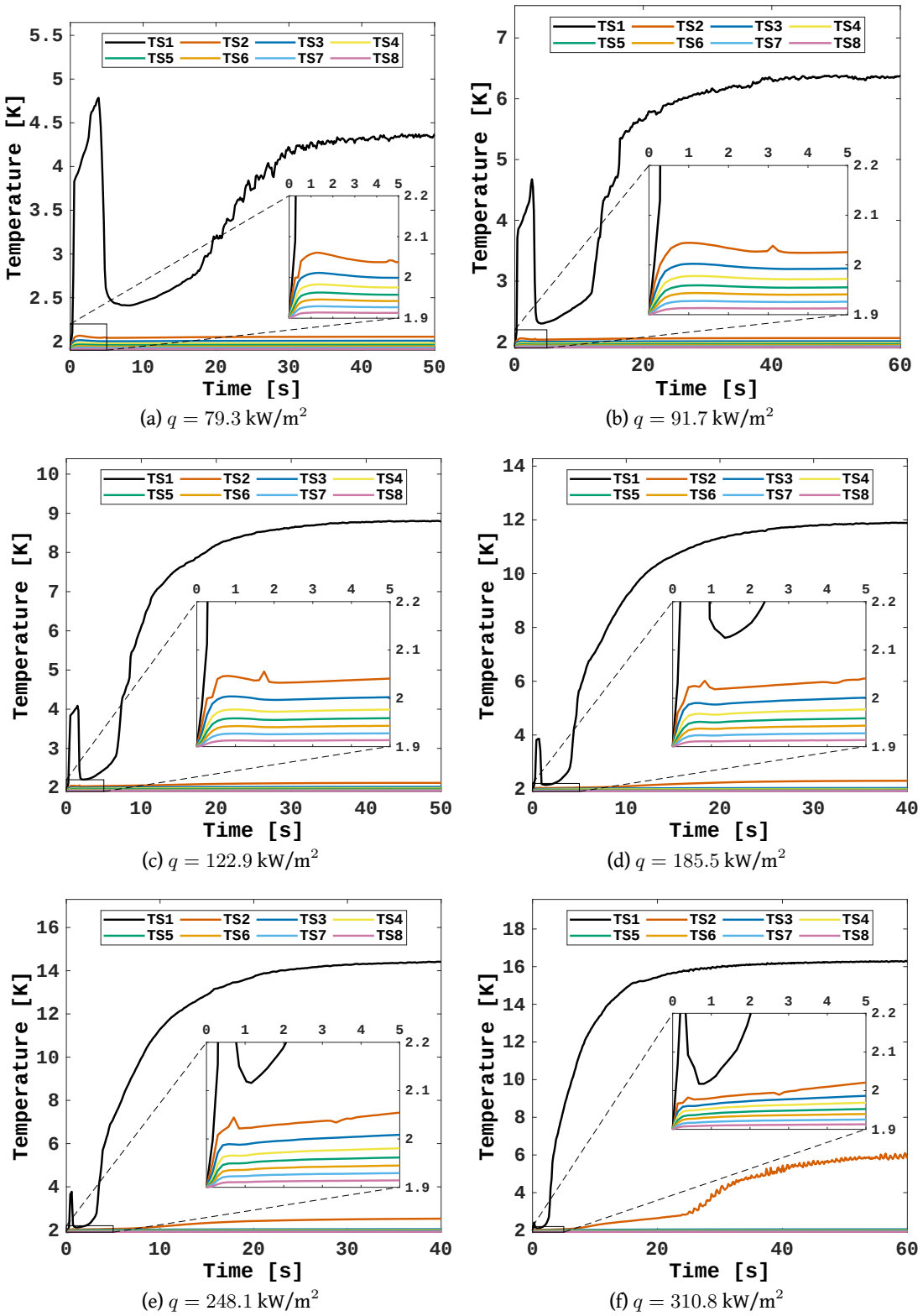

(a) $q = 79.3\ \mathrm{kW/m^2}$ (b) $q = 91.7\ \mathrm{kW/m^2}$

(c) $q = 122.9\ \mathrm{kW/m^2}$ (d) $q = 185.5\ \mathrm{kW/m^2}$

(e) $q = 248.1\ \mathrm{kW/m^2}$ (f) $q = 310.8\ \mathrm{kW/m^2}$

Figure A.9: Temperature evolution in the vertical 0.2 mm thick channel at $T_b = 1.9$ K and different downward heat fluxes q.

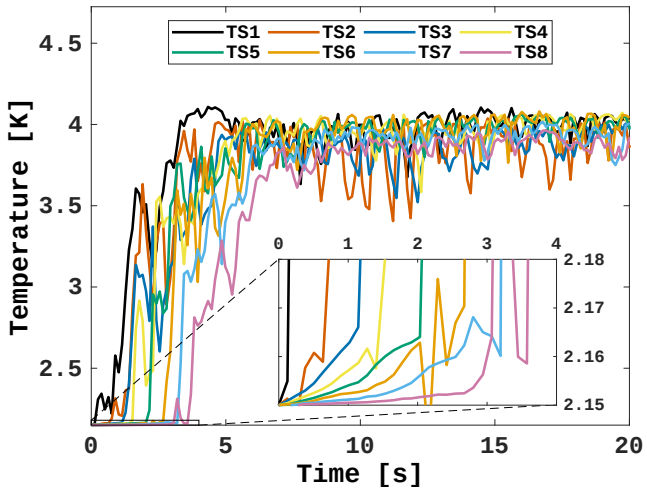

(a) $q = 35.4\ \mathrm{kW/m^2}$

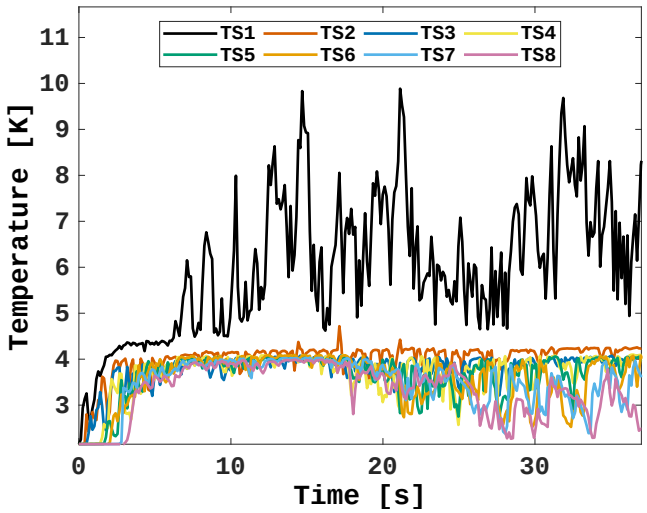

(b) $q = 154.2\ \mathrm{kW/m^2}$

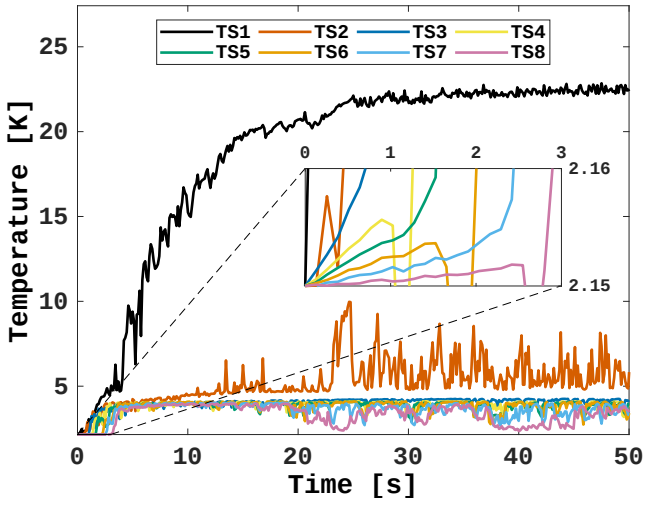

(c) $q = 560.9\ \mathrm{kW/m^2}$

Figure A.10: Temperature evolution in the vertical 0.2 mm thick channel at $T_b = 2.15$ K and different upward heat fluxes q.

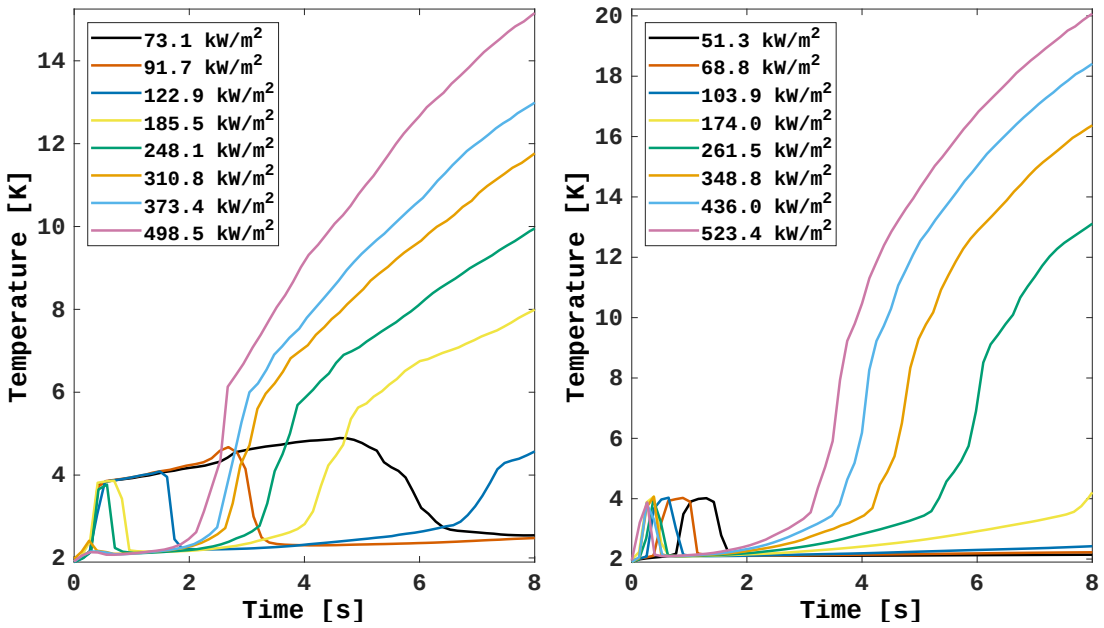

(a) 0.2 mm thick channel (b) 0.5 mm thick channel

Figure A.11: Comparison of TS1 between the two channels in vertical position for various downward heat fluxes.

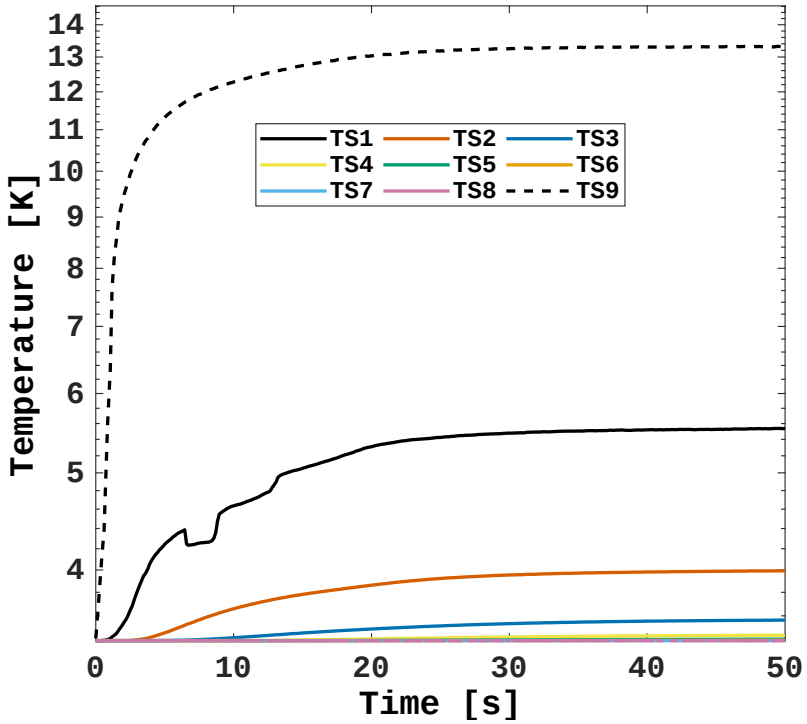

Figure A.12: Temperature evolution in the downward vertical 0.5 mm thick channel at $T_b = 3.4$ K and the heater at 13.4 K.

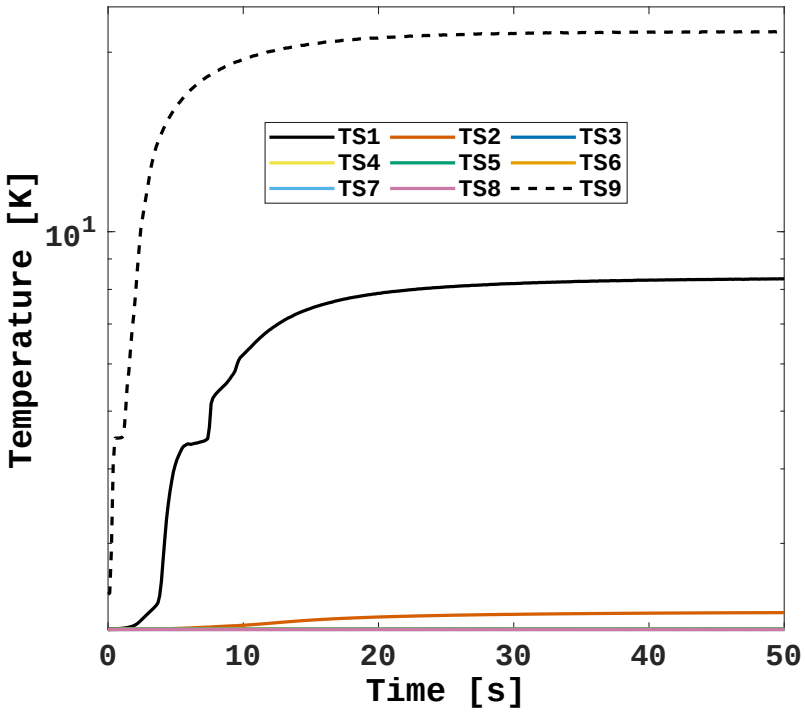

Figure A.13: Temperature evolution in the downward vertical 0.5 mm thick channel at $T_b = 2.15$ K and the heater at 21.6 K.

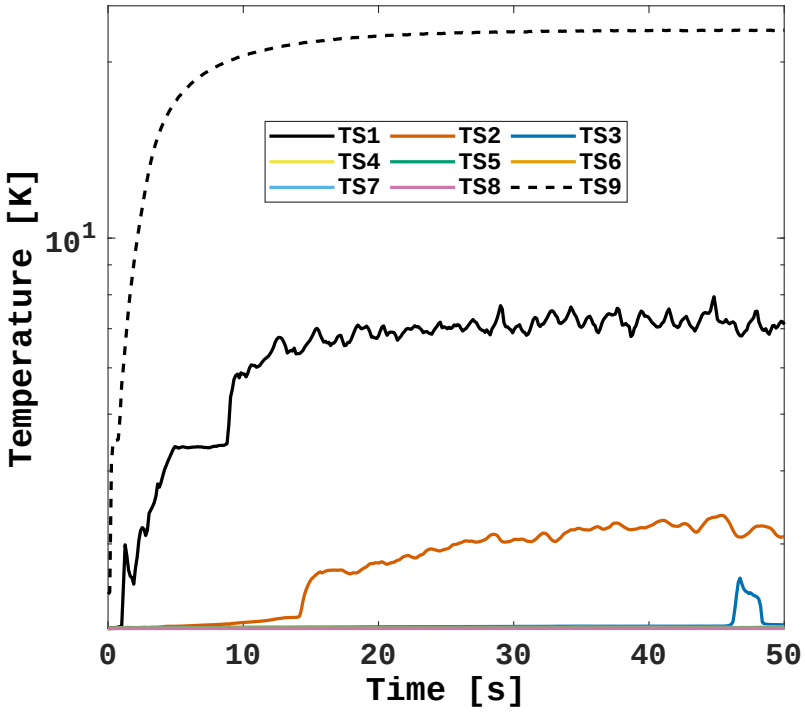

Figure A.14: Temperature evolution in the horizontal 0.5 mm thick channel at $T_b = 2.15$ K and the heater at 22.7 K.

A.2 Temperature Profiles

The differences in the steady state profiles are due to the difficulty to reproduce the same exact dissipated energy at each experimental session. The heat fluxes applied differ, indeed, in few tens of W/m^2.

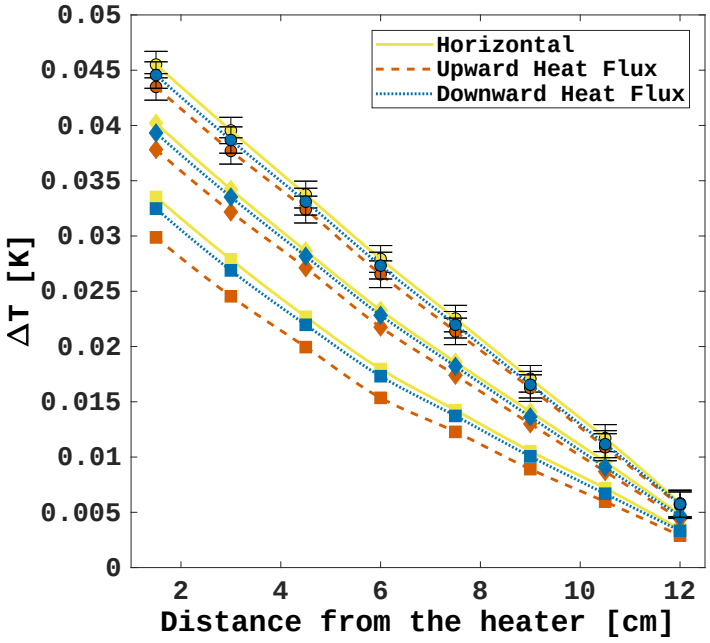

(a) $T_b = 1.8$ K

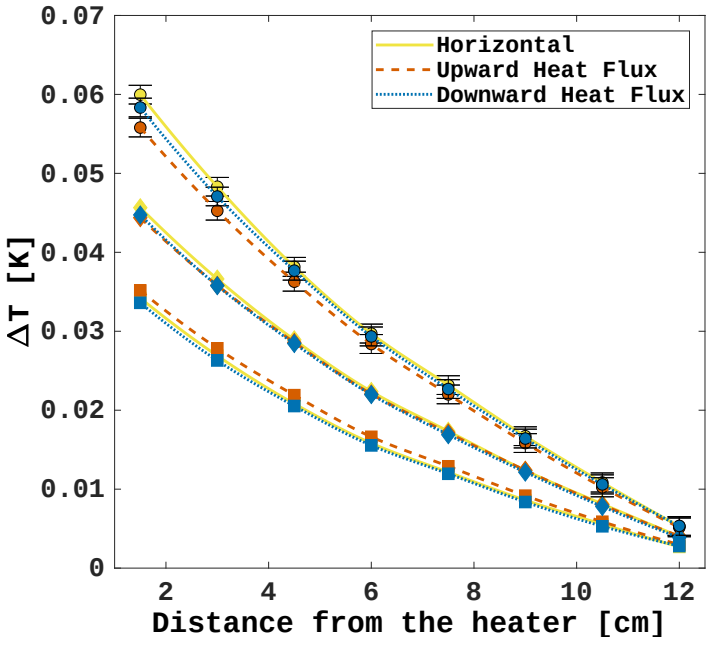

(b) $T_b = 2$ K

Figure A.15: Temperature profile comparison between different orientations of the 0.5 mm thick channel at different bath temperatures and a heat flux $q = 15.7$ kW/m^2. The profiles are presented for different moments of the transient: (a) 0.2 s (squares), 0.4 s (diamonds), steady state (circles); (b) 0.4 s (squares), 0.8 s (diamonds), steady state (circles). The lines are computed through the piecewise cubic Hermite interpolation.

APPENDIX *B*

Analysis and Simulations

B.1 Heat Leaks Study

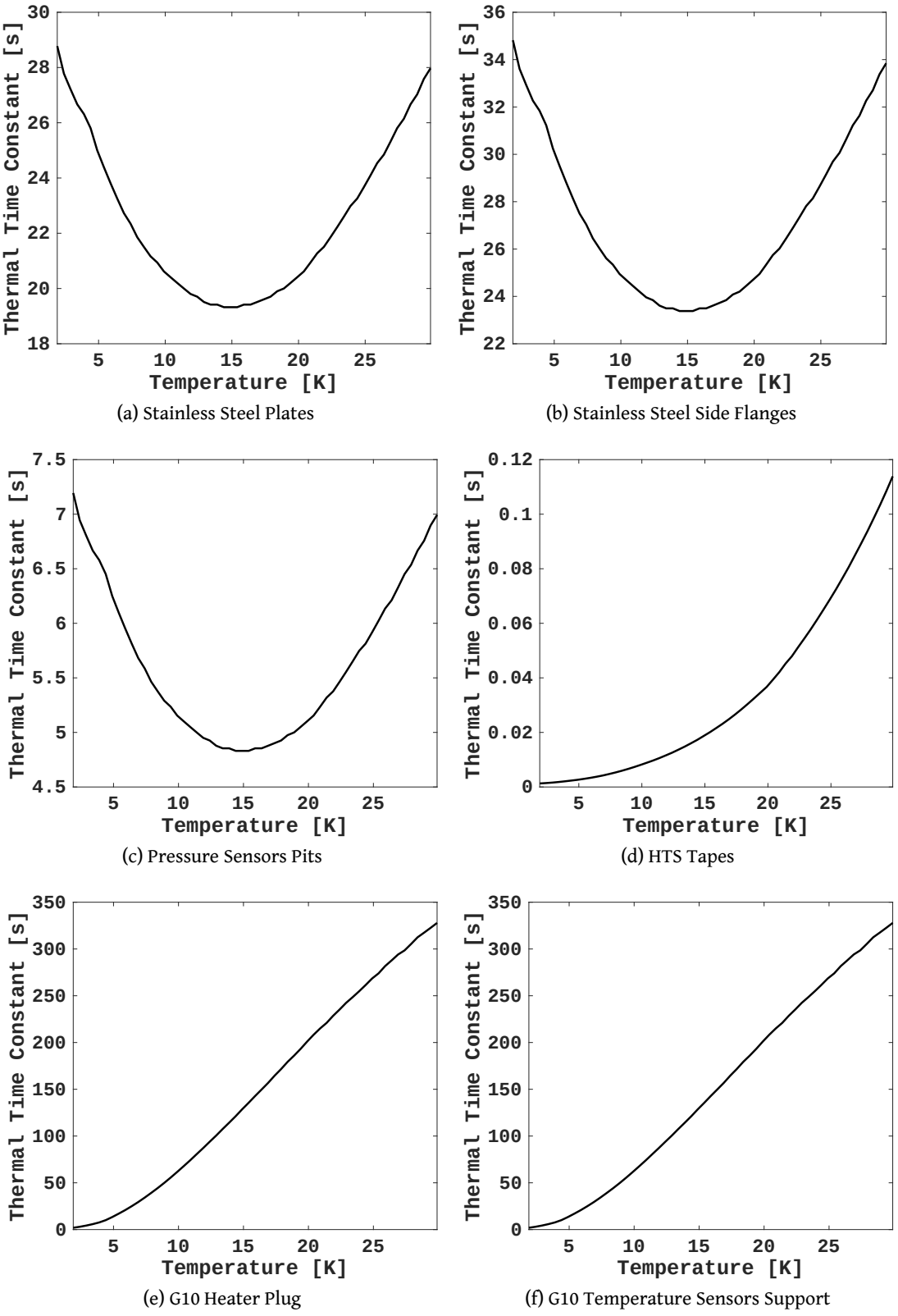

(a) Stainless Steel Plates

(b) Stainless Steel Side Flanges

(c) Pressure Sensors Pits

(d) HTS Tapes

(e) G10 Heater Plug

(f) G10 Temperature Sensors Support

Figure B.1: Thermal time constant of the solid parts surrounding the helium channel.

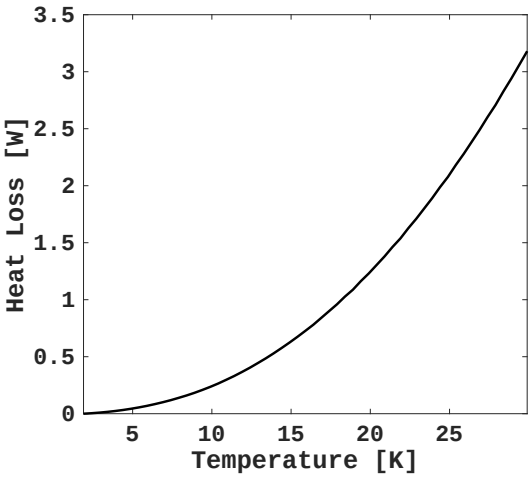

(a) Stainless Steel Plates (until TS1)

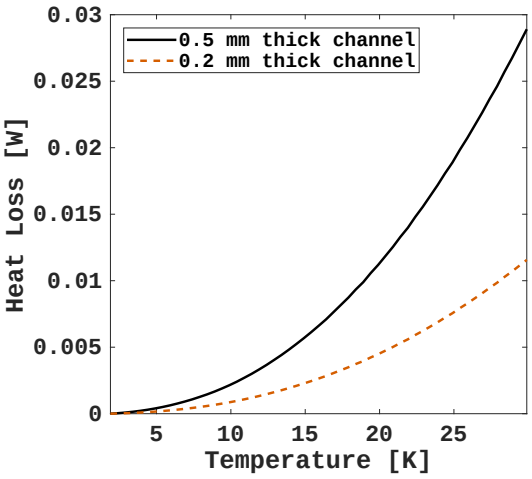

(b) Stainless Steel Side Flanges (until TS1)

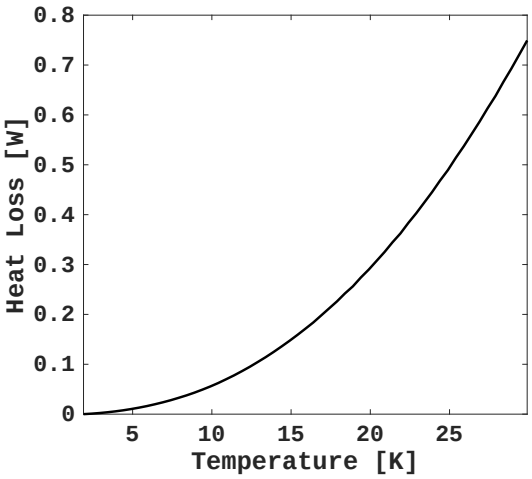

(c) Pressure Sensors Pits

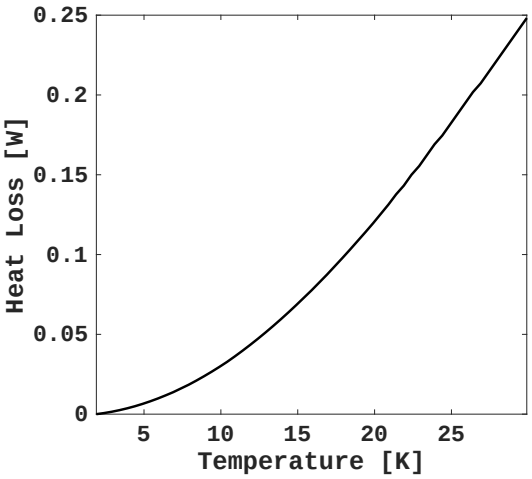

(d) HTS Tapes

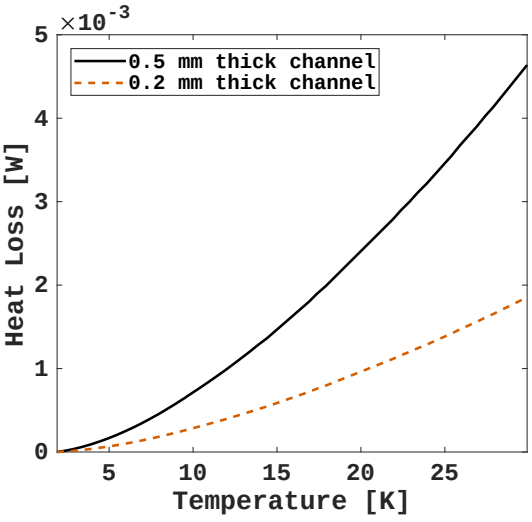

(e) G10 Heater Plug

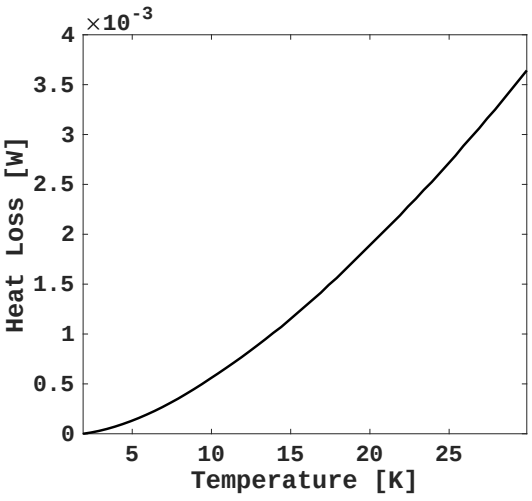

(f) G10 Temperature Sensors Support

Figure B.2: Heat leaks through the solid parts surrounding the helium channel.

B.2 Computational Domains

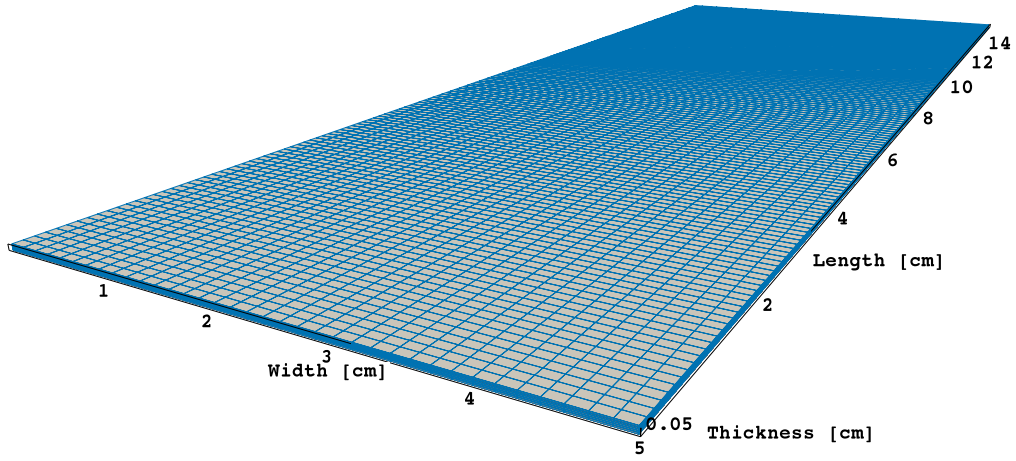

Figure B.3: 3D computational model of the 0.5 mm thick channel. Regular structured grid constituted by $36 \times 150 \times 5$ elements.

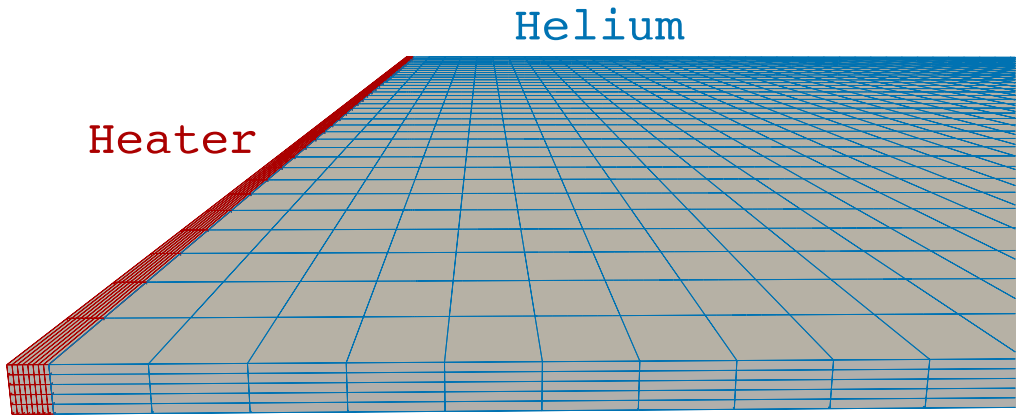

Figure B.4: Cutout of the 3D computational model of the 0.5 mm thick channel including the Manganin® strip. Regular structured grid constituted by $36 \times 158 \times 5$ elements.

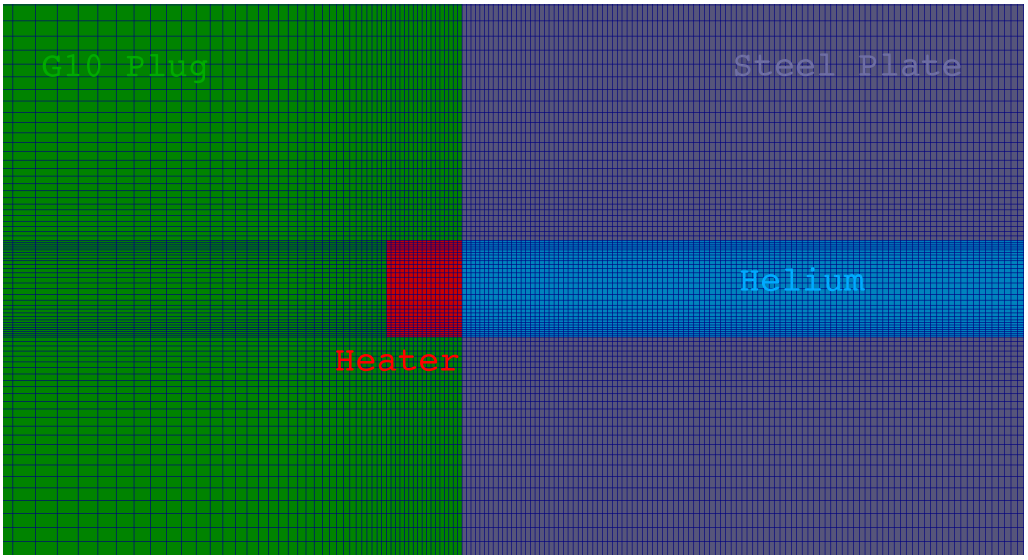

Figure B.5: Close-up picture of the mesh of the channel setup model. It accounts for 303864 hexahedra in total, with a cell size in the direction of the channel length of 35 µm.

B.3 Simulations

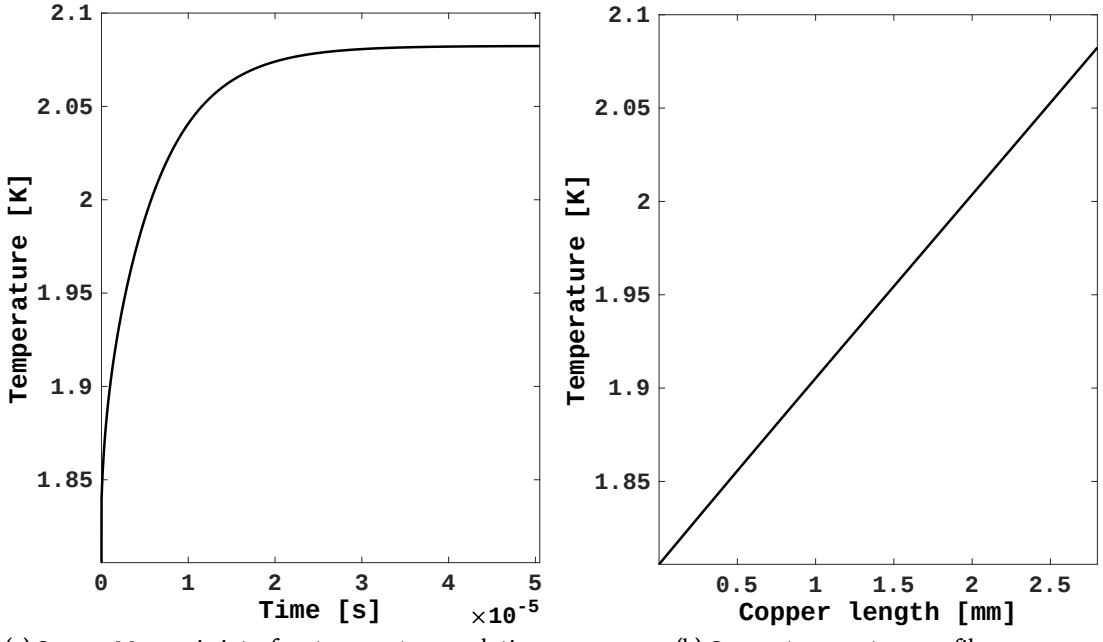

(a) Copper-Manganin interface temperature evolution

(b) Copper temperature profile

Figure B.6: One-dimensional simulation of the copper piece housing TS9: (a) temperature evolution at the interface with the heater; (b) steady state temperature profile. The boundary conditions refer to the test in the horizontal 0.2 mm thick channel at a bath temperature $T_b = 1.8$ K and a heat flux $q = 22.5$ kW/m^2.

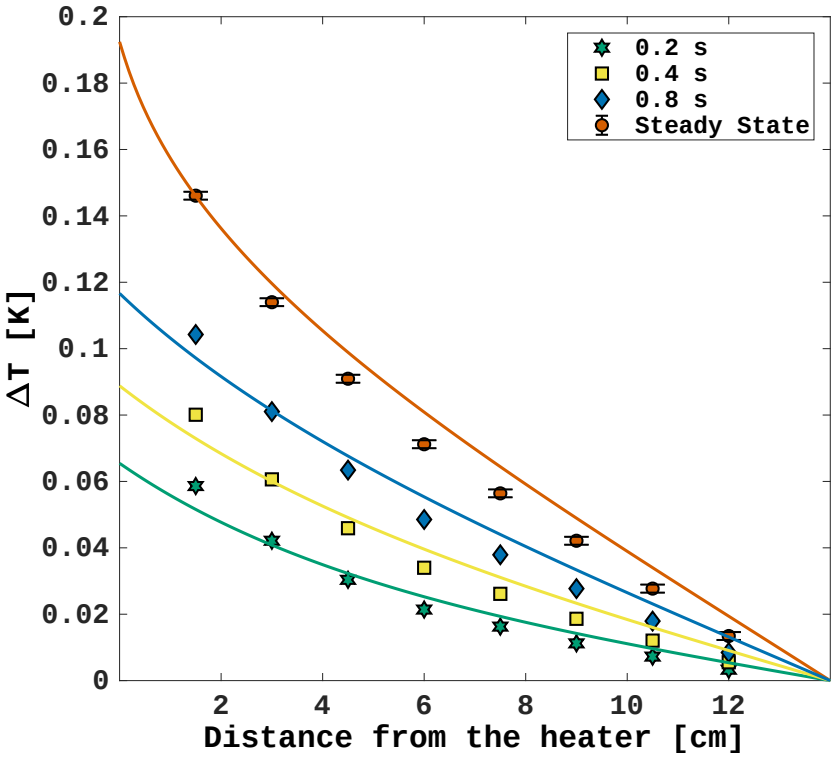

Figure B.7: Transient temperature profiles comparison between *heliumChtFoam* and data from an experiment in the vertical 0.2 mm thick channel at a bath temperature $T_b = 1.9$ K and a downward heat flux $q = 22.6$ kW/m^2.

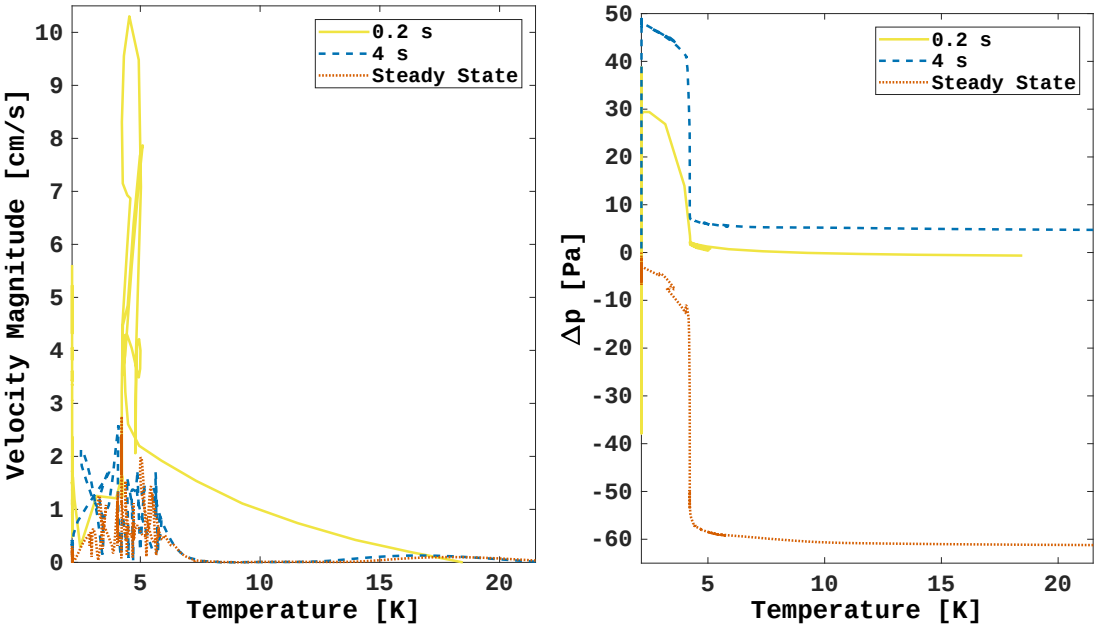

(a) Velocity Magnitude (b) Pressure Difference

Figure B.8: Simulated velocity and pressure as a function of temperature at the centerline of the downward vertical 0.5 mm thick channel at a bath temperature $T_b = 2.15$ K and the heater at 21.6 K.

B.4 Correction Algorithm Analysis

It is interesting to make a few considerations about the applicability and efficiency of the Newton-Raphson method to this particular problem. Since all the parameters on the RHS of Eqs. (5.10a) and (5.10b) are known at each time step, let us group them into a coefficient B, which is always non-negative. Let us consider then the following function:

$$f(\gamma) = B\gamma^{\frac{1}{n}} + \gamma - 1. \tag{B.1}$$

Fig. B.9 shows the function $f(\gamma)$ for two plausible values of B and $n = 3.4$. We are interested in finding the root γ_0 of $f(\gamma)$, which will be the result of the nonlinear equation. The Newton-Raphson method searches for the roots of a given function by iteratively computing its tangent at a spot that is closer to the root at each iteration. The convergence of this method strongly depends on the initial guess value. For example, the presence of an inflection point between the guess value and the root might make the method diverge. Therefore, it is important to choose a proper guess value γ_g that ensures convergence regardless of the location of the lambda front and hence the value of B. Let us first calculate the first derivative of $f(\gamma)$:

$$f'(\gamma) = \frac{\mathrm{d}f(\gamma)}{\mathrm{d}\gamma} = 1 + \frac{B}{n}\gamma^{\frac{1-n}{n}}. \tag{B.2}$$

Thus, $f'(\gamma)$ is always positive for any B, which means that $f(\gamma)$ has no stationary point, and that the minimum and maximum possible values of γ_0 can be determined through the following limits:

$$\lim_{B\to 0}\left[f(\gamma) = 0\right] \quad \Rightarrow \quad \gamma_0 = 1, \tag{B.3a}$$

$$\lim_{B\to +\infty}\left[f(\gamma) = 0\right] \quad \Rightarrow \quad \lim_{B\to +\infty}\left[\gamma^{\frac{1}{n}} + \frac{\gamma}{B} - \frac{1}{B} = 0\right] \quad \Rightarrow \quad \gamma_0 = 0. \tag{B.3b}$$

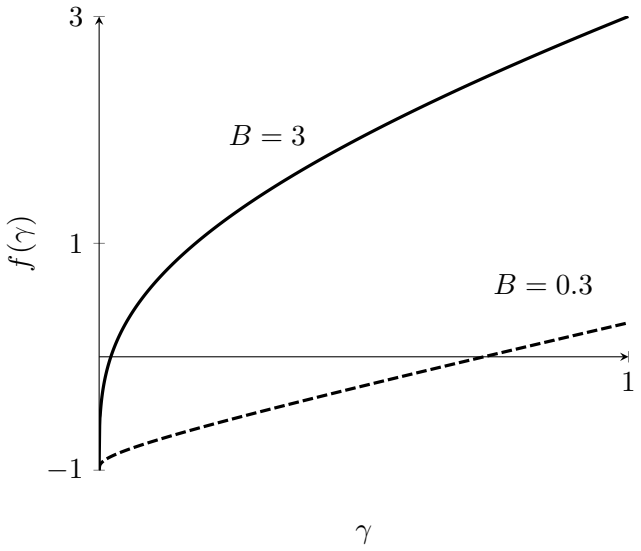

Figure B.9: Function $f(\gamma)$ for $n = 3.4$ and two different values of B.

As initially expected, the values of γ_0 range from 0 to 1 for any B.

In the Newton-Raphson method, the new guess value $\gamma_{g,new}$ is calculated at each iteration as follows:

$$\gamma_{g,new} = \gamma_g - \frac{f(\gamma_g)}{f'(\gamma_g)}. \tag{B.4}$$

When the difference between $\gamma_{g,new}$ and γ_g is below a pre-defined tolerance tol, the loop is stopped. Because of the degree of Eq. (B.1), γ_g has to be always non-negative for $f(\gamma_g)$ to be computed numerically. Moreover, for γ_g that tends to 0, $f'(\gamma)$ tends to infinite, giving rise to floating point error. This means that $\gamma_{g,new}$ at each iteration has to be always positive:

$$\gamma_{g,new} > 0 \quad \Rightarrow \quad \gamma_g < \left[\frac{n}{(n-1)\,B}\right]^n. \tag{B.5}$$

For B tending to infinite, γ_g tends to 0, which means that above a certain value B_{tol} such that

$$f(tol) = 0 \quad \Rightarrow \quad B_{tol} = \frac{1 - tol}{tol^{\frac{1}{n}}}, \tag{B.6}$$

γ_g will be less than the tolerance value, making the loop pointless. Therefore, for $B \geq B_{tol}$, γ_0 is set to tol. When $B < B_{tol}$, if tol is also used as the initial value for γ_g, then Eq. (B.5) requires that

$$tol < \left[\frac{n}{(n-1)\,B}\right]^n \quad \Rightarrow \quad B_{max} = \frac{n}{(n-1)\,tol^{\frac{1}{n}}}, \tag{B.7}$$

where B_{max} is the maximum value of B that allows the use of tol as initial value for γ_g. It is thus necessary that $B_{tol} \leq B_{max}$, which imposes the following condition on tol:

$$tol \geq \frac{1}{1-n}. \tag{B.8}$$

Since n is either equal to 3 or 3.4, Eq. (B.8) is always met regardless of the desired order of accuracy for the algorithm.

The inequality (B.5) sets a condition on the initial guess value to properly initiate the loop. However, this is not enough to ensure the convergence of the algorithm. In order to check so, let us calculate the second derivative of $f(\gamma)$ as

$$f''(\gamma) = \frac{\mathrm{d}^2 f(\gamma)}{\mathrm{d}\gamma^2} = \frac{B\,(1-n)}{n^2}\gamma^{\frac{1-2n}{n}}. \tag{B.9}$$

Considering the possible values of n, it is clear that $f''(\gamma)$ is always non-positive. This means that $f''(\gamma)$ never changes sign and hence $f(\gamma)$ has no inflection point. Therefore, as long as the condition in (B.5) is satisfied, the loop will surely converge to the root.

As a last consideration, it is useful to qualitatively estimate the convergence speed of the algorithm depending on the value of γ_0. Let us analyze how the first guess $\gamma_g = tol$

could affect the number of iterations needed to reach convergence through the following limits:

$$\lim_{B \to B_{tol}} [f(\gamma) = 0] \quad \Rightarrow \quad \gamma_0 \simeq \gamma_g, \tag{B.10a}$$

$$\lim_{B \to 0} \left[f'(\gamma)\right] \quad \Rightarrow \quad f'(\gamma) = 1. \tag{B.10b}$$

The limit (B.10a) indicates that the greater B, the closer the root to the initial guess. Whereas the second limit implies that for B tending to small values, the tangent of the curve tends to a constant value, pointing immediately to an area nearby the root. Therefore, in the limiting cases, the convergence seems to be facilitated.

ANNEXE *C*

Résumé Détaillé

La présente étude porte sur les phénomènes de transfert de chaleur et de masse dans l'hélium superfluide dans deux canaux de section rectangulaire à haut rapport d'aspect. Les deux canaux ont une longueur de 14 cm et une largeur de 5 cm, tandis que leurs épaisseurs sont de 0.5 mm et 0.2 mm. Les expériences ont été menées à la pression atmosphérique dans un bain d'hélium superfluide, où le montage des canaux était submergé. Une ouverture des canaux est fermée par un chauffage, tandis que l'autre est maintenue ouverte au bain. Des composants en acier épais entourant le montage sont destinés à isoler l'hélium contenu dans le canal du bain. Les expériences ont consisté en des tests de flux de chaleur bridés, dans lesquels le réchauffeur libère une charge thermique dans le canal. La température de l'hélium a été enregistrée à huit endroits également espacés le long de la ligne centrale du canal. Les tests ont été effectués à différentes températures de bain (c'est-à-dire 1.8 K, 1.9 K, 2 K, 2.15 K) et orientations du canal (c'est-à-dire horizontale, vers le bas, vers le haut). Le flux thermique appliqué allait de quelques milliers à plusieurs centaines de milliers de watts par mètre carré, afin d'étudier le comportement thermique de He II dans le régime de Gorter-Mellink ainsi que les transitions de phase du premier et du second ordre. La différence d'épaisseur entre les deux canaux a permis d'explorer l'effet du confinement géométrique sur la propagation des fronts de changement de phase en présence de vapeur d'hélium. Contrairement au canal de 0.5 mm d'épaisseur, le nombre de confinement Co associé au canal plus mince est supérieur à une certaine valeur qui est connue pour être le seuil au-delà duquel les effets de confinement influencent la dynamique des écoulements multiphasiques.

Un modèle numérique transitoire basé sur la FVM pour des grilles multidimensionnelles a été développé pour simuler la dynamique thermo-fluide de He II. Les équations du modèle classique à deux fluides ont été étudiées en profondeur pour formuler de nouveaux nombres sans dimension associés à la composante superfluide de He II. Ces nombres ont permis de valider l'hypothèse qui sous-tend les équations directrices mises en œuvre dans le code. Ces équations constituent une version avancée d'un modèle monofluide existant, qui est ici dérivé à nouveau avec une loi de puissance de chaleur

conductrice plus généralisée. Le modèle numérique est également destiné à simuler le transfert de chaleur conjugué entre l'hélium et les solides, ce qui a nécessité la mise en œuvre de conditions aux limites personnalisées pour reproduire la résistance de Kapitza et le glissement partiel superfluide. Ce modèle He II a été enrichi de nouveaux modules pour la simulation des phénomènes de changement de phase. À cette fin, un algorithme pour les grilles orthogonales non uniformes fixes a été conceptualisé pour traiter la transition lambda. La transition de phase du premier ordre a été traitée par un calcul explicite des fractions volumiques du mélange d'hélium et par l'introduction de forces de tension de surface.

C.1 Conclusions

Les travaux expérimentaux et numériques de cette étude permettent de tirer quelques conclusions qui sont résumées dans la liste suivante.

Expériences sur He II

1. L'augmentation maximale de la température enregistrée lors des essais de flux clampé varie clairement avec la température du bain. Plus précisément, l'augmentation à 1.9 K est inférieure à celle mesurée à des températures de bain plus élevées et plus basses. Ceci représente une confirmation expérimentale de la dépendance à la température de la fonction de conductivité thermique de l'He II, dont on sait qu'elle atteint son maximum aux alentours de 1.95 K.

2. L'intégration de la fonction de conductivité thermique avec l'exposant empirique (c'est-à-dire 3.4) à partir d'une certaine température du bain jusqu'au point λ sur la longueur du canal prédit assez précisément la valeur du flux thermique critique nécessaire pour déclencher la transition lambda.

3. Indépendamment de l'épaisseur du canal, l'orientation des canaux à fort rapport d'aspect n'affecte pas de manière significative le gradient de température ou son évolution.

He II Modèle numérique et simulations

1. En manipulant les équations de la dynamique des fluides de l'hélium superfluide, il est possible de dériver des nombres sans dimension (associés à la composante superfluide de He II) qui sont exprimés en termes de flux de chaleur, de vitesse totale et de propriétés thermophysiques uniquement, sans prendre en compte de manière singulière les vitesses des composantes fluides.

2. L'analyse des nombres sans dimension associés à la composante superfluide de l'He II a révélé que la force de friction mutuelle et l'effet thermomécanique ont tendance

à s'égaler pour les flux de chaleur élevés, ce qui légitime l'hypothèse à la base des équations gouvernantes monofluide.

3. Une évaluation comparative des modèles numériques a permis de valider une version modifiée du modèle à fluide unique pour He II avec une erreur relative typique des profils de température transitoire inférieure à 1 %. Ce modèle, qui est un code multidimensionnel basé sur la FVM, comprend une loi de puissance de chaleur conductrice généralisée, dont l'utilisation est étendue à l'équation de quantité de mouvement ainsi qu'à l'équation d'énergie. Le modèle comprend également une condition limite de glissement partiel superfluide personnalisée qui capture le comportement dynamique thermo-fluide correct de He II aux parois.

4. Un module de transfert de chaleur conjugué de type ségrégué lié au modèle He II permet de simuler correctement la relation thermique entre He II et les solides grâce à l'utilisation d'une condition limite de résistance de Kapitza personnalisée, qui passe en douceur d'un régime caractérisé par de faibles différences de température entre l'hélium et le solide à un régime où la différence de température est comparable à la température du bain.

Expériences de transition de phase

1. L'application de flux de chaleur bridés au-dessus de la valeur critique lambda déclenche la transition de phase de second ordre, qui entraîne une augmentation soudaine de la température due à la chute brutale de la capacité thermique spécifique de He II à He I.

2. De la majorité des expériences, on peut déduire que, à presque toutes les températures du bain, dans les canaux minces de rapports d'aspect élevés, le flux de chaleur minimum nécessaire pour déclencher la transition de phase de second ordre est suffisamment important pour initier également l'ébullition. A la température de saturation, la température du mélange fluide connaît une évolution régulière due à la chaleur latente de vaporisation. La durée et la pente de cette évolution sont affectées par le flux thermique : plus le flux thermique est élevé, plus l'évolution est courte et raide à un certain endroit.

3. Des profils de température en régime permanent très différents peuvent être distingués dans le canal confiné horizontal en fonction du flux thermique appliqué. En subdivisant qualitativement les flux de chaleur en valeurs faibles, modérées et élevées, on peut distinguer trois zones phénoménologiques différentes. L'augmentation du flux thermique a des effets différents dans chaque zone (voir Fig. 6.1) : la phase He I occupe une partie croissante du canal, tandis que la vapeur d'hélium est confinée à côté de l'élément chauffant (zone basse) ; la région He I se raccourcit progressivement après une expansion initiale et He II revient occuper la majorité du canal (zone intermédiaire) ; la phase He I occupe une petite partie du canal entre He

II et la phase vapeur en expansion (zone haute). Ces comportements opposés sont dus à des régimes multiphasiques différents. Aux faibles flux de chaleur, la phase vapeur est constituée de manière hétérogène par de petites régions qui permettent de maintenir un lien thermique direct entre le réchauffeur et He II. En conséquence, le taux de transformation He II-He I croît proportionnellement au flux de chaleur et, par conséquent, la phase He I se dilate rapidement. À des flux de chaleur modérés, les régions de vapeur coalescent lentement en un film isolant homogène qui recouvre l'élément chauffant (c'est-à-dire l'ébullition du film) et interrompt le transfert de chaleur vers He II. Il s'ensuit que la propagation du front λ ralentit et s'arrête plus tôt avant de s'éloigner en raison de l'élimination de la chaleur du bain de He II. À des flux de chaleur élevés, le début de l'ébullition du film a lieu si rapidement que la transformation He II-He I est entravée depuis le début du transitoire. La phase vapeur se dilate alors proportionnellement au flux thermique.

4. Pour les flux de chaleur élevés, un incrément de température temporaire en forme de bosse est toujours observé au début des tests de flux clampés. Cette augmentation diminue vers le bain mais se produit au même moment à chaque endroit du canal. En tant que tel, il a été attribué à une augmentation de température par diffusion qui s'arrête au début de l'ébullition du film, lorsque la température redescend dans la gamme He II. Le pic de la bosse diminue avec des flux de chaleur plus importants jusqu'à ce qu'il disparaisse. De plus, le phénomène est absent à des températures de bain plus élevées (c'est-à-dire proches du point λ), où le début de l'ébullition du film se produit presque immédiatement après l'application du flux thermique.

5. Pour des flux de chaleur élevés et une température du bain proche du point λ, l'évolution de la température aux endroits éloignés de l'élément chauffant connaît une forte augmentation de la pente qui ne se produit à aucune température significative (c'est-à-dire entre les points lambda et de saturation). Lorsque l'ébullition commence au niveau du réchauffeur, la phase vapeur s'étend et les grandes différences de densité qui en résultent provoquent des phénomènes d'advection qui altèrent le caractère diffusif du transport de chaleur dans le canal.

6. L'orientation du canal a un impact significatif sur l'évolution de la température si l'He II subit des transitions de phase pendant l'essai. Étant donné que l'expansivité thermique de l'hélium liquide change de signe à travers le point λ, une augmentation de la température de l'He I et de la vapeur entraîne des flux de convection naturelle en amont. Par conséquent, dans les canaux verticaux, les phases fluides plus légères ont tendance à rester en haut du canal dans le cas de flux de chaleur descendants ou à remonter le canal vers le bain dans le cas de flux de chaleur ascendants. Dans ce dernier cas, l'extraction de la chaleur due à l'ébullition entraîne une augmentation plus faible de la température de l'élément chauffant.

7. Contrairement à l'orientation horizontale, dans les canaux verticaux descendants, la région He I ne s'étend jamais à une grande partie du canal. Comme le renforcement du film de vapeur est assisté par la gravité, même les faibles flux de chaleur sont suffisamment importants pour générer un film isolant stable. Comme expliqué précédemment, il en résulte une phase mince de He I restreinte entre He II et la vapeur.

8. L'évolution de la température dans les canaux ascendants atteint l'état d'équilibre en moins de secondes que dans l'orientation horizontale. Dans cette configuration, à des flux de chaleur faibles et modérés, la température fluctue fortement dans la gamme He I dans la majeure partie du canal. Les fluctuations diminuent avec l'augmentation des flux de chaleur. Ce comportement instable est associé à un processus d'ébullition en cours, qui est atténué par l'apparition du régime d'ébullition en film. Lorsque l'énergie dissipée est suffisamment élevée pour soutenir le film de vapeur, le transfert de chaleur diminue et la température loin du réchauffeur retourne dans la gamme He II.

9. L'épaisseur des canaux détermine la proportion relative entre les différentes phases de l'hélium. Contrairement au canal de 0.2 mm d'épaisseur, dans le canal plus épais, la phase He I ne couvre pas une grande partie du canal indépendamment du flux de chaleur (voir Fig. 6.2). Par conséquent, plus le canal est mince, plus la phase He I s'étend longitudinalement. On peut en conclure que l'épaisseur de la région He I diminue avec l'augmentation des dimensions caractéristiques de la géométrie jusqu'à atteindre une valeur minimale déterminée par He II et la vapeur.

10. Dans le canal descendant non confiné (c'est-à-dire d'une épaisseur de 0.5 mm), l'augmentation temporaire de température induite par la diffusion au début des transitoires se résout beaucoup plus rapidement par rapport au canal confiné. De plus, l'augmentation du flux thermique raccourcit la durée du pic mais n'affecte pas sa valeur maximale.

11. Dans le canal ascendant non confiné, la plus grande surface de chauffe par rapport au canal confiné ainsi que l'action de la gravité retardent le début de l'ébullition du film, qui est responsable de l'interruption de la connexion thermique entre le réchauffeur et He II. En conséquence, il n'a pas été identifié de flux de chaleur au-dessus duquel la température loin du réchauffeur retourne en dessous du point λ, comme dans le cas du canal plus fin.

Propagation à double front

1. Si la température est suffisamment inférieure à T_λ et que le flux de chaleur est modérément faible (c'est-à-dire inférieur à 10^5 W/m^2), la vitesse du front λ est inversement proportionnelle à la racine cubique de la position du front dans le canal. Cependant, si la température est proche de T_λ ou si le flux de chaleur est

trop important, la pente du profil de vitesse change, modifiée par la phase vapeur croissante.

2. Dans le canal confiné, à un endroit constant non éloigné de la surface chauffante, la vitesse du front λ varie différemment selon la gamme de flux thermique. En référence à la catégorisation introduite au point 3 du paragraphe précédent, il est possible de distinguer trois zones principales : la vitesse augmente fortement avec le flux thermique (zone basse) ; la vitesse diminue avec l'augmentation du flux thermique (zone intermédiaire) ; la vitesse augmente faiblement avec le flux thermique (zone haute). Étant donné que, dans la zone intermédiaire, la propagation du front λ ralentit et s'arrête plus tôt, cette zone est absente aux endroits les plus éloignés de l'appareil de chauffage. En raison du changement de comportement entre la zone basse et la zone intermédiaire, il existe une vitesse maximale et une longueur maximale couverte par le front.

3. Le front d'ébullition se déplace beaucoup plus lentement que le front λ. Contrairement à ce dernier, le front d'ébullition ne présente que deux zones de comportement : la vitesse augmente avec le flux thermique avec une dérivée seconde négative jusqu'à une valeur maximale (première zone) ; la vitesse augmente faiblement avec le flux thermique au même rythme que le front λ (deuxième zone). La première zone correspond approximativement à la zone basse du front λ. Étant donné que la deuxième zone correspond à la fois à la zone de front λ modéré et à la zone de front λ élevé, le taux de croissance similaire dans la deuxième zone indique que la propagation du front λ est principalement déterminée par l'expansion de la phase vapeur et donc de la propagation du front d'ébullition.

4. Les différents niveaux de confinement géométrique affectent de manière significative la relation entre la vitesse du front d'ébullition et le flux thermique. Dans le canal non confiné, seules deux zones peuvent être distinguées : la vitesse augmente fortement avec le flux thermique (zone basse) ; la vitesse varie faiblement avec le flux thermique (zone haute). Comme le niveau de confinement est plus faible, les phases vapeur et He I se dilatent plus facilement et, par conséquent, la vitesse du front λ dans la zone haute est supérieure à la valeur maximale atteinte dans le canal confiné.

5. En raison de l'augmentation de la température due à la diffusion dans les premiers instants des transitoires (voir le point 4 du paragraphe précédent), le front λ peut traverser deux fois le même endroit dans le canal. Le front primaire est dû à la diffusion et se déplace à la vitesse typique d'un front λ, tandis que le front secondaire est dû à l'expansion de la vapeur et se déplace à la vitesse typique d'un front d'ébullition.

Modélisation et simulations des changements de phase

1. La comparaison des données recueillies lors des expériences He I à flux thermique modéré avec un modèle numérique multiphase pour les phénomènes d'ébullition a révélé une bonne précision du modèle avec une erreur relative des profils de température transitoire autour de 10 %. Ce modèle exploite la dépendance enthalpique des propriétés thermophysiques pour dériver les fractions de masse et de volume de manière explicite sans suivre l'interface vapeur-He I. Le modèle implémente également un module de force de surface continue pour le calcul des forces de tension de surface agissant sur l'interface du mélange.

2. En combinant les équations de transfert de chaleur de He I et He II, il est possible de dériver une équation non linéaire pour la position du front λ dans des grilles de calcul orthogonales non uniformes fixes. La résolution de cette équation par la méthode itérative de Newton-Raphson a donné des résultats cohérents et rapides.

3. La comparaison des données recueillies au cours des expériences He II à flux thermique modéré avec un modèle numérique multiphase pour les phénomènes triphasés a révélé une bonne précision du modèle avec une erreur relative des profils de température transitoire autour de 10 %. Le modèle est basé sur un algorithme PIMPLE modifié, qui inclut le module pour l'identification de l'emplacement du front λ. Ce module additionnel permet de corriger au front λ les champs de He II qui dépendent du gradient de température. La position prédite du front λ varie faiblement avec la taille des volumes de contrôle.

4. Le modèle numérique triphasé simule de manière satisfaisante la propagation des fronts de changement de phase. La partie du canal occupée par la phase He I ressemble à celle observée dans les expériences du canal non confiné. Les simulations ont révélé que l'interface de saturation entre la vapeur et l'He I est plus mince si l'ébullition se produit dans un environnement initialement constitué uniquement d'He II.

C.2 Travaux futurs

La présente étude n'est pas exempte d'améliorations potentielles, tant sur le plan expérimental que numérique. En raison des propriétés thermophysiques comparables entre la vapeur d'hélium et les matériaux solides constituant le montage, les expériences ont souffert d'inévitables pertes d'énergie. De plus, les capteurs de pression n'ont pas mesuré de variation pertinente pendant les essais. Pour résoudre ce type de problèmes, le montage du canal peut être amélioré sous différents aspects, qui sont énumérés ci-dessous :

- Afin d'assurer le contact exclusif de la surface chauffante avec l'hélium, le réchauffeur pourrait être plutôt installé au milieu du canal, qui serait maintenu ouvert au bain dans les deux ouvertures.

- Le canal pourrait être isolé davantage pour minimiser les pertes de chaleur en réalisant les expériences sous vide, le bain n'étant connecté qu'aux ouvertures.
- Puisque les capteurs de pression semblaient perturber les mesures de température, la configuration des sondes pourrait être modifiée pour maximiser l'espace entre elles.
- Afin de mesurer des changements de pression significatifs, il pourrait être nécessaire de fermer l'ouverture du canal pour maintenir des conditions isochoriques comme dans le cas du bain stagnant entourant les dipôles magnétiques du LHC.
- L'utilisation de techniques de visualisation permettrait de découvrir plus d'informations sur la propagation du double-front dans des environnements tridimensionnels.

Le modèle numérique présenté dans ce travail peut représenter un outil utile dans la prédiction des phénomènes de quench en combinaison avec les solveurs magnétiques. Cependant, à cette fin, le modèle doit être amélioré de plusieurs façons, dont quelques-unes sont énumérées ci-dessous :

- Les équations gouvernantes de He II pourraient être modifiées pour inclure le terme de chute de pression pour les applications à écoulement forcé.
- En changeant les schémas de discrétisation et les solveurs matriciels, et en introduisant différents niveaux de facteurs de relaxation, il pourrait être possible d'améliorer la robustesse du code, permettant d'exécuter des simulations à des flux de chaleur plus élevés.
- L'algorithme de correction du gradient de température pourrait être généralisé pour le rendre applicable aux grilles non orthogonales ou non structurées.
- Les tables d'interpolation des propriétés thermophysiques de l'hélium pourraient être remplacées par des tables à deux variables pour inclure la dépendance à la pression.
- Le calcul polynomial des propriétés thermophysiques des solides pourrait être remplacé par des tables d'interpolation pour accélérer le solveur et augmenter la précision.

université PARIS-SACLAY

ÉCOLE DOCTORALE
Particules, hadrons, énergie et noyau : instrumentation, imagerie, cosmos et simulation (PHENIICS)

Titre : Etude des Transferts de Masse et de Chaleur en Hélium Superfluide en Milieux Confinés

Mots clés : hélium superfluide, transition de phase, multiphase, transfert de chaleur, cryogénie

Résumé : Les accélérateurs de particules jouent un rôle central dans l'avancement de la recherche en physique fondamentale. Dans les accélérateurs circulaires tels que le Large Hadron Collider (LHC) du CERN, la trajectoire des faisceaux de particules doit être courbée par des champs magnétiques. À cette fin, le LHC utilise des aimants dipolaires supraconducteurs, qui permettent au courant électrique de circuler sans résistance. Un système de refroidissement à l'hélium superfluide (He II) assure l'état supraconducteur en maintenant les aimants à des températures inférieures à 2 K. Toutefois, les structures confinées qui entourent les bobines dipôlaires entravent le processus de refroidissement. Les colliers métalliques, qui permettent de contrer les forces électromagnétiques, sont espacés de 200 microns les uns des autres. Si les aimants perdent leurs propriétés supraconductrices (par exemple, lors d'un quench de l'aimant), l'énergie dissipée est telle que l'hélium subit des changements thermodynamiques drastiques, pouvant entraîner la défaillance de la machine et de graves dommages à ses composants. Le présent travail se concentre sur les phénomènes thermiques en He II se produisant à ce niveau de confinement géométrique lorsqu'il est soumis à des flux de chaleur élevés. Des expériences ont été menées dans un cryostat en He II pressurisé à différentes températures de bain. Les essais ont consisté à appliquer un flux de chaleur de confinement dans des canaux de section rectangulaire avec des rapports d'aspect élevés, ressemblant à l'espace entre les colliers métalliques. De nombreux essais ont été réalisés avec différentes orientations et épaisseurs de canaux. Un modèle numérique dynamique thermo-fluide a été développé pour simuler le transfert de chaleur et de masse dans l'He II. De nouveaux nombres sans dimension ont été dérivés pour valider l'hypothèse à la base des équations gouvernantes monofluide mises en œuvre dans le modèle. Le modèle numérique, qui est basé sur la méthode des volumes finis, est capable de simuler des événements transitoires de transfert de chaleur conjugués dans des géométries multidimensionnelles. De plus, un nouvel algorithme a été conceptualisé pour traiter les transitions de phase de second et premier ordre que l'hélium subit au-dessus des flux de chaleur critiques. À la pression atmosphérique, la transition de second ordre (c'est-à-dire la transition lambda) est associée au seuil de l'état superfluide, tandis que la transition de premier ordre relie l'hélium liquide à la vapeur d'hélium. Les expériences en He II ont permis d'obtenir des mesures de température fiables avec une incertitude de précision d'environ 0.12 %. Le modèle de l'hélium superfluide a été validé avec succès par rapport aux données expérimentales de la littérature et de ce travail avec une erreur relative d'environ 1 %. Les expériences impliquant plusieurs phases de l'hélium ont révélé une dépendance significative de la proportion entre les différentes phases sur l'épaisseur et l'orientation du canal, ainsi que sur la température initiale du fluide. La vitesse à laquelle l'interface hélium liquide-He II se déplace semble être fortement affectée par la présence d'un film de vapeur d'hélium. À des flux de chaleur élevés, les fronts de changement de phase se propagent à une vitesse similaire, indiquant une forte corrélation entre les deux. L'algorithme des transitions de phase a été testé à des flux de chaleur modérés dans de l'hélium liquide sous-refroidi et de l'He II. La comparaison avec les expériences en canal a montré un accord satisfaisant dans les profils de température et la propagation des fronts de changement de phase avec une erreur relative d'environ 10 %. Le modèle de calcul peut constituer la base d'un développement ultérieur du code pour la simulation d'événements à des variations de pression et de température plus importantes.

université PARIS-SACLAY

ÉCOLE DOCTORALE
Particules, hadrons, énergie et noyau : instrumentation, imagerie, cosmos et simulation (PHENIICS)

Title : Study of Heat and Mass Transfer in Superfluid Helium in Confined Geometries

Keywords : superfluid helium, phase transition, multiphase, heat transfer, cryogenics

Abstract : Particle accelerators play a central role in the advancement of fundamental physics research. In circular accelerators such as the Large Hadron Collider (LHC) at CERN, the trajectory of the particle beams must be bent with magnetic fields. For this purpose, the LHC utilizes superconducting dipole magnets, which allow the electric current to flow without resistance. A cooling system of superfluid helium (He II) ensures the superconducting state by maintaining the magnets at temperatures below 2 K. However, the confined structures surrounding the dipole coils hinder the cooling process. The metal collars, which restrict the dipoles to counter the electromagnetic forces, are spaced 200 microns apart from each other. If the magnets lose the superconductive properties (i.e., during a magnet quench), the energy dissipated is such that helium undergoes drastic thermodynamic changes, causing the failure of the machine and severe damages to its components. The present work focuses on the thermal phenomena occurring at this level of geometrical confinement in He II when subject to high heat fluxes. Experiments were conducted in a cryostat with pressurized He II at various bath temperatures. The tests consisted of applying a clamped heat flux in rectangular cross-section channels with high aspect ratios, resembling the gap between the collars. Numerous tests were carried out with different channel orientations and thicknesses. A thermo-fluid dynamic numerical model was developed to simulate the heat and mass transfer in He II. Novel dimensionless numbers were derived to validate the assumption at the basis of the single-fluid governing equations implemented in the model. The numerical model, which is based on the finite volume method, is capable of simulating transient conjugate heat transfer events in multi-dimensional geometries.

Moreover, a novel algorithm was conceptualized to deal with the second and first-order phase transitions that helium undergoes above the critical heat fluxes. At atmospheric pressure, the second-order one (i.e., lambda transition) is associated with the threshold of the superfluid state, whereas the first-order one relates liquid helium to helium vapour. The experiments in He II resulted in reliable temperature measurements with a precision uncertainty of around 0.12 %. The superfluid helium model was successfully validated against experimental data from both the literature and this work with a relative error around 1 %. The experiments that involved multiple helium phases revealed a significant dependence of the proportion between the different phases on the channel thickness and orientation, as well as the initial temperature of the fluid. The speed at which the liquid helium-He II interface travels appears to be highly affected by the presence of a helium vapour film. At high heat fluxes, the phase change fronts propagate at a similar rate, indicating a strong correlation between the two. The phase transitions algorithm was tested at moderate heat fluxes in both subcooled liquid helium and He II. The comparison with the channel experiments showed satisfactory agreement in the temperature profiles and propagation of the phase change fronts with a relative error around 10 %. The computational model may constitute the basis of further development of the code for the simulation of events at greater pressure and temperature variations.